Should research animals get names? *p. 941*

RNA interference targets Colorado potato beetle *pp. 950 & 991*

Optical twists and turns make a Möbius strip *p. 964*

Science

$10
27 FEBRUARY 2015
sciencemag.org

AAAS

Locked in

Blocking an ion channel keeps Ebola virus from escaping cell vesicles

pp. 947 & 995

CONTENTS

945 & 998

How wheat got to Britain

27 FEBRUARY 2015 • VOLUME 347 • ISSUE 6225

NEWS

IN BRIEF

IN DEPTH

FEATURES

INSIGHTS

PERSPECTIVES

PHOTO: © JOANNA B. PINNEO

BOOKS *ET AL.*

LETTERS

Published by AAAS

CONTENTS

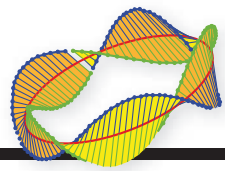

964 Twisting light into a Möbius strip

27 FEBRUARY 2015 • VOLUME 347 • ISSUE 6225

ON THE COVER

Ebola virus enters into cells in small vesicles called endosomes. Virus eventually moves into endosomes that have both NPC1 (dark blue rods) and TPC2 (yellow spikes) proteins on their membranes and then into vesicles with TPC2 only. By disrupting the function of TPC2 with drugs, the virus is locked into the endosome, unable to be released to infect the cell. See pages 947 and 995. *Illustration: Valerie Altounian*/Science

948 & 985

SCIENCE (ISSN 0036-8075) is published weekly on Friday, except the last week in December, by the American Association for the Advancement of Science, 1200 New York Avenue, NW, Washington, DC 20005. Periodicals mail postage (publication No. 484460) paid at Washington, DC, and additional mailing offices. Domestic individual membership and subscription (51 issues): $153 ($74 allocated to subscription). Domestic institutional subscription (51 issues): $1282; Foreign postage extra: Mexico, Caribbean (surface mail) $55; other countries (air assist delivery) $85. First class, airmail, student, and emeritus rates on request. Canadian rates with GST available upon request, GST #1254 88122. Publications Mail Agreement Number 1069624. **Printed in the U.S.A.**
Change of address: Allow 4 weeks, giving old and new addresses and 8-digit account number. **Postmaster:** Send change of address to AAAS, P.O. Box 96178, Washington, DC 20090–6178. **Single-copy sales:** $10.00 current issue, $15.00 back issue prepaid includes surface postage; bulk rates on request.

Published by AAAS

EDITORIAL

Wider attention for GOF science

In October 2014, the U.S. government paused funding for so-called gain-of-function (GOF) research involving pathogens with pandemic potential, to allow for a systematic assessment of its benefits and risks. The topic raises critical questions for society as a whole, and decisions cannot be left with the scientific community alone.

The current suspension in funding is the latest twist in unsteady policy-making regarding GOF research that is designed to enhance the transmissibility or pathogenicity of disease-causing agents. The issue came to public notice in 2012 over the question of whether to publish experiments that showed it was possible to develop variants of the H5N1 avian influenza virus that would transmit readily in a mammal. Scientists engaged in this research adopted a voluntary suspension of studies so that there could be more discussion and public education, and later lifted the self-imposed moratorium. The U.S. National Science Advisory Board for Biosecurity (NSABB), charged with reviewing such matters, initially voted to publish redacted versions of the work, but after meetings in which the science and implications of the information were clarified, relented in a split vote. After several unrelated incidents of mishandling of dangerous pathogens in federal laboratories came to light in 2014, the U.S. government paused funding for GOF research on coronaviruses that cause severe acute respiratory syndrome (SARS) and Middle Eastern respiratory syndrome (MERS), as well as influenza virus.

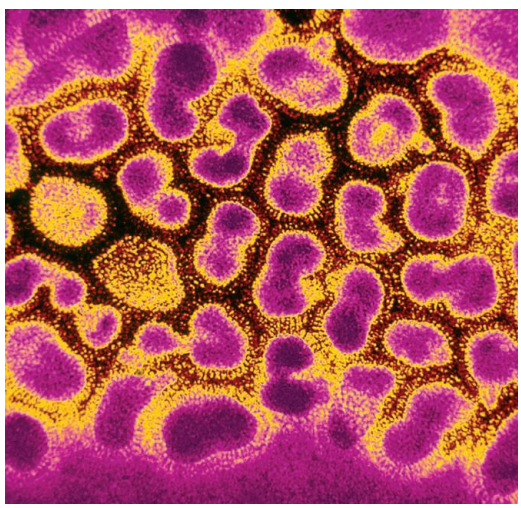

"...decisions cannot be left with the scientific community alone."

Proponents of GOF research argue that it may aid in recognizing emerging pandemic strains and help identify optimal vaccine strains. Proponents of caution raise questions about whether the research will be conducted safely and the potential for discoveries to be intentionally misused. The NSABB now has the lead in conducting a process of assessment and advice over the next 12 months, which will take advantage of input from workshops organized by the U.S. National Academies* and will include an independent evaluation of benefits and risks.

The task ahead is complex and difficult. Important but subtle scientific distinctions have to be made, as evidenced by the lifting of the latest moratorium (2 months after it was instituted) for MERS viruses, which have no laboratory animal model and cellular receptors that vary markedly across species. A particular challenge in conducting a risk/benefit analysis is considering the combination of very low-probability events and potentially catastrophic consequences. Intelligent policy will need to be explicit, defining precisely under what circumstances and conditions distinct types of research in specified locations should go forward. Policy will need to take into account the perspectives and concerns of both biosecurity and biosafety.

Implications for attracting scientists to or discouraging them from crucial fields of investigation are a genuine concern. From a global perspective, policies and practices will need to be harmonized across countries if the world is to maintain a strategic and coherent approach. The World Health Organization is a logical (if problematic) place to seek such coherence in international policy and practice.

Even a comprehensive and well-informed risk/benefit analysis will not itself lead to clear-cut answers. Judgments by those from different scientific and lay perspectives will be critical to sound decision-making. The input of scientists and funders is no longer sufficient to make appropriate, socially defensible choices about research that has such social dimensions. This is different from corporate judgments or governments deciding what is in their national interests. The benefits and risks of doing such research do not apply equally to all people, institutions, or countries, and a rigorous risk/benefit analysis will have to be mindful of these inequities and hear from various stakeholders.

How scientists participate in the deliberations, as engaged listeners even more than as expert instructors, can serve to reinforce public confidence in science, well beyond the specific types of studies that are in question.

– Harvey V. Fineberg

Harvey V. Fineberg is president of the Gordon and Betty Moore Foundation and chaired the planning committee for the 2014 National Research Council–Institute of Medicine workshop on GOF research. E-mail: harvey.fineberg@moore.org*

*http://dels.nas.edu/resources/static-assets/bls/miscellaneous/gofagenda.pdf.

10.1126/science.aaa7711

IMAGES: (INSET) SCIENCE SOURCE; (RIGHT) WEBER SHIH

NEWS

> "We have so much great data ... this data is the citizens' data."
>
> **New U.S. Chief Data Scientist DJ Patil**, in a 20 February "memo to the American people" outlining how he will advise the White House on investing in data science and research.

IN BRIEF

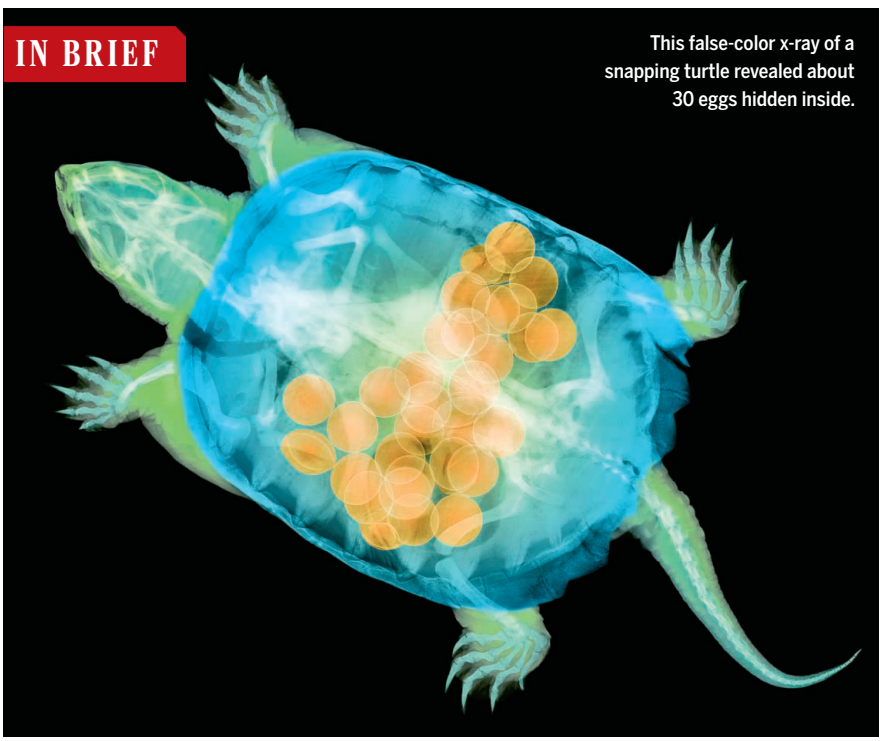

This false-color x-ray of a snapping turtle revealed about 30 eggs hidden inside.

Science is beautiful

A snapping turtle's hidden eggs, a forest of neurons, and the seahorse-shaped hippocampus were among the colorful, complex muses for the winning entries in the 2015 Vizzies, or Visualization Challenge, sponsored by the National Science Foundation and *Popular Science*. Each category—photography, video, illustration, posters & graphics, and games & apps—includes an Experts' Choice prize of $2500 and a People's Choice prize of $1000. The Experts' Choice winner for photography, shown here, was a false-color x-ray image of a snapping turtle that revealed several dozen eggs inside her. In the posters & graphics category, the Experts' Choice prize went to a creative depiction of the brain's hippocampus, responsible for acquiring some memories; real hippocampal neurons were digitally added to a pair of seahorses. Both the Experts' Choice and People's Choice prizes in illustration went to "Neuroforest," an image taken from a graphic novel depicting the adventures of a man who fell into a brain and wanders through a dense forest network of brain cells and neurons. A full list of winners and more information on the competition is available at http://www.nsf.gov/news/special_reports/scivis/index.jsp.

PHOTO: TED KINSMAN/NSF/*POPULAR SCIENCE*

AROUND THE WORLD

E.U.'s first stem cell therapy

BRUSSELS | Europe's first commercial stem cell product, developed to reverse blindness caused by burns and chemical damage to the eye's surface, was authorized by the European Commission on 19 February. The therapy, called Holoclar, uses stem cells from the healthy part of a patient's limbus (the border between the cornea and the white of the eye). The cells are lab-cultured and then implanted into the damaged eye. Holoclar was first developed by the University of Modena and Reggio Emilia in Italy and will be commercialized by Chiesi Farmaceutici. The commission's final approval followed the European Medicines Agency's green light for the therapy in December 2014.

New rapid Ebola test

GENEVA, SWITZERLAND | The World Health Organization (WHO) has approved the first rapid diagnostic test for Ebola. Unlike current PCR-based tests, which require a blood sample taken by needle, secure transport of the blood to a properly equipped laboratory with trained staff, and at least several hours to return results, the new test needs no electricity, requires just a few drops of blood from a finger prick, and can return results in 15 minutes. Produced by Broomfield, Colorado–based Corgenix, the test uses antibodies to identify a specific Ebola virus protein. WHO notes that it correctly identifies 92% of infected people and 85% of uninfected ones. It will cost about $15, although discounts will be available for bulk purchases and suppliers for use in Africa. http://scim.ag/rapidebola

Resistant malaria nears India

HOMALIN, MYANMAR | Malaria parasites that are resistant to the most powerful antimalaria drug may have spread to the border of Myanmar and India, a potential disaster for global malaria control. A genetic study of malaria parasites across Myanmar, published online on 19 February in *The Lancet Infectious Diseases*, found

Published by AAAS

Shall we play a game?

Those Space Invaders may have finally met their match. A team of scientists has developed an artificial intelligence system that has taught itself to play dozens of classic computer games—and in many cases, it plays them better than professional gamers, the researchers note this week in *Nature*. Led by Volodymyr Mnih of Google DeepMind in London, the team trained their new artificial "agent" to master 49 different Atari 2600 games—which requires adapting to a variety of tasks—solely from its study of data, rather than from any programmed behavior. The agent, called a deep Q-network, combines reinforcement learning techniques with a biologically inspired artificial neural network known as a deep neural network. To "learn" how to beat the games (and human games testers), the deep Q-network examined large data sets and learned what would increase its score.

An AI system has mastered *Space Invaders* and 48 other classic Atari games.

widespread mutations in a gene that plays a key role in resistance to artemisinin, the best drug available to cure the disease. Follow-up studies are needed to confirm that the mutations correspond to clinical resistance in patients, but the pattern is worrisome, the authors say. Resistant parasites appeared a decade ago in Cambodia and Thailand, and experts have been warning that they would spread. The new study suggests they may have spread farther and faster than experts had realized—or feared.

Nature offers double-blind reviews

LONDON | Nature Publishing Group (NPG) announced last week that most of its publications, including flagship journal *Nature*, will offer authors the option of double-blind peer review, in which both submitters and referees remain anonymous. Traditionally, scientific journals adhere to a single-blind system in which authors don't know the identity of reviewers, but that has led to concerns about antiauthor biases. NPG began testing the double-blind system with *Nature Climate Change* and *Nature Geoscience* in May 2013, a trial that "gave us plenty to be confident about," says Véronique Kiermer, director of author and reviewer services at NPG. But, she says, the option of complete anonymity will be "an ongoing experiment." Meanwhile, editors at other journals, including *Science*, haven't made the jump, in part out of concern that reviewers may still be able to guess the identity of authors, particularly in small fields.
http://scim.ag/dblblind

FINDINGS

Eating peanuts cuts allergy risk

In news that electrified the allergy world this week, a group of scientists reported that eating peanuts slashes the chance of an allergy, at least in children at high risk of developing one. The trial, published in *The New England Journal of Medicine*, is the largest and longest running of its kind, enrolling 640 babies and following them until they were 5 years old. It found that 17% of children who avoided peanuts became allergic, compared with 3% of those who ate modest amounts several times a week. The authors argued that many babies and toddlers who avoid peanut develop allergy because they are still exposed through the skin and that ingesting peanut products helps the body learn to tolerate them. The results are likely to catapult a long-standing theory into mainstream medicine.
http://scim.ag/peanuteat

Peanuts consumption may prevent allergies.

NEWSMAKERS

Court overrules misconduct panel

A Danish court has overturned a committee's verdict of scientific misconduct and awarded 400,000 Danish kroner ($61,000) in legal expenses to a physiologist at the University of Copenhagen. In December 2013, the Danish Committees on Scientific Dishonesty found **Bente Klarlund Pedersen** guilty of "gross negligence" for failing to detect images that had been manipulated by a co-author and found that her reuse of biopsy samples in multiple papers constituted "unclear construction of data." Klarlund challenged the verdict in court, arguing that using biopsies for multiple studies was common practice and that failing to detect fraud committed by a co-author was a mistake but not gross negligence. On 18 February the court ruled in her favor on both counts, stating that there is a "crucial difference" between deliberately manipulating images and failing to detect manipulations by collaborators.

IPCC head resigns

Rajendra Pachauri, chair of the Intergovernmental Panel on Climate Change (IPCC) since 2002, stepped down on 24 February amid allegations of sexual harassment by a female colleague at The Energy and Resources Institute, a New Delhi–based think tank led by Pachauri. In a letter addressed to U.N. Secretary-General Ban Ki-moon, Pachauri said that "[t]he IPCC needs strong leadership and dedication of time ... which, under the current circumstances, I may be unable to provide." The staffer's complaint, now under investigation by local police, states that Pachauri sent her messages with sexual undertones. Pachauri's lawyers have countered that his computer had been hacked; Pachauri himself was unavailable for comment. Vice Chair Ismail El Gizouli will be acting IPCC chair until elections are held for the position in October.

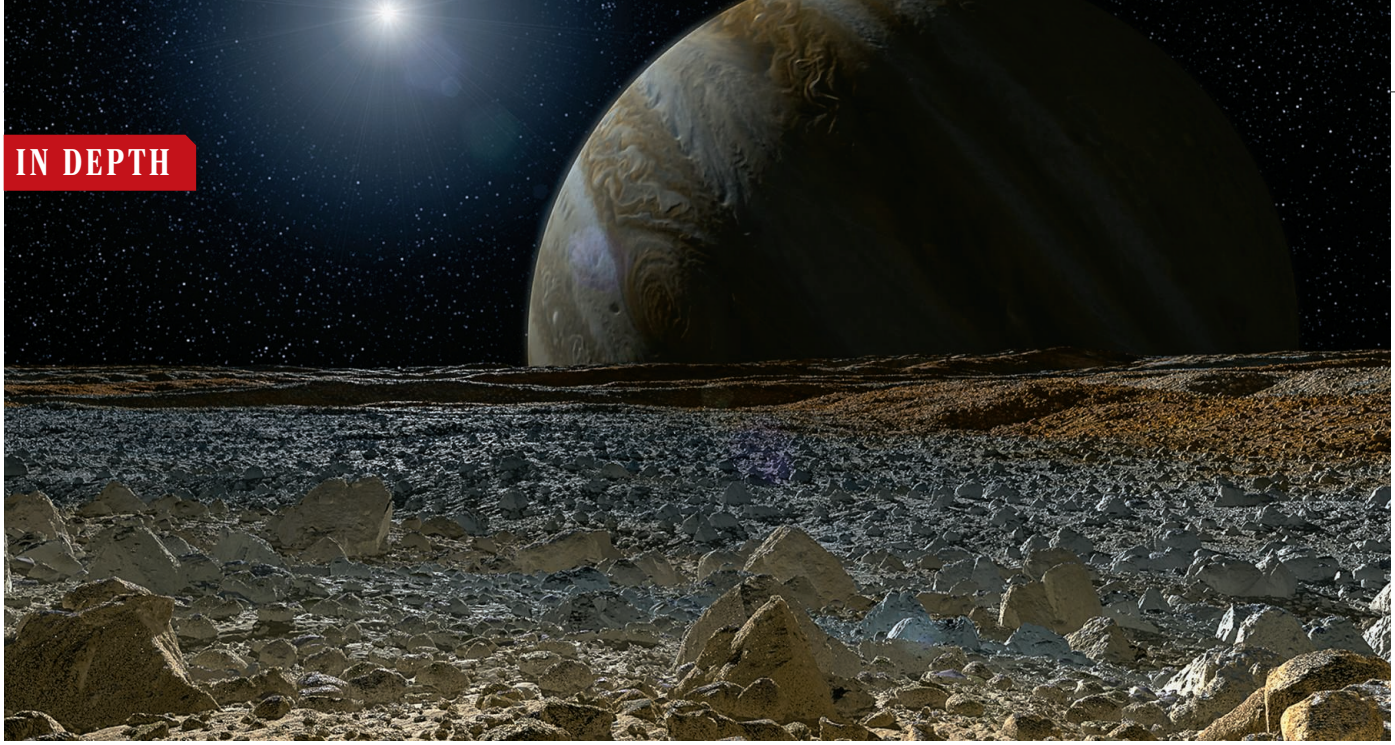

IMAGE: NASA/JPL-CALTECH

PLANETARY SCIENCE

Plumes on Europa tease NASA mission planners

Astrobiologists covet chance to sample subterranean ocean, but plumes may come and go

By **Eric Hand**

A proposed NASA mission to Jupiter's moon Europa is gathering momentum. Congress has long been enthusiastic, and earlier this month the White House finally signed on to the $2 billion mission to investigate the habitability of Europa, which might host life in its deep, hidden saltwater ocean. Lately the mission has also gained a tantalizing target: plumes of water vapor that seem to erupt through the moon's icy crust, presumably sweeping any organic molecules into space, where they might be detectable.

The trouble is, the plumes might not exist. Observers spotted them with the Hubble Space Telescope in 2012, detecting the fluorescence of oxygen and hydrogen in the water molecules as they were bombarded by electrons whipped up by Jupiter's intense magnetic fields. But dozens of other observational campaigns have failed to spot any plume. That posed a dilemma for the scientists who gathered last week at NASA's Ames Research Center in Mountain View, California, to discuss how the presence of plumes—or their absence—should affect planning for the mission.

Some say the payload instruments, which are to be selected by the end of April, should not be radically altered to go after something so tenuous and spotty. But others, including Ames astrobiologist Chris McKay, say that a plume—likely to be fresh from the underground ocean—would offer a special chance to look for life, and the craft should be equipped to study it. For now, planners expect to equip the spacecraft with cameras and a radar that would focus on understanding the structure and geologic history of the ice shell. "The current [recommended] payload is for a geophysics mission," McKay says. "It's not an astrobiology mission; it's not a life-detection mission. If you have the chance to fly through a plume, it's time to go organic."

He and his colleagues are fighting for that chance. On 2 February, U.S. President Barack Obama's budget request for 2016 included $30 million to start a Europa mission, which could launch in the mid-2020s. The move signaled the end of a spat between the administration and Congress, which had consistently allocated money to explore Europa—even though NASA had not yet agreed to the mission. "I'm thrilled, obviously," says Robert Pappalardo, who is removing the "pre" from his title as preproject scientist for the Europa Clipper mission concept at the Jet Propulsion Laboratory (JPL) in Pasadena, California. "We've been working for over 15 years in looking at mission concepts."

NASA says the mission won't officially start until later this year, but planetary scientists have already embraced a mission concept developed for Clipper. Europa orbits deep inside a belt of fierce radiation surrounding Jupiter. To limit the spacecraft's exposure, the Clipper concept envisions orbiting Jupiter rather than the moon and swooping in for 45 flybys of varying altitude. In July 2014, even before the administration backed the mission, NASA had put out a call for payload instrumentation.

Now researchers are debating the implications for the mission of the Hubble plume study, which was published in *Science* in 2014 (10 January, p. 171). One of the authors of the study, Kurt Retherford, a planetary astronomer at the Southwest Research Institute in San Antonio, Texas, says he would not shift the mission too much toward plume-chasing. The plumes had appeared in December 2012, just after Europa passed apocenter, the point in its orbit farthest from Jupiter. That's where tension would be highest on the moon's tidally stressed ice shell, making cracks most likely to open up. Yet in about 15 other attempts clustered around apocenter, Retherford's team has tried and failed to see plumes, he says. Retherford has booked time on Hubble for another 10 tries this year. "Until we know these plumes are recurrent, I wouldn't have all the [mission] instruments be focused on it, to be sure."

William Sparks, an astronomer at the Space Telescope Science Institute in Baltimore, Maryland, has been given Hubble time

Artist's impression of Jupiter as viewed from the icy surface of the moon Europa.

for a slightly different technique: watching Europa as it transits Jupiter's face and its thin atmosphere is lit up from behind. He says he has "intriguing" images from early 2014 that could show a plume but so far hasn't confirmed them.

Part of the problem is that, in Europa's stronger gravity, plumes will never spurt as high as they do at Saturn's moon Enceladus, where water escapes the moon's gravity altogether and helps form one of Saturn's rings. As a result, plumes at Europa would be more difficult both to observe remotely and to sample. There are also reasons to think the plumes might come and go, says Alyssa Rhoden, a planetary scientist at Johns Hopkins University's Applied Physics Laboratory in Laurel, Maryland. Europa has a small inclination in its orbital axis that wobbles with time. Rhoden's models suggest that this wobble causes the stress states in the ice to wander, too, opening and closing cracks. She, too, doesn't want too much instrumental capability centered on plume sampling. "Planning a mission around one data point would be a very dangerous proposition."

The jets themselves may seal cracks in the ice shell, says Sascha Kempf, a planetary scientist at the University of Colorado, Boulder. As water vapor rises through fissures in the ice, it can condense along the fissure walls and weld them shut, he says. In case the plumes exist—or even just for picking up traces of Europa's wispy atmosphere—Kempf thinks the Clipper should carry instruments similar to two spectrometers on NASA's Cassini Saturn probe, which is using them to identify the composition of both solid particles and gases in the Enceladus plume. (The spectrometers have identified a variety of organic molecules at Enceladus, but not the fragile, complex ones associated with life, such as amino acids.)

But Peter Willis, an astrobiologist at JPL, says such Cassini-style instruments probably won't help much with life detection if the Clipper flies through a plume at high speeds that destroy organic molecules. He wants to cushion the impact by capturing plume material with an aerogel—a kind of lightweight silica foam—like the one used to capture cosmic dust in the NASA Stardust mission. The material could then be dissolved in water or some other solvent before being fed into a spectrometer for detection. Willis would look for two things: the types of amino acids present, and also their chirality, or handedness. The 70 or so amino acids so far discovered in space show no preference for left- or right-handedness, but the 20 amino acids that make up proteins on Earth are exclusively left-handed.

McKay says the Clipper could also drop small independent satellites to sample a plume closer to the source, at slower speeds. Cassini did something similar when it released a probe called Huygens, contributed by the European Space Agency (ESA), which landed on Saturn's moon Titan in 2005. In a talk to planetary scientists after the Ames meeting, NASA's planetary division director, James Green, hinted that he was in discussion with ESA about another mission contribution. Green also suggested that the Europa payload could be changed later on if the plume science firms up. "Perhaps some additional instruments may need to be brought on," he says.

McKay isn't holding his breath. "I'm imagining they'll say 'life search' is the *next* mission," he says. ■

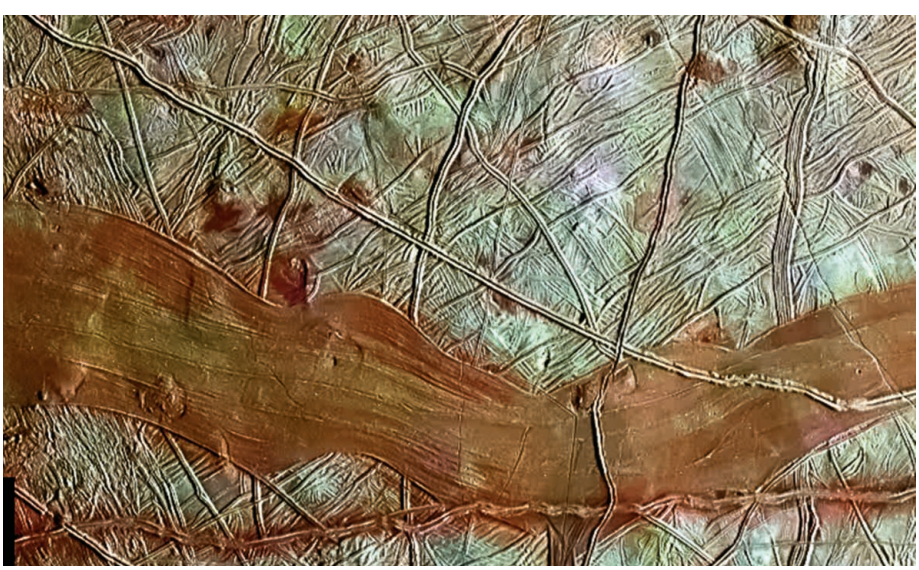

PHOTO: NASA/JPL-CALTECH/SETI INSTITUTE

Fissures and smooth plains indicate that an ocean sometimes erupts to resurface Europa.

SEISMIC RISK

New jitters over megaquakes in Himalayas

Large earthquakes in teeming region could strike anywhere, anytime

By **Priyanka Pulla**, *in Bangalore, India*

Seismologists worried about the prospect of a massive earthquake in the shadow of the Himalayas, where it could devastate cities such as Kathmandu and Delhi, have long cast a wary glance at an eerily calm region called the central seismic gap (CSG). A massive earthquake in southwestern Tibet in 1505 C.E., researchers proposed a decade ago, relieved enough strain to quiet that stretch of the restive Himalayas. But new findings now suggest that the 1505 temblor was smaller than thought and was just one of a cluster of potent quakes to rattle the region within a few centuries. If so, major quakes in the Himalayas, unlike in many other seismic hot spots, may not relieve enough strain to forestall later quakes—meaning that authorities must gird for a megaearthquake anywhere at any time.

Thrust up by the continuing collision of the Indian subcontinent with Asia, the Himalayas are frequently rattled by major earthquakes. But for several centuries, the CSG, a 600-kilometer-long region extending northeast of Delhi, has been quiet, even though it straddles major faults. In 2003, the late Greek geologist Nicholas Ambraseys and Roger Bilham, a geophysicist at the University of Colorado, Boulder, proposed that a large earthquake on 6 June 1505, known from Tibetan annals and the *Akbarnama*, a chronicle of the 16th century Mughal emperor Akbar's reign, could have relieved some of the strain building up at the CSG. Based on severe structural damage to Tibetan monasteries located nearly 700 kilometers apart, Ambraseys and Bilham estimated that the 1505 quake would have registered at 8.2 or so on the moment magnitude scale, which measures the energy released during an earthquake.

The geological smoking gun for the quake seemed to materialize a few years later. After digging six trenches at points along a 250-kilometer stretch of the CSG in 2006, ge-

ologist Senthil Kumar, who was then at the University of Nevada, Reno, and colleagues uncovered faults that could be radiocarbon dated using charcoal in the sediments. They attributed the faults to an earthquake between 1400 and 1422 C.E. But written records do not mention a major quake during this period, and because the charcoal dating's error bars encompassed 1505 C.E., Kumar's group chalked up the findings to the 1505 Tibetan quake. Also cited as evidence for that quake was a trench in western Nepal described only in an abstract in 2006.

Other experts, however, have doubted the 1505 earthquake's potency. Many medieval monasteries in the region are built from rock masonry without mortar, making them vulnerable to even moderate earthquakes, says Chittenipattu Rajendran, a paleoseismologist at the Jawaharlal Nehru Centre for Advanced Scientific Research here. Such damage, therefore, "is not realistic to use as an indicator of magnitude," says Rajendran, who adds that there is no historical record of extensive damage in Indian cities like Agra and Delhi in 1505.

To get a fresh perspective on the CSG's seismic history, Rajendran's group dug a new trench in the Uttarakhand district of Ramnagar, adjacent to a trench Kumar's team had excavated. They got lucky, uncovering a colluvial wedge of sediment—the geological signature of any quake that ruptures the earth's surface. The rupture briefly pushes up a scarp, which crumbles to form a wedge. Rajendran's team found that the material in the wedge had been ruptured not once, but twice, which could only mean two earthquakes, they say. Carbon dating linked both ruptures to earthquakes in 1255 C.E. and 1344 C.E. that are known from historical records, the team reports in an article posted online last month in the *Journal of Geophysical Research: Solid Earth*. Yet the trench showed no sign of a later, large earthquake.

R. Jayangondaperumal, a geologist at the Wadia Institute of Himalayan Geology in Dehradun and a member of Kumar's team in 2006, says a reanalysis he has conducted on their 2006 trenches also suggests a pair of earthquakes rather than a single one. The finding not only casts doubt on the extent of the strain-relieving quake in 1505 but also "confirms an irregular cycle for the earthquakes in Himalaya," says Jean-Louis Mugnier, a geologist at the University of Savoy, Bourget-du-Lac, in France who wasn't part of the study.

Bilham declined to comment on the new findings. But Laurent Bollinger, a geologist at France's Alternative Energies and Atomic Energy Commission, argues that the evidence so far is not persuasive enough to verify the clustering hypothesis or rule out the big 1505 quake. "There is a risk that there are some very big earthquakes that are being missed in the historical chronicles," he says. What's needed, he says, are more data from more trenches.

In the meantime, Mugnier says, disaster management authorities need to recognize that a massive temblor can strike anywhere in the Himalayas, at any time. "The level of risk is stable: always high." In 2013, India's National Disaster Management Authority estimated that an earthquake of magnitude 8 or greater just about anywhere in the rapidly urbanizing Himalayas would kill, on average, about 800,000 people. ■

An illusory calm

A 1505 earthquake thought to have relieved strain and lowered earthquake risk in the central seismic gap may have been smaller than thought and just one of a cluster of potent quakes to rattle the gap within a few centuries.

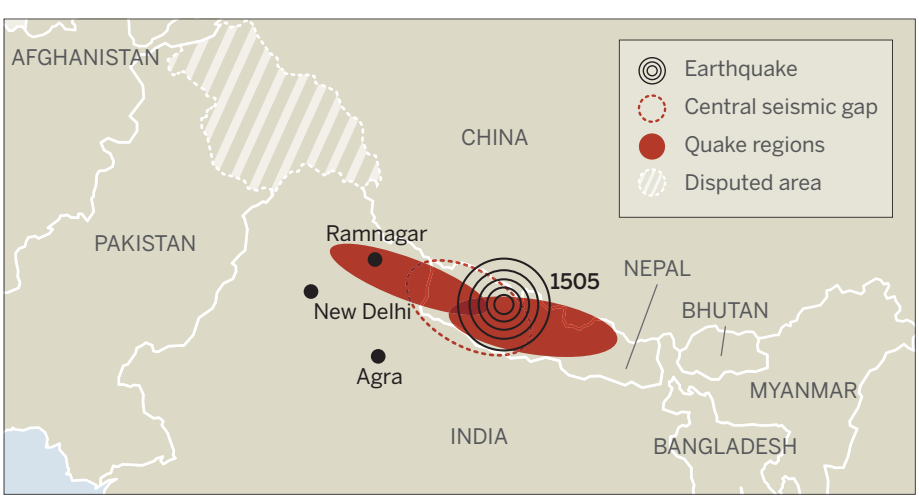

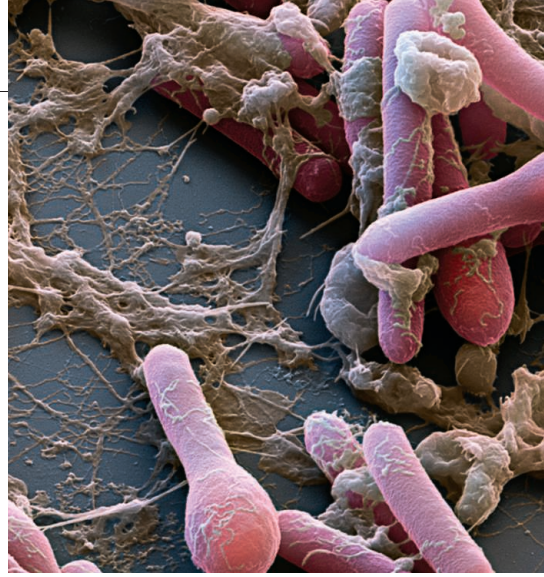

PHOTO: EYE OF SCIENCE/SCIENCE SOURCE

BIOSECURITY

As new botulism threat implodes, more questions

Secrecy around "toxin H" hampered research, government scientists say

By **Martin Enserink**

It appeared to be a serious new threat to biosecurity that justified an unusual level of scientific secrecy—until, suddenly, it wasn't. In 2013, Stephen Arnon of the California Department of Public Health (CDPH) reported finding a novel type of botulinum toxin against which no existing antitoxins offered protection, leaving society defenseless against bioterrorists who might manage to produce the compound and spread it through food or air. To protect against the threat, Arnon decided not to reveal the genetic sequence of the microbe that produced the toxin in his papers, a move that attracted considerable media attention.

But late last year, U.S. government researchers concluded that the secrecy was unnecessary because the toxin poses no special threat at all. They went on to post the entire sequence in GenBank. Their as-yet-unpublished findings were met with a sigh of relief in biodefense circles. But even today, many in the small field of botulinum research wonder how two labs could arrive at such radically different conclusions. And many say the episode could have ended much earlier—or been prevented altogether—if Arnon had been willing to share the strain of *Clostridium botulinum* with other labs sooner.

Clostridium botulinum produces the most lethal toxin in the world.

Arnon, a well-respected scientist who focuses on infant botulism, did not respond to repeated requests for comment for this story. *Science* sent him and CDPH a detailed list of questions on 29 January, which a representative said the agency would try to answer; it still hadn't done so on 23 February, when this story went to press.

Botulinum toxins, proteins that block the release of the neurotransmitter acetylcholine, are the most poisonous substances in the world: Less than a kilogram could, in theory, paralyze or kill every human alive. Scientists can produce antidotes to them by inoculating rabbits or horses with an inactivated version and then harvesting their antibody-laden serum. When a toxin isn't neutralized by any of the known antitoxins, it is called a new type. By this definition, scientists have discovered seven toxin types in the past century, dubbed A through G (see table).

In two papers in *The Journal of Infectious Diseases* (*JID*) in October 2013, Arnon's team described its research on a 5-gram stool sample from an infant. The *C. botulinum* strain they cultured produced the well-known toxin B, but also smaller quantities of another, unknown toxin. A genomic analysis showed that one end of the new substance most closely resembled an F toxin, while the other end looked more like a type A toxin. No known antitoxin could neutralize it, the researchers said, so it qualified as a new type, which they called H.

The case seemed a classic example of dual use research of concern, the scientific twilight zone in which some research is deemed too dangerous to publish. In an accompanying piece, *JID* editors Martin Hirsch and David Hooper explained that, given the threat, they had allowed Arnon not to publish the sequence of the strain, as *JID* normally requires. Arnon had consulted with representatives of 11 federal agencies, they explained, who had approved this solution.

A tussle had broken out long before the papers appeared. As National Public Radio (NPR) revealed last year, Arnon had notified U.S. government researchers about his discovery as early as 2011, but had initially refused to share the *C. botulinum* strain with them, apparently because he was worried it might fall into the wrong hands. Arnon finally sent the strain to the U.S. Centers for Disease Control and Prevention (CDC) in 2014, well after the publication of the papers; through an intermediary agency, CDC later made it available to other labs, including the Food and Drug Administration (FDA). "I would much rather have gotten my hands on the strain right away," says Donald Zink, a senior science adviser at FDA.

The U.S. government has denied that it urged that sequence data be withheld. In a letter in *JID* in May 2014, George Korch, a senior science adviser at the U.S. Department of Health and Human Services, confirmed that Arnon had talked to federal officials. But he said they hadn't read his manuscripts, and that "the US government did not approve or disapprove publication of the manuscript, did not recommend withholding the gene sequence, and did not place any conditions on the publication of the manuscript."

Arnon's boss, CDPH Director Ron Chapman, acknowledged errors and apologized in another letter in the journal. "Although the CDPH indicated to the media that this decision [to withhold the sequence data] was made at the behest of federal agencies, we now know that this is not the case," Chapman wrote.

Once they had the strain, CDC scientists concluded that Arnon's key scientific finding didn't hold up either, as NPR reported in December. Their work hasn't been published yet, but at an October meeting in Philadelphia and another in Lisbon in January, CDC reported that the toxin, although novel, is in fact neutralized by a commercially available antitoxin mix that protects against all seven previously known types. Further studies suggested that the protection was conferred by antibodies against toxin type A, which are part of the cocktail. Those findings removed any worries about bioterrorism, says Suzanne Kalb of CDC in Atlanta.

A team at FDA that sequenced the strain initially inquired about posting their data in GenBank with some form of a password protection, so that only legitimate researchers could access it. "I guess we wanted to be as deferential to Arnon's initial decision as possible," Zink says. But after consultations with CDC and the National Institutes of Health, the researchers posted the entire sequence in October 2014. Zink says they did not consult with Arnon.

If CDC is right and existing antitoxins protect against the new toxin, there is no reason to call it a new type, says Andreas Rummel, a botulinum researcher at Hannover Medical School in Germany. In a short paper in *Genome Announcements* in December, the FDA group called it a "New FA Mosaic Type" instead of type H; CDC has used the term "F/A Hybrid."

Why CDC and Arnon's lab reached such different conclusions about the neutralization isn't clear. In the *JID* paper, Arnon did report that very high concentrations of the heptavalent antitoxin appeared to inhibit the new toxin, but concluded this was due to an aspecific process that didn't count as proper neutralization. FDA's Zink says such discrepancies are a normal part of science. "Somebody does some work, they do it to the best of their ability, they reach a conclusion and they publish it," he says. "And sometimes other labs can't confirm it."

The alarm over the new toxin could have been prevented if Arnon had made the strain available to trusted labs earlier, says Eric Johnson of the University of Wisconsin, Madison, who wrote an angry letter in *JID* in May 2014 and received the strain from CDC in the fall. Johnson says his lab is better equipped to study the new toxin because it has the molecular techniques to knock out the gene for toxin B, which the microbe also produces, and which can confound the research. "It's coming along extraordinarily well," he says, "but we could have done this years ago." ■

A bioterror threat that wasn't

The seven botulinum toxin types found over the past century come from various sources and locations. The discovery of an eighth is disputed.

1895, TYPE B
Ham, Belgium

1904, TYPE A
Canned beans, Germany

1922, TYPE C
Chickens in the U.S., cattle in Australia

1928, TYPE D
Cattle, South Africa

1936–37, TYPE E
Fish in New York and Ukraine

1958, TYPE F
Homemade liver paste, Denmark

1970, TYPE G
Soil, Argentina

2013, TYPE H?
Infant with botulism, residence unknown

SOURCE: MICHEL POPOFF, *THE JOURNAL OF INFECTIOUS DISEASES*

Kew's historic grounds, including the Palm House, run up a maintenance bill of £8 million a year.

PLANT BIOLOGY

Research at Kew overhauled for leaner times

World-leading collection focuses on its strengths following critical reviews and budget cuts

By **Erik Stokstad**

The Royal Botanic Gardens, Kew, one of the world's largest collections of plants and fungi, has had to prune itself, trimming 47 research jobs and focusing its science on its own holdings. "It's the most substantial reorganization in a century," says Director Richard Deverell. In the face of declining budgets, "it was about the survival of the institution." He hopes the strategy, detailed in a 5-year plan released this week, will help stabilize government funding and win new research grants.

The shake-up, which has resulted in an 18% reduction in research positions, has been painful and controversial. "What is happening at Kew is causing dismay around the world and will severely damage a globally recognized institution," wrote Michael Heinrich, who studies medicinal plants at University College London, along with 93 others in a letter to the House of Commons Science and Technology Committee, which held a hearing in December on Kew's budget woes and job cuts. But Neil Chalmers, former director of London's Natural History Museum, says the strategy represents an effective response to Kew's situation. "It is good to see Kew taking this on with a lot of intelligence and determination."

Founded in 1759, Kew holds irreplaceable collections of plants and fungi. Every year, thousands of scientists from around the world visit its herbarium to study rare specimens. Kew's Millennium Seed Bank, 70 kilometers away at Wakehurst Place, contains 2 billion seeds from 35,000 species. The £55-million-a-year operation also includes two public botanic gardens with more than 40 historic buildings—including 19th century conservatories streaked with rust and algae—that run up an annual maintenance bill of £8 million.

In 2010, an independent review led by Chalmers concluded that Kew's research program was spread too thin and needed focus. A subsequent review led by Georgina Mace of Imperial College London concurred. Both recommended that a new position of science director be created and a clear strategy drafted. Deverell, who had worked at BBC for almost 20 years, became the first nonscientist to lead the institution in 2012, and the next year he recruited Kathy Willis, an ecologist at the University of Oxford, as science director.

Kew's new leaders had to plug a deepening budget hole. The government ministry that provides 45% of Kew's budget—the Department for Environment, Food & Rural Affairs—cut its contribution by a third over the past 2 years, as part of the United Kingdom's overall austerity program. And the charitable Kew Foundation also had to reduce its support. Deverell found himself with an unprecedented £5 million operating deficit for 2014. "We had an urgent need to reduce cost," he says.

Willis led the drafting of a science strategy, scaling back applied work in restoration ecology while emphasizing fungi and plant health. "They are focusing on their collections," Mace says. "That's a very sensible thing to do." Willis also restructured the research division. The new Science Directorate has six departments, including collections and taxonomy, and Willis has plans to hire an additional three plant scientists and seven mycologists.

Other positions at the institution were trimmed. "I became aware quite quickly of a lot of duplication of posts," Willis explained to the parliamentary committee at the December hearing. But the committee heard dissenting views. In letters to the committee, one Kew scientist denied there was duplication, while another described "an atmosphere of profound demoralization."

The strategic plan sets concrete targets. By 2020, for example, Kew scientists will completely chart the evolutionary relatedness of plant and fungal species by sequencing the genomes of representative samples from the collections. Kew will cover the initial costs, then raise funds and establish partnerships to complete the task. A new website will offer comprehensive information on traits, distributions, and evolutionary relationships of plants and fungi.

Starting in December, an annual report, called the *State of the World's Plants*, will identify important issues in plant health and conservation. Kew scientists will also designate Tropical Important Plant Areas in seven countries, highlighting the economic and cultural importance of species. A new master's course in plant and fungal taxonomy, diversity, and conservation will train 100 students by 2020.

The changes impress Charles Godfray, a population biologist at Oxford and a former trustee of Kew. "They have produced a science organization that is better fitted for the challenge of rapidly changing times," he says. What's needed now is stable funding. The Commons committee will soon release a report with recommendations. Although Parliament does not control spending, it can influence the government: The day before its public hearing in December, the treasury announced it had found an additional £2.3 million for Kew's 2015 to 2016 budget. ■

PHOTO: JOHN LAMB/GETTY IMAGES

Japan looks to instill global mindset in grads

New program to internationalize universities hopes to put nation on more competitive footing

By **Dennis Normile**, *in Tokyo*

Japanese companies are struggling to compete overseas—and the root of the problem may be the nation's inward-looking higher education system. "Business people are saying that Japanese university students are useless," says Kuniaki Sato, deputy director of international planning at Japan's education ministry. Graduates equipped with the skill sets and moxie to operate in an international environment, he says, "are extremely rare." And things are getting worse. Fewer and fewer Japanese students are going abroad for study. The number of foreign students in Japan is trending downward. And non-Japanese professors are uncommon.

Responding to a directive from Prime Minister Shinzo Abe's Cabinet to produce more internationally minded graduates, the education ministry has just launched the Top Global University Project. Under the program, 13 research universities deemed by the ministry capable of attaining top-100 status worldwide will each receive $3.5 million a year for 10 years. And 24 smaller universities will get $1.4 million a year over that period. The funding is modest, but it should allow the universities to become more in sync with international norms, by revamping tenure systems and overhauling curricula, for example. Most participating universities plan to adopt quarterly terms to facilitate exchanges with overseas partners, which start the school year in the fall. (Japanese schools start in April.)

"We are trying to improve the quality of education and research and our globalization," says Yoshinao Mishima, president of the Tokyo Institute of Technology (Tokyo Tech). His lofty goal is for Tokyo Tech to become "one of the world's top ten research universities by 2030." (It's now ranked 141st in the *Times Higher Education* list, and 68th in the QS World University Rankings.) Sato notes that the 37 universities in the program represent 20% of Japan's student and faculty community. "We think this is enough of a critical mass to make a change in society," he says.

This is not Japan's first stab at internationalizing its universities. Other programs have had little lasting impact, say skeptics, who doubt the new program will be any different. Japan has initiated "one short-term program after another with no continuity," says Robert Geller, a geophysicist who became the first non-Japanese tenured faculty member at the University of Tokyo in 1984. Others believe that the parade of programs have made incremental but significant improvements that the Top Global project can build on. The universities are changing "slowly but steadily" says Toshio Nomura, a London-based consultant who has helped Kyoto University establish ties with universities in the United Kingdom.

The University of Tokyo hopes to get more foreign students through its gates.

Recent trends, though, are disheartening. According to the education ministry, the number of Japanese going abroad for education at all levels peaked at 82,945 in 2004 before eroding to 57,501 in 2011, the last year for which data are available. The number of foreign students at Japan's tertiary institutions has declined from a high of 141,774 in 2010 to 135,519 in 2013. Meanwhile, last year the 86 national universities had only 2329 full-time foreign faculty, making up just 3.6% of the rolls.

Many Japanese academics play down the importance of international rankings, but they also feel the nation is underrepresented. Japan has only two schools in the top 100, by the *Times Higher Education* ranking: the University of Tokyo in 23rd place and Kyoto University in 59th.

If participating universities achieve their Top Global targets, the percentage of Japanese students earning college credits overseas will rise from the current 3.3% to 13.8%; the ratio of non-Japanese to Japanese students will increase from 6.5% to 13.1%; and the percentage of faculty members who are foreigners or Japanese who earned advanced degrees overseas will increase from 27.6% to 47.1%.

Academia is far from being the only pillar of Japanese society weakened by an island mentality. Hideto Matsumoto, director of international planning at the education ministry, decries a gap between corporate pleas for internationally minded employees and recruiting practices that favor those who followed the standard path straight through a Japanese university. Sooner or later, Nomura says, companies must start giving preference to graduates with English skills and experience abroad. Only then, he argues, will many students strive to go overseas. "They know their job prospects, so if the companies don't change, the students won't." ■

Going nowhere

The number of Japanese students going abroad for study has ebbed since 2009 (data available through 2011). At the same time, fewer foreign students are coming to Japan.

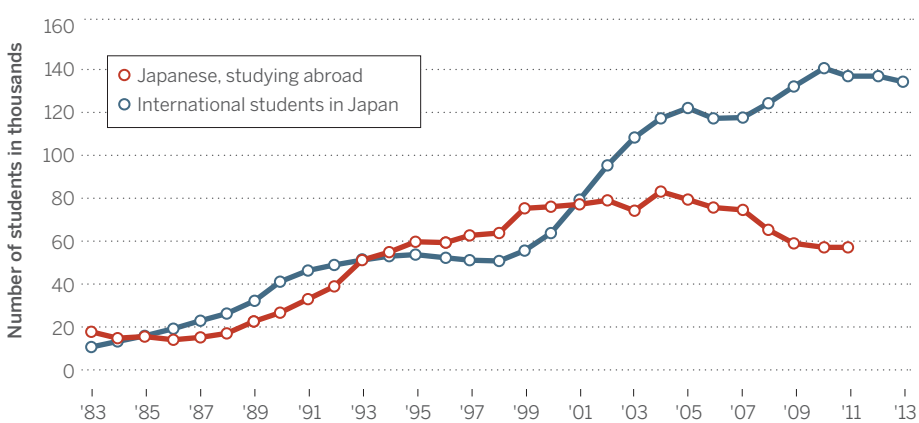

PHOTO: © AFLO/CORBIS

FEATURES

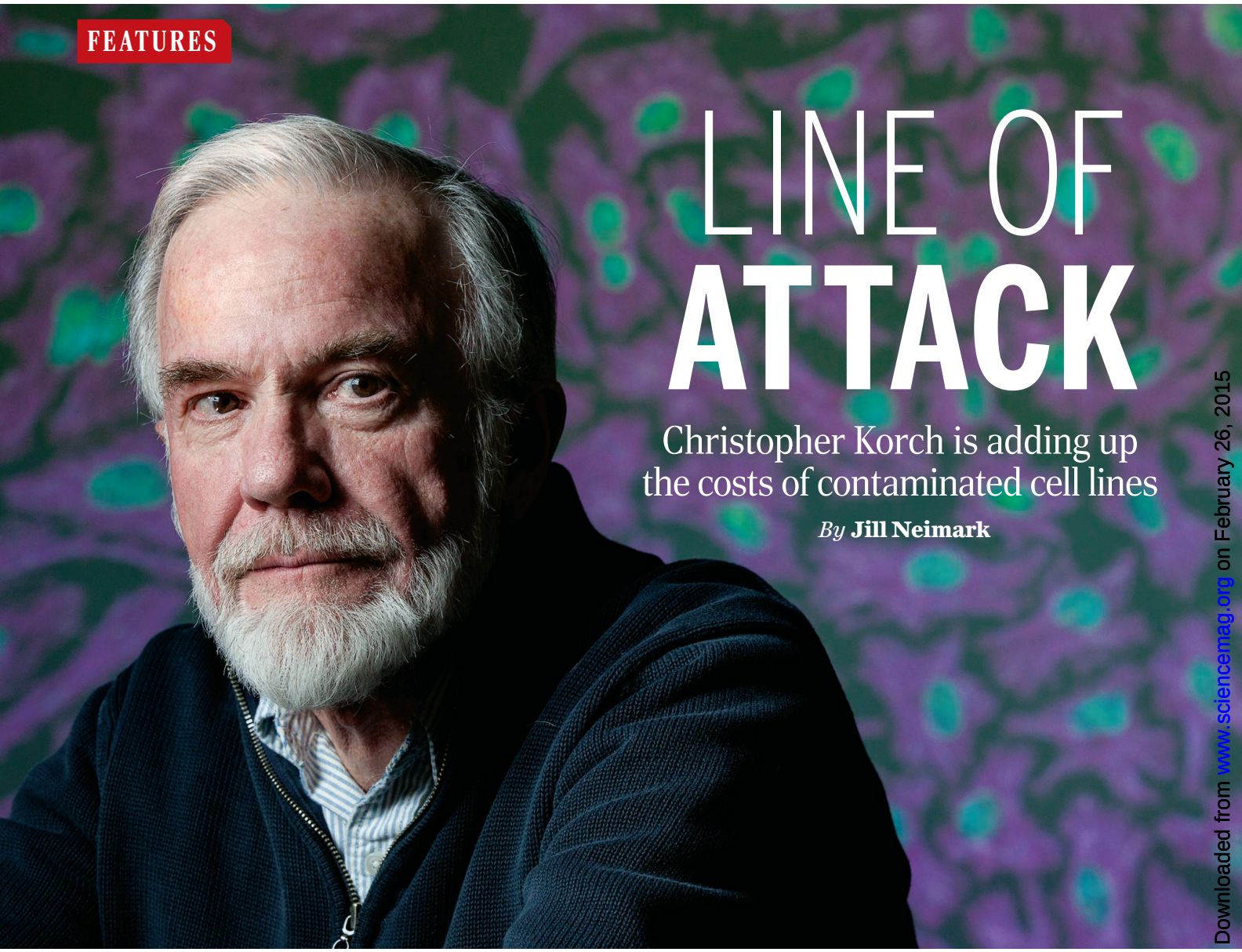

LINE OF ATTACK

Christopher Korch is adding up the costs of contaminated cell lines

By **Jill Neimark**

"I call myself a corrector," says University of Colorado geneticist Christopher Korch. What Korch passionately wants to correct is the contamination of laboratory cell cultures, a problem that has bedeviled biomedical research for more than half a century. Over the past 15 years, he has published on 78 widely used cell lines that turned out to be overgrown with other cells. Thyroid lines were actually composed of melanoma cells, prostate tissue was displaced by bladder cancer, and normal uterine cultures turned out to be nothing but breast cancer, casting doubt on countless studies of basic biology and disease.

And yet until recently he has felt more like a voice in the wilderness than a catalyst for change. "All too often, scientists have ignored my findings," Korch says. "Not one of my published papers has led to a retraction by a journal or scientist. Less than 10 corrections have been issued, when each false line I discovered affects the conclusions of hundreds or thousands of papers."

Now Korch has a band of allies and, he hopes, a novel way to persuade recalcitrant biologists: Zoom out from individual cases of contamination to show the big picture. After a year of intensive data gathering and analysis, he believes he has for the first time begun to quantify the damage done to the scientific enterprise by contaminated cell lines. "We're looking at tens of thousands of publications, millions of journal citations, and potentially hundreds of millions of research dollars," he says.

Many widely studied cell lines continue to be overrun by HeLa cancer cells (displayed behind Korch).

A few scientists who have seen a preliminary draft of Korch's white paper, which is now under review at a journal, have been moved to set changes in motion. "What impresses me about Dr. Korch's analysis is that the problem is more pervasive than I might have predicted," says Ferric Fang, a University of Washington, Seattle, microbiologist who recently co-authored a study estimating the amount of National Institutes of Health (NIH) funding wasted on a decade's worth of papers that had been retracted.

Fang, who edits the journal *Infection and Immunity*, says he will present Korch's findings to the leadership of the American

PHOTO: © JOANNA B PINNEO

Society for Microbiology, which publishes 13 journals, including his. But Fang cautions that "not all research using misidentified cell lines necessarily represents wasted effort." Some studies may still yield useful information, he says, adding "I am wary of sensationalizing the problem with large dollar amounts that are imprecise."

Korch acknowledges it's impossible to determine an exact dollar amount, but he feels that his financial estimate is actually conservative. His goal, he says, "is to give an idea of the enormity of the problem. We need to rattle the cage of complacency to get the attention of scientists, granting agencies, journals, and universities."

A TALL, GENTLE SWEDE with silvery hair, a neatly trimmed beard, and—according to his wife—the patience of Penelope, Korch arrived in Aurora, Colorado, in 1995, after several decades of steady but unspectacular genetics research in Sweden, France, Norway, and the United States. He was soon asked to direct the university's DNA sequencing facility, and became one of the world's experts in analyzing cell lines to determine their true genetic identity. Korch, now 70, uses a standard method called short tandem repeat (STR) profiling, which looks at specific DNA sequences that vary in number from one individual to the next. The technique, which the FBI and other law enforcement groups have long used to genetically fingerprint DNA from blood and other tissue at a crime scene, can also distinguish cell lines that come from different individuals.

"Christopher is definitely the CSI Crime Scene hero of science," says Paul Bunn, founder of the University of Colorado Cancer Center. And as the director of the sequencing center, Bunn says, "he was utterly free to pursue his obsession without pushback."

Immortal cell lines start as tissue samples that are coaxed, sometimes with great difficulty, to grow and multiply indefinitely in nutrient-rich plastic flasks. Cell lines are assumed to retain the properties of the original tissue, functioning as a living, physiologic test tube to explore the most important questions in basic biology and biomedicine, such as how cancers and normal tissues respond to drugs.

A cell line's immortality, however, is both its great strength and its most striking weakness. It allows experiments to be repeated again and again to confirm a finding. But as those same cell lines are passed from person to person and lab to lab over many decades, they can be contaminated by other cells. The interlopers can outgrow the original cells, ultimately displacing the authentic culture completely. Based on his and other investigators' research, Korch estimates that about 20% of cell lines are contaminated.

A tale of two impostors

Christopher Korch estimated the impact of research on two cell lines, HEp-2 and INT 407. Due to contamination long ago, both are now widely acknowledged to be composed of cancer cells called HeLa.

5789
ARTICLES
in **1182** journals may have used HEp-2 inappropriately, producing an estimated **174,000** citations

1336
ARTICLES
in **271** journals may have used INT 407 inappropriately, producing an estimated **40,000** citations

$713
MILLION
Estimated amount spent on the original articles published on **INT 407** and **HEp-2**

$3.5
BILLION
Estimated amount spent on subsequent work based on those papers

Researchers have mostly ignored or denied the problem. In the 1970s, biologist Walter Nelson-Rees aggressively exposed impostor cell lines and pushed for regular authentication, earning so much vilification for his efforts that he left science altogether. And less than a decade ago, cell biologist Roland Nardone took up the fight, chastising journals and funding agencies for not requiring that cell lines be tested to verify their identity (*Science*, 16 February 2007, p. 929). He, too, made little headway.

Now Korch has joined the fray. In 2012 he joined a newly formed volunteer global organization of 20 scientists, the International Cell Line Authentication Committee (ICLAC), dedicated to cleaning up the cell line literature. Chaired by Australian cell biologist Amanda Capes-Davis, ICLAC curates a free, online database of misidentified lines, which now number 475. Members meet by teleconference, publish articles on cell culture practices that minimize contamination risk, and add notations on impostor lines to PubMed Commons, an online tool that allows participating scientists to add a comment below any abstract indexed on PubMed. The group also offers assistance to journals and scientists trying to authenticate cell lines. Says Capes-Davis: "We don't use picket lines, bash down doors with a pickax, or brandish signs; we use data to convince our colleagues." Thanks in part to ICLAC's efforts, 28 journals now require cell line authentication, and some institutions do as well.

Starting in 2013, Korch also set out to quantify the damage from misidentified lines. His first case studies are HEp-2, thought to have originated in 1955 in a sample of a squamous cell laryngeal cancer, and INT 407, cultured in 1957 from the finely minced jejunum and ileum of a 2-month-old embryo. In 1967, geneticist Stanley Gartler unmasked both lines as HeLa, the most studied and rapaciously aggressive cancer cell line in biology, which must have contaminated and displaced the original cells around the time they were first cultured. Yet HEp-2 has been extensively used to study laryngeal cancer, while INT 407 is widely accepted as a model for normal intestinal cells.

Cutting his laboratory time to 2 days a week, Korch spent most of the next year at home, compiling and quantifying a mountain of data, to measure the footprint that the two contaminated lines have left in the scientific literature. Each has multiple monikers, he found. (HEp-2 is also HEp 2, Hep2, Hep-2c, Hep 2c, Hep2c, H.Ep.-2, H. Ep.-2, H.Ep. #2, H. Ep.-2, or H. Ep. #2. INT 407's aliases include Intestine 407, Henle 407, INT407, and INT-407.) Once he had all their iterations, he searched PubMed, Google Scholar, Web of Science, and many other journal databases from publishers such as Stanford University's HighWire, the American Society for Microbiology, and Elsevier. He found that HEp-2 has been used in more than 5700 published articles, under its cloak-and-dagger disguise of laryngeal cancer. INT 407 has been used in 1300-plus published articles, in its fraudulent identity as normal intestine.

In some cases, Fang contends, the mistaken identity does not undermine the

findings. "The first paper to describe how *Salmonella* invades host cells was made in 'INT 407' cells," he says, explaining that they were thought to be a good model for the intestinal cells the bacterium attacks. "This is one of the most important papers in the *Salmonella* field and has been cited more than 600 times." Even though the cells are HeLa, not intestinal cells, Fang see no reason to question its conclusions. "*Salmonella* uses this same mechanism to invade a wide variety of cells."

In other cases the cells' identity is critical. Last October, *Current Microbiology* published a study of a gene that allows another food-borne pathogen, *Listeria*, to invade cells. The study compared how the bacterium invaded three ostensibly different cell lines: INT 407, thought to be a model of the pathogen's intestinal target, and HEp-2 and HeLa. In truth, the study tested a single cervical cancer cell line, HeLa, three times.

"We used three different cell lines because we hoped to find a general mechanism that would work in many tissues," says Radosław Stachowiak of the University of Warsaw, one of the study's authors. "I was aware there were some issues with some cell lines, especially INT 407, but did not know about the scale of the problem." He goes on to echo many scientists who have a hard time believing a line is false. "I have to admit it is hard to accept all these lines are HeLa in fact, given their different appearance and even growing conditions. Since it turns out we tested only in HeLa we don't know if the mechanism is restricted to HeLa alone." Stachowiak has contacted the journal to request that it add a correction to the paper.

KORCH FINDS that even after scientists know their favorite cell line is contaminated, they may keep studying it. A typical case is ECV304, believed to be a good model for blood vessel cells because it was thought to originate in a sample of umbilical vein. In fact, a team led by geneticist Wilhelm Dirks of the German biobank DSMZ discovered in 1999 that it is a bladder cancer. More than a thousand papers have been published on ECV since then, and in 2011 two researchers explained why they have stuck with the cell line, in a letter in *The Journal of Biological Chemistry*. Wen-Cheng Xiong of the Medical College of Georgia in Augusta and her colleague Sylvia Simon of CNS and Pain Innovative Medicines in Södertälje, Sweden, acknowledged that the line was misidentified but said the bladder cancer cells have features of endothelial tissue, such as blood vessels. "[I]n the absence of an ideal model, we believe that ECV304 cells remain useful in studies of endothelial functions," they concluded.

To ICLAC, such sentiments are profoundly annoying. "This is typical of the wishful thinking adopted by scientists trying to evade the truth," fumes experimental pathologist John Masters of University College London, an ICLAC member. Korch is a bit more charitable. "They look at their line and are convinced it's still a valid model, because its behavior seems to match their expectations."

Take the case of Korch's fellow Swede Anita Sjölander, whose work has been a focus of ICLAC for 2 years. Her group at the Faculty of Medicine at Lund University in Malmö, Sweden, published 41 articles on INT 407 between 1988 and 2011, consistently referring to it as normal intestine even though Gartler had exposed it as HeLa 2 decades earlier. In 2001, Masters and colleagues confirmed the mistaken identity in 250 "blinded" samples of cell lines, including INT 407, from the major U.S. and European cell banks and five cancer research institutes. STR genotyping showed that "every known stock of INT 407 is HeLa," he says.

> ***"We need to rattle the cage of complacency to get the attention of scientists, granting agencies, journals, and universities."***
>
> **Christopher Korch**, University of Colorado

Yet Sjölander was not convinced. She had tested the cells extensively over the years, and their behavior and morphology convinced her they were genuine intestinal cells. "All that functional testing, though interesting, is unreliable," Korch says. "For example, intestinal cells have microvilli. But so do HeLa cells."

Korch and ICLAC kept up the pressure on Sjölander. "I don't mind if the scientists get mad at me. I'm friendly, but I'm not afraid," Korch says. He often sent along Swedish greetings before urging her to get STR fingerprinting done on her samples. Sjölander explained that she had done so but told him that the results were not conclusive. So Korch persisted, pushing her in December 2014 to request a re-evaluation of the data that he himself could review. The results clearly identified her stock as HeLa, Korch says, and Sjölander now agrees that her batch of INT 407 cells are impostors. Sjölander studies mediators of inflammation in the intestine, but her 41 studies using INT 407 are not applicable to the intestine, Korch says. "She should add a correction to all her INT 407 papers." (Sjölander declined to answer when *Science* asked if she planned to correct or retract her papers, beyond saying that cell line contamination "is a serious problem and we treat it as such.")

SJÖLANDER'S INT 407 WORK suggests how big a shadow contaminated cell lines can cast on the literature. Korch extrapolated from the average citation rate of Sjölander's INT 407 papers to calculate the broader impact of the published work on the cells. "I calculated there may be as many as 40,000 citations that refer to work (directly or indirectly) using the impostor cell line INT 407 over the last half century, all referring to it as normal intestinal epithelium." HEp-2 is worse: Korch estimates that as many as 174,000 papers cite HEp-2 studies that may not be valid.

Then there's the financial cost. Masters estimates that $100,000 is the typical cost of an average cell study. Using that figure, Korch says $713 million has been spent on published work involving just HEp-2 and INT 407. The tally could be as high as $2.8 billion, if the per study value is $400,000—the figure that Fang and coauthors used in their 2014 analysis of the cost of retracted articles. "That's only two lines," Korch says. "The consequences to research based on all the 475 impostor cell lines on the ICLAC website are nearly inconceivable."

Will Korch's new study of the costs wake the scientific community out of a half century of inertia? Or will he go the way of Nelson-Rees, Nardone, and others who have sounded the alarm about cell line contamination and gone unheeded? "We at NIH agree entirely that this is a serious issue and one that the time has come to really address," says Jon Lorsch, director of the National Institute of General Medical Sciences in Bethesda, Maryland, who reviewed Korch's analysis. Recently, Lorsch, along with Francis Collins, the director of NIH, and Jennifer Lippincott-Schwartz, the 2014 president of the American Society for Cell Biology, issued another call for biologists to take cell line identity seriously, hinting that NIH may require grant applicants to verify their cell lines (*Science*, 19 December 2014, p. 1452).

All of this makes Korch optimistic at last. "I see the floodgates beginning to open, actually," he says. "Scientists everywhere are starting to demand reproducibility. I hope my work is one extra push in the right direction. We all want pyramids of literature built up solidly on sound foundations." ■

Jill Neimark is a writer based in Atlanta.

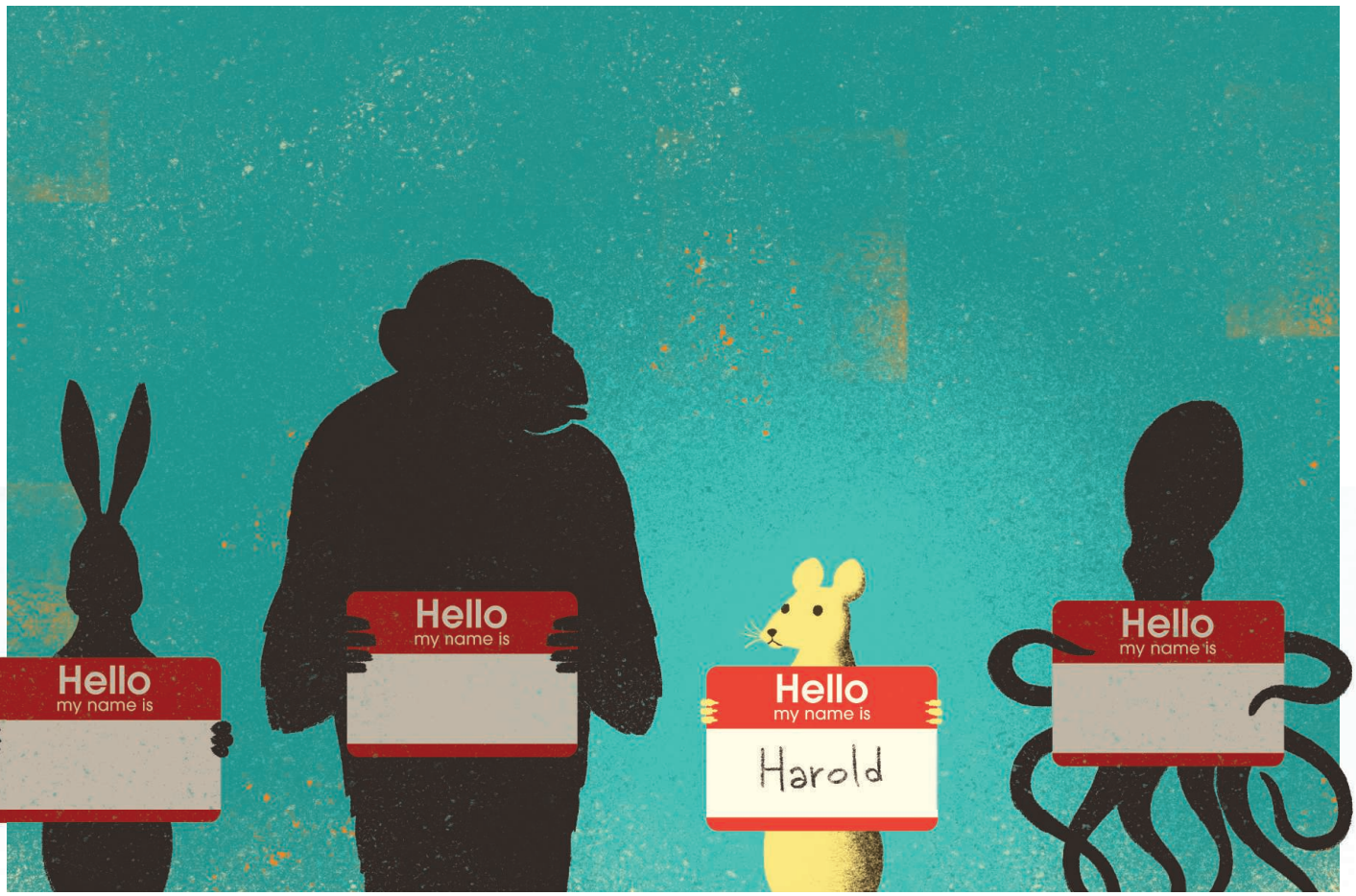

What's in a name?

Naming research animals may improve their well-being—or bias experiments

By **Michael Erard**

Freckle, a male rhesus monkey, was greeted warmly by his fellow monkeys at his new home in Amherst, Massachusetts, when he arrived in 2000. But he didn't return the favor: He terrorized his cagemate by stealing his fleece blanket and nabbed each new blanket the researchers added, until he had 10 and his cagemate none. After a few months, Freckle had also acquired a new name: Ivan, short for Ivan the Terrible.

Freckle/Ivan, now at Melinda Novak's primate research lab at the University of Massachusetts, may be unusual in having two names, but all of his neighbors have at least one moniker, Novak says. "You can say, 'Kayla and Zoe are acting out today,' and everybody knows who Kayla and Zoe are," Novak says. "If you say 'ZA-56 and ZA-65 are acting up today,' people pause."

Scientists once shied away from naming research animals, and many of the millions of mice and rats used in U.S. research today go nameless, except for special individuals. But a look at many facilities suggests that most of the other 891,161 U.S. research animals have proper names, including nonhuman primates, dogs, pigs, rabbits, cats, and sheep.

Rats are Pia, Splinter, Oprah, Persimmon. Monkeys are Nyah, Nadira, Tas, Doyle. One octopus is called Nixon. Breeder pairs of mice are "Tom and Katie," or "Brad and Angelina." If you're a mouse with a penchant for escape, you'll be Mighty Mouse or Houdini. If you're a nasty mouse, you'll be Lucifer or Lucifina.

Animals in research are named after shampoos, candy bars, whiskeys, family members, movie stars, and superheroes. They're named after Russians (Boris, Vladimir, Sergei), colors, the Simpsons, historical figures, and even rival scientists. These unofficial names rarely appear in publications, except sometimes in field studies of primates. But they're used daily.

Is this practice good or bad for research? Some scientists worry that names lead to anthropomorphizing and carry associations that could trigger bias—aggressive

ILLUSTRATION: DAVIDE BONAZZI



Research celebrities. Animals of all kinds have been named and remembered by scientists. From left, chimpanzee Freud, observed by Jane Goodall as he grew to be an alpha male; Ham, a young chimpanzee who was sent into space in 1961 and managed to survive the flight; and Dolly the sheep, the first mammal to be cloned from an adult cell.

Ivan might also be seen as more cunning than Freckle. But others argue that animals that are named, and therefore seen as individuals, may be tended more carefully. That makes them less stressed and better for study, says Cindy Buckmaster, president of the American Association for Laboratory Animal Science (AALAS) and director of the Center for Comparative Medicine at Baylor College of Medicine in Houston, Texas.

Whatever its effects, for many researchers naming is a practice whose time has come. "I can count on one hand the people I run into who say, 'I work for somebody who tells me I can't name the animals,' " Buckmaster says. "I ask them if they do it anyway, and they say 'Yup.' "

WHEN HE WAS A GRADUATE STUDENT in the 1970s, ethologist Marc Bekoff worked with a cat that was able to swiftly learn visual discrimination tasks even with part of its visual system removed. Impressed, he named it Speedo. But senior researchers disapproved. "I said 'I'm naming him because he's an individual, he's really cool, he's really fast,' " Bekoff recalls. "That really pissed off a number of the professors."

In those days, emotional detachment from research subjects was prized. Few studies have analyzed lab animal naming practices, but in the late 1980s sociology graduate student Mary Phillips spent 3 years observing 23 labs that experimented on a variety of animals. She found naming was "rare," as she wrote in *Qualitative Sociology* in 1994. Only two labs used proper names; in one, names were given as jokes, while in the other, the namer was the student assistant rather than the researcher. Researchers told Phillips that they didn't name because they dealt with so many animals and were interested in them as sources of enzymes or data points, not as individuals. Six out of 27 researchers said they wanted to maintain emotional distance from animals they were going to kill.

Such attitudes were once typical in science, Buckmaster says. "An old guard used to preach detachment," she says. "In their mindset, you could not collect objective data if you allowed emotion to become part of anything you did."

That's why Jane Goodall's chimpanzee names (Bare Bum, Paleface, Freud, Fifi), were controversial when she first studied the Kasakela chimpanzee community in Tanzania in the early 1960s. "They are as distinct, one from another, as human beings," Goodall wrote, an observation that sparked skepticism at the time.

And yet even then, some lab animals were unofficially named. In the late 1950s, when psychologist Harry Harlow did his famous, often-vilified experiments removing infant monkeys from their mothers, he named as well as numbered the animals. The first infants were named after stones (Mill Stone, Grind Stone, Sand Stone, Moon Stone) because the work of hand-rearing them proved more difficult than anticipated.

Harlow knew that names matter—he had changed his own last name from "Israel" to avoid being perceived as Jewish, which he wasn't. In his lab at the University of Wisconsin, Madison, naming of individual animals was part and parcel of a key discovery, says Steve Suomi, a former Harlow graduate student who is now director of comparative ethology at the National Institute of Child Health and Human Development.

Harlow's group began to appreciate that individual monkeys differed in scientifically meaningful ways. Some monkeys were highly stressed; others were playful. "We would have certain manipulations where we wanted everybody to react the same way, but they never worked," Suomi recalls. "There was always predictable variation, based on the individual subject."

Recognizing these individual differences led to the discovery of the genetics and epigenetics of personality in monkeys, which has clinically relevant implications for humans, too, Suomi says. These insights "probably wouldn't have been possible if we hadn't gone through this individual difference route," he says.

Today at his institute, Suomi encourages naming as a useful tool and also as an emblem of the science of individual differences. "Working closely with monkeys who do have individual characteristics and personalities, it's almost impossible for them to not acquire names one way or another," he says.

Naming comes naturally with other animals, too. When AALAS's Buckmaster put out a call to the researchers, technicians, and veterinarians on her Listserv asking about naming rodents, she got dozens of replies listing rodent names, among them Copernicus ("a smart rat"), Harold ("he looked just like a Harold"), Snow and Blizzard ("albino rats born during a snow emergency"), and Dudley ("a breeding rat that was sterile"). Said one person: "I personally give rodents names when they need to be euthanized, just as a sort of courtesy."

Naming improves animals' lives, argues Brenda McCowan, a scientist at the California National Primate Research Center at the University of California, Davis, who manages the behavioral enrichment program for 5000 rhesus and titi monkeys. "Naming helps create positive human-animal interaction, which is better for the welfare of those animals," she says. Buckmaster adds that naming has become more accepted because "people realized the scientific value of the stress-free animal. … We have to make sure these are really

PHOTOS (LEFT TO RIGHT): © KENNETH LOVE/*NATIONAL GEOGRAPHIC*; NASA; © NAJLAH FEANNY/CORBIS/SABA

happy animals, or none of the information that we get from them will be valid."

Buckmaster and others were unable to cite a study that compares research outcomes in named and unnamed animals, however. One study, in *Anthrozoos* in 2009, found a small but significant effect in 516 dairy farms in the United Kingdom: On the 46% of farms where cows were called by name, milk production was 3% higher than on farms where cows weren't named, suggesting that the use of names reflects an environment in which the cows get better care. (Study author Catherine Douglas of Newcastle University's School of Agriculture, Food and Rural Development in the United Kingdom notes that one farmer proffered this advice: Never name an animal after your mother-in-law.)

Lab animals are highly sensitive to environmental factors, notes University of Alabama, Birmingham, psychologist Robert Sorge, but no one is claiming that the animals themselves respond to their names. At a National Institutes of Health (NIH) facility in Poolesville, Maryland, infant monkeys move into cages elaborately decorated with their new proper names, but animal care manager Michelle Miller acknowledges that the monkeys never learn their names. Naming "is more for the humans," she says.

Mrs. Stone, a female rhesus monkey in Harry Harlow's laboratory at the University of Wisconsin in the 1950s, and a number of her adopted offspring.

PHOTO: ROBERT O. DODSWORTH

THE RHESUS MONKEY called Teefour was an outlier. Mean and nasty, he forced low-ranking females to groom him, and then yanked out chunks of their hair. "He would have been considered an abusive husband," recalls primatologist Novak. In her lab, every monkey gets a proper name. But not Teefour. No name ever stuck to him, not "Darth," not "Horrible." He was known only by the alphanumeric sequence tattooed on his chest: T-4.

Did his lack of a name affect what researchers observed about him? It could have, depending on the study, says psychologist Matthew Novak (no relation to Melinda Novak) of Central Oregon Community College in Bend. When he was a researcher at the NIH rhesus facility in Poolesville from 2002 to 2011, he argued that none of the monkeys should be named, and when they were, he didn't want to know the names, because he feared it would bias data collection. His argument: Say you're studying reaching behaviors in infant monkeys named Moose and Peach. Both make a random motor movement. It's coded as a deliberate reach for Peach but not for Moose, who's supposed to act big and dumb. "Naming not only changes our expectations, it changes what we see the animal doing," he says.

But as with the advantages of naming, there's no research to directly back up this idea. "To my knowledge, not a single study has been conducted to support the assumption that research data are at risk of being biased if names have been given to the research subjects; this applies to animals and humans," says Viktor Reinhardt, a veterinarian and former member of the scientific committee of the Animal Welfare Institute in Washington, D.C.

Still, Matthew Novak and others say it's possible to extrapolate from the social psychology literature, which is replete with experiments showing the subtle psychological effects that names exert on humans. Recent research shows that a poem with the name of a famous writer attached is perceived to be more poetic; food described with appealing adjectives is judged more nutritious; faces shown next to exotic-looking names are judged more multiracial.

In certain social settings, such as prisons and the military, people have been deliberately referred to by numbers in order to dehumanize them. Some argue that this is a factor even in medicine, where patients may be referred to by date of birth, Social Security or medical record number, or illness ("the appendicitis in room 312"). Such "deindividuating practices" can make doctors less sensitive to patients' pain and generally less empathetic, social psychologists Adam Waytz of Northwestern University in Evanston, Illinois, and Omar Sultan Haque of Harvard University argued in 2012 in *Perspectives on Psychological Science*.

The converse is also true: Names can make objects like robots and self-driving cars seem more human, Waytz says. People judged self-driving cars to be safer when the cars had some attributes of human agency, such as voices, genders, and names, he and colleagues reported in the *Journal of Experimental Social Psychology* in 2014. The voice is the strongest cue to humanness, but "a name goes a long way as well," Waytz says.

The effect is rooted in the brain. "Whether people are looking at robots or gadgets or animals, you get more activity in regions of the brain involved in social cognition" when they're perceived as more human, Waytz said. The brain's medial prefrontal cortex, he says, is activated when we make inferences about what others might be thinking—that is, when we perceive them to have minds as we do. That's true for everyone. "Even if people don't think they're anthropomorphizing by naming an animal, subconsciously, they are likely doing so," Waytz says.

If so, scientists need not worry that names will bias some researchers more than others. But naming might still skew how researchers perceive individual animals. Scientists routinely control for such potential sources of bias with study design, but haven't focused on names. One obvious solution, says Matthew Novak, is to assign names randomly, not based on personality or looks. "Make the names as unattachable to meaning as possible," he says, "and then train your staff as well as possible." In that case, Teefour had the right name all along. ■

Michael Erard is based in South Portland, Maine, and is the author of Babel No More: The Search for the World's Most Extraordinary Language Learners.

Pop-up shapes from thin films *p. 949*

Insecticidal RNA *p. 950*

PERSPECTIVES

PLASMA PHYSICS

Understanding particle acceleration in astrophysical plasmas

Simulations reveal new scenarios to accelerate electrons to extremely high energies

By **Hantao Ji**[1,2] *and* **Ellen Zweibel**[3]

Energetic electrons are ubiquitous in astrophysical plasmas, as they are considered to be behind the surges of emission across the electromagnetic spectrum at wavelengths from radio to gamma rays. These dynamic phenomena include stellar flares, supernova explosions (see the figure) (*1*), gamma ray bursts, and extragalactic jets. Energetic electrons are also directly observed in situ during terrestrial substorms. Despite these rich observations and substantial progress in theory, numerical simulations, and laboratory experiments over the past few decades, however, the mechanisms by which the electrons obtain their energy still remain elusive. On page 974 of this issue, Matsumoto *et al.* (*2*) make progress toward resolving these issues.

Shocks are an attractive venue for particle acceleration at the expense of energy from supersonic flows. Although the primary energy release sites are often relatively small (a thin electric current sheet for a stellar flare, a collapsing stellar core for a supernova), the shocks they drive have a large geometrical cross section, allowing many more particles to tap that energy. And whereas shocks in dense, homogeneous fluids are thin, laminar structures mediated by viscosity, high-velocity shocks in plasmas are known to spawn a complex array of plasma waves and insta-

[1]*Department of Astrophysical Sciences and Princeton Plasma Physics Laboratory, Princeton University, Princeton, NJ 08544, USA.* [2]*Laboratory for Space Environment and Physical Sciences, Harbin Institute of Technology, Harbin, Heilongjiang 150001, P.R. China.* [3]*Departments of Astronomy and Physics, University of Wisconsin, Madison, WI 53706, USA. E-mail: hji@princeton.edu*

A cosmic accelerator. The Crab Nebula as a remnant of a supernova explosion exhibiting a dramatic example of synchrotron emission from energetic electrons, shown in bluish glow. Powerful gamma ray flares have been observed during which electrons are accelerated to the PeV energy range. Blue in the filaments in the outer part of the nebula represents neutral oxygen, green is singly ionized sulfur, and red indicates doubly ionized oxygen. Orange filaments are remains of the star and consist mostly of hydrogen. Size of image is about 6 light-years.

PHOTO: NASA, ESA, AND J. HESTER/ARIZONA STATE UNIVERSITY

bilities that thermalize flow energy within a broad and turbulent transition layer (*3*). Inhomogeneities in the upstream fluid only exacerbate the turbulence generation process. In the best-known shock acceleration scenario, diffusive shock acceleration (DSA), ions become trapped within this layer and are energized by the overall converging shock flow through a so-called first-order Fermi process. DSA operating in young supernova remnants may be the source of galactic cosmic rays (*4*).

But DSA is thought not to work as well for electrons. To reach both sides of the converging shock flow separated by ion scales would require a large initial threshold energy. Various mechanisms based on resonant electromagnetic waves to accelerate electrons to the threshold energy have been proposed, but whether these waves are sufficiently coherent for efficient acceleration in a turbulent shock remains unresolved.

"efficient electron acceleration is accomplished by combining two different mechanisms ..."

Alternatively, charged particles can be accelerated by magnetic reconnection, during which magnetic energy is rapidly released through the rearrangement of field lines (*5*, *6*). Highly dynamic structures such as outflow jets and contracting islands during the development of turbulent multiscale reconnecting current sheets can energize electrons efficiently [e.g., (*7*, *8*)]. Some models (*9*) have been proposed to accelerate electrons through reconnection in attempts to explain the recently observed gamma ray flares from the Crab Nebula (*10*, *11*). Unlike shocks, however, specific astrophysical scenarios for the realization of such turbulent reconnection with multiple temporospatial scales still remain to be developed.

In the scenario proposed by Matsumoto *et al.*, multiscale turbulent reconnection is realized in a shock propagating into a uniform medium with a weak magnetic field parallel to the plane of the shock. The background ions, reflecting from the shock, form a beam that propagates upstream and excites the electromagnetic Weibel instability (*12*). As the Weibel modes grow to nonlinear amplitude, they draw out the upstream magnetic field into thin, hairpin-like structures with oppositely directed field lines in close proximity. This magnetic field reconnects, producing structures with multiple scales. Electrons that encounter these structures are rapidly energized, producing a high-energy tail in the initial electron distribution. It is estimated that 1% of the flow energy can be transferred to a relativistic electron population this way. Thus, efficient electron acceleration is accomplished by combining two different mechanisms (turbulent shock and turbulent reconnection) into one united, self-consistent mechanism (a shock undergoing turbulent reconnection) through a chain that transforms flow energy to electromagnetic energy and then to particle energy. Because energization occurs in multiple small structures, the fraction of particles that are boosted to high energies is larger than in the case where the primary energy release mechanisms are localized in a single site, but energization is far from ubiquitous. Thus, this is a true acceleration process rather than a bulk heating process, in the sense that only a small fraction of particles are energized.

Many questions remain and are sure to be topics for future work. The simulations achieve a high numerical resolution and a fairly high ion-to-electron mass ratio at the cost of two-dimensionality; the turbulence could appear quite different in three dimensions. Whether ions are accelerated as well remains unclear, and an accurate assessment would require a large simulation domain. The reconnection sites and the electromagnetic fields within them are not well resolved. Scaling studies are not reported. All of these problems could be addressed by more and larger simulations, which should be a high priority given the promise of these initial results. Finally, laboratory plasma experiments could be used to test some of these key ideas, either in flow-dominated regimes in focusing on turbulent collisionless shocks (*13*, *14*) or in magnetically dominated regimes focusing on turbulent reconnection, as will be feasible in the soon-to-be-deployed FLARE (Facility for Laboratory Reconnection Experiments) (*15*) at Princeton and the planned Space Physics Research Facility as part of the Space Environment Simulation and Research Infrastructure at Harbin, China. ■

REFERENCES

1. J. Hester, *Annu. Rev. Astron. Astrophys.* **46**, 127 (2008).
2. Y. Matsumoto *et al.*, *Science* **347**, 974 (2015).
3. R. A. Treumann, *Astron. Astrophys. Rev.* **17**, 409 (2009).
4. R. Blandford, D. Eichler, *Phys. Rep.* **154**, 1 (1987).
5. E. Zweibel, M. Yamada, *Annu. Rev. Astron. Astrophys.* **47**, 291 (2009).
6. M. Yamada *et al.*, *Rev. Mod. Phys.* **82**, 603 (2010).
7. J. F. Drake *et al.*, *Nature* **443**, 553 (2006).
8. M. Hoshino, *Phys. Rev. Lett.* **108**, 135003 (2012).
9. D. Uzdensky *et al.*, *Astrophys. J.* **737**, L40 (2011).
10. M. Tavani *et al.*, *Science* **331**, 736 (2011).
11. A. A. Abdo *et al.*, *Science* **331**, 739 (2011).
12. E. S. Weibel, *Phys. Rev. Lett.* **2**, 83 (1959).
13. W. Fox *et al.*, *Phys. Rev. Lett.* **111**, 225002 (2013).
14. C. Huntington *et al.*, *Nat. Phys.* **11**, 173 (2015).
15. H. Ji, W. Daughton, *Phys. Plasmas* **18**, 111207 (2011).

10.1126/science.aaa6113

ANTHROPOLOGY

How wheat came to Britain

Wheat reached Britain from the Near East at least 2000 years before the arrival of wheat farming

By **Greger Larson**

Settled communities dependent on agriculture and animal husbandry emerged independently on several continents over the past ~10,000 years. In many cases, farmers began to disperse out of regions where plants and animals were domesticated and into areas occupied by hunter-gatherer populations. This process of Neolithization certainly took place in Europe. Dating of artifacts and bones indisputably associated with human farming has led to a chronological framework for the spread of the Neolithic along two primary routes into Europe that ended with the arrival of farming in Britain ~6000 years ago (*1*). Yet, on page 998 of this issue, Smith *et al.* (*2*) report genomic sequences of wheat in an ~8000-year-old soil sample collected off the coast of southern England, suggesting that domestic crops first appeared on the British Isles long before they were cultivated there.

By ~10,500 years ago, farmers in ancient Anatolia possessed a full complement of domestic plants and animals, yet farmers only arrived in the Balkans between ~8000 and ~9000 years ago. From there, they spread west across the Mediterranean and north along the Danube, reaching western France and the central Rhineland by ~7500 years ago. The first evidence for cereal cultivation on what is now mainland Britain dates back only to ~6000 years ago, suggesting a substantial temporal gap between the two sides of the English Channel (*1*). Because rising sea levels created the English Channel in the early Holocene, it is possible that agricultural products arrived before their accepted appearance on mainland Britain, but that the evidence was flooded by the incoming sea.

A preserved ancient layer of soil had previously been identified at a site called Bouldnor Cliff that rests under marine sediments off the coast of the Isle of Wight (*3*).

bilities that thermalize flow energy within a broad and turbulent transition layer (*3*). Inhomogeneities in the upstream fluid only exacerbate the turbulence generation process. In the best-known shock acceleration scenario, diffusive shock acceleration (DSA), ions become trapped within this layer and are energized by the overall converging shock flow through a so-called first-order Fermi process. DSA operating in young supernova remnants may be the source of galactic cosmic rays (*4*).

But DSA is thought not to work as well for electrons. To reach both sides of the converging shock flow separated by ion scales would require a large initial threshold energy. Various mechanisms based on resonant electromagnetic waves to accelerate electrons to the threshold energy have been proposed, but whether these waves are sufficiently coherent for efficient acceleration in a turbulent shock remains unresolved.

"efficient electron acceleration is accomplished by combining two different mechanisms ..."

Alternatively, charged particles can be accelerated by magnetic reconnection, during which magnetic energy is rapidly released through the rearrangement of field lines (*5*, *6*). Highly dynamic structures such as outflow jets and contracting islands during the development of turbulent multiscale reconnecting current sheets can energize electrons efficiently [e.g., (*7*, *8*)]. Some models (*9*) have been proposed to accelerate electrons through reconnection in attempts to explain the recently observed gamma ray flares from the Crab Nebula (*10*, *11*). Unlike shocks, however, specific astrophysical scenarios for the realization of such turbulent reconnection with multiple temporospatial scales still remain to be developed.

In the scenario proposed by Matsumoto *et al.*, multiscale turbulent reconnection is realized in a shock propagating into a uniform medium with a weak magnetic field parallel to the plane of the shock. The background ions, reflecting from the shock, form a beam that propagates upstream and excites the electromagnetic Weibel instability (*12*). As the Weibel modes grow to nonlinear amplitude, they draw out the upstream magnetic field into thin, hairpin-like structures with oppositely directed field lines in close proximity. This magnetic field reconnects, producing structures with multiple scales. Electrons that encounter these structures are rapidly energized, producing a high-energy tail in the initial electron distribution. It is estimated that 1% of the flow energy can be transferred to a relativistic electron population this way. Thus, efficient electron acceleration is accomplished by combining two different mechanisms (turbulent shock and turbulent reconnection) into one united, self-consistent mechanism (a shock undergoing turbulent reconnection) through a chain that transforms flow energy to electromagnetic energy and then to particle energy. Because energization occurs in multiple small structures, the fraction of particles that are boosted to high energies is larger than in the case where the primary energy release mechanisms are localized in a single site, but energization is far from ubiquitous. Thus, this is a true acceleration process rather than a bulk heating process, in the sense that only a small fraction of particles are energized.

Many questions remain and are sure to be topics for future work. The simulations achieve a high numerical resolution and a fairly high ion-to-electron mass ratio at the cost of two-dimensionality; the turbulence could appear quite different in three dimensions. Whether ions are accelerated as well remains unclear, and an accurate assessment would require a large simulation domain. The reconnection sites and the electromagnetic fields within them are not well resolved. Scaling studies are not reported. All of these problems could be addressed by more and larger simulations, which should be a high priority given the promise of these initial results. Finally, laboratory plasma experiments could be used to test some of these key ideas, either in flow-dominated regimes in focusing on turbulent collisionless shocks (*13*, *14*) or in magnetically dominated regimes focusing on turbulent reconnection, as will be feasible in the soon-to-be-deployed FLARE (Facility for Laboratory Reconnection Experiments) (*15*) at Princeton and the planned Space Physics Research Facility as part of the Space Environment Simulation and Research Infrastructure at Harbin, China. ■

REFERENCES

1. J. Hester, *Annu. Rev. Astron. Astrophys.* **46**, 127 (2008).
2. Y. Matsumoto *et al.*, *Science* **347**, 974 (2015).
3. R. A. Treumann, *Astron. Astrophys. Rev.* **17**, 409 (2009).
4. R. Blandford, D. Eichler, *Phys. Rep.* **154**, 1 (1987).
5. E. Zweibel, M. Yamada, *Annu. Rev. Astron. Astrophys.* **47**, 291 (2009).
6. M. Yamada *et al.*, *Rev. Mod. Phys.* **82**, 603 (2010).
7. J. F. Drake *et al.*, *Nature* **443**, 553 (2006).
8. M. Hoshino, *Phys. Rev. Lett.* **108**, 135003 (2012).
9. D. Uzdensky *et al.*, *Astrophys. J.* **737**, L40 (2011).
10. M. Tavani *et al.*, *Science* **331**, 736 (2011).
11. A. A. Abdo *et al.*, *Science* **331**, 739 (2011).
12. E. S. Weibel, *Phys. Rev. Lett.* **2**, 83 (1959).
13. W. Fox *et al.*, *Phys. Rev. Lett.* **111**, 225002 (2013).
14. C. Huntington *et al.*, *Nat. Phys.* **11**, 173 (2015).
15. H. Ji, W. Daughton, *Phys. Plasmas* **18**, 111207 (2011).

10.1126/science.aaa6113

ANTHROPOLOGY

How wheat came to Britain

Wheat reached Britain from the Near East at least 2000 years before the arrival of wheat farming

By **Greger Larson**

Settled communities dependent on agriculture and animal husbandry emerged independently on several continents over the past ~10,000 years. In many cases, farmers began to disperse out of regions where plants and animals were domesticated and into areas occupied by hunter-gatherer populations. This process of Neolithization certainly took place in Europe. Dating of artifacts and bones indisputably associated with human farming has led to a chronological framework for the spread of the Neolithic along two primary routes into Europe that ended with the arrival of farming in Britain ~6000 years ago (*1*). Yet, on page 998 of this issue, Smith *et al.* (*2*) report genomic sequences of wheat in an ~8000-year-old soil sample collected off the coast of southern England, suggesting that domestic crops first appeared on the British Isles long before they were cultivated there.

By ~10,500 years ago, farmers in ancient Anatolia possessed a full complement of domestic plants and animals, yet farmers only arrived in the Balkans between ~8000 and ~9000 years ago. From there, they spread west across the Mediterranean and north along the Danube, reaching western France and the central Rhineland by ~7500 years ago. The first evidence for cereal cultivation on what is now mainland Britain dates back only to ~6000 years ago, suggesting a substantial temporal gap between the two sides of the English Channel (*1*). Because rising sea levels created the English Channel in the early Holocene, it is possible that agricultural products arrived before their accepted appearance on mainland Britain, but that the evidence was flooded by the incoming sea.

A preserved ancient layer of soil had previously been identified at a site called Bouldnor Cliff that rests under marine sediments off the coast of the Isle of Wight (*3*).

Ahead of the agricultural revolution?

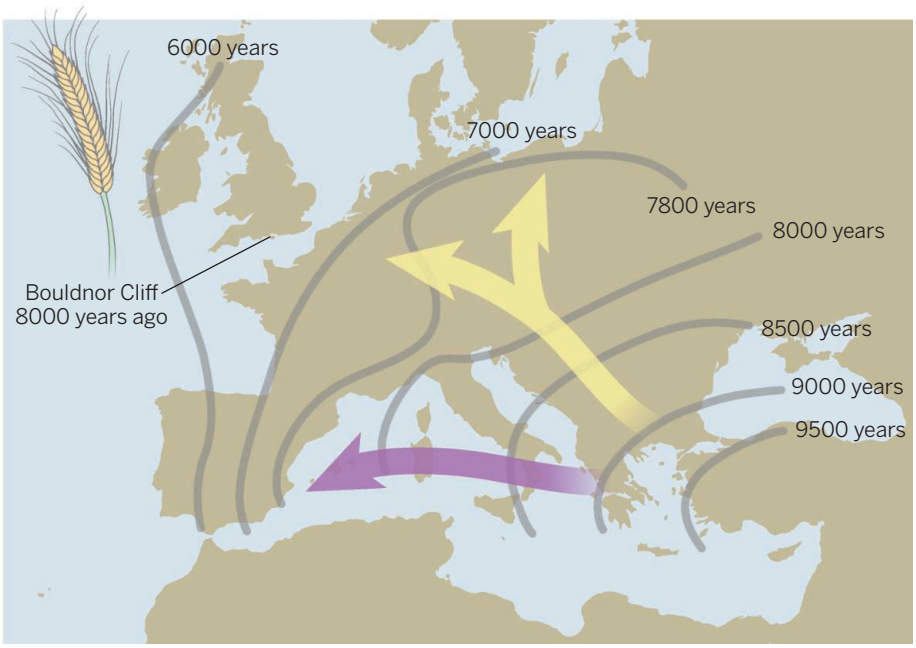

How wheat spread across Europe. Agriculture first appeared in the Near East and then proceeded along two primary routes into Europe (north along the Danube and west through the Mediterranean). Wheat DNA recovered at now-submerged Bouldnor Cliff site shows that wheat was present at least 2000 years before it was first cultivated in Britain.

The former terrestrial soil (in which worked wood, burnt flint, and hazelnut shells have been found) was covered by a peat bog before marine inundation drowned the landscape ~8000 years ago. Characterizing the environment before the flooding of the English Channel required an approach with sufficient resolution to detect the presence of species associated with the hunter-gatherer landscape in the absence (or near-absence) of macrobotanical or fossil remains.

Smith *et al.* therefore turned to ancient DNA. The generation of sequence data has traditionally relied on discrete sources of material linked to individual plants or animals (*4*). Using individual samples is more straightforward, allowing researchers to amplify DNA specific to the organism in question while filtering out exogenous sources that have permeated the samples. However, DNA can also survive in, and be extracted from, environmental contexts, including soil (*5*). The organismal sources of the DNA preserved in disseminated contexts are necessarily uncertain; this is a benefit, because by amplifying and sequencing all recovered DNA, it becomes possible to reconstruct the full complement of ancient environments (*4*).

This method rests, however, on the assumption that once freed from the degraded source material, DNA does not move vertically between archaeological strata. In places where this assumption holds, it has been possible to show how patterns of taxonomic diversity have shifted in Siberia over 400,000 years (*5*), that woolly mammoths and horses persisted in Beringia for several thousand years longer than assumed based on bone evidence alone (*6*), and that Greenland was home to a forest before it was covered by thick glaciers (*7*). But DNA does not always remain fixed in situ. For example, the simultaneous presence of sheep and moa DNA in the same stratigraphic position in a New Zealand cave suggests that sheep urine carrying DNA permeated the sediment and crept into layers once tread upon by moas (*8*).

By sequencing DNA extracted from four radiocarbon-dated soil samples at different intervals along a core taken from Bouldnor Cliff, Smith *et al.* demonstrate a lack of vertical movement; none of their samples contained DNA associated with marine environments, a result corroborated by simultaneous microgeomorphological and microfossil analyses. The peat bog above the ancient soil had effectively capped the terrestrial layers and prevented marine sediments from leaching downward, even as the sea level rose. The DNA profiles reveal sequences of trees (including oak, poplar, and apple), grasses, and herbs that were also detected in a pollen analysis.

Most surprisingly, Smith *et al.* not only detect the presence of DNA sequences associated with wheat, but also show that these wheat sequences represent an increasing proportion of the plant profile in the soil samples dated closer to the present. These sequences match Near Eastern wheat and are genetically distinct from distantly related species in northern Europe and Britain. Pollen analysis did not reveal the presence of wheat, and no archaeological evidence supports cultivation at Bouldnor Cliff. Smith *et al.* therefore conclude that the wheat was not grown on the site but was likely imported. The study provides support for previous work, in which agricultural products and domestic animals were found well outside their production zone in regions occupied by hunter-gatherers (*9*).

The strength of Smith *et al.*'s study lies not only with the empirical evidence, but also in the careful consideration and refutation of the myriad of ways in which the wheat DNA signatures could be the result of false positives or contamination. More generally, the results highlight the pitfalls of focusing on the visible remains in archaeological contexts. Extinct megafauna [such as mammoths (*6*)] survived later than the final bone evidence, and agricultural products appeared earlier than the first evidence of their production as they spread on a wave in front of early farming practices.

The ability to sequence DNA no longer associated with the macroscopic remains from which it originated presents a range of possibilities that begins with a refinement of accepted chronologies. The unexpectedly early appearance of wheat in Britain should force a rethinking of both the strength of the relationships between early farmers and hunter-gatherers, and the origins of settled agricultural communities in Europe. As more analyses of this nature are carried out on suitable archaeological sites, we can begin to reassess the processes responsible for the dispersal (human-assisted and otherwise) of numerous plant and animal species. ■

Palaeogenomics and Bio-Archaeology Research Network, Research Laboratory for Archaeology and the History of Art, University of Oxford, Oxford OX1 3QY, UK.
E-mail: greger.larson@arch.ox.ac.uk

REFERENCES

1. A. Tresset, J.-D. Vigne, *C. R. Biol.* **334**, 182 (2011).
2. O. Smith *et al.*, *Science* **347**, 998 (2015).
3. G. Momber *et al.*, in *Mesolithic Occupation at Bouldnor Cliff and the Submerged Prehistoric Landscapes of the Solent*, G. Momber, D. Tomalin, R. Scaife, J. Satchell, J. Gillespie, Eds. (Council for British Archaeology Research Report, York, 2011), vol. 164, pp. 66–93.
4. N. J. Rawlence *et al.*, *J. Quat. Sci.* **29**, 610 (2014).
5. E. Willerslev *et al.*, *Science* **300**, 791 (2003).
6. J. Haile *et al.*, *Proc. Natl. Acad. Sci. U.S.A.* **106**, 22352 (2009).
7. E. Willerslev *et al.*, *Science* **317**, 111 (2007).
8. J. Haile *et al.*, *Mol. Biol. Evol.* **24**, 982 (2007).
9. C. Jeunesse, *Rev. Alsace* **129**, 97 (2003).

10.1126/science.aaa6113

VIROLOGY

Delineating Ebola entry

A specific calcium channel is required for Ebola virus to infect a cell

By **Darryl Falzarano**[1] *and* **Heinz Feldmann**[2]

The means by which Ebola virus enters a cell are becoming less mysterious. Although a definitive cell surface receptor for the virus, if there is one, remains to be identified, the mechanism of gaining entry is beginning to be fleshed out. Once inside the cell, the importance of numerous sequential processes is becoming better understood. On page 995 of this issue, Sakurai *et al.* (*1*) add another element to the viral entry pathway by showing that a calcium channel called two-pore channel 2 (TPC2) is required for release of the viral genome into the host cell.

After Ebola's surface glycoprotein binds to receptors, which may be nonspecific and possibly comprise numerous carbohydrate proteins (*2*), the virus enters the cell via macropinocytosis, a nonselective process of engulfment (*3*, *4*) (see the figure). Once internalized into a membrane-bound vesicle (endosome), Ebola glycoproteins are cleaved (*5*) while being exposed to an increasingly acidic and reducing environment. All this occurs in the endosome where an essential interaction with a protein called Niemann-Pick C1 (NPC1) was proposed to result in the release of the virus's genetic material in a process known as fusion (*6*, *7*).

A small interfering RNA screen identified calcium signaling in the host cell, among other events, as necessary for Ebola virus entry (*8*). L-type calcium channels were initially pinpointed as the key element involved. However, one of five compounds that block these channels did not prevent Ebola infection, suggesting that another mechanism is also involved. The effective inhibitors also block nicotinic acid adenine dinucleotide phosphate (NAADP)–stimulated intracellular calcium channels—known as the TPCs. These channels are mainly localized to endosomes and lysosomes (acidic compartments where contents are degraded). Through the use of cells lacking TPC2, small interfering RNA, and small-molecule inhibitors, Sakurai *et al.* determined that TPC2 is required for Ebola entry. Moreover, the requirement for TPC2 was shown to be specific to the glycoprotein of Ebola virus, suggesting a highly specific endosomal processing pathway. Previous work demonstrated that NPC1 is also essential for Ebola virus entry and proposed that it may function as an endosomal receptor that triggers fusion (*7*). However, the findings of Sakurai *et al.* suggest that NPC1 is not likely required for fusion itself because late endosomes expressing TPC2, but not NPC1, correlated with productive infection in cultured cells. This indicates that interaction of the cleaved glycoprotein with NPC1 occurs before the glycoprotein interaction with TPC2 and prior to fusion.

Sakurai *et al.* further demonstrate the relevance of TPC2 by blocking the channel's activity with the drug tetrandrine, which improved survival of Ebola-infected mice. This supports the important role of TPC2 for Ebola virus infection; however, it does not indicate that a viable treatment is close at hand. The partial effectiveness of the drug in mice was further reduced by delaying treatment by 1 day. This questions whether any protection would be observed in a macaque model (the "gold standard" for Ebola drug efficacy testing) (*9*). Tetrandrine, originally a traditional Chinese medicine (found in the plant *Stephania tetrandra*), is not approved for use in humans (except in China). In addition, the dose given to mice by Sakurai *et al.* was many times the half-maximal inhibitory dose observed in tissue culture, and likely exceeds doses that would be considered safe for humans. Given the mode of action, it seems unlikely that tetrandrine treatment would be superior to the most advanced Ebola post-

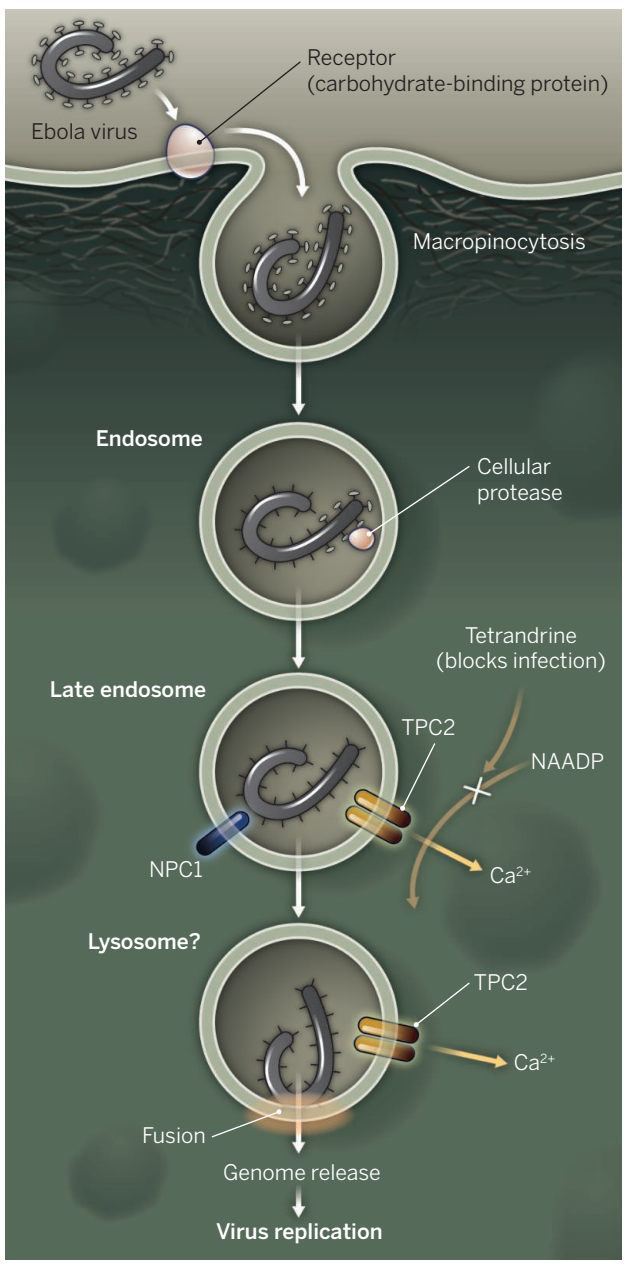

Ebola's entry. A model of infection shows that once the virus is internalized into an endosome, the viral glycoprotein is cleaved and binds to NPC1. The calcium channel TPC2 is then activated prior to a fusion event that releases the viral genome into the cell. The drug tetrandrine blocks TPC2.

[1]*Vaccine and Infectious Disease Organization–International Vaccine Centre, University of Saskatchewan, Saskatoon, SK Canada.* [2]*Laboratory of Virology, Division of Intramural Research, National Institute of Allergy and Infectious Disease, National Institutes of Health, Hamilton, MT, USA.*
E-mail: feldmannh@niaid.nih.gov

ILLUSTRATION: ADAPTED BY C. BICKEL/*SCIENCE*

exposure treatments (including a cocktail of three monoclonal antibodies and an approach based on RNA interference).

Nearly all of the 65 or so antiviral drugs approved for clinical use in the United States are for treating chronic virus infections (including human immunodeficiency virus, hepatitis B virus, and hepatitis C virus). Drugs for more acute viral infections (such as influenza viruses, poxviruses, and herpesviruses) tend to be less effective overall, and translating data from cell culture studies into clinical use is challenging. As Ebola infection typically progresses quickly, the standard metric of the effective concentration values that reduce virus titers by 50% should probably be discarded for this virus. Reducing virus concentrations by 50% is highly unlikely to provide any clinical benefit; rather, aiming for a 90 or 99% reducwtion is more applicable for Ebola. Interestingly, tetrandrine functions in this range in vitro, but given its mode of action as a viral entry inhibitor, it may be better as a prophylactic than as a treatment unless used in combined therapy.

Currently, there are over 60 compounds that have been suggested to be effective against Ebola and/or Marburg virus infections (*10*), but most of these compounds do not have a clear mechanism of action, whereas there is some such understanding for tetrandrine. A few of the compounds have advanced to clinical trials for Ebola (e.g., brincidofovir and favipiravir) largely in the absence of convincing preclinical data. As one may find ethical arguments to support such trials in the current situation, one needs to be concerned about lack of efficacy that may do more harm than good.

Deriving improved versions of drugs such as tetrandrine may eventually lead to a therapeutic approach, but as it stands (the same hold true for other anti-Ebola compounds), that day is not just around the corner. ■

REFERENCES

1. Y. Sakurai *et al.*, *Science* **347**, 995 (2015).
2. C. L. Hunt, N. J. Lennemann, W. Maury, *Viruses* **4**, 258 (2012).
3. M. F. Saeed, A. A. Kolokoltsov, T. Albrecht, R. A. Davey, *PLOS Pathog.* **6**, e1001110 (2010).
4. A. Nanbo *et al.*, *PLOS Pathog.* **6**, e1001121 (2010).
5. K. Chandran, N. J. Sullivan, U. Felbor, S. P. Whelan, J. M. Cunningham, *Science* **308**, 1643 (2005).
6. J. E. Carette *et al.*, *Nature* **477**, 340 (2011).
7. M. Côté *et al.*, *Nature* **477**, 344 (2011).
8. A. A. Kolokoltsov, M. F. Saeed, A. N. Freiberg, M. R. Holbrook, R. A. Davey, *Drug Dev. Res.* **70**, 255 (2009).
9. X. Qiu *et al.*, *Nature* **514**, 47 (2014).
10. E. Picazo, F. Giordanetto, *Drug Discov. Today* 10.1016/j.drudis.2014.12.010 (2014).

ACKNOWLEDGMENTS

This work was supported in part by the Division of Intramural Research, National Institute of Allergy and Infectious Diseases, National Institutes of Health.

10.1126/science.aaa8121

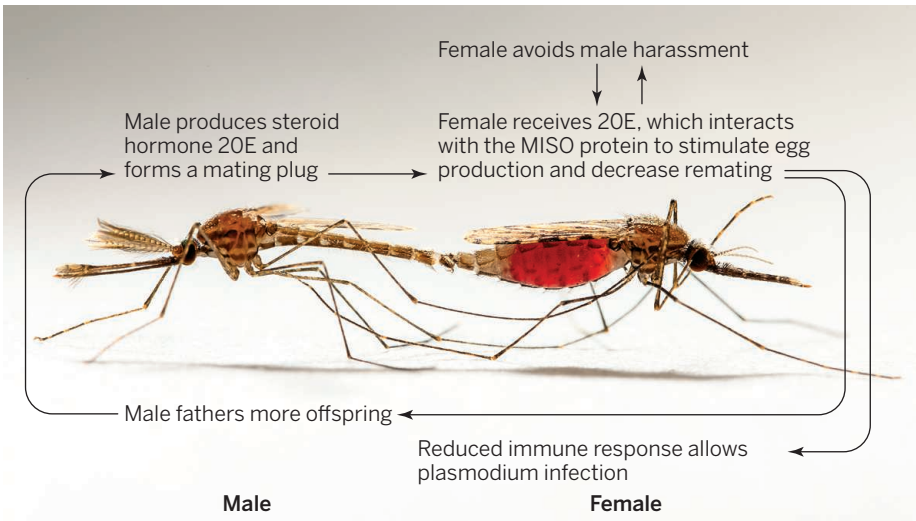

Coevolved sexual traits in male and female mosquitoes. Mitchell *et al*. show that as anophelene mosquitoes evolved, so have the traits that affect interactions between the sexes, and likely also their capacity as vectors of human malaria.

EVOLUTION

An unexpected cost of sex

Coevolution of male and female mosquitoes influences whether mosquitoes transmit human malaria

By **Suzanne H. Alonzo**

Selection arising from interactions between the sexes is responsible for some of the most striking diversity on the planet. These interactions generate coevolutionary dynamics between males and females that have shaped traits such as the striking courtship displays of male birds and the less winsome mating appendages of some male insects (*1*). But research on sexual selection has relevance beyond understanding the weird sex lives of animals. For example, human disturbance of sexual selection can lead to the loss of native species (*2*) and sexually selected male harassment of females can increase a species' risk of extinction (*3*). On page 985 of this issue, Mitchell *et al.* (*4*) show that sexual selection can also be relevant to human health.

The authors report evidence of a coevolved suite of male and female sexual traits in the mosquitoes that transmit the vector responsible for human malaria (see the figure). These traits include the evolution of a "mating plug" that allows males to transfer not only sperm but also the steroid hormone 20-hydroxyecdysone (20E) to females. In the female's reproductive tract, 20E sets off a cascade of processes that increase egg production and decrease the rate at which females mate with other males. Yet, this only happens in species where these male and female traits have coevolved.

Mitchell *et al.* also demonstrate rapid evolution of the mating-induced stimulator of oogenesis (MISO) protein, which is produced by females and interacts with 20E inside the female to increase egg production. In the main vector of malaria, *Anopheles gambiae*, proteins that stimulate egg production are known to decrease female innate immunity, which increases the susceptibility of female mosquitoes to infection by the plasmodium that causes malaria (*5*). It is not currently known why this suite of traits arose in some but not all mosquitoes and if their presence can be used to predict whether a species will transmit human malaria.

Mosquitoes are not exceptional in having a suite of coevolved traits that suggest a complex history of interactions between males and females. In most species with internal fertilization, males transfer ejaculates that contain much more than sperm (*6*). This "cocktail" has been found to reduce competition from other males and induce females to produce eggs, sometimes at a cost to female

Department of Ecology and Evolutionary Biology, and Institute of Marine Sciences, University of California Santa Cruz, CA, USA. E-mail: shalonzo@ucsc.edu

PHOTO: SAM COTTON

survival and immunity (*7*). But females are not innocent dupes in this process. They actively produce compounds and structures that bias which males fertilize their eggs and use male compounds to increase egg production and reduce harassment from other males (*6*). Interactions between the sexes involve a complex web of shared interests and intense conflict. For example, in another insect relevant to human health, the bedbug, males pierce the body cavity of the female to transfer sperm and other compounds. Being pierced carries a risk of infection that decreases female survival (*8*). Yet, males also transfer compounds during mating that increase the number of offspring a female produces over her lifetime (*9*).

Given the potential for rapid evolution in mosquitoes (*10*, *11*), Mitchell *et al.*'s results suggest that any future changes to these male and female sexual traits are likely to influence which mosquitoes transmit human malaria. To use this information to inform the management of malaria, we need to know much more about how the female's reproductive tract responds to the male's ejaculate (*5*). Specific biomarkers, such as the MISO protein, might be used to assess which species will transmit the plasmodium responsible for malaria. The mechanistic interactions between these compounds and female immunity to the malaria-causing plasmodium have only been demonstrated in *A. gambaie* and must therefore also be verified in additional mosquito species.

Mitchell *et al.*'s findings go well beyond current understanding of sexually transmitted diseases and suggest that scientists must also consider how sexual selection affects disease dynamics across species. Who would have guessed that subtle details of the sex lives of mosquitoes could help to explain why some mosquitoes transmit human malaria? Sexual selection may have driven the evolution of malaria transmission by mosquitoes, but scientists can now use their extensive knowledge of sexual selection in these and other species to help manage malaria transmission in the future. ■

REFERENCES

1. S. H. Alonzo, *Trends Ecol. Evol.* **25**, 99 (2010).
2. J. L. Ward, M. J. Blum, *Evol. Appl.* **5**, 901 (2012).
3. J.-F. Le Galliard, P. S. Fitze, R. Ferrière, J. Clobert, *Proc. Natl. Acad. Sci. U.S.A.* **102**, 18231 (2005).
4. S. N. Mitchell *et al.*, *Science* **347**, 985 (2015).
5. M. K. Rono *et al.*, *PLOS Biol.* **8**, e1000434 (2010).
6. J. C. Perry, L. Sirot, S. Wigby, *Trends Ecol. Evol.* **28**, 414 (2013).
7. L. A. McGraw *et al.*, *BioEssays* **37**, 142 (2015).
8. M. T. Siva-Jothy, *Phil. Trans. R. Soc. B* **361**, 269 (2006).
9. K. Reinhardt, R. A. Naylor, M. T. Siva-Jothy, *Proc. Natl. Acad. Sci. U.S.A.* **106**, 21743 (2009).
10. A. G. Hoi, B. D. Roitberg, *Evol. Med. Public Health* **2014**, 162 (2014).
11. D. E. Neafsey *et al.*, *Science* **347**, 43 (2015).

10.1126/science.aaa6495

ACTUATING MATERIALS

Shape-shifting liquid crystals

A new approach to photopatterning liquid crystals produces programmable, shape-shifting soft solids

By **Rafael Verduzco**

Liquid crystal displays (LCDs) contain tens of thousands of pixels filled with a birefringent fluid known as a liquid crystal, in which molecular orientations fluctuate (like a liquid) but still have an average alignment (like a crystal). The moving images we see on a display are created by controlling the net orientation of the molecules, which changes the optical polarization of the liquid so that it either blocks or transmits light. But what if instead of producing an image on a flat screen, your LCD television could transform into different three-dimensional (3D) objects, and then back to a flat screen? Is it possible for soft materials to reproduce shapes instead of images? On page 982 of this issue, Ware *et al.* (*1*) demonstrate this possibility with liquid crystal elastomers (LCEs).

LCEs are soft, elastic solids that can change shape in response to a variety of stimuli: heat, light, and electric and magnetic fields (*2*). They are made up of liquid crystal molecules chemically bonded to a rubbery (flexible) polymer network. The shape of LCEs is coupled with the liquid crystalline ordering, and vice-versa. Changing the orientation or degree of ordering of the liquid crystals produces shape changes in LCEs. Depending on the structure of the liquid crystals and how they are connected to the polymer network, shape changes can be large—LCEs can double or triple in length (*3*).

In theory, LCEs with ideal network structures exhibit what is known as "soft elasticity" and can easily transform between different shapes. The challenge in practice is to dictate and control the liquid crystal ordering in LCEs. A widely used approach for preparing shape-responsive materials, the "two-step" method, simultaneously stretches and cross-links the LCE (*4*). The molecules align in a single direction, and relatively simple shape changes, such as elongation, contraction, bending, and twisting, are possible (*5*, *6*). Achieving more sophisticated shapes requires more complex liquid crystal orientations. An alternative approach, light-mediated patterning and alignment, offers exquisite control over the liquid crystal orientation (*7*–*9*). However,

Department of Chemical and Biomolecular Engineering, Rice University, Houston, TX. E-mail: rafaelv@rice.edu

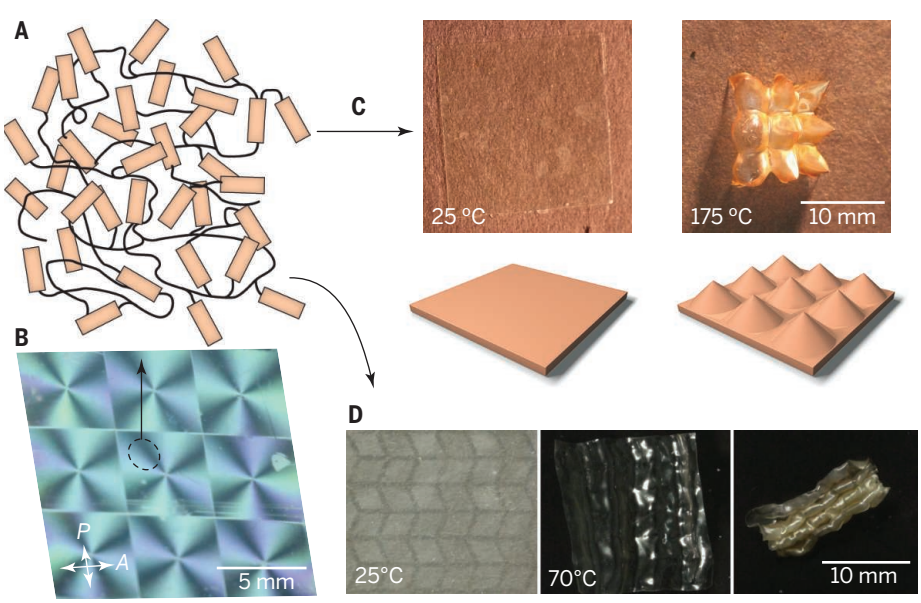

The shaping of things to come? Schematics for (**A**) an LCE with (**B**) patterned liquid crystal "voxels." (**C** and **D**) Analogous to pixels in an LCD screen that define an image, the liquid crystal ordering within the voxels controls the shape of the LCE, resulting in programmed shape change of a thin film.

this produces networks that are stiff and unable to undergo large shape changes.

Ware *et al.* demonstrate an approach to produce complex director orientations in soft, elastic LCEs, and, as a result, effect complex shape changes. First, photoalignment defines a complex liquid crystal pattern on a surface. Next, this pattern is imprinted into an LCE with a liquid crystal fluid that polymerizes slowly to form a polymer network. Ware *et al.* implement chemistry that proceeds without added solvent to form a soft, elastic polymer network. In an analogy to the tens of thousands of pixels in an LCD screen that produce images on a screen, they produce LCEs with 3D patterned elements known as "voxels." Their light-patterning and polymerization technique can produce more than 20,000 voxels that dictate how the LCE changes shape. By changing the pattern in the alignment layer and within these voxels, they produce a conical actuator, a polymer hinge, and a self-foldable Miura Ori pattern, all from an initially flat film.

The work of Ware *et al.* is an important step toward realizing materials that can assume arbitrary and programmable shapes, but a number of challenges remain, especially the incorporation of smart, real-time control over the shape of the LCE. This capability would require integration of the LCE with an electronic system capable of turning the liquid crystal orientation within each voxel. Adding nanomaterials could produce a faster and more sensitive shape-response to a variety of signals (*10*), and reversible chemistry may enable materials that can be reprogrammed to assume different shapes (*11*). Eventually, we might have access to implantable biomaterials that can respond to their surrounding environment or self-folding devices that can disassemble and shrink to small sizes for storage and transport. ■

REFERENCES

1. T. H. Ware, M. E. McConney, J. J. Wie, V. P. Tondiglia, T. J. White, *Science* **347**, 982 (2015).
2. M. Warner, E. M. Terentjev, *Liquid Crystal Elastomers* (Oxford Univ. Press, Oxford, England, 2003).
3. Y. Hong *et al.*, *J. Am. Chem. Soc.* **41**, 15000 (2009).
4. J. Küpfer, H. Finkelmann, *Macromol. Chem. Rapid Commun.* **12**, 717 (1991).
5. N. Torras, K. E. Zinoviev, J. Esteve, A. Sanchez-Ferrer, *J. Mater. Chem. C* **1**, 5183 (2013).
6. A. Agrawal, T. Yun, S. L. Pesek, W. G. Chapman, R. Verduzco, *Soft Matter* **10**, 1411 (2014).
7. L. T. de Haan, C. Sánchez-Somolinos, C. M. W. Bastiaansen, A. P. H. J. Schenning, D. J. Broer, *Angew. Chem. Int. Ed.* **51**, 12469 (2012).
8. M. E. McConney *et al.*, *Adv. Mater.* **25**, 5880 (2013).
9. J. S. Evans *et al.*, *Phys. Rev. Lett.* **110**, 187802 (2013).
10. C. Ohm, M. Brehmer, R. Zentel, *Adv. Mater.* **22**, 3366 (2010).
11. Z. Pei *et al.*, *Nat. Mater.* **13**, 36 (2014).

10.1126/science.aaa6579

PLANT SCIENCE

Insecticidal RNA, the long and short of it

Transgenic plants that express insect-specific RNA in chloroplasts kill pests through RNA interference

By **Steve Whyard**

Insects cost the agricultural sector billions of dollars every year in lost crop yields and insecticide expenditures. The continued use of chemical insecticides has inadvertently selected for more resistant pest strains, prompting higher doses and more frequent applications to control them. The advent of transgenic plants, such as those expressing insecticidal *Bacillus thuringiensis* (Bt) toxins, reduces the use of chemicals while offering protection to some crops (*1*), but not all insects are affected by Bt toxins, and continued use of Bt technologies will eventually see the rise of Bt-resistant insects. To stay ahead of the pests will require additional technologies. On page 991 of this issue, Zhang *et al.* (*2*) describe a clever modification to an existing transgenic plant technology that produces insecticidal RNAs. The trick is to express lethal RNA in the plant's photosynthetic organelles, the chloroplasts.

RNA interference (RNAi) is a mechanism that suppresses gene expression through the presence of double-stranded RNA (dsRNA). Within a eukaryotic cell, long dsRNA is cleaved by the enzyme Dicer into short interfering RNAs (siRNAs), which are about 21 nucleotides in length. The siRNAs, in conjunction with an RNA-induced silencing complex, scan the cell's RNA molecules until a complementary match is found. Once recognized, the target RNA is destroyed. This means of RNA repression therefore silences the corresponding gene.

Sequence-specific gene silencing may enable the development of a new generation of pesticides. Feeding insects dsRNAs that target essential genes through the RNAi mechanism can result in death of the insect, and the in-built gene specificity of this process offers the potential to design dsRNAs that kill one or a few species but have no effect on nontarget species (*3*). Indeed, plants have been engineered to express dsRNAs that greatly reduce insect damage (*4*–*8*), although in most of these studies, not all insects were completely eradicated or protection of the plant was incomplete.

Zhang *et al.* compared transgenic potato plants engineered to produce insecticidal dsRNAs either within chloroplasts or in the cell's cytoplasm. As such, transgenes encoding anti-insect dsRNA were incorporated either into the chloroplast DNA (the organelle harbors its own genome) or the plant's nuclear genome. The results were dramatic: All of the potato beetles feeding on the chloroplast-transformed plants died after 5 days, whereas beetles feeding on plants with dsRNA in the cytoplasm were not affected. Previous dsRNA-feeding studies (*8*, *9*) indicated that ingested long dsRNAs were much more effective than ingested siRNAs at initiating the RNAi response in insects. Chloroplasts lack the cellular RNAi machinery and therefore, long dsRNA produced in these organelles are protected from being cleaved by Dicer. Thus, beetles that fed on the chloroplast-transformed plants ate almost entirely long dsRNA, whereas beetles that ate nuclear-transformed plants consumed mostly siRNAs. The beetles that fed on the chloroplast-derived long dsRNA showed substantial reduction of the target RNAs and ultimately died from lack of the critical RNA and corresponding protein. By contrast, beetles that fed on the plants with dsRNA expressed in the cytoplasm showed only weak RNAi responses—gene expression in these insects was unaffected.

> ***"... the potential for RNAi to control some of the most costly pest insects is great."***

RNAi induced by ingested dsRNA was first observed in the nematode *Caenorhabditis elegans* (*10*), where it was found that the dsRNA did not remain in the worm's gut cells but spread systemically throughout most of the organism. The uptake and systemic spread of dsRNA in *C. elegans* is

Department of Biological Science, University of Manitoba, Winnipeg, Manitoba R3T 2N2, Canada.
E-mail: steve.whyard@umanitoba.ca

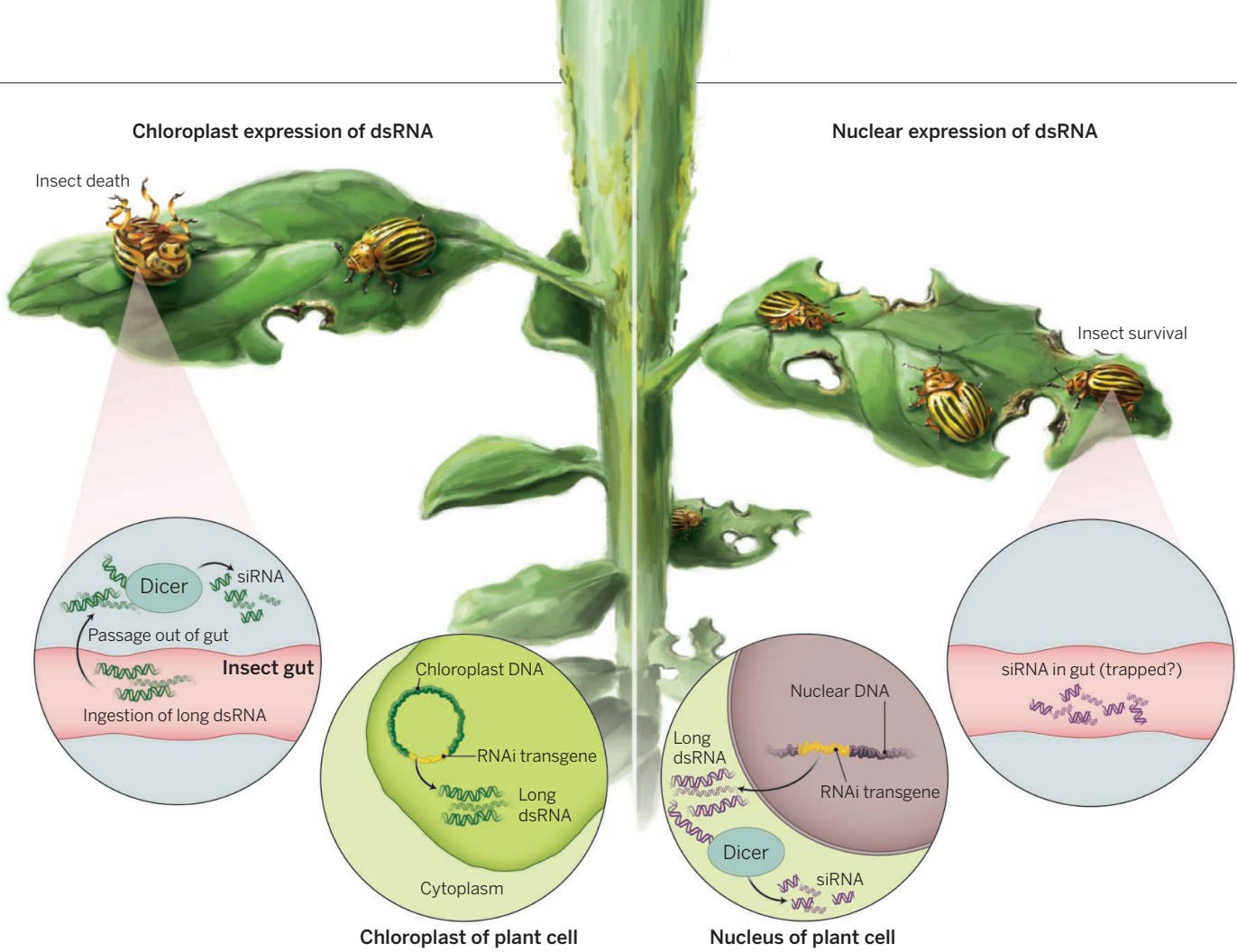

Anti-insect RNA. Transgenic potato plants engineered to express insect-specific long dsRNA in chloroplasts kill potato beetles, whereas those plants expressing dsRNA in the plant cell cytoplasm do not. Chloroplasts do not process dsRNA into siRNA. Therefore, beetles that feed on the chloroplast-transformed plants ingest almost entirely long dsRNA, whereas beetles feeding on nuclear-encoded dsRNAs consume mostly short interfering RNAs (siRNAs). Long dsRNAs are readily absorbed by the beetle's gut cells, and a strong RNAi response is elicited, resulting in high mortalities of the feeding pests. The siRNAs either may not be readily absorbed in the gut or are not in a form suitable to induce RNAi effectively.

facilitated by two transmembrane proteins called systemic RNA interference–defective protein 1 (SID-1) and SID-2 (*11*). Most insects have proteins that share some similarity to the nematode's SID proteins (which function like channels), but their role in dsRNA uptake has not been adequately defined. In the few studies that have examined SID-like proteins in insects, loss of function of the SID-like proteins did not have a large impact on RNAi. Other dsRNA uptake mechanisms, such as receptor-mediated endocytosis (an engulfment process), may play a more important role in dsRNA uptake in insects (*12*). Long dsRNAs, rather than siRNAs, are selectively taken into the gut cells of feeding corn rootworm beetle larvae, but the mechanism of uptake and its curious selectivity for long over short dsRNAs were not identified (*12*). It will be interesting to determine whether different insects use different dsRNA uptake mechanisms, and whether all such mechanisms preferentially select long dsRNAs. Systemic RNAi has also been observed in many insects after ingestion of dsRNA (*12*), but nothing is known of how the RNAi signal is propagated from cell to cell.

It is also unclear whether all crop plants process dsRNA with the same efficiency as the potato plant studied by Zhang *et al.* Indeed, in the few other studies where other plants (corn, cotton, rice, tobacco) were engineered to express anti-insect dsRNAs, the dsRNAs were synthesized in the cytoplasm and presumably were subjected to the host plant's RNAi machinery (Dicer). Each of these studies reported either more pronounced RNAi or better efficacy at controlling pest insects using a cytoplasm-derived dsRNA than did Zhang *et al.*, which could indicate that these plants do not process long dsRNAs as effectively as the potato plants.

Despite the many uncertainties surrounding how insects acquire dsRNAs from their diet and whether all insects will be equally affected by insecticidal dsRNAs, the potential for RNAi to control some of the most costly pest insects is great. With continued improvements in optimizing delivery of the dsRNAs to insects, combined with the specificity that they can confer regarding gene silencing, dsRNA-based insecticides could provide a new generation of environmentally safe insect control technologies to keep crops safe from the hungry mouths of our insect competitors. ■

ILLUSTRATION: V. ALTOUNIAN/*SCIENCE*

REFERENCES

1. A. Bravo, S. Likitvivatanavong, S. S. Gill, M. Soberón, *Insect Biochem. Mol. Biol.* **41**, 423 (2011).
2. J. Zhang *et al.*, *Science* **347**, 991 (2015).
3. S. Whyard, A. D. Singh, S. Wong, *Insect Biochem. Mol. Biol.* **39**, 824 (2009).
4. J. A. Baum *et al.*, *Nat. Biotechnol.* **25**, 1322 (2007).
5. Y. B. Mao *et al.*, *Nat. Biotechnol.* **25**, 1307 (2007).
6. W. Zha *et al.*, *PLOS ONE* **6**, e20504 (2011).
7. M. Pitino, A. D. Coleman, M. E. Maffei, C. J. Ridout, S. A. Hogenhout, *PLOS ONE* **6**, e25709 (2011).
8. P. Kumar, S. S. Pandit, I. T. Baldwin, *PLOS ONE* **7**, e31347 (2012).
9. R. Bolognesi *et al.*, *PLOS ONE* **7**, e47534 (2012).
10. L. Timmons, A. Fire, *Nature* **395**, 854 (1998).
11. J. S. Whangbo, C. P. Hunter, *Trends Genet.* **24**, 297 (2008).
12. N. Wynant, D. Santos, J. Vanden Broeck, *Int. Rev. Cell Mol. Biol.* **312**, 139 (2014).

10.1126/science.aaa7722

CLIMATE CHANGE

Why the Pacific is cool

Natural ocean variability modulates global warming

By **Ben B. Booth**

After a period of rapid global warming, the rate of global temperature rise has slowed markedly in the past 10 to 15 years. Is this "hiatus" a result of natural climate variability, or does it signify a change in the drivers of global warming? On page 988 of this issue, Steinman *et al.* (*1*) present time-series estimates of Atlantic and Pacific variability from state-of-the-art climate modeling. They show that in the past 130 years, periods of natural variability both in the Atlantic and Pacific have at times enhanced or counteracted the underlying global warming trend. The results support the conclusion that cool Pacific temperatures have played a key role in modulating atmospheric temperature increases in the past 10 years (*2*), only partially offset by modest warming in the Atlantic.

An established literature links observed sea surface temperature (SST) variability—mainly in the Atlantic—to substantial decadal-scale shifts in drought, precipitation, temperature extremes, and the frequency of tropical storms. For example, comparatively cool temperatures in the Atlantic during the 1960s and 1970s were linked to prolonged African drought (*3*, *4*), whereas warmer temperatures in the past 20 years have been associated with more Atlantic tropical storms (*5*) and a propensity for drought in the central United States (*6*) and northeast Brazil (*4*). Steinman *et al.*'s study points to at what times these observed changes can be attributed to "natural" climate variations rather than human and volcanic activities.

The analysis suggests that much of the Atlantic variations in the first half of the 20th century arose from ocean variability. In contrast, during the second half of the century, more of the observed Atlantic decadal variations could be explained as responses to volcanic and industrial aerosols (*7*, *8*), with a smaller contribution from ocean-driven changes. The analysis makes it clear that the processes behind natural and external drivers of SST variability in both the Atlantic and the Pacific must be considered in projections of future climate change.

The results offer an opportunity to revisit how we talk about SST variability. Fifteen years ago, Richard Kerr coined the phrase "Atlantic multidecadal oscillation" (AMO) to describe the apparent 40- to 80-year oscillation in observed North Atlantic SSTs (*9*). At the time, the observed variability and natural ocean variability were taken to be synonymous. Since then, research has identified industrial and volcanic aerosols and solar changes as drivers of observed SST variations (*7*, *8*, *10*). This has led to confusion, with papers either referring to the total SST variability (both natural and externally driven) as the AMO (*8*) or only the natural ocean component as the AMO (as done in Steinman *et al.*). There is a real need in the community to agree on common terms to distinguish the two. One possibility would be to use Atlantic multidecadal variability (AMV) to refer to the total temperature variability and AMO for the natural component.

Steinman *et al.* provide insight into the natural ocean contributions—but only if current climate models correctly represent both the external drivers of past climate and the climate responses to them. There are reasons for being cautious on both fronts. For example, Schmidt *et al.* (*11*) identify two climate-forcing factors missing from many current climate simulations: the interactions of aerosols and clouds (for which Steinman *et al.* include the "CMIP5-AIE" best estimate) and the influence of a cluster of tropospheric volcanic eruptions in the past 10 years that is not accounted for in current climate simulations (and hence lies outside Steinman *et al.*'s analysis). Even for those models that include aerosol-cloud interactions, ocean variability estimates are subject to uncertainty due to the way in which these interactions are modeled.

Current models may also miss or inadequately represent key mechanisms. For example, recent studies have linked the cool Pacific conditions identified in (*1*, *2*) to a strengthening of the trade winds (*12*) that is unprecedented in the observational record (*13*). Nevertheless, this wider context does not take away from the value of Steinman *et al.*'s study, which provides much-needed longer-term context for the role that natural ocean-driven variations have played in past climate change. ■

Ocean-driven temperature variability

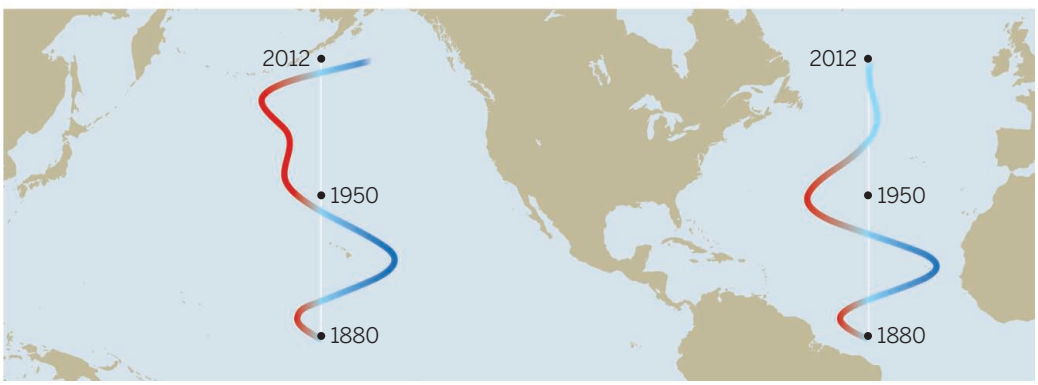

Natural variability. On the basis of current climate simulations and observed temperature records, Steinman *et al*. estimate the role that natural ocean variability has played in modulating temperature trends over the past 130 years.

Met Office Hadley Centre, Exeter EX1 3PB, UK.
E-mail: ben.booth@metoffice.gov.uk

REFERENCES

1. B. A. Steinman, M. E. Mann, S. K. Miller, *Science* **347**, 988 (2015).
2. Y. Kosaka, S.-P. Xie, *Nature* **501**, 403 (2013).
3. M. J. Hoerling, J. Hurrell, J. Eischeid, J. Phillips, *J. Clim.* **19**, 3989 (2006).
4. J. R. Knight, C. K. Folland, A. A. Scaife, *Geophys. Res. Lett.* **33**, L17706 (2006).
5. S. B. Goldenberg, C. W. Landsea, A. M. Mestas-Nunez, W. M. Gray, *Science* **293**, 474 (2001).
6. G. J. McCabe, M. A. Palecki, J. L. Betancourt, *Proc. Natl. Acad. Sci. U.S.A.* **101**, 4136 (2004).
7. B. B. Booth, N. J. Dunstone, P. R. Halloran, T. Andrews, N. Bellouin, *Nature* **484**, 228 (2012).
8. M. F. Knudsen, B. H. Jacobsen, M. S. Seidenkrantz, J. Olsen, *Nat. Commun.* **5**, 3323 (2014).
9. R. A. Kerr, *Science* **288**, 1984 (2000).
10. T. Wang, O. H. Otterå, Y. Gao, H. Wang, *Clim. Dyn.* **39**, 2917 (2012).
11. G. A. Schmidt, D. T. Shindell, K. Tsigaridis, *Nat. Geosci.* **7**, 158 (2014).
12. M. Watanabe *et al.*, *Nat. Clim. Change* **4**, 893 (2014).
13. M. H. England *et al.*, *Nat. Clim. Change* **4**, 222 (2014).

10.1126/science.aaa6113

SUSTAINABILITY

Prediction, precaution, and policy under global change

Emphasize robustness, monitoring, and flexibility

By **Daniel E. Schindler*** *and* **Ray Hilborn**

A great deal of research to inform environmental conservation and management takes a predict-and-prescribe strategy in which improving forecasts about future states of ecosystems is the primary goal. But sufficiently thorough understanding of ecosystems needed to reduce deep uncertainties is probably not achievable, seriously limiting the potential effectiveness of the predict-and-prescribe approach. Instead, research should integrate more closely with policy development to identify the range of alternative plausible futures and develop strategies that are robust across these scenarios and responsive to unpredictable ecosystem dynamics.

Calls for improving forecasts of future ecosystem states are common [e.g., (*1*)]. It is often assumed that poor performance of forecasting models (*2*) derives from weak understanding of ecological complexity and that developing richer mechanistic appreciation of ecological interactions will improve forecasts (*3*). There is also belief that statistical down-scaling of global climate models will improve the accuracy of coupled climate-ecosystem models [e.g., (*4*)]. The utility of this information for improving forecasts of ecosystems is likely small; it is most useful for explaining observed ecological dynamics post hoc. The primary values of ecosystem models are as heuristic tools for communication and for developing scenarios to express uncertainties and test policies; reliable forecasts will remain elusive.

POLICY

Scenario planning is used in many disciplines to assist policy development in situations with deep and irreducible uncertainties (*5*–*7*). A range of information sources, which can include models, is used to develop alternative plausible trajectories of ecosystems; uncertainties about the future are represented by the range of conditions captured by the ensemble of scenarios. In contrast, forecasts narrowly limit uncertainties to those associated with a single potential outcome that is assumed to be predictable; policy developed under this premise will prepare us poorly for the unpredictable (*7*).

LIMITS OF MODELS. Ecosystems are organized around a seemingly infinite number of biological, chemical, and physical processes that play out across enormous ranges of space and time scales (*8*). Feedback mechanisms provide stability such that ecosystems appear stable during some time frames but can abruptly shift to express new structures in others (*9*). Our abilities to make observations are limited to a small range of space and time scales (*8*), limiting our capacity for understanding ecosystems and forecasting how they will respond to local and global change. Thus, environmental management will always operate in a realm where uncertainties dominate (*10*). Although more detailed knowledge about ecological processes will certainly be produced, reliable forecasts will likely accumulate much slower than will be useful for contributing to effective policy for sustainability or conservation, and ecosystems will likely change faster than knowledge accumulates.

PHOTO: KHLONGWANGCHAO/THINKSTOCK

A wide range of modeling approaches is used to explore and forecast ecosystem dynamics. However, models are prone to errors that can mislead policy if not treated with appropriate skepticism (*11*). For example, in statistical models, historical time series are often compared to quantify cause-and-effect relationships between resources and environmental variables. Without controlled manipulations and appropriate reference systems, such comparisons can lead to false conclusions, based on spurious correlations, about cause-and-effect relationships. For example, a reanalysis of 47 previously published relationships between environmental variation and recruitment in marine fish—after including an additional decade of new data—revealed that only one of the previous statistically determined relationships was still used in management because the initial correlations failed to persist through time (*12*).

Nonstationarity in ecosystem relationships (i.e., evolution of parameters that quantify them) adds substantial uncertainty to models, even if statistical relationships are based on real interactions in ecosystems. For example, changing climate and land-use are fundamentally changing the statistical relationships (e.g., between precipitation and river flow) that provide the foundation for water resource planning (*13*). Retrospective analyses of relationships between interacting variables are often used as the basis for forecasting tools. However, in ecological models, statistical parsimony often selects retrospective models that have more mechanistic detail than can be supported when evaluating their forecast performance; the best forecast models are typically mechanism-free, relying on emergent statistical properties of data to make short-term projections (*2*, *14*).

It is typical to validate or verify a numerical model by assessing its ability to accurately simulate observed changes in an ecosystem. However, in even modestly complicated models, simulations can recapture observed dynamics, but for entirely wrong mechanistic reasons (*11*, *15*). Thus, current approaches to verification and validation of ecosystem models likely produce overly optimistic impressions of the reliability of forecasts underlying management and conservation prescriptions.

School of Aquatic and Fishery Sciences, University of Washington, Seattle, WA 98195, USA.
**E-mail: deschind@uw.edu*

ROBUST, FLEXIBLE, MONITORED. Instead of hoping that revealing mechanistic details of ecosystems will provide solutions for achieving sustainability, we summarize the following general principles for developing effective environmental policy.

Policy robustness. In development of environmental policy and the science to support it, emphasis should be placed on assessing robustness: the ability of policies to perform well despite scientific uncertainty (*6*). Risk management through strategies like hedging is an obvious component of this. For example, analysis of freshwater wetlands suggests that a risk dispersion approach to maintaining habitat networks will look substantially different than prescriptions that emerge from assuming causal relationships are known and stationary (*16*). In this case, climate and habitat models can be used to develop scenarios that capture uncertainties in our knowledge of climate effects.

Heterogeneity and options. Effective policy should pursue mechanisms for developing resilience to risks associated with unknowable future changes in ecosystems. Management that maintains ecosystem heterogeneity may improve the reliability of important resource flows [e.g., (*17*)] because response diversity increases the probability that some components will maintain ecological functions under new environmental conditions. Strategic investment in networks of current and possible future habitats under different climate and land-use scenarios does not necessarily require precise forecasts about future climate conditions or effects (*18*). Policies that maintain options for habitats, organisms, and genes will likely be least sensitive to uncertain future risks.

Monitoring and assessment. More emphasis needs to be placed on high-quality monitoring and assessment of ecosystems (*19*). Monitoring must be tailored to address specific questions about ecosystem conditions, and rigorous assessment of data within the context of prevailing theory needs to be routine to evaluate ecological responses to management.

As budgets for science and management shrink, there is a tendency to scale back on investments in monitoring and assessment [e.g., (*20*)] and switch funding to support mechanistic science and predictive modeling. This is a mistake. Although generally not considered as intellectually rich as mechanistic science, accurate assessments of resource states and ecosystem services must be given high priority (*19*). Without monitoring and assessment, we have no way to determine when changes to management are needed (*21*).

Management flexibility and responsiveness. The precautionary approach is widely invoked in situations with deep uncertainty in cause-and-effect relationships and in estimating environmental damage from human activities. The typical application of precautionary management is to limit human activities to within a range over which acceptable levels of damage have been observed. This "better safe than sorry" approach may have unintended consequences that make it a weak strategy. First, there is little opportunity to learn when managing solely within the range of past variation; active probing is usually needed to determine how ecosystems respond to perturbations (*21*). Second, slow response times in ecosystem processes may give the false impression that an ecosystem is unresponsive to specific perturbations until the system is sufficiently degraded that it is difficult to restore (*9*). Third, we should expect that the future is not likely to be a simple extrapolation of the recent past. We should ask (i) what are we doing to detect and quantify shifts to new ecosystem states (*22*) and (ii) what could management regimes do if we were to arrive in these new conditions?

"the best forecast models are typically mechanism-free, relying on emergent statistical properties of data to make short-term projections ..."

Policy should embrace a different dimension of precaution: flexibility. The ability to adapt to ecosystem changes revealed by monitoring and assessment is likely to be a far more powerful strategy than assuming that what has worked in the past will work in the future. Research is needed to establish benchmarks for assessing potential policy performance at the development phase, not after it is apparent that a given policy is failing. The best management and conservation plans will likely be those that can harness unexpected opportunities, while having strategies to adapt when the system moves to undesirable states. A critical step in developing flexible policies is identifying reliable metrics of ecosystem condition to which policy strategies can adjust (*6*). Planning efforts should consider the costs to future actions of any specific policy; those that will be costly to reverse should be discounted.

Such policy flexibility would have been useful in sustaining fishing communities in eastern Canada after changing climate and overfishing caused economic extinction of the Atlantic cod fishery. Freed of predation from cod, production of shellfish and crustaceans more than compensated for economic losses due to closure of cod fisheries (*23*). However, due to rigid regulation of fishing permits (people who had not harvested shellfish in recent years did not hold shellfish permits), families that depended on cod were out of work, replaced by an entirely different sector that harvested shellfish and crustaceans. Had policy enabled fishers to switch among the species they harvested as populations waxed and waned, there might have been less pressure to continue exploiting cod, and the social meltdown that cost Canadians billions of dollars might have been avoided. Policies that lock fishers into specific species and gears are not robust to changes in abundance or species composition of marine ecosystems. Policies that allocate fishing rights across a range of species to communities rather than individuals are likely to be more robust (*24*, *25*).

Resource management and conservation will always involve substantial trial and error, despite huge efforts in basic science to reduce and understand uncertainties. The best we can likely do is enable our abilities to change course as new limits to ecosystems or new opportunities are discovered. ■

REFERENCES AND NOTES

1. J. S. Clark *et al.*, *Science* **293**, 657 (2001).
2. E. J. Ward, E. E. Holmes, J. T. Thorson, B. Collen, *Oikos* **123**, 652 (2014).
3. J. Travis *et al.*, *Proc. Natl. Acad. Sci. U.S.A.* **111**, 581 (2014).
4. J. Franklin *et al.*, *Glob. Change Biol.* **19**, 473 (2013).
5. P. J. H. Schoemaker, *Sloan Manage. Rev.* **36**, 25 (1995).
6. R. J. Lempert, M. E. Schlesinger, *Clim. Change* **45**, 387 (2000).
7. G. D. Peterson, G. S. Cumming, S. R. Carpenter, *Conserv. Biol.* **17**, 358 (2003).
8. S. A. Levin, *Ecology* **73**, 1943 (1992).
9. C. S. Holling, *Ecosystems* **4**, 390 (2001).
10. D. Ludwig, R. Hilborn, C. Walters, *Science* **260**, 17 (1993).
11. J. T. Schnute, L. J. Richards, *Can. J. Fish. Aquat. Sci.* **58**, 10 (2001).
12. R. A. Myers, *Rev. Fish Biol. Fish.* **8**, 285 (1998).
13. P. C. Milly *et al.*, *Science* **319**, 573 (2008).
14. C. T. Perretti, S. B. Munch, G. Sugihara, *Proc. Natl. Acad. Sci. U.S.A.* **110**, 5253 (2013).
15. N. Oreskes, K. Shrader-Frechette, K. Belitz, *Science* **263**, 641 (1994).
16. A. W. Ando, M. L. Mallory, *Proc. Natl. Acad. Sci. U.S.A.* **109**, 6484 (2012).
17. D. E. Schindler *et al.*, *Nature* **465**, 609 (2010).
18. J. Lawler *et al.*, *Front. Ecol. Environ* **8**, 35 (2010).
19. G. M. Lovett *et al.*, *Front. Ecol. Environ* **5**, 253 (2007).
20. C. Lorenz, H. Kunstmann, *J. Hydrometeorol.* **13**, 1397 (2012).
21. C. Walters, *Adaptive Management of Renewable Resources* (MacMillan, New York, (1986)
22. M. Scheffer *et al.*, *Science* **338**, 344 (2012).
23. R. Hilborn, A. E. Punt, J. Orensanz, *Bull. Mar. Sci.* **74**, 493 (2004).
24. M. Makino, H. Matsuda, *Mar. Policy* **29**, 441 (2005).
25. J. C. Castilla, O. Defeo, *Rev. Fish Biol. Fish.* **11**, 1 (2001).

ACKNOWLEDGMENTS

We thank the U.S. National Science Foundation–Dynamics of Coupled Natural and Human Systems Program, and the Harriet Bullitt Professorship for funding.

10.1126/science.1261824

ECOLOGY

The hitchhiker's guide to the Anthropocene

Finding our place in the world we created

By **Hillary Young**

Adventures in the Anthropocene
A Journey to the Heart of the Planet We Made
Gaia Vince
Milkweed Editions, 2014. 465 pp.

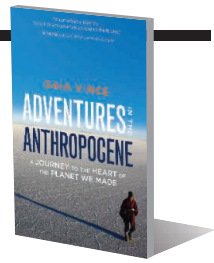

By 2016, a small group of humans, the members of the International Commission of Stratigraphy (ICS), will decide whether our species has so changed the world that even the rocks around us are no longer the same. Has the Holocene epoch that nurtured the flowering of modern humanity now given way to the Anthropocene? Have we, a single ape species with bad backs, hit the earth with a force as powerful as a 6-teraton meteoric explosion?

Although the ICS verdict will be intellectually satisfying, Gaia Vince points out in her new book, *Adventures in the Anthropocene*, that the mark of the Anthropocene has already been indelibly printed upon our planet and our bodies. Nearly half of the nitrogen coursing through our veins was produced in a factory, she informs us, and the current ratio of plastic to marine life in the world's major marine gyres is 6 to 1 by weight. Carbon dioxide levels are nearly 40% higher than in preindustrial times, and soil is eroding between 17 and 57 times as fast as it can be replaced. Through such rich detail, Vince seeks to convince us that we are living in a new kind of world. She surprisingly forgoes the traditional state-of-the planet journalistic narrative, instead spinning rigorous science deftly into an absorbing, and occasionally even light-hearted, around-the-world travelogue. As we methodically review the declining state of the various components of our changed planet (e.g., oceans, rocks, and forests), we are introduced to a mixed flock of characters who are coping with new environments. In Nepal, we meet an enterprising, elderly civil engineer who has returned to his hometown to help local communities deal with declining glacial melt. He does so by redirecting water runoff into a large depression near the village, where it refreezes and packs into an artificial glacier. Each of these glaciers provides an estimated 6 million gallons of water annually to communities in desperate need of it. In Peru, we encounter a poor father of three who is physically painting the nearby mountain white, to increase reflectance and promote local cooling. The future, we are led to believe, will depend on improvisation, intelligence, and the collective strength of individual action. All of these anecdotes are given power because they are wrapped seamlessly into rich biophysical, evolutionary, ecological, and social contexts, thereby drawing readers deeply and painlessly into otherwise overwhelming or impenetrable scientific topics.

Residents of Licapa, Peru, paint the base of a mountain white in the hope that this will lead to reduced temperatures and bring back the glacier that once supplied water to the region.

PHOTO: © NICK PATTINSON

Given the many unknowns and the complexities of the issues, it was refreshing to find Vince unafraid of weighing in with strong opinions on a wide range of contentious topics, including genetically modified foods, valuation of ecosystem services, and population control. In almost every case, she succinctly backs up her position with powerful, and generally well-referenced, arguments. There are some, perhaps unavoidable, examples of oversimplification—for example, a discussion of the effects of climate change on Pacific Island nations glosses over science that explores the complexities of how island atoll geomorphology may mute the effects of sea-level rise and facilitate island persistence. However, for the most part, Vince does an admirable job both of acknowledging the unknowns and of addressing the complex blend of social, biophysical, and economic factors that will be critical to finding solutions.

The book's personal narrative style was particularly compelling in addressing the social component of environmental sustainability that is too often either missing or rendered as meaningless abstraction. For instance, Vince tells of a Ugandan woman whose education was interrupted and whose family was brutalized by recurring social conflict. She is now using improved seeds and training from a government outreach program to manage her land more sustainably and effectively and thus is able to pull her family out of poverty. This tale brings life to a broader discussion of the vital importance of women's education and empowerment in environmental and human sustainability.

The book's critical contribution is in convincing readers that the path to a vital and hospitable planet in this new era is only daunting and not impassable. Hydroponic crops can be fed on saltwater, freshwater can be harvested from the air, and artificial trees can be designed to remove carbon dioxide and cool our planet. Scientists, farmers, slum dwellers, and investors will all play critical roles in finding and implementing these solutions. By the end of this self-help guide for humanity, one is left convinced that we are not only the cause but also the potential cure of our sick planet.

The reviewer is at the Department of Ecology, Evolution, and Marine Biology, Noble Hall 2116, University of California, Santa Barbara, Santa Barbara, CA 93106-9620, USA. E-mail: hillary.young@lifesci.ucsb.edu

10.1126/science.aaa0999

COMPUTER SCIENCE

The computer connection

A closer look at the collaborations that fueled the digital revolution

By **Dov Greenbaum[1,2]* and Mark Gerstein[2]**

Inspired by successes of the late 20th century—including large-scale genomics projects and deep-space missions—everyone in science today seems to extol the virtues of multidisciplinary teamwork. It's now de rigeur, for example, to unite teams of chemists, clinicians, and geneticists for a big translational research project. But how do teams really work? And, more to the point, how do you build teams that function successfully?

In his deftly researched and presented book *The Innovators: How a Group of Hackers, Geniuses, and Geeks Created the Digital Revolution*, Walter Isaacson tells the story of the people who invented the computer and the Internet. Although historical in nature, the book provides insights into the nature of teamwork that are directly applicable to the science of today.

Throughout the narrative, Isaacson makes a compelling case that the most transformational advances in computing have come from combinations of people with complementary skillsets. From the collaboration of theoretical physicist John Bardeen and experimental physicist Walter Brattain, who invented the first transistor, to that of programmer Grace Hopper and hardware specialist Howard Aiken, who developed the first computer that automatically executed long computations, Isaacson maintains that "most of the great innovations of the digital age sprang from an interplay of creative individuals." He singles out solo players, like John Atanasoff—who is often credited with producing the first electronic, digital computer—as less impactful, arguing that "innovation comes from teams more often than from the lightbulb moments of lone geniuses."

In some instances, the teams Isaacson describes seem almost straight out of Hollywood casting, featuring members with similar expertise but with very diverse dispositions and outlooks. For example, the team that founded Intel—electronics mavens Robert Noyce, Gordon Moore, and Andy Grove—had very different personalities: Noyce provided the strategic vision, Moore was detail-oriented and couldn't delegate responsibility, and Grove was the goal-oriented tactician.

Successful collaborations can still exist when individuals dislike or even hate each other. Isaacson uses the contentious relationship of Larry Roberts and Bob Taylor, who worked together to create the global Internet precursor, ARPANET, and the infamous feud between Steve Jobs and Bill Gates—who liberally misappropriated work from each other and from Alan Kay—to illustrate this point.

Isaacson even includes teams not consciously working together in his analysis, demonstrating how one individual can provide the vision and the other the execution. For instance, although they never worked together, computer scientist Tim Berners-Lee provided the vision and conceptual underpinning of the Web, while software engineer Marc Andreessen wrote the first user-friendly browser.

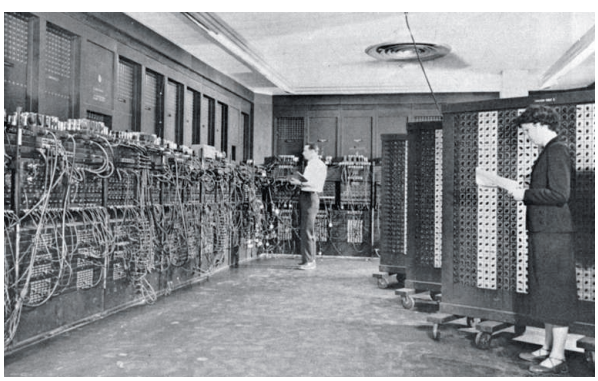

Betty Snyder and Glen Beck program ENIAC, the first general-purpose electronic, digital computer.

Successful teams were frequently embedded in larger institutional structures that promoted disruptive innovation by forcing multidisciplinary collaborations. Isaacson credits Vannevar Bush, the director of the U.S. Office of Scientific Research and Development during World War II, with establishing a successful framework for collaboration across academic, military, and industrial institutions. Perhaps unintentionally, these institutions may have further facilitated innovation by giving many of Isaacson's protagonists a wide berth. For example, a pervasive laissez-faire attitude regarding the use of computing infrastructure allowed an early Google to exploit Stanford's bandwidth and a budding Microsoft to take advantage of Harvard's military-funded computing facilities. The generous sharing of proprietary innovations by Xerox, AT&T, and other established companies also helped fledgling tech companies such as Apple, Texas Instruments, and Fairchild to freely build upon earlier accomplishments.

Isaacson does more than just describe the individuals who were involved in the creation of computing and the Internet. He also elaborates on many technical innovations in a clear and accessible fashion, allowing a broad readership access to the inner workings of the Difference Engine, integrated circuit, and PageRank algorithm, among others. Nonetheless, there are some important contributions missing from his story. Despite the text lavished on Linux, for example, there's little discussion of the early history of its precursor, Unix. There is also a dearth of information on the initial founding of IBM. These notable omissions notwithstanding, one is left with an intuitive understanding of the history of computing from mechanical calculators to electronic computers and, eventually, to software algorithms.

From complementary duos and collegial co-workers to synergistic rivals and unaware collaborators, one can find elements of Isaacson's teams in many contemporary big-science endeavors. However, recent shifts away from traditional, institutionalized science may moot many of Isaacson's take-home lessons. The phenomenon known as "citizen science" harnesses large groups of disparate, unconnected individuals with even more diverse personalities and expertise, who lack the structure and incentives of large institutions and often even lack classical scientific training. Citizen science initiatives are nevertheless successfully coalescing under unified goals and have led to productive collaborations in fields including structural biology and astronomy (*1*, *2*).

The Innovators
How a Group of Hackers, Geniuses, and Geeks Created the Digital Revolution
Walter Isaacson
Simon and Schuster, 2014.
559 pp.

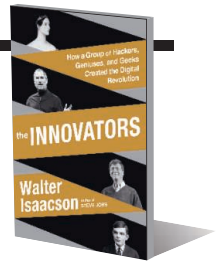

REFERENCES AND NOTES

1. Foldit: Solve Puzzles for Science; http://fold.it.
2. Galaxy Zoo; http://galaxyzoo.org.

10.1126/science.aaa0848

[1]*Zvi Meitar Institute for Legal Implications of Emerging Technologies, Radzyner Law School, Interdisciplinary Center, Herzliya, Israel.* [2]*Computational Biology and Bioinformatics, Yale University, New Haven, CT 06520, USA.*

LETTERS

Edited by **Jennifer Sills**

Reindeer Ewenki's fading culture

THE INDIGENOUS "REINDEER Ewenki" peoples of China use a traditional reindeer herding system unique to the Siberian taiga forests. Yet since the 1970s, this reindeer population has decreased by at least 28% (*1*), posing a threat to both the reindeer and the indigenous peoples whose culture depends on them.

Along with climate change, compromised habitat due to timber production, and land management that restricts foraging and seasonal migration, socioeconomic change in China threatens the reindeer herding system and reindeer population size. Reindeer and Ewenki communities were relocated in 1957, 1965, and 2003 (*2*), and in 1984, the household responsibility herding system replaced the collective reindeer herding system (*3*). After the 2003 relocation, in which reindeer were moved 280 km southward to their current location, the population declined abruptly owing to the unsuitable climate, habitat condition, and a shortage of food (*4*). Moreover, national and regional wildlife and forest protection programs, along with programs banning hunting for Ewenki herders (*5*), have allowed large mammalian predators to flourish and prey upon young reindeer (*1*).

Because of the increasing importance of tourism as a revenue source, the whole nomadic herding system, including reindeer and Ewenki, has gradually become sedentary, causing overgrazing and forageshortage (*4*–*6*). Meanwhile, Ewenki herders are increasingly attracted to the lifestyle offered by regional centers of urbanization. Currently, fewer than 100 Ewenki are directly or indirectly involved in reindeer herding, and fewer than 50 Ewenki regularly live in campsites. Across all Ewenki communities, there are no more than 40 people who can speak the traditional Ewenki language (*2*). Indigenous cultural practices have declined, including shamanistic performances, traditional medicinal use, and traditional dress, whereas the incidence of alcoholism has increased (*4*).

Because of the threat to both the reindeer population and the development, culture, and even survival of the herding system and indigenous communities, their conservation should be prioritized. The current International Union for Conservation of Nature classification of global reindeer of "least concern" should be corrected to reflect the reindeer's population and distribution (*7*–*8*). Reindeer in China should be recognized as "wildlife" or at least "semidomesticated wildlife" by the government and included into the national protected species list. Ecologically suitable nature reserves should be established with different functions such as reintroduction, field-releasing, feralizing, herding culture conservation, and commercial ecotourism.

Reindeer and herding conservation and resource management should be based on the socioecological development of local Ewenki communities, in which economic compensation mechanisms should be initiated whereby the losses resulting from predation, climate change, and some governmental activities can be compensated, and the locals should be provided paid positions as rangers and managers to join all aspects of the management and conservation of reindeer, and the herding cultural system.

Jing Wang,[1] Junping Sun,[1] Achyut Aryal,[2] David Raubenheimer,[3] Deguang Liu,[4] Yan Sheng,[1] Dunhu Chang,[1] Lei Shi,[1] Jian Wu,[1] Zhong Ma,[1] Hongchen Wang,[1] Xiuxiang Meng[1]*

[1]School of Environment and Natural Resources, Renmin University of China, Beijing 100872, China. [2]Institute of Natural and Mathematical Sciences, Massey University, Auckland, New Zealand. [3]Charles Perkins Centre and Faculty of Veterinary Science and School of Biological Sciences, the University of Sydney, Sydney, NSW, Australia. [4]College of Plant Protection, Northwest A & F University, Yangling, Shaanxi 712100, China.

*Corresponding author. E-mail: meng2014@ruc.edu.cn

PHOTO: AP PHOTO/ANDY WONG

A member of the Ewenki walks his reindeer at a forest park in Genhe, Inner Mongolia, China.

REFERENCES

1. X. Meng *et al.*, *J. Nat. Conserv.* **22**, 539 (2014).
2. R. Fraser, *Inner Asia* **12**, 317 (2010).
3. H. Beach, *Cultural Survival Quart.* **27**, 33 (2003).
4. A. Kolås, *Hum. Org.* **70**, 397 (2011).
5. Y. Guo *et al.*, *Chinese J. Appl. Environ. Biol.* **20**, 892 (2014) [in Chinese].
6. P. Wang *et al.*, *Chinese J. Appl. Ecol.* **25**, 2529 (2014) [in Chinese].
7. L. S. Vors, M. S. Boyce, *Glob. Change Biol.* **15**, 2626 (2009).
8. B. C. Forbes *et al.*, *Proc. Natl. Acad. Sci. U.S.A.* **106**, 22041 (2009).

Genetic privacy: Trust is not enough

IN HER NEWS story "Trust me, I'm a medical researcher" (special section on The end of privacy, 30 January, p. 501), J. Couzin-Frankel concludes that mutual trust is key for truthful collaboration between patients and medical researchers. The comparison to collaborations between service providers and users of Uber (a crowdsourced taxi service) and Airbnb (a crowdsourced hotel service) is compelling, but inaccurate: Customers of these companies can easily opt out of service when unsatisfied, with no long-term consequences. By contrast, once a person's DNA sequence is present in public databases, there is no way to contain its dissemination (*1*). Whereas credit cards may be cancelled, sharing of genetic data cannot be undone, and data donors cannot, at least for the foreseeable future, replace their genetic code.

Our world has become a global village, where people often move between countries in search of a livelihood, education, career, or relationship. A person who consented to the open sharing of her genome sequence in a country where she felt protected from misuse of her personal genetic information owing to laws forbidding it, such as the Genetic Information

Nondiscrimination Act of 2008 (GINA) in the United States (*2*), may later move to another country where such protections are nonexistent. There, she could face severe consequences such as denial of health or life insurance or mortgage (which typically requires life insurance), if her genome contains risk alleles for severe illness such as certain types of cancer or neurodegenerative disease. Moreover, even in the United States, GINA does not protect individuals from discrimination by bankers or providers of life or disability insurance (*3*, *4*).

Thus, in the context of assuring the genetic privacy of research participants, mutual trust between patients and researchers is vital, but insufficient. There are no simple solutions for the conflict between genetic privacy and biomedical research needs. Given that trust cannot be enforced, easing such tensions could best arise from further countries passing comprehensive genetic information nondiscrimination laws.

David Gurwitz

Department of Human Molecular Genetics and Biochemistry, Sackler Faculty of Medicine, Tel-Aviv University, Tel-Aviv, 69978, Israel.
E-mail: gurwitz@post.tau.ac.il

REFERENCES

1. J. E. Lunshof, R. Chadwick, D. B. Vorhaus, G. M. Church, *Nat. Rev. Genet.* **9**, 406 (2008).
2. R. Korobkin, R. Rajkumar, *N. Engl. J. Med.* **359**, 335 (2008).
3. D. Gurwitz, I. Fortier, J. E. Lunshof, B. M. Knoppers, *Science* **325**, 818 (2009).
4. Genetic Information Nondiscrimination Act, Public Law No. 110-233.

Navigating Massive Open Online Courses

WE AGREE WHOLEHEARTEDLY with J. Reich that research on the effectiveness of Massive Open Online Courses (MOOCs) must focus on learning rather than mere clicking ("Rebooting MOOC research," Education Forum, 2 January, p. 34). Our biggest challenge will be figuring out what is most appropriate for an individual student at a given moment.

Ideally, a MOOC would work like the GPS navigation device in your car. You tell it where you want to go, it figures out where you are, and it guides you along the most optimal route. Keeping with the analogy, current MOOCs are like having all GPS navigation devices instruct every car driver to turn right at 9:15 on Monday morning.

If we can't adapt teaching and practice to the individual learner, MOOCs will never be more than a digital version of classroom teaching. To personalize the learning experience, we first need a detailed description of what a student already can and cannot do. Such information can be determined by traditional tests or by more powerful methods such as the practice-based trackers that already exist in other domains of online education (*1*). The A/B testing discussed in the Education Forum provides us with ideal methodology to start putting roads on the educational map. Once we gather information about various conditions, we can map each student's optimal route.

Alexander O. Savi,[1]* Han L. J. van der Maas,[1] Gunter K. J. Maris[1,2]

[1]Department of Psychological Methods, University of Amsterdam, Weesperplein 4, 1018 XA, Amsterdam, Netherlands. [2]Cito, Amsterdamseweg 13, 6814 CM, Arnhem, Netherlands.

*Corresponding author. E-mail: o.a.savi@gmail.com

REFERENCE

1. S. Klinkenberg, M. Straatemeier, H. van der Maas, *Comput. Educ.* **57**, 1813 (2011).

ACKNOWLEDGMENTS: Funding by NWO (The Netherlands Organisation for Scientific Research), grant number CI1-12-S037.

AAAS president sees desire for global collaboration

AAAS can help its members build scientific partnerships in developing countries, says Geraldine Richmond.

By **Becky Ham**

Geraldine Richmond (left center, white shirt) visits with scientists as part of the COACh Cameroon Program.

PHOTO: COURTESY GERALDINE RICHMOND

Geraldine Richmond started this year with visits to Thailand and Vietnam in her role as U.S. science envoy for the Lower Mekong Delta. She saw scientists there grappling with issues of coastal flooding, the impacts of dam building, and field tests of vaccines for HIV. She also saw opportunities for scientists in the U.S. and those countries to work together.

"We have a lot to learn from people and scientists in these developing countries, because many of these problems, such as those associated with climate change and water issues, are merely foreshadowing what we in the United States will have in years to come," Richmond said.

"It just reinforced my strong belief that scientific partnerships at the scientist level—boots on the ground, lab to lab—are so critically needed on both sides," she continued. "I believe scientists in the U.S. want to play a role in this, and that AAAS can be valuable in helping make those connections."

Richmond wants to encourage these collaborations in her year as AAAS president, which began on 16 February. "The most challenging global problems we face require a broader integration of expertise than we've ever needed before," she said. "AAAS uniquely embraces and provides an integrative platform for bringing together the physical, the biological, and the social sciences that are so essential for addressing these issues."

AAAS has done much to facilitate broader science policy engagement by seeking partnerships with other national and international scientific associations, Richmond noted, through the work of its Center for Science Diplomacy and other international programs. This outreach will continue under Richmond's direction of the 2016 AAAS Annual Meeting, where the theme will be global engagement as it relates to developing countries.

In March, she will visit Laos and Cambodia and hopes to solicit applications to the meeting from scientists there. "When I go to these other countries and see how many exciting things are going on between the U.S. and these countries, I want everyone to know about it," she said.

Richmond's own international experience extends to Africa, Latin America, India, and the Middle East through COACh, a career training and networking program for women scientists and engineers that she founded in 1998. The program's workshops in communication, negotiation, and leadership skills have reached more than 12,000 participants, and follow-up studies show that 90% of those participants go on to mentor others in these skills. COACh's international program serves both men and women researchers in developing countries and brings women from the U.S. and other countries together for scientific conferences.

She has been delighted to see the program's "multiplier effect" continuing, with coaches from Cameroon traveling to coach other women in Nigeria, for example. "That's been our plan in the U.S. and globally, to train women, to understand their issues, and give them the career skills that they might not always learn in their traditional science education," said Richmond.

Richmond is the Presidential Chair in Science and professor of chemistry at the University of Oregon. Her research looks at the molecular processes in liquid surfaces, with applications in environmental remediation, energy production, and climate change. She has served on several national scientific advisory boards, including a current appointment to the National Science Board.

Born to a Kansas farmer and a beautician, Richmond said her mother encouraged her to learn math as a critical career skill. "She knew the precariousness of employment, after living through the Depression and World War II, and she had four daughters who had to make a living for themselves," she recalled. "In her mind, as long as you knew math, or were good at math, you could do anything."

After that, she "fell in love slowly" with science, Richmond said, and research remains at the heart of her career. "I have a fabulous lab here, and I can't give that up, as a practicing scientist and educator. My office is in the back of my lab, so I'm sitting here right now with my lasers operating 20 feet away."

Richmond said AAAS offers many ways for scientists and engineers to become involved beyond the lab. "In my year as president I want to expand our outreach to get engagement of more of our scientists who would never have thought about AAAS beyond *Science* magazine," she said, "and to realize that getting engaged with this global network can be extraordinarily important in career advancement, as well as satisfying passions in making a real difference by being involved in global activities." ■

RESEARCH

Shape-shifting 2D to 3D liquid-crystal microactuators

Ware et al., *p. 982*

IN *SCIENCE* JOURNALS

Edited by **Stella Hurtley**

The Colorado potato beetle (*Leptinotarsa decemlineata*)

PEST CONTROL

Bypassing a plant's defense for pest defense

Colorado potato beetles can skeletonize the leaves on a potato plant, devastating crop yields. Insecticides are increasingly useless as the beetle evolves resistance. Zhang *et al.* used RNA interference to take down this beetle (see the Perspective by Whyard). Success required shifting production of the double-stranded RNA to the plastids to evade the plant's own RNA management mechanisms. The insect's own RNA interference mechanisms then inactivated two everyday genes that the beetle can't do without. — PJH

Science, this issue p. 991; see also p. 950

MOSQUITO BIOLOGY

Mating plugs promote malaria parasites

Males of some of the malaria-transmitting mosquitoes "plug" females after copulation to stop interloping males from mating. The mating plug also delivers a steroid hormone into the female uterus. This hormone pulse promotes egg production and stimulates egg laying. It also curbs the mosquitoes' immune responses, which allows parasites such as malaria to develop unhindered. Mitchell *et al.* discovered that plugs are a recent evolutionary acquisition (see the Perspective by Alonzo). South American anopheline mosquitoes lack these plugs altogether, whereas African and Indian species have complex plugs replete with hormones. It is unlikely to be a coincidence that the most elaborate mosquito plugs are also found in regions where malaria transmission rates are highest. — CA

Science, this issue p. 985; see also p. 948

SURFACE CHEMISTRY

Catching CO oxidation

Details of the transition state that forms as carbon monoxide (CO) adsorbed on a ruthenium surface is oxidized to CO_2 have been revealed by ultrafast excitation and probe methods. Öström *et al.* initiated the reaction between CO and adsorbed oxygen atoms with laser pulses that rapidly heated the surface and then probed the changes in electronic structure with oxygen x-ray absorption spectroscopy. They observed transition-state configurations that are consistent with density functional theory and a quantum oscillator model. — PDS

Science, this issue p. 978

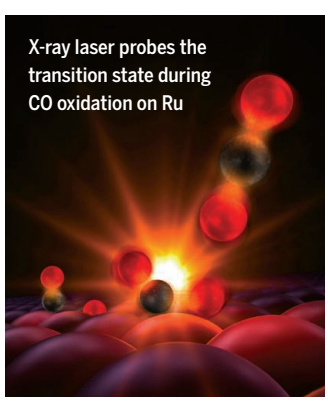

X-ray laser probes the transition state during CO oxidation on Ru

OPTICS

Light with twist and structure

Möbius strips are three-dimensional structures consisting of a surface with just a single side. Readily demonstrated by snipping a paper ring, adding a twist, and then joining the ends of paper together again, these structures have intriguing mathematical properties in terms of topology and geometry. Bauer *et al.* used a liquid crystal to engineer the wavefront of a laser beam to make an optical version of the Möbius strip by effectively "snipping and twisting" the polarization properties of the light beam. — ISO

Science, this issue p. 964

CLIMATE CHANGE

Is the end of the warming hiatus nigh?

Which recent climate changes have been forced by greenhouse gas emissions, and which have been natural fluctuations of the climate system? Steinman *et al.* combined observational data and a large collection of climate models to assess the Northern Hemisphere climate over the past

150 years (see the Perspective by Booth). At various points in time, the Pacific Decadal Oscillation and the Atlantic Multidecadal Oscillation have played particularly large roles in producing temperature trends. Their effects have combined to cause the apparent pause in warming at the beginning of the 21st century, known as the warming "hiatus." This pause is projected to end in the near future as temperatures resume their upward climb. — HJS

Science, this issue p. 988; see also p. 952

ARCHAEOLOGY

Early wheat movement into Britain

The transition into the New Stone Age, or Neolithic period, in Great Britain and Europe was characterized by a change from hunter-gatherers to farmers. However, the early stages of this transition are not well understood. Smith *et al.* studied archaeological remains at an 8000-year-old site that has been underwater ever since the Neolithic (see the Perspective by Larson). The finds include evidence of wheat (or a relative of wheat) 2000 years before the first documented farmers in Britain. It seems that trade may have preceded the adoption of farming. — LMZ

Science, this issue p. 998; see also p. 945

LUNG DISEASE

Mucus: It's the quality that counts

In patients with cystic fibrosis (CF) or other lung diseases, airway mucus can be highly elastic and very difficult to clear, leading to airflow obstruction and lung infection. Now, Yuan *et al.* show that the biophysical properties of mucus from CF patients are altered because of neutrophilic oxidative stress. To combat this, they targeted mucin disulfide crosslinks with a thiol-modified carbohydrate and produced fast-acting mucolytic activity toward CF sputum. Their findings support the use of mucolytics as a therapeutic strategy for treating CF and related inflammatory lung diseases. — ACC

Sci. Transl. Med. **7**, 276ra27 (2015).

FUEL CELLS

Metal-free catalysts for fuel cell technology

Metal-free catalysts have recently been designed for use in alkaline fuel cells. Dai *et al.* have successfully used a metal-free catalyst in an acidic polymer electrolyte membrane fuel cell: the mainstream fuel cell technology. Nitrogen-doped carbon nanotubes and their graphene composites catalyzed oxygen reduction in these practical fuel cells. The carbon-based catalysts showed both excellent activity and durability and offer an inexpensive alternative to metal-based catalysts. Such an approach could potentially reduce the manufacturing cost of fuel cells dramatically and open the door for their commercialization. — ZHK

Sci. Adv. 10.1126/sciadv.1400129 (2015).

EBOLA VIRUS

Channeling Ebola virus entry into the cell

The current outbreak of Ebola virus in West Africa highlights the need for antiviral therapies. One strategy would be to block the Ebola virus's ability to enter host cells. Cells engulf Ebola virus particles, which then traffic into the cell in structures called endosomes. Sakurai *et al.* now report that the Ebola virus requires calcium channels called two-pore channels (TPCs) in endosomal membranes for successful entry (see the Perspective by Falzarano and Feldmann). The Ebola virus could not enter cells lacking TPCs or cells treated with a TPC inhibitor. Blocking TPCs therapeutically allowed 50% of mice to survive an ordinarily lethal Ebola virus infection. — KLM

Science, this issue p. 995; see also p. 947

IN OTHER JOURNALS

Edited by **Kristen Mueller** *and* **Jesse Smith**

Five small rocky planets orbit the star Kepler-444

EXOPLANET DETECTION

Untangling dips and pulses in starlight

The menagerie of known exoplanets continues to grow with Kepler data. The NASA spacecraft has monitored stars for brightness dips due to planetary transits, enabling Campante *et al.* to find five rocky planets orbiting the K star Kepler-444—all between Mercury and Venus in size. Kepler's precise photometry also allowed the team to measure the star's asteroseismic pulsations. A comparison of those values with stellar evolution models revealed an age of 11.2 ± 1.0 billion years, or 80% as old as the universe itself. A planetary system this old (over twice the age of Earth) demonstrates the wide time frame in which Earth-sized planets have existed and helps astronomers discern the earliest times of planet formation. — MMM

Astrophys. J. 10.1088/0004-637X/799/2/170 (2015).

PHYSICS

Hunting the elusive (quasi)particles

Majorana fermions, particles that are their own antiparticles, have not yet been observed in nature. There have, however, been several possible sightings of their counterparts in solid-state systems, which may eventually lead to advances in quantum computing. Xu *et al.* used scanning tunneling microscopy to observe signatures of these Majorana modes in a system consisting of a conventional superconductor with a topological insulator (TI) layer on top of it. The authors observed a distinct change of the experimental signal as the thickness of the TI layer crossed a threshold value, which they interpreted as evidence for the Majorana modes. — JS

Phys. Rev. Lett. **114**, 017001 (2015).

ILLUSTRATION: TIAGO CAMPANTE/PETER DEVINE

ALSO IN *SCIENCE* JOURNALS

Edited by **Stella Hurtley**

SUSTAINABILITY

Seeking systems-based solutions

Without sustainable solutions, the world's most pressing environmental concerns will continue to persist or worsen. Achieving the goal of sustainability involves so many factors—from economics to ecology—that investigating one or even a handful of variables at a time often overlooks major parts of the problem. Liu *et al.* review systems-based approaches that are beginning to provide tenable ways to assess sustainability. Further integrating coupled human and natural components of a problem across multiple dimensions, including how one solution can create unintended consequences elsewhere, is essential for developing effective policies that seek global sustainability. — NW

Science, this issue p. 963

PLASMA PHYSICS

Shocking! Particle accelerators in space

The acceleration of charged particles to high energies has been a major mystery, with a number of competing theories based on plasma physics. Many include the concept of turbulence, but with different roles. For example, shock-based theories emphasize the importance of turbulence developed from an unstable shock layer, whereas turbulent reconnection theories emphasize interactions of multiple reconnection sites. Matsumoto *et al.* present results of a large particle-in-cell simulation and examine how electrons are accelerated in the transition layer of a fast nonrelativistic shock (see the Perspective by Ji and Zweibel). Surprisingly, they find that when the shock is strong enough, charged particles (electrons in this case) are efficiently accelerated by turbulent reconnection within a turbulent shock layer containing multiscale structures. — MMM

Science, this issue p. 974; see also p. 944

GENE REGULATION

Uncaging promoter and enhancer dynamics

In order to understand cellular differentiation, it is important to understand the timing of the regulation of gene expression. Arner *et al.* used cap analysis of gene expression (CAGE) to analyze gene enhancer and promoter activities in a number of human and mouse cell types. The RNA of enhancers was transcribed first, followed by that of transcription factors, and finally by genes that are not transcription factors. — LMZ

Science, this issue p. 1010

ACTUATING MATERIALS

Making small actuators more effective

Liquid-crystal molecules orient locally in response to external fields. When long-chain liquid-crystalline molecules are cross-linked together, changes in local orientation can lead to significant volume changes. Ware *et al.* made efficient microactuators that can change their shape from flat to three-dimensional structures (see the Perspective by Verduzco). By patterning volume elements so that each has a different preferred alignment for the liquid-crystalline molecules, they could fine-tune the volume changes. — MSL

Science, this issue p. 982; see also p. 949

STEM CELLS

mRNA modification regulates pluripotency

When stem cells progress from an embryonic pluripotent state toward a particular lineage, molecular switches dismantle the transcription factor network that keeps the cell pluripotent. Geula *et al.* now show that N6-methyladenosine (m6A), a messenger RNA (mRNA) modification present on transcripts of pluripotency factors, drives this transition. Methylation destabilized mRNA transcripts and limited their translation efficiency, which promoted the timely decay of naïve pluripotency. This m6A methylation was also critical for mammalian development. — BAP

Science, this issue p. 1002

CANCER

The downstream effects of false promotion

Special DNA sequences at the ends of chromosomes, called telomeres, are replenished by a dedicated enzyme called telomerase. A subset of human tumors harbors mutations in the promoter region of the TERT gene, which codes for a subunit of telomerase. Borah *et al.* explored the downstream effects of TERT promoter mutations in cells derived from urothelial (urinary tract) cancers. The mutations were associated with aberrantly high levels of TERT mRNA, TERT protein and telomerase activity, and longer telomeres. A small study of clinical samples suggested that high levels of TERT mRNA may be a marker of more aggressive urothelial cancers. — PAK

Science, this issue p. 1006

TRANSCRIPTION

Keeping repressed genes repressed

Hox genes confer positional identity to cells and tissues. Maintaining precise spatial patterns of *Hox* gene expression is vital during metazoan development. The transcriptional repressor CTCF is involved in the regulation of chromatin architecture. Narendra *et al.* show that a CTCF protein binding site insulates regions of active and repressed *Hox* gene expression from each other. This protects heterochromatin containing repressed *Hox* genes from the encroaching spread of active chromatin. The CTCF protein appears to organize the active and repressed chromatin regions into distinct architectural domains. — GR

Science, this issue p. 1017

EVOLUTION

Losing and then regaining flagella

The ability to adapt to changes in the function of gene regulators, as opposed to structural genes, is a crucial aspect of evolutionary change. Taylor *et al.* mutated a central regulator for the formation of flagella in the bacterium *Pseudomonas fluorescens*. They then put the mutated flagella-free bacteria under strong selection pressure to regain mobility. The mutated bacteria regained the lost flagella, and motility, within 4 days. Two stereotypical mutations diverted an evolutionarily related regulator that normally controls nitrogen uptake to control flagella biosynthesis. The mutations increased the levels of the co-opted regulator, then altered its specificity for the flagella pathway. — GR

Science, this issue p. 1014

INFLAMMATION

Itching to reduce inflammation

The kinase p38 is activated in various inflammatory skin disorders, but drugs that block p38 activity can cause toxicity. Mice deficient in the E3 ubiquitin ligase Itch have itchy skin. Theivanthiran *et al.* studied the α isoform of p38 in these mice. Skin cells from Itch-deficient mice had more active p38α and higher levels of

the p38α-binding protein Tab1. In skin cells from normal mice, Tab1 was targeted for degradation by Itch. Skin inflammation in Itch-deficient mice was decreased after injection with a peptide that blocked the Tab1-p38α interaction, suggesting an alternative way to target p38α in inflammatory disorders. — JFF

Sci. Signal. **8**, ra22 (2015).

SOLAR CELLS

Balanced carrier diffusion in perovskites

The efficient operation of solar cells based on inorganic-organic perovskites requires balanced transport of positive and negative charge carriers over long distances. Dong *et al.* used a top-seeded solution growth method to obtain millimeter-scale single crystals of the organolead trihalide perovskite $CH_3NH_3PbI_3$. Under low light illumination, the electron and hole diffusion lengths exceeded 3 mm, and under full sunlight illumination, they exceeded 175 μm. — PDS

Science, this issue p. 967

WATER SPLITTING

An enduring catalyst built from carbon

Splitting water into its constituent elements, hydrogen and oxygen, generally requires the assistance of metal catalysts. Liu *et al.* now show that a metal-free hybrid material composed of carbon and nitrogen can promote this reaction all on its own, with the help of some visible light. The photocatalyst combines one material (C_3N_4) known to split water into hydrogen and peroxide with a second material (CDot) that breaks the peroxide down before it can damage the first. The robust stability of this hybrid bodes well for practical implementation of optimized analogs in solar energy storage schemes. — JSY

Science, this issue p. 970

150 years (see the Perspective by Booth). At various points in time, the Pacific Decadal Oscillation and the Atlantic Multidecadal Oscillation have played particularly large roles in producing temperature trends. Their effects have combined to cause the apparent pause in warming at the beginning of the 21st century, known as the warming "hiatus." This pause is projected to end in the near future as temperatures resume their upward climb. — HJS

Science, this issue p. 988; see also p. 952

ARCHAEOLOGY

Early wheat movement into Britain

The transition into the New Stone Age, or Neolithic period, in Great Britain and Europe was characterized by a change from hunter-gatherers to farmers. However, the early stages of this transition are not well understood. Smith *et al.* studied archaeological remains at an 8000-year-old site that has been underwater ever since the Neolithic (see the Perspective by Larson). The finds include evidence of wheat (or a relative of wheat) 2000 years before the first documented farmers in Britain. It seems that trade may have preceded the adoption of farming. — LMZ

Science, this issue p. 998; see also p. 945

LUNG DISEASE

Mucus: It's the quality that counts

In patients with cystic fibrosis (CF) or other lung diseases, airway mucus can be highly elastic and very difficult to clear, leading to airflow obstruction and lung infection. Now, Yuan *et al.* show that the biophysical properties of mucus from CF patients are altered because of neutrophilic oxidative stress. To combat this, they targeted mucin disulfide crosslinks with a thiol-modified carbohydrate and produced fast-acting mucolytic activity toward CF sputum. Their findings support the use of mucolytics as a therapeutic strategy for treating CF and related inflammatory lung diseases. — ACC

Sci. Transl. Med. **7**, 276ra27 (2015).

FUEL CELLS

Metal-free catalysts for fuel cell technology

Metal-free catalysts have recently been designed for use in alkaline fuel cells. Dai *et al.* have successfully used a metal-free catalyst in an acidic polymer electrolyte membrane fuel cell: the mainstream fuel cell technology. Nitrogen-doped carbon nanotubes and their graphene composites catalyzed oxygen reduction in these practical fuel cells. The carbon-based catalysts showed both excellent activity and durability and offer an inexpensive alternative to metal-based catalysts. Such an approach could potentially reduce the manufacturing cost of fuel cells dramatically and open the door for their commercialization. — ZHK

Sci. Adv. 10.1126/sciadv.1400129 (2015).

EBOLA VIRUS

Channeling Ebola virus entry into the cell

The current outbreak of Ebola virus in West Africa highlights the need for antiviral therapies. One strategy would be to block the Ebola virus's ability to enter host cells. Cells engulf Ebola virus particles, which then traffic into the cell in structures called endosomes. Sakurai *et al.* now report that the Ebola virus requires calcium channels called two-pore channels (TPCs) in endosomal membranes for successful entry (see the Perspective by Falzarano and Feldmann). The Ebola virus could not enter cells lacking TPCs or cells treated with a TPC inhibitor. Blocking TPCs therapeutically allowed 50% of mice to survive an ordinarily lethal Ebola virus infection. — KLM

Science, this issue p. 995; see also p. 947

IN OTHER JOURNALS

Edited by **Kristen Mueller** *and* **Jesse Smith**

Five small rocky planets orbit the star Kepler-444

EXOPLANET DETECTION

Untangling dips and pulses in starlight

The menagerie of known exoplanets continues to grow with Kepler data. The NASA spacecraft has monitored stars for brightness dips due to planetary transits, enabling Campante *et al.* to find five rocky planets orbiting the K star Kepler-444—all between Mercury and Venus in size. Kepler's precise photometry also allowed the team to measure the star's asteroseismic pulsations. A comparison of those values with stellar evolution models revealed an age of 11.2 ± 1.0 billion years, or 80% as old as the universe itself. A planetary system this old (over twice the age of Earth) demonstrates the wide time frame in which Earth-sized planets have existed and helps astronomers discern the earliest times of planet formation. — MMM

Astrophys. J. 10.1088/0004-637X/799/2/170 (2015).

PHYSICS

Hunting the elusive (quasi)particles

Majorana fermions, particles that are their own antiparticles, have not yet been observed in nature. There have, however, been several possible sightings of their counterparts in solid-state systems, which may eventually lead to advances in quantum computing. Xu *et al.* used scanning tunneling microscopy to observe signatures of these Majorana modes in a system consisting of a conventional superconductor with a topological insulator (TI) layer on top of it. The authors observed a distinct change of the experimental signal as the thickness of the TI layer crossed a threshold value, which they interpreted as evidence for the Majorana modes. — JS

Phys. Rev. Lett. **114**, 017001 (2015).

ILLUSTRATION: TIAGO CAMPANTE/PETER DEVINE

RNA EDITING

Squid are hyper-editors when it comes to RNA

During RNA editing, specific enzymes alter nucleotides in mRNA transcripts so that the resulting protein differs in amino acid sequence from what was encoded by the original DNA. Such RNA editing is a means to generate greater protein diversity; however, most organisms only use it sparingly. Alon *et al.*, however, now report an exception. They sequenced RNA and DNA from the squid nervous system and discovered that 60% of the transcripts exhibited RNA editing. Such "recoding" occurred largely in genes with cytoskeletal or neuronal functions and may be advantageous to organisms such as squid that must respond quickly and continually to environmental changes. — LC

eLife **4**, e05198 (2015).

The nervous system of squid contains an unusually high amount of edited RNA

SOCIAL SCIENCE

Trading growth for happiness

Does the dawn-to-dusk fasting practiced by Muslims during the holy month of Ramadan affect labor supply and productivity? The timing of Ramadan follows the lunar calendar, and day length varies with latitude and season; Campante and Yanagizawa-Drott use these sources of exogenous variation to demonstrate that longer fasting results in a lower rate of growth in gross domestic product. They also find that an increase in subjective well-being serves as recompense for what is a costly religious practice, probably via well-established cultural mechanisms that have contributed to the evolution of many prosocial religions, as described by Norenzayan *et al.* — GJC

Quart. J. Econ. **130,** 10.1093/qje/qjv002 (2015); *Behav. Brain Sci.* 10.1017/S0140525X14001356 (2014).

Muslims pray before breaking fast during the holy month of Ramadan

PROTEOMICS

The secrets of blood proteins revealed

The levels of particular proteins in your blood can provide important insight into your health. However, to what degree environmental factors versus heritability influence the relative abundance of all blood proteins is unknown. To find out, Liu *et al.* used mass spectrometry on plasma samples collected from monozygotic and dizygotic twins at two different times. They detected 342 unique proteins overall, and although 80 showed evidence of heritability, they found that the expression of many proteins varied widely. Proteins used as clinical biomarkers showed less variability in expression overall; however, some were still quite variable, suggesting that scientists still need to better characterize the predictive value of these blood biomarkers. — LMZ

Mol. Syst. Biol. **11**, 786 (2015).

EDUCATION

Achievement viewed through a genetic lens

Why is educational achievement so highly heritable? To investigate, Krapohl *et al.* used a multivariate analysis to determine how nine broad domains of educational achievement, including intelligence, self-efficacy, personality, well-being, parent-rated behavior problems, child-rated behavior problems, health, perceived school environment, and home environment, contributed to the performance of 6653 pairs of twins on a nationwide exam administered in the United Kingdom at age 16. Results showed that although intelligence was the dominant domain, the other eight domains collectively influenced the heritability of educational achievement at a level equivalent to that of intelligence alone. These results demonstrate that a wide array of heritable factors contributes to academic achievement. — MM

Proc. Natl. Acad. Sci. U.S.A. **111**, 42 (2014).

RECEPTOR CHEMISTRY

Easier binding the second time around

The hemoglobin protein that shuttles oxygen around our blood manifests a well-known example of cooperative binding: Once one oxygen jumps aboard, the protein conformation shifts to accommodate others more easily. Gan *et al.* present a synthetic x-shaped receptor complex that similarly binds two oxocarbon anions cooperatively. Spectroscopic monitoring revealed an order-of-magnitude enhancement in binding of the second anion relative to the first. The receptor is held together by cadmium ions, and swapping them out for copper, in conjunction with a solvent switch induced efficient release of both bound guests. — JSY

J. Am. Chem. Soc. **137**, 10.1021/ja5120437 (2015).

PHOTOS: (TOP TO BOTTOM) © JEFF ROTMAN/ALAMY; © DIVYAKANT SOLANKI/EPA/CORBIS

REVIEW SUMMARY

SUSTAINABILITY

Systems integration for global sustainability

Jianguo Liu,* Harold Mooney, Vanessa Hull, Steven J. Davis, Joanne Gaskell, Thomas Hertel, Jane Lubchenco, Karen C. Seto, Peter Gleick, Claire Kremen, Shuxin Li

BACKGROUND: Many key global sustainability challenges are closely intertwined (examples are provided in the figure). These challenges include air pollution, biodiversity loss, climate change, energy and food security, disease spread, species invasion, and water shortages and pollution. They are interconnected across three dimensions (organizational levels, space, and time) but are often separately studied and managed. Systems integration—holistic approaches to integrating various components of coupled human and natural systems (for example, social-ecological systems and human-environment systems) across all dimensions—is necessary to address complex interconnections and identify effective solutions to sustainability challenges.

ADVANCES: One major advance has been recognizing Earth as a large, coupled human and natural system consisting of many smaller coupled systems linked through flows of information, matter, and energy and evolving through time as a set of interconnected complex adaptive systems. A number of influential integrated frameworks (such as ecosystem services, environmental footprints, human-nature nexus, planetary boundaries, and telecoupling) and tools for systems integration have been developed and tested through interdisciplinary and transdisciplinary inquiries. Systems integration has led to fundamental discoveries and sustainability actions that are not possible by using conventional disciplinary, reductionist, and compartmentalized approaches. These include findings on emergent properties and complexity; interconnections among multiple key issues (such as air, climate, energy, food, land, and water); assessment of multiple, often conflicting, objectives; and synergistic interactions in which, for example, economic efficiency can be enhanced while environmental impacts are mitigated. In addition, systems integration allows for clarification and reassignment of environmental responsibilities (for example, among producers, consumers, and traders); mediation of trade-offs and enhancement of synergies; reduction of conflicts; and design of harmonious conservation and development policies and practices.

ON OUR WEB SITE

Read the full article at http://dx.doi.org/10.1126/science.1258832

Illustrative representation of systems integration. Among Brazil, China, the Caribbean, and the Sahara Desert in Africa, there are complex human-nature interactions across space, time, and organizational levels. Deforestation in Brazil due to soybean production provides food for people and livestock in China. Food trade between Brazil and China also contributes to changes in the global food market, which affects other areas around the world, including the Caribbean and Africa, that also engage in trade with China and Brazil. Dust particles from the Sahara Desert in Africa—aggravated by agricultural practices—travel via the air to the Caribbean, where they contribute to the decline in coral reefs and soil fertility and increase asthma rates. These in turn affect China and Brazil, which have both invested heavily in Caribbean tourism, infrastructure, and transportation. Nutrient-rich dust from Africa also reaches Brazil, where it improves forest productivity. [Photo credits clockwise from right top photo: Caitlin Jacobs, Brandon Prince, Rhett Butler, and David Burdick, used with permission]

OUTLOOK: Although some studies have recognized spillover effects (effects spilling over from interactions among other systems) or spatial externalities, there is a need to simultaneously consider socioeconomic and environmental effects rather than considering them separately. Furthermore, identifying causes, agents, and flows behind the spillover effects can help us to understand better and hence manage the effects across multiple systems and scales. Integrating spillover systems with sending and receiving systems through network analysis and other advanced analytical methods can uncover hidden interrelationships and lead to important insights. Human-nature feedbacks, including spatial feedbacks (such as those among sending, receiving, and spillover systems), are the core elements of coupled systems and thus are likely to play important roles in global sustainability. Systems integration for global sustainability is poised for more rapid development, and transformative changes aimed at connecting disciplinary silos are needed to sustain an increasingly telecoupled world. ■

The list of author affiliations is available in the full article online.
*Corresponding author. E-mail: liuji@msu.edu
Cite this article as J. Liu *et al.*, *Science* **347**, 1258832 (2015).
DOI: 10.1126/science.1258832

REVIEW

SUSTAINABILITY

Systems integration for global sustainability

Jianguo Liu,[1]* Harold Mooney,[2] Vanessa Hull,[1] Steven J. Davis,[3] Joanne Gaskell,[4] Thomas Hertel,[5] Jane Lubchenco,[6] Karen C. Seto,[7] Peter Gleick,[8] Claire Kremen,[9] Shuxin Li[1]

Global sustainability challenges, from maintaining biodiversity to providing clean air and water, are closely interconnected yet often separately studied and managed. Systems integration—holistic approaches to integrating various components of coupled human and natural systems—is critical to understand socioeconomic and environmental interconnections and to create sustainability solutions. Recent advances include the development and quantification of integrated frameworks that incorporate ecosystem services, environmental footprints, planetary boundaries, human-nature nexuses, and telecoupling. Although systems integration has led to fundamental discoveries and practical applications, further efforts are needed to incorporate more human and natural components simultaneously, quantify spillover systems and feedbacks, integrate multiple spatial and temporal scales, develop new tools, and translate findings into policy and practice. Such efforts can help address important knowledge gaps, link seemingly unconnected challenges, and inform policy and management decisions.

The goal of achieving global sustainability is to meet society's current needs by using Earth's natural resources without compromising the needs of future generations (*1*). Yet, many disparate research and management efforts are uncoordinated and unintentionally counterproductive toward global sustainability because a reductionist focus on individual components of an integrated global system can overlook critical interactions across system components. Although our planet is a single system comprising complex interactions between humans and nature, research and management typically isolate system components (such as air, biodiversity, energy, food, land, water, and people). As a result, the compounding environmental impacts of human activities have too often been missed because they go beyond the organizational level, space, and time of focus. For example, large amounts of affordable and reliable energy are available in fossil fuels, but concomitant emissions of carbon dioxide (CO_2) will alter global climate and affect other human and natural systems—a trade-off that current policies have not adequately addressed (*2*). Likewise, attention to growing more food on land may inadvertently result in excess use of fertilizers and in turn eutrophication of downstream coastal waters that compromises food production from the ocean. Progressing toward global sustainability requires a systems approach to integrate various socioeconomic and environmental components that interact across organizational levels, space, and time (*3*–*5*).

Systems integration generates many benefits compared with isolated studies, including understanding of interconnectivity and complexity (Table 1). Here, we review recent advances in developing and quantifying frameworks for systems integration of coupled human and natural systems; illustrate successful applications, focusing on unexpected impacts of biofuels and hidden roles of virtual water and discuss future directions for using systems integration toward global sustainability.

Framework development and quantification

The development and quantification of frameworks are critical steps in integrating human and natural systems (*6*–*9*). For instance, interactions between sectors and stakeholders in the human system or between biotic and abiotic factors in the natural system at different organizational levels (for example, government agencies from local to national levels, and food trophic levels from producers to consumers in ecosystems) lead to emergent properties that individual components do not have (*10*). All coupled systems evolve over time as complex adaptive systems (*11*). Their interactions, emergence, evolution, and adaptation also vary with spatial scales (*12*). Accordingly, integration along organizational, spatial, and temporal dimensions is needed to avoid sustainability solutions in one system that cause deleterious effects in other systems. Such integration can also enhance positive and reduce negative socioeconomic and environmental effects across multiple systems at various organizational levels over time (Table 1).

Integration requires blending and distilling of ideas, concepts, and theories from multiple natural and social science disciplines as well as engineering and medical sciences (*4*, *13*), various tools and approaches (such as simulation, remote sensing, and life cycle assessment), and different types and sources of biophysical and socioeconomic data (*14*). For example, integrated assessment models such as those used by the Intergovernmental Panel on Climate Change (IPCC) analyze information from diverse fields to understand complex environmental problems (such as acid rain, climate change, energy shortages, and water scarcity) (*15*, *16*). The Global Trade Analysis Project has recently evolved from a database for analyzing global trade-related economic issues to a platform for integrating trade with global land use and associated greenhouse gas (GHG) emissions (*17*). The Global Biosphere Management Model analyzes and plans land use among sectors (agriculture, forestry, and bioenergy) across the globe in an integrated way (*18*). Below, we illustrate the development and quantification of some important integration frameworks that have led to substantial advances.

Ecosystems services, environmental footprints, and planetary boundaries

Human and natural systems interact in a multitude of ways. Several integration frameworks bring multiple aspects of human-nature interactions together (Fig. 1). Quantifying the services that ecosystems provide (Fig. 1A) for societal needs (such as clean water, nutrient cycling, and recreation) (*6*) helps assign value to natural components for humans. Recent advances consider a variety of ecosystem services simultaneously in order to evaluate trade-offs and synergies among them (*19*). Environmental footprint (*20*) and planetary boundary (*21*) frameworks attempt to quantify the negative effects that human activities have on natural systems. The environmental footprints framework quantifies resources (such as natural capital) consumed and wastes generated by humans (Fig. 1B) (*20*). Recent manifestations of the concept go beyond the previously developed ecological footprints framework by including more diverse types of footprints [for example, water, carbon, and material footprints (*20*)]. Planetary boundaries are threshold levels for key Earth system components and processes (such as stratospheric ozone, global freshwater, and nitrogen cycling) beyond which humanity cannot safely be sustained (*21*) (Fig. 1C).

Quantifying the above frameworks relies on systems integration. For instance, organizational integration in environmental footprint analysis demonstrates how different human activities contribute to human impacts at local to global levels (*20*). Spatial integration is illustrated in integrated

[1]Center for Systems Integration and Sustainability, Department of Fisheries and Wildlife, Michigan State University, East Lansing, MI, USA. [2]Department of Biology, Stanford University, Stanford, CA, USA. [3]Department of Earth System Science, University of California, Irvine, CA, USA. [4]World Bank, Washington, DC, USA. [5]Department of Agricultural Economics, Purdue University, West Lafayette, IN, USA. [6]Department of Integrative Biology, Oregon State University, Corvallis, OR, USA. [7]School of Forestry and Environmental Studies, Yale University, New Haven, CT, USA. [8]The Pacific Institute, Oakland, CA, USA. [9]Department of Environmental Science, Policy and Management, University of California, Berkeley, CA, USA.
*Corresponding author. E-mail: liuji@msu.edu

Table 1. Example benefits of systems integration.

Benefit	Illustrative study
Revealing mechanisms of ecological degradation in protected areas	Socioeconomic factors (such as forest harvesting, fuelwood collection, and increases in household numbers) are responsible for ecological degradation in protected areas for giant pandas (which are supposed to be protected from human activities) (*100*).
Understanding complexity	Agricultural intensification schemes may promote further agricultural expansion over the long term; responses varied across space and were nonlinearly related to agricultural inputs (*101*).
Improving economic efficiency	Integrated assessment modeling shows specific cost estimates for delaying climate change mitigation with respect to geophysical, technological, social, and political factors (*102*).
Reducing environmental impacts in distant places	Integrated cross-boundary management suggests ways of decreasing the spread of pollution and spillover of climate-change effects to distant places around the globe (*15*).
Addressing multiple issues simultaneously	The climate change–health–food security nexus demonstrates ways that management measures can improve all three key issues at the same time (*103*).
Assessing the feasibility of multiple and conflicting goals	Integrated coastal zone management allows for multiorganizational management for competing interests such as recreation, fisheries, and biodiversity conservation (*104*).
Developing priorities for research and sustainability action	Integrated modeling of global water, agriculture, and climate change pinpoints areas vulnerable to future water scarcity and puts forth actionable strategies for mitigation (*16*).
Identifying complementary conservation and management strategies	Coupling global energy security policy with climate change and air pollution policies (the air-climate-energy nexus) would decrease oil consumption compared to implementing energy policy alone (*46*).
Enhancing synergies among factors	Cross-site integration of natural resource management approaches in response to disturbances shows opportunities for reframing ecosystem management to enhance collaboration among institutions (such as NGOs, government agencies, research organizations, businesses) (*105*).
Anticipating feedbacks	A lag between fire control management and the response of the forests to such changes affects the eagerness of landowners to continue implementing control measures (*106*).
Detecting latencies	The latent effect of mosquito ditch construction on fish populations only emerged during new pressures from residential development and recreational fisheries (*107*).
Maximizing economic gains and minimizing environmental costs	Integrated soil-crop management system could maximize grain yields, while minimizing applications of fertilizers and GHG emissions (*108*).

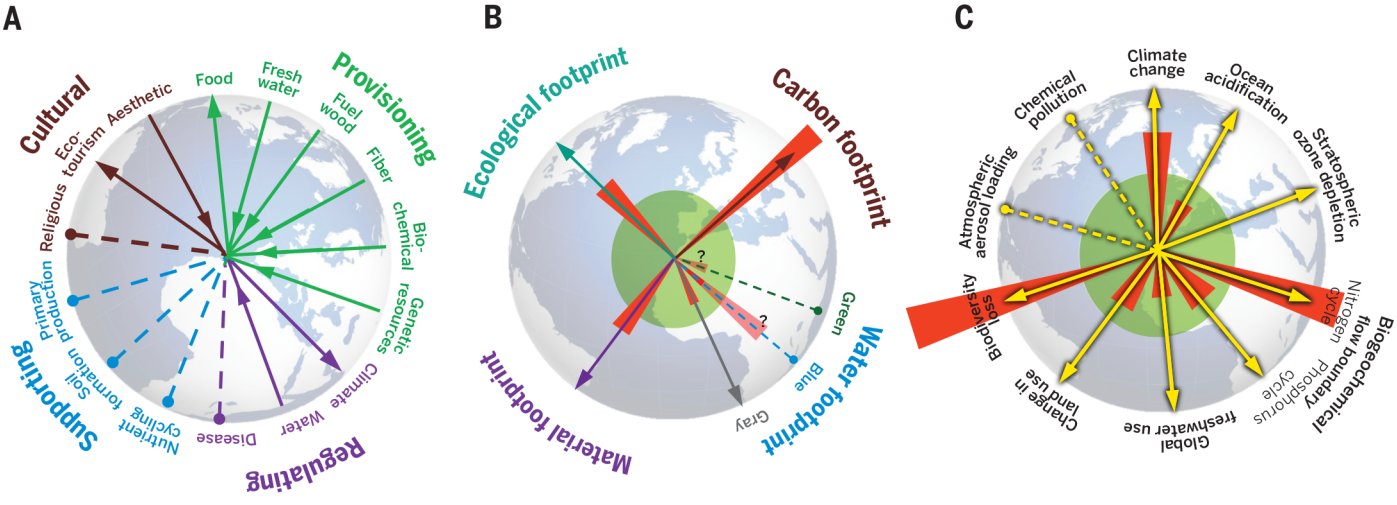

Fig. 1. Examples of ecosystem services, environmental footprints, and planetary boundaries. (**A**) Ecosystem services. (**B**) Environmental footprints. (**C**) Planetary boundaries. Outward arrows in (A to C) indicate increases in the values, inward arrows indicate decreases, and dashed lines indicate no data. In (B) and (C), the inner green shading represents maximum sustainable footprints (*20*) and safe operating space for nine planetary system variables (*21*), respectively. Red wedges refer to the estimated current positions for the variables. Most of the ecosystem services in (A) decreased between the 1950s to early 2000s (*94*). In (B), at least three types of footprints (ecological, carbon, and material) have exceeded maximum sustainable footprints (*20*). Blue water footprint was 1690 billion m^3/year (1985–1999) (*81*), gray water footprint increased during 1970–2000 (*95*), and green water footprint is 6700 billion m^3/year (without reference point) (*20*). Question marks indicate that the information is uncertain. Carbon footprint increased during 1960–2009 (*96*). With every 10% increase in gross domestic product, the average national material footprint increases by 6% (*97*). For (C), all planetary system variables have increased in values between preindustry and 2000s, and three boundaries have been crossed (*21*).

landscape planning for ecosystem services, which allows for coordination across space. For example, it can promote afforestation and reforestation in upland areas above irrigated agricultural systems, thus reducing erosion, protecting waterways, minimizing flooding, providing drinking water, and facilitating sustainable agricultural production (*22*). Temporal integration is crucial to quantify the planetary boundaries framework, as short-term fluctuations in key Earth system processes are scaled up to predict long-term trends, many of which cannot be accurately predicted without a systems approach (*21*). Temporal integration can also reveal legacy effects of prior human-nature couplings. For example, carbon footprints are driven in large part by past land use (*23*). A condition termed "carbon lock-in" has been used to describe systems that have evolved over long time frames to become dependent on fossil fuels (*24*, *25*). The fossil energy system is comprised of long-lived infrastructure such as power plants, which represent an investment in future CO_2 emissions. Retiring this infrastructure before the end of its economic or physical lifetime would entail substantial costs. As of 2013, it is estimated the global committed emissions related to existing fossil infrastructure are roughly 700 billion tons of CO_2 (*26*).

Human-nature nexuses

In contrast to the conventional decision-making that takes place within separate disciplines or sectors, the human-nature nexus framework recognizes the interdependency between two or more issues (or nodes) and addresses them together. For example, the energy-food nexus considers both the effects of energy on food production, processing, transporting, and consumption, and the effects of food (such as corn) production on the generation of energy (such as ethanol) (*27*).

The nexus framework can help anticipate otherwise unforeseen consequences, evaluate trade-offs, produce co-benefits, and allow the different and often competing interests to seek a common ground (*28*) and co-optimization (*29*). The vast majority of the 229 human-nature nexus studies recorded in the Web of Science (as of 16 August 2014) analyzed two-node nexuses (80%), with only 16 and 4% of the nexus studies including three and four nodes, respectively. Although the concept of food-energy nexus first appeared in 1982, there was no paper recorded in the Web of Science for many years. The interest in the nexus framework has reemerged recently and has grown rapidly since 2010. Several two-node nexuses have received special focus, including energy-water nexus, food-water nexus, energy-food nexus, air-climate nexus, health-water nexus, and energy-national security nexus. Among the more commonly examined three- and four-node nexuses are economy-environment-land nexus and climate-energy-food-water nexus. Adding more nodes to a nexus framework leads to more complexity but also captures greater reality. For instance, the climate-energy-food nexus considers not only the interrelationships between energy and food, but also the relationships between energy and climate (for example, energy use emits CO_2, and climate change affects energy demand such as heating and cooling) and interrelationships between food and climate (for example, climate changes affect food production, and CO_2 is emitted throughout the food production, processing, transporting, and consumption).

The nodes in the nexus framework are mediated by and influence many organizational levels. For example, energy production and use are shaped by international markets and policies at different government organizations and at the same time influence many trophic levels of animals, plants, and microorganisms (*30*). Building on the increasing recognition of conceptual interconnections among various nodes, efforts are under way to quantify their relationships, such as via hydro-economic modeling (*31*), structural and nonstructural economic models (*32*), and life cycle assessments (*33*). Scenario analysis is particularly promising for teasing out roles of different organizations functioning at different scales (*34*, *35*). For example, the Agrimonde model has been used to examine intersections between food and numerous other sectors (including energy and water) worldwide under different growth and consumption scenarios (*35*) and illustrates the effects of diverse individual governments on global cross-sector dynamics.

Temporal integration is also a key element of the nexus framework. For example, recent long-term quantitative integration studies on the economy-energy nexus show that reductions in energy use can have negative impacts on gross domestic product (GDP) in the short-term but little detectable effect over the long term (*36*). Alternatively, one model predicted that a small increase in foreign trade in Indonesia will lead to substantial increases in long-term per capita CO_2 emissions, although its contribution to CO_2 emissions is negligible in the short term (*37*).

Telecoupling

Many studies on sustainability have been place-based even if they look at coupled systems [for example, the energy-water nexus in the United States (*38*)]. However, economic production and resource use in different regions or countries may lead to very different consequences. Furthermore, there are increasing distant interactions around the world so that local events have consequences globally (*39*). For example, each year several hundred million tons of dust from Africa (especially the Sahara desert) travel via the air across the Atlantic Ocean to distant places such as the Caribbean, where it causes severe impacts, including decline in coral reefs, increase in asthma, disease spread, and loss of soil fertility (*40*, *41*). Greenhouse gases emitted into the atmosphere from a point source become mixed and transported globally, affecting societies and ecosystems far distant from the point sources of origin. Many of the changes to the biotic composition of local places can also affect society regionally and globally through ever-increasing global trade as well as the often dramatic impact of invasive species and disease transmission. In other words, patterns and processes at one place may enhance or compromise sustainability in other places (*42*). Human actions [such as production of biofuels (*43*)] in one place may create unintended consequences elsewhere [such as carbon leakage (*44*), biodiversity losses (*45*, *46*), and pollution (*47*)]. Although external factors originating from other systems are sometimes considered in sustainability research and practices, they are typically treated as one-way drivers of changes in the system of interest, with little attention to the feedbacks between the system of interest and other systems (*6*, *42*).

The framework of telecoupling (socioeconomic and environmental interactions over distances) has been developed to tie distant places together (*42*). It is a natural extension of the frameworks of coupled human and natural systems and built on disciplinary frameworks such as climate teleconnections (distant interactions between climate systems), urban land teleconnections (land changes that are linked to underlying urbanization dynamics) (*7*), and economic globalization (distant interactions between human systems). So far, the telecoupling framework has been applied to a number of important issues across spatial scales, such as global land-use and land-change science (*39*, *48*, *49*), international land deals (*39*), species invasion (*39*, *42*), payments for ecosystem services programs (*50*), and trade of food (*42*) and forest products (*9*).

The framework is particularly effective for understanding socioeconomic and environmental interactions at international scales. For example, the flow of coal from Australia (sending system) to a number of countries and regions (receiving systems; for example, Japan, the European Union, and Brazil) reflects abundant Australian coal supplies and the demand for coal in receiving systems (Fig. 2). The coal trade is facilitated by many agents in receiving and sending systems (such as government agencies that make coal trade policies) and international organizations (such as shipping companies). Many other countries (such as those in Africa) are spillover systems—systems that may be affected by the coal flows because of financial flows between sending and receiving systems as well as the CO_2 emissions produced when the coal is burned. Global efforts to address this and similar feedbacks, such as the REDD+ program to mitigate CO_2 emissions from deforestation (*51*) and the Green Climate Fund to facilitate low-emission projects in developing nations (*52*), should focus on all countries.

The telecoupling framework can also be useful at regional or national scales. For example, the 20 million residents in China's capital city of Beijing (receiving system) receive clean water from the Miyun Reservoir watershed (sending system), more than 100 km away from the city (*50*). The framework explicitly links agents, causes, and effects in the sending and receiving systems. For instance, the quantity and quality of the water flows are made possible through the Paddy Land-to-Dry Land program, an ecosystem services payment program that Beijing established with the farmers in the watershed who converted rice cultivation in paddy land to corn production

in dry land to provide clean water for Beijing in exchange for cash payments (*53*). Through systematic analysis, the framework also helps identify research and governance gaps, such as spillover systems—regions that are affected by water and cash flows between the watershed and Beijing but have received little attention from researchers and government agencies (*50*).

The telecoupling framework also emphasizes temporal dynamics. A lack of temporal integration may miss key dynamics and create a misunderstanding of infrequent but drastic changes, such as disasters, wars, outbreaks of deadly diseases such as Ebola (*54*), regime shifts, and profound policy changes. For instance, in the Wolong Nature Reserve of China designated for conserving the endangered giant pandas, the devastating earthquake in 2008 substantially altered the telecouplings between Wolong and outside systems [for example, collapse of tourism and agricultural trade (*55*)]. Studies omitting the earthquake impacts could misrepresent the mechanisms behind the system dynamics (such as increases in landslides and relocation of households).

Applications of systems integration

Systems integration has been applied successfully to many sustainability issues. Integrated Coastal Zone Management (*56*), Marine Spatial Planning (*57*), and Ecosystem-Based Management (*58*) all integrate multiple dimensions for natural resource management. Although some of these practices have existed for several decades, there have been continued efforts for more integration, new advances, and novel insights. For example, Ecosystem-Based Management has expanded to tackle issues not traditionally thought of within natural resource management, such as food security (*59*), politics (*60*), and disease (*61*). The examples of biofuels and virtual water below also illustrate the importance of systems integration in detail. We chose to focus on these two examples because they are emerging and contentious global phenomena that represent challenging sustainability issues, and they have unexpected and hidden socioeconomic and environmental effects that were impossible to reveal without systems integration.

Unexpected impacts of biofuels

The environmental and socioeconomic impacts of biofuels have been among the most hotly contested policy issues over the past decade. The United States, European Union, and nearly three dozen other countries in Africa, Asia, and the Americas have developed biofuel mandates or targets (*62*). This enthusiasm was buoyed by the prospect of displacing high-priced oil imports, generating rural incomes, and contributing to climate change mitigation. As of 2006, it was suggested that biofuels could be both economically and environmentally beneficial. However, with the implementations of these policies and systems integration research, serious concerns have arisen about their geospatial impacts and the temporal viability of these mandates.

Biofuels are a prime topic for systems integration research because biofuel production and consumption as well as their impacts vary across time, space, and organizational levels. For instance, the carbon fluxes after conversion of new croplands depend not only on below- and aboveground carbon at present, but also on the legacy effects stemming from historical land use such as land clearing as well as subsequent cultivation and cropping practices (*63*). The United States and Brazil were responsible for 90% of the global biofuel production of 105 billion liters in 2011, but several other countries with new mandates such as China, Canada, and Argentina are increasing the spatial extent of production (*64*). Assessing organizational impacts on biofuel production encompasses analysis that integrates across institutions. For example, when and where additional cropland is converted for biofuel production depends critically on local, national, and international institutions, as well as the global supply chain.

The systems integration frameworks discussed above have direct relevance to biofuels. For example, the environmental footprint framework has been applied to assess the impacts of biofuels. It is estimated that the global footprint from biofuels was ~0.72 billion gha in 2010 and expected to rise by 73% in 2019 (consisting of land use, carbon, embodied energy, materials and waste, transport, and water) (*65*). From the perspective of ecosystem services, biofuels have both positive (for example, energy) and negative (for example, loss of food and freshwater services) impacts. Biofuel production also affects several planetary boundaries, including climate change, land-use change (proportion of cropland), nutrient cycles (increased use of phosphorus and nitrogen), and biodiversity loss (*66*). For instance, it is estimated that corn-based ethanol nearly doubles greenhouse emissions across the world over a 30-year period because of land-use change (*43*).

Biofuels have also been studied under the human-nature nexus framework—in particular, the energy-food nexus and energy-food-water nexus. Rising demand for ethanol feedstocks bid

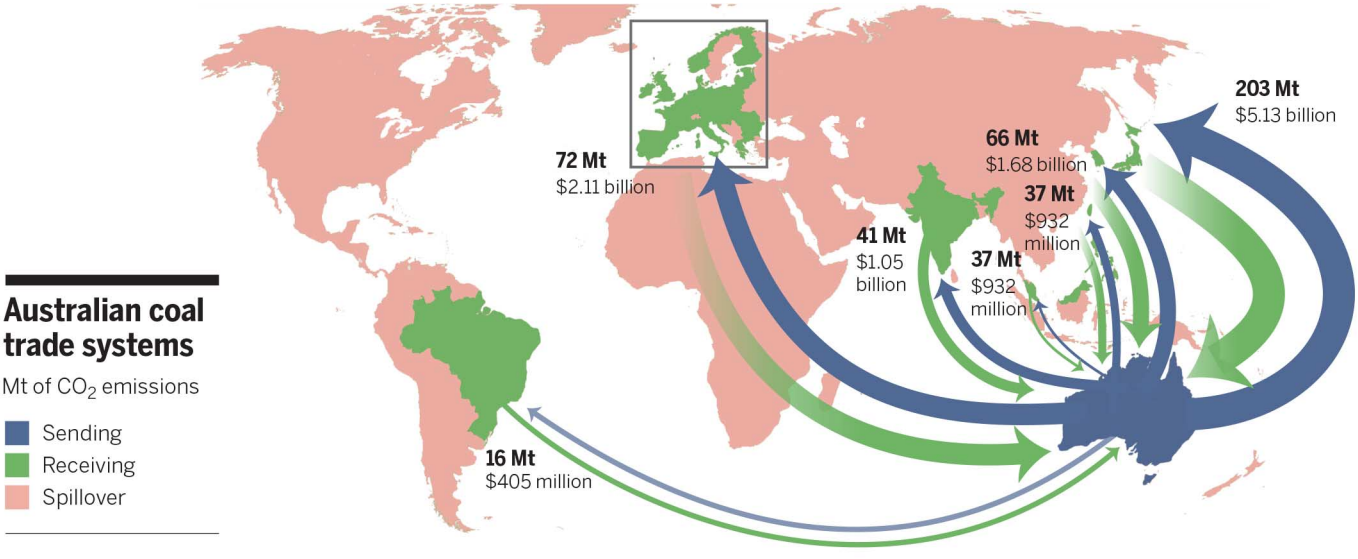

Fig. 2. Illustrative example of sending, receiving, and spillover systems, as well as flows under the telecoupling framework. In the case of trade in Australian coal in 2004 [measured in megatons (Mt) of CO_2 emissions], Australia is a sending system (in blue), the main receiving systems are in green (destinations of the coal are Japan, South Korea, Taiwan, Malaysia, India, the European Union, and Brazil), and the spillover systems are in light red (all other countries and regions are affected by CO_2 emissions from using the coal produced in Australia and consumed in the receiving systems). The arrows show the magnitude of the flows. Countries that receive less than 10 Mt of emissions of Australian coal are not included. Flows to Europe are aggregated to include all 28 member states of the European Union [data from (*44*)]. Financial flows take place between sending and receiving systems but may also affect financial conditions in spillover systems indirectly [data from (*98*)].

up food price (67), which has major implications for food security (68). And, questions have been raised about the adverse interplay between biofuel mandates and increased interannual variability in crop production anticipated under future climate change (69). Water also comes into play, as limits on the future availability of water for irrigated agriculture will shift the location of cropland conversion owing to biofuel expansion toward regions with carbon-rich rainfed agriculture. Overall, accounting for hydrological constraints boosts estimated GHG emissions from land use by 25% (70).

Telecoupled processes such as international trade and flows of information (for example, global market prices) cause biofuel programs in one part of the world to translate spatially into land conversion in other regions (indirect land use). They have already contributed to cropland expansion in the United States and overseas and to cascading and spillover effects over long distances (Fig. 3). National biofuel programs, which looked environmentally beneficial at first blush, might in fact lead to increased environmental damage when viewed over time and at the global scale (42, 71). Unlike early analyses (42) that assumed that higher prices effectively influenced all agents in the market equally, subsequent research has revealed that some agricultural suppliers (such as the United States and Argentina) are more closely telecoupled than others (72). The spatial pattern and extent of land conversion stemming from biofuels are also affected by geophysical characteristics such as potential productivity of the newly converted lands.

Hidden roles of virtual water

Although many sustainability studies have focused on flows of real material and energy such as biofuels, there has been increasing interest in the flows of "virtual" material and energy, such as "virtual water," "virtual energy," "virtual land," and "virtual nutrients" (73). Virtual resources are those resources used for production and incorporated into goods and services in the same way that related pollution and impacts are embodied (or hidden) in these products. In the case of water, for example, it is used to grow crops, raise livestock and grow their food, and produce marketable goods. Virtual water is traded among countries as goods are traded. Globally, the volume of virtual water trade and the number of links (pairs of trading countries) have both doubled from 1986 to 2010 (74). With roughly 27 trillion m^3 of water traded virtually worldwide in 2010 (74), virtual water trade from water-rich countries has helped mitigate water shortages in water-poor countries (75). The concept of virtual resources has helped analysts think more clearly about the real risks of resource scarcity and the role that trade plays in mitigating or worsening those risks (76, 77). Targeted trade policies may help to further prevent water scarcity by encouraging more water-efficient trade links (78).

Virtual water is a good target for systems integration research because the issues involved are dynamic across time, space, and organizational levels. Global water scarcity issues are inherently temporally sensitive, with cumulative effects

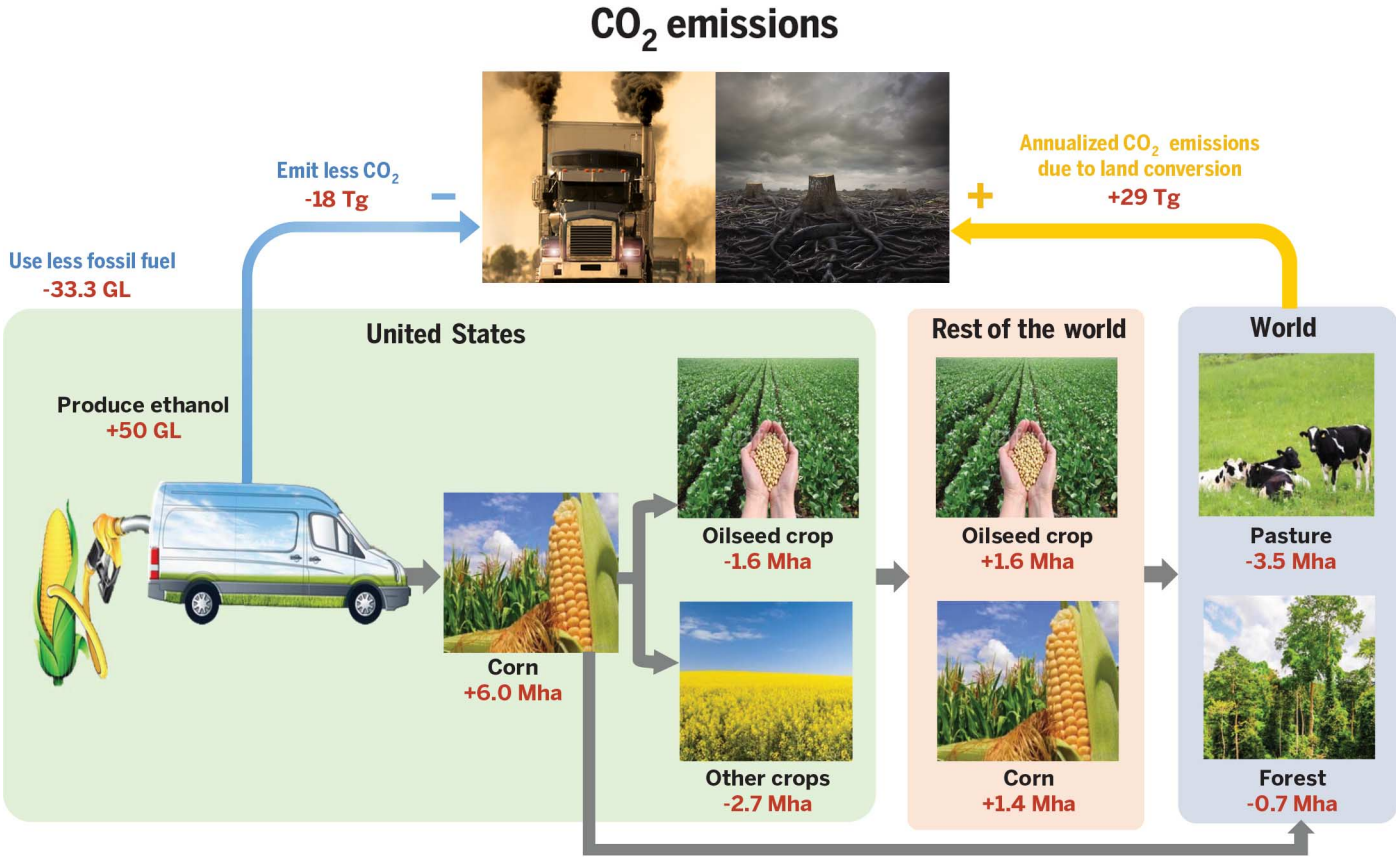

Fig. 3. Cascading and spillover effects of biofuel production on land conversion and CO_2 emissions, as revealed by systems integration. Meeting the Renewable Fuel Standard mandate [to produce 50 Gigaliters (GL) of additional ethanol on top of the 2001 production level] in the United States reduces the use of petroleum but requires additional corn area (99). The expansion in U.S. corn area leads to reduction in harvested area of oilseeds and other crops in the United States. This boosts world prices for these crops and encourages more production of oilseeds and corn in the rest of the world. The expansion of cropland in the United States and the rest of the world leads to more emissions of CO_2 and the conversion of pasture and forest lands around the world. This land conversion also releases CO_2, offsetting the reduction of CO_2 emissions from using less fossil fuels and more biofuels (assuming a 2/3 ethanol/petroleum energy conversion rate). Estimates are on an annual basis over a 30-year production period for the biofuel facilities and in approximate amounts derived from (99). Arrows indicate the direction of influences. Symbols "−" and "+" refer to decrease and increase, respectively, in land area, ethanol, fossil fuel, or CO_2. Tg, teragrams; Mha, million ha. [Graphics are used with permissions from Fotolia.com]

stemming from legacies of overuse of water interacting with new drivers such as climate change. Estimates suggest that global virtual water trade may decrease with climate change because of the difficulty of growing crops in warmer, drier climates [water savings from reduction in growing rice, soybeans, and wheat may amount to up to 1.5 trillion m^3 in 2030 (*78*)]. Also, there was a profound shift in the spatial distribution of human populations (thus, water demand) relative to water distribution over the past few decades. In 1986, 68% of the world's population was in water-exporting countries, but by 2010, the distribution was almost completely reversed, with 60% of the global population in water-importing countries (*74*). One of the greatest organizational concerns related to virtual water is that a few countries control the majority of the global trade, which leaves the market vulnerable to the decisions made by a few key players (*74*). In addition, there is unequal distribution of resources within countries and a tendency for local agrarian communities to be marginalized owing to trade dictated by country-level agencies (*79*).

The ecosystem services framework has contributed to virtual water research in many ways. For example, Canada is a major exporter of virtual water worldwide (95 Gm^3 /year); exporting virtual water affects the ecosystem services provided by the nation's boreal forests, which make up nearly 60% of Canada's territory (*80*). Production of commodities through processes such as hydroelectric power generation, oil extraction, crop irrigation, and livestock-rearing contributes to virtual water exports, which in turn threaten freshwater resources that are a key part of the boreal forests. Boreal freshwater comprises 80 to 90% of Canada's lakes and 25% of the entire Earth's wetlands (*80*). Removal of water compromises the estimated annual gain of $703 billion in ecosystem services that the boreal forests provide, including carbon storage, flood control and water filtering, biodiversity conservation, and pest control (*80*).

The environmental footprints framework has informed virtual water research by depicting the water resources used for production of goods and services ("water footprints"). For example, 2,320 Gm^3/year of the total global water footprint of 9087 Gm^3/year comes from virtual water trade (*81*). There is a close relationship between virtual water and planetary boundaries because one of the nine key planetary boundaries identified is the limit to global freshwater use (*21*). A related concept—"peak water"—helps to illustrate how close global freshwater bodies are to this threshold. Global water consumption has already reached a peak and begun to decline in many areas because of limited remaining water (*13*). Furthermore, scarcity in global freshwater is in large part linked to the virtual water embedded in agricultural production and trade (*81*). The human-nature nexus framework is also useful for virtual water research. For example, a study on water-food nexus indicates that 76% of virtual water trade is attributed to crops or crop-derived products (*81*).

Virtual water trade varies spatially and is an important telecoupling process. The main virtual water exporters (sending systems) are water-rich regions in North and South America and Australia, whereas Mexico, Japan, China, and water-poor regions in Europe are the main importers (receiving systems) (Fig. 4) (*75*). Sending and receiving systems involved in virtual water trade have dynamic roles. Asia recently switched its virtual water imports from North America to South America (*82*). On the other hand, North America has engaged in an increased diversification of intraregional water trade while trading with distant countries in Asia (*82*). China has undergone a dramatic increase in virtual water imports since 2000, via products such as soybeans from Brazil (nearly doubling from 2001 to 2007 and amounting to 13% of the total global world water trade) (*82*). The spatial shift in the use of soybean products in Brazil from domestic to international has led to water savings in other countries, but at the cost of deforestation in Brazilian Amazon (*82*). Within-country virtual water transfer is also common. For example, virtual water flow through grain trade from North China to South China goes in the opposite direction of real water transfer through large projects, such as the South-to-North Water Transfer Project, that aim to alleviate water shortages in North China.

Future directions

Despite the substantial progress in systems integration illustrated above, many important challenges remain. For example, the integrated frameworks have been studied largely in isolation, although they are interconnected through human activities (for example, using more ecosystem services may lead to larger environmental footprints). Achieving a greater degree of integration would involve analyzing and managing coupled human and natural systems over longer time periods, larger spatial extents (for example, macrosystems and ultimately the entire planet), and across more diverse organizations at different levels. Below, we suggest several ways to advance systems integration with the intent of improving its theoretical foundations, expanding its tool box, and providing broad implications for management and policy.

Incorporate more human and natural components simultaneously

Although some previous studies have considered multiple components of coupled human and natural systems, many components are either not

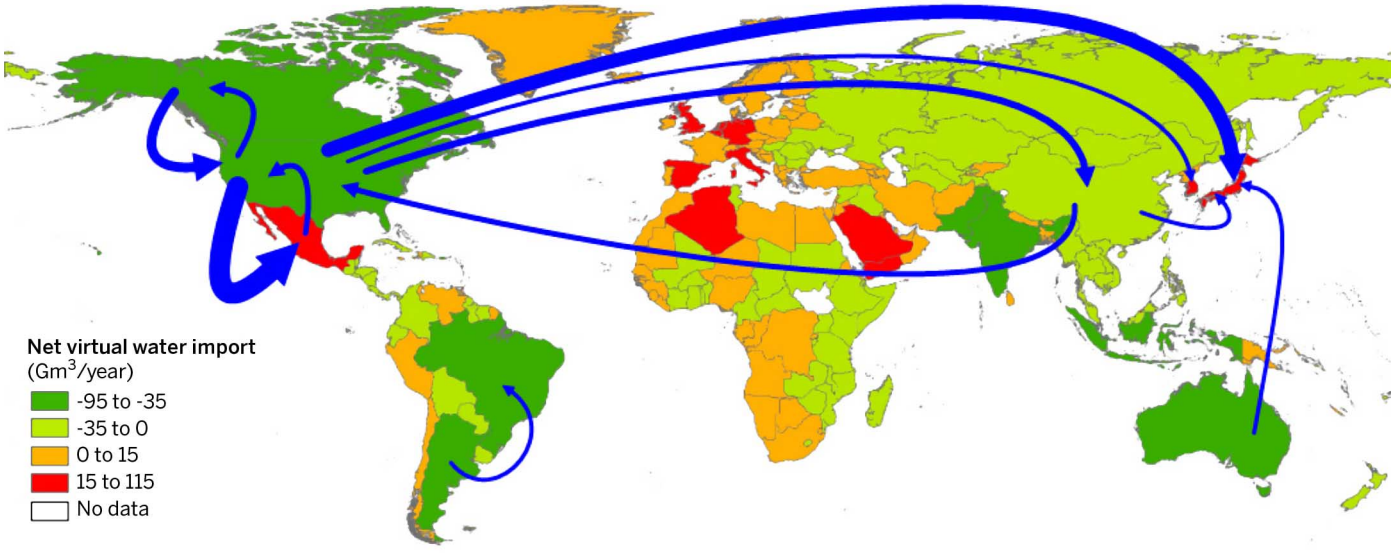

Fig. 4. Balance and flows of virtual water related to trade of agricultural and industrial products during 1996–2005. Net exporters (sending systems) are in green, and net importers (receiving systems) are in red. The arrows indicate the relative sizes of large gross virtual water flows between sending and receiving systems (> 15 Gm^3/year). Countries without arrows are potential spillover systems of the large virtual water flows. Data are from (*81*).

considered or treated as exogenous variables, leading to biases and even incorrect conclusions. For example, a food-water nexus study without considering GHG emissions during groundwater extraction for irrigation of crops in China underestimated GHG emissions by as much as 33.1 $MtCO_2e$ (*83*). One way to correct this problem is to convert more variables from exogenous to endogenous—internalize all important relevant variables—so that their dynamics and feedback effects are explicitly studied. For instance, considering multiple telecoupling processes (such as species invasion, trade, disease spread, and technology transfers) at the same time can help link many seemingly disconnected, distant interactions. Unifying evolutionary approaches such as seen with complex adaptive systems (*84*) may provide productive ways to integrate disparate ideas and understand temporal dynamics and sustainability of coupled systems.

Identify and quantify spillover systems

Previous research on issues such as trade often focused on sending and receiving systems (for example, trade partners), with little attention to spillover systems (for example, nontrade partners)—other systems affected by the interactions between sending and receiving systems. Although some previous studies have recognized some spillover effects [such as spatial externalities (*85*, *86*)], they were often on either socioeconomic or environmental effects, rather than all effects simultaneously. Furthermore, they rarely consider other components of spillover systems (causes, agents, and flows) as articulated in the telecoupling framework (*41*). Identifying and quantifying other components of spillover systems related to spillover effects may help understand the mechanisms behind the spillover effects and develop more effective management strategies. Connecting spillover systems with sending and receiving systems through network analysis (*87*) may generate fruitful outcomes, such as the appreciation of dynamic interrelationships among different systems.

Explicitly account for feedbacks

Human-nature feedbacks are a core component of coupled systems. For instance, an important negative feedback in Wolong Nature Reserve for giant pandas in China occurred when deforestation and panda habitat degradation by local households prompted the government to develop and implement new conservation programs that provide subsidies for local households to monitor forests and thus reduce deforestation and improve panda habitat (*88*). This feedback has helped forest and habitat recovery while increasing income for local households. More innovative measures such as this are needed to identify and use feedbacks as mechanisms for sustainability.

Integrate multiple temporal and spatial scales

Human and natural processes and patterns at multiple scales may be different, and they can interact with each other. For example, food production at the local scale may create jobs at the local scale but may not affect overall job creation at the global scale. Many urban sustainability efforts focus on locally specific solutions that may not be scalable (*7*). Thus, considering multiple spatial scales at the same time can help identify all important factors, their interdependence, and their effects and nonlinear relationships. Temporally, short-term studies should be combined with long-term studies in order to maximize the strengths of each approach. For instance, short-term studies may capture more nuanced immediate changes in system behavior, but long-term studies may account for temporal dynamics, time lags, cumulative effects, legacy effects, and other phenomena (such as rare events) that cannot be seen over shorter terms. More systematic incorporation of human dimensions to long-term studies such as the Long-term Ecological Research sites and the National Ecological Observatory Network is needed.

Develop and use new tools

More effective integration requires developing and using powerful tools to overcome difficult barriers (for example, mathematical and computational challenges, quantification of impacts at one scale on other scales, and relationships among patterns and processes across scales and across borders) and to predict emergence of unexpected threats for sustainability policy and management. Examples include spatially explicit life cycle assessment, supply chain analysis, and multilevel modeling. Agent-based models are particularly promising tools because they take interactions (such as human adaptation to environmental changes) at different scales into account and model coupled systems as complex adaptive systems. Agent-based models create virtual worlds that mimic the real world, in contrast to traditional empirical statistical models (such as econometric models) that are fitted to past data and fail when the future differs from the past, and dynamic stochastic general equilibrium models that presume a perfect world and ignore disturbances or crises (*89*). Many agent-based models have been developed in various disciplines to provide insights on complexities and information for policymaking in issues such as economic development and management of common spaces (*90*, *91*). However, new models are needed to account for telecoupled systems. Also, increasing computational power will allow agent-based models to include more agents in larger areas and ultimately all important agents across the world. As more high-resolution data become available, it is necessary to develop and use big data tools (such as distributed databases, massively parallel processing, and cloud computing) for effective and efficient searching, retrieving, analysis, and integration (*92*).

Translate findings into policy and practice

Systems integration can provide more unbiased information for policy and practice to help clarify responsibilities, mediate trade-offs, reduce conflicts, and anticipate future trends. It is necessary to foster coordination among multiple national and international policies and minimize situations in which different policies offset one another because of conflicting goals and counterproductive implementation. Unfortunately, institutions and regulations have traditionally focused on single issues and often do not have the mandate or infrastructure to address the organizational connections and detrimental spillovers. The World Trade Organization, for example, has the principal mandate of promoting global trade. One of the spillover effects of this mission is the global transmission of invasive species, but the means to address invasive species are weak compared with the forces driving the global market (*93*). Adopting the telecoupling framework can help assign responsibilities of addressing spillover effects (such as CO_2 emissions and species invasion) to consumers and producers (for example, via regulation at the source of extraction or consumption) as well as others such as traders of goods and products across space. Last, governments need to incorporate long-term studies into their policies to account for the complex dynamics of coupled systems (such as time lags). More applications of systems integration frameworks and methods such as those discussed in this paper can accelerate understanding and solving global sustainability challenges.

REFERENCES AND NOTES

1. World Commission On Environment and Development, *Our Common Future* (Oxford Univ. Press, Oxford, 1987).
2. M. A. Hanjra, M. E. Qureshi, Global water crisis and future food security in an era of climate change. *Food Policy* **35**, 365–377 (2010). doi: 10.1016/j.foodpol.2010.05.006
3. J. Liu *et al.*, Complexity of coupled human and natural systems. *Science* **317**, 1513–1516 (2007). doi: 10.1126/science.1144004; pmid: 17872436
4. H. A. Mooney, A. Duraiappah, A. Larigauderie, Evolution of natural and social science interactions in global change research programs. *Proc. Natl. Acad. Sci. U.S.A.* **110** (suppl. 1), 3665–3672 (2013). doi: 10.1073/pnas.1107484110; pmid: 23297237
5. W. Steffen *et al.*, *Global Change and the Earth System: A Planet Under Pressure. IGBP Science 4* (Springer Verlag, Heidelberg, Germany, 2004).
6. Millennium Ecosystem Assessment, *Ecosystems & Human Well-being: Synthesis* (Island Press, Washington, DC, 2005).
7. K. C. Seto *et al.*, Urban land teleconnections and sustainability. *Proc. Natl. Acad. Sci. U.S.A.* **109**, 7687–7692 (2012). doi: 10.1073/pnas.1117622109; pmid: 22550174
8. E. Ostrom, A general framework for analyzing sustainability of social-ecological systems. *Science* **325**, 419–422 (2009). doi: 10.1126/science.1172133; pmid: 19628857
9. J. Liu, Forest sustainability in China and implications for a telecoupled world. *Asia Pacific Pol. Stud.* **1**, 230–250 (2014).
10. J. Norberg, G. S. Cumming, *Complexity Theory for a Sustainable Future* (Columbia Univ. Press, New York, 2013).
11. S. A. Levin, Ecosystems and the biosphere as complex adaptive systems. *Ecosystems (N.Y.)* **1**, 431–436 (1998). doi: 10.1007/s100219900037
12. E. F. Lambin, Conditions for sustainability of human–environment systems: Information, motivation, and capacity. *Glob. Environ. Change* **15**, 177–180 (2005). doi: 10.1016/j.gloenvcha.2005.06.002
13. P. H. Gleick, M. Palaniappan, Peak water limits to freshwater withdrawal and use. *Proc. Natl. Acad. Sci. U.S.A.* **107**, 11155–11162 (2010). doi: 10.1073/pnas.1004812107; pmid: 20498082
14. J. Cools *et al.*, Coupling a hydrological water quality model and an economic optimization model to set up a cost-effective emission reduction scenario for nitrogen. *Environ. Model. Softw.* **26**, 44–51 (2011). doi: 10.1016/j.envsoft.2010.04.017

15. S. Reis *et al*., From acid rain to climate change. *Science* **338**, 1153–1154 (2012). doi: 10.1126/science.1226514; pmid: 23197517
16. M. Hejazi *et al*., Long-term global water projections using six socioeconomic scenarios in an integrated assessment modeling framework. *Technol. Forecast. Soc.* **81**, 205–226 (2014). doi: 10.1016/j.techfore.2013.05.006
17. GTAP, Global Trade Analysis Project, www.gtap.agecon.purdue.edu (2014).
18. IIASA, Global Biosphere Management Model (GLOBIOM); www.globiom.org (2014).
19. E. M. Bennett, G. D. Peterson, L. J. Gordon, Understanding relationships among multiple ecosystem services. *Ecol. Lett.* **12**, 1394–1404 (2009). doi: 10.1111/j.1461-0248.2009.01387.x; pmid: 19845725
20. A. Y. Hoekstra, T. O. Wiedmann, Humanity's unsustainable environmental footprint. *Science* **344**, 1114–1117 (2014). doi: 10.1126/science.1248365; pmid: 24904155
21. J. Rockström *et al*., A safe operating space for humanity. *Nature* **461**, 472–475 (2009). doi: 10.1038/461472a; pmid: 19779433
22. C. Kremen, A. Miles, Ecosystem services in biologically diversified versus conventional farming systems: Benefits, externalities, and trade-offs. *Ecol. Soc.* **17**, 40 (2012).
23. J. Fargione, J. Hill, D. Tilman, S. Polasky, P. Hawthorne, Land clearing and the biofuel carbon debt. *Science* **319**, 1235–1238 (2008). doi: 10.1126/science.1152747; pmid: 18258862
24. P. J. Vergragt, N. Markusson, H. Karlsson, Carbon capture and storage, bio-energy with carbon capture and storage, and the escape from the fossil-fuel lock-in. *Glob. Environ. Change* **21**, 282–292 (2011). doi: 10.1016/j.gloenvcha.2011.01.020
25. G. C. Unruh, Understanding carbon lock-in. *Energy Policy* **28**, 817–830 (2000). doi: 10.1016/S0301-4215(00)00070-7
26. M. R. Raupach *et al*., Sharing a quota on cumulative carbon emissions. *Nature Clim. Change* **4**, 873 (2014). doi: 10.1038/nclimate2384
27. R. L. Naylor, *The Evolving Sphere of Food Security* (Oxford Univ. Press, Oxford, 2014).
28. J. I. Agboola, A. K. Braimoh, Strategic partnership for sustainable management of aquatic resources. *Water Resour. Manage.* **23**, 2761–2775 (2009). doi: 10.1007/s11269-009-9407-4
29. A. Santhosh, A. M. Farid, K. Youcef-Toumi, The impact of storage facility capacity and ramping capabilities on the supply side economic dispatch of the energy–water nexus. *Energy* **66**, 363–377 (2014). doi: 10.1016/j.energy.2014.01.031
30. S. C. Doney *et al*., Climate change impacts on marine ecosystems. *Annu. Rev. Mar. Sci.* **4**, 11–37 (2012). doi: 10.1146/annurev-marine-041911-111611
31. J. Granit, M. Fogde, S. Holger Hoff, J. Joyce, *Unpacking the Water-Energy-Food Nexus: Tools for Assessment and Cooperation Along a Continuum* (Stockholm International Water Institute, Stockholm, Sweden, 2013), pp. 45–50.
32. G. Oladosu, S. Msangi, Biofuel-food market interactions: A review of modeling approaches and findings. *Agriculture* **3**, 53–71 (2013). doi: 10.3390/agriculture3010053
33. S. Nair, B. George, H. M. Malano, M. Arora, B. Nawarathna, Water–energy–greenhouse gas nexus of urban water systems: Review of concepts, state-of-art and methods. *Resour. Conserv. Recycling* **89**, 1–10 (2014). doi: 10.1016/j.resconrec.2014.05.007
34. P. Criqui, S. Mima, European climate–energy security nexus: A model based scenario analysis. *Energy Policy* **41**, 827–842 (2012). doi: 10.1016/j.enpol.2011.11.061
35. B. Hubert, M. Rosegrant, M. A. J. S. van Boekel, R. Ortiz, The future of food: Scenarios for 2050. *Crop Sci.* **50** (suppl. 1), S33–S-50 (2010). doi: 10.2135/cropsci2009.09.0530
36. R. Coers, M. Sanders, The energy–GDP nexus; Addressing an old question with new methods. *Energy Econ.* **36**, 708–715 (2013). doi: 10.1016/j.eneco.2012.11.015
37. B. Saboori, J. B. Sulaiman, S. Mohd, An empirical analysis of the environmental Kuznets curve for CO_2 emissions in Indonesia: The role of energy consumption and foreign trade. *Int. J. Econ. Fin.* **4**, 243 (2012).
38. A. S. Stillwell, D. C. Hoppock, M. E. Webber, Energy recovery from wastewater treatment plants in the United States: A case study of the energy-water nexus. *Sustainability* **2**, 945–962 (2010). doi: 10.3390/su2040945
39. J. Liu *et al*., in *Rethinking Global Land Use in an Urban Era*, K. Seto, A. Reenberg, Eds. (MIT Press, Cambridge, MA, 2014), pp. 119–139.
40. J. M. Prospero, O. L. Mayol-Bracero, Understanding the transport and impact of African dust on the Caribbean basin. *Bull. Am. Meteorol. Soc.* **94**, 1329–1337 (2013). doi: 10.1175/BAMS-D-12-00142.1
41. D. W. Griffin, C. A. Kellogg, V. H. Garrison, E. A. Shinn, The global transport of dust. *Am. Sci.* **90**, 228 (2002). doi: 10.1511/2002.3.228
42. J. Liu *et al*., Framing sustainability in a telecoupled world. *Ecol. Soc.* **18**, art26 (2013). doi: 10.5751/ES-05873-180226
43. T. Searchinger *et al*., Use of U.S. croplands for biofuels increases greenhouse gases through emissions from land-use change. *Science* **319**, 1238–1240 (2008). doi: 10.1126/science.1151861; pmid: 18258860
44. S. J. Davis, G. P. Peters, K. Caldeira, The supply chain of CO_2 emissions. *Proc. Natl. Acad. Sci. U.S.A.* **108**, 18554–18559 (2011). doi: 10.1073/pnas.1107409108; pmid: 22006314
45. M. Lenzen *et al*., International trade drives biodiversity threats in developing nations. *Nature* **486**, 109–112 (2012). doi: 10.1038/nature11145; pmid: 22678290
46. S. L. Pimm *et al*., The biodiversity of species and their rates of extinction, distribution, and protection. *Science* **344**, 1246752 (2014). doi: 10.1126/science.1246752; pmid: 24876501
47. J. Bollen, S. Hers, B. Van der Zwaan, An integrated assessment of climate change, air pollution, and energy security policy. *Energy Policy* **38**, 4021–4030 (2010). doi: 10.1016/j.enpol.2010.03.026
48. H. Eakin *et al*., in *Rethinking Global Land Use in an Urban Era*, K. Seto, A. Reenberg, Eds. (MIT Press, Cambridge, MA, 2014), pp. 141–161.
49. B. Wicke, in *Rethinking Global Land Use in an Urban Era*, K. Seto, A. Reenberg, Eds. (MIT Press, Cambridge, MA, 2014), pp. 163–181.
50. J. Liu, W. Yang, Integrated assessments of payments for ecosystem services programs. *Proc. Natl. Acad. Sci. U.S.A.* **110**, 16297–16298 (2013). doi: 10.1073/pnas.1316036110; pmid: 24072648
51. M. C. Thompson, M. Baruah, E. R. Carr, Seeing REDD+ as a project of environmental governance. *Environ. Sci. Pol.* **14**, 100–110 (2011).
52. F. I. Khan, D. S. Schinn, Triple transformation. *Nature Clim. Change* **3**, 692 (2013). doi: 10.1038/nclimate1965
53. H. Zheng *et al*., Benefits, costs, and livelihood implications of a regional payment for ecosystem service program. *Proc. Natl. Acad. Sci. U.S.A.* **110**, 16681–16686 (2013). doi: 10.1073/pnas.1312324110; pmid: 24003160
54. L. O. Gostin, D. Lucey, A. Phelan, The Ebola epidemic: A global health emergency. *JAMA* **312**, 1095–1096 (2014). doi: 10.1001/jama.2014.11176; pmid: 25111044
55. A. Viña *et al*., Effects of natural disasters on conservation policies: The case of the 2008 Wenchuan earthquake, China. *Ambio* **40**, 274–284 (2011). doi: 10.1007/s13280-010-0098-0; pmid: 21644456
56. M. E. Portman, L. S. Esteves, X. Q. Le, A. Z. Khan, Improving integration for integrated coastal zone management: An eight country study. *Sci. Total Environ.* **439**, 194–201 (2012). doi: 10.1016/j.scitotenv.2012.09.016; pmid: 23063925
57. C. White, B.S. Halpern, C.V. Kappel, Ecosystem service tradeoff analysis reveals the value of marine spatial planning for multiple ocean uses. *Proc. Natl. Acad. Sci. U.S.A.* **109**, 4696–4701 (2012).
58. R. C. Szaro, W. T. Sexton, C. R. Malone, The emergence of ecosystem management as a tool for meeting people's needs and sustaining ecosystems. *Landsc. Urban Plan.* **40**, 1–7 (1998). doi: 10.1016/S0169-2046(97)00093-5
59. R. T. Munang, I. Thiaw, M. Rivington, Ecosystem management: Tomorrow's approach to enhancing food security under a changing climate. *Sustainability* **3**, 937–954 (2011). doi: 10.3390/su3070937
60. T. Hahn, Self-organized governance networks for ecosystem management: Who is accountable? *Ecol. Soc.* **16**, 18 (2011).
61. S. E. Shackleton, C. M. Shackleton, Linking poverty, HIV/AIDS and climate change to human and ecosystem vulnerability in southern Africa: Consequences for livelihoods and sustainable ecosystem management. *Int. J. Sustain. Dev. World Ecol.* **19**, 275–286 (2012). doi: 10.1080/13504509.2011.641039
62. B. Digest, Biofuels Mandates around the World 2012; www.biofuelsdigest.com/bdigest/2012/11/22/biofuels-mandates-around-the-world-2012 (2014).
63. S. J. Davis, J. A. Burney, J. Pongratz, K. Caldeira, Methods for attributing land-use emissions to products. *Carbon Management* **5**, 233–245 (2014). doi: 10.1080/17583004.2014.913867
64. Worldwatch Institute, Biofuels make a comeback despite tough economy (2011); available at www.worldwatch.org/biofuels-make-comeback-despite-tough-economy.
65. G. P. Hammond, S. M. Seth, Carbon and environmental footprinting of global biofuel production. *Appl. Energy* **112**, 547–559 (2013). doi: 10.1016/j.apenergy.2013.01.009
66. V. Galaz *et al*., 'Planetary boundaries'—Exploring the challenges for global environmental governance. *Curr. Opin. Environ. Sustain.* **4**, 80–87 (2012). doi: 10.1016/j.cosust.2012.01.006
67. P. Westhoff, *The Economics of Food* (Financial Times Press, NJ, 2010).
68. M. Ivanic, W. Martin, Implications of higher global food prices for poverty in low-income countries. *Agric. Econ.* **39**, 405–416 (2008). doi: 10.1111/j.1574-0862.2008.00347.x
69. N. S. Diffenbaugh, T. W. Hertel, M. Scherer, M. Verma, Response of corn markets to climate volatility under alternative energy futures. *Nat. Clim. Chang.* **2**, 514–518 (2012). pmid: 23243468
70. F. Taheripour, T. W. Hertel, J. Liu, The role of irrigation in determining the global land use impacts of biofuels. *Energy Sustain. Soc.* **3**, 1 (2013).
71. J. M. Melillo *et al*., Indirect emissions from biofuels: How important? *Science* **326**, 1397–1399 (2009). doi: 10.1126/science.1180251; pmid: 19933101
72. N. B. Villoria, T. W. Hertel, Geography matters: International trade patterns and the indirect land use effects of biofuels. *Am. J. Agric. Econ.* **93**, 919–935 (2011). doi: 10.1093/ajae/aar025
73. J. N. Galloway *et al*., International trade in meat: The tip of the pork chop. *Ambio* **36**, 622–629 (2007). doi: 10.1579/0044-7447(2007)36[622:ITIMTT]2.0.CO;2; pmid: 18240675
74. J. A. Carr, P. D'Odorico, F. Laio, L. Ridolfi, Recent history and geography of virtual water trade. *PLOS ONE* **8**, e55825 (2013). doi: 10.1371/journal.pone.0055825; pmid: 23457481
75. S. Suweis, A. Rinaldo, A. Maritan, P. D'Odorico, Water-controlled wealth of nations. *Proc. Natl. Acad. Sci. U.S.A.* **110**, 4230–4233 (2013). doi: 10.1073/pnas.1222452110; pmid: 23359709
76. J. A. Allan, *'Virtual Water': A Long Term Solution for Water Short Middle Eastern Economies?* (School of Oriental and African Studies, University of London, 1997).
77. A. Y. Hoekstra, P. Hung, "Virtual water trade: A quantification of virtual water flows between nations in relation to international crop trade," Value of Water Research Report Series 11 (IHE Delft, Delft, Netherlands, 2002).
78. M. Konar, Z. Hussein, N. Hanasaki, D. Mauzerall, I. Rodriguez-Iturbe, Virtual water trade flows and savings under climate change. *Hydrol. Earth Syst. Sci.* **17**, 3219–3234 (2013). doi: 10.5194/hess-17-3219-2013
79. R. Boelens, J. Vos, The danger of naturalizing water policy concepts: Water productivity and efficiency discourses from field irrigation to virtual water trade. *Agric. Water Manage.* **108**, 16–26 (2012). doi: 10.1016/j.agwat.2011.06.013
80. D. Schindler, P. Lee, Comprehensive conservation planning to protect biodiversity and ecosystem services in Canadian boreal regions under a warming climate and increasing exploitation. *Biol. Conserv.* **143**, 1571–1586 (2010). doi: 10.1016/j.biocon.2010.04.003
81. A. Y. Hoekstra, M. M. Mekonnen, The water footprint of humanity. *Proc. Natl. Acad. Sci. U.S.A.* **109**, 3232–3237 (2012). doi: 10.1073/pnas.1109936109; pmid: 22331890
82. C. Dalin, M. Konar, N. Hanasaki, A. Rinaldo, I. Rodriguez-Iturbe, Evolution of the global virtual water trade network. *Proc. Natl. Acad. Sci. U.S.A.* **109**, 5989–5994 (2012). doi: 10.1073/pnas.1203176109; pmid: 22474363
83. J. Wang *et al*., China's water–energy nexus: Greenhouse-gas emissions from groundwater use for agriculture. *Environ. Res. Lett.* **7**, 014035 (2012). doi: 10.1088/1748-9326/7/1/014035
84. S. A. Levin, J. Lubchenco, Resilience, robustness, and marine ecosystem-based management. *Bioscience* **58**, 27 (2008). doi: 10.1641/B580107
85. B. S. Halpern, S. E. Lester, J. B. Kellner, Spillover from marine reserves and the replenishment of fished stocks. *Environ. Conserv.* **36**, 268–276 (2009). doi: 10.1017/S0376892910000032
86. K. S. Andam, P. J. Ferraro, A. Pfaff, G. A. Sanchez-Azofeifa, J. A. Robalino, Measuring the effectiveness of protected area networks in reducing deforestation. *Proc. Natl. Acad. Sci. U.S.A.* **105**, 16089–16094 (2008). doi: 10.1073/pnas.0800437105; pmid: 18854414
87. B. D. Anderson, S. Vongpanitlerd, *Network Analysis and Synthesis: A Modern Systems Theory Approach* (Courier Dover Publications, Mineola, NY, 2006).
88. W. Yang *et al*., Nonlinear effects of group size on collective action and resource outcomes. *Proc. Natl. Acad. Sci. U.S.A.* **110**, 10916–10921 (2013). doi: 10.1073/pnas.1301733110; pmid: 23776222

89. J. D. Farmer, D. Foley, The economy needs agent-based modelling. *Nature* **460**, 685–686 (2009). doi: 10.1038/460685a; pmid: 19661896
90. M. A. Janssen, E. Ostrom, Empirically based, agent-based models. *Ecol. Soc.* **11**, 37 (2006).
91. E. Ostrom, V. Ostrom, *Choice, Rules and Collective Action: The Ostroms on the Study of Institutions and Governance* (ECPR Press, Colchester, UK, 2014).
92. D. Agrawal, S. Das, A. El Abbadi, in *Proceedings of the 14th International Conference on Extending Database Technology*. (ACM, New York, 2011), pp. 530–533.
93. M. Margolis, J. F. Shogren, Disguised protectionism, global trade rules and alien invasive species. *Environ. Resour. Econ.* **51**, 105–118 (2012). doi: 10.1007/s10640-011-9490-x
94. S. R. Carpenter *et al*., Science for managing ecosystem services: Beyond the Millennium Ecosystem Assessment. *Proc. Natl. Acad. Sci. U.S.A.* **106**, 1305–1312 (2009). doi: 10.1073/pnas.0808772106; pmid: 19179280
95. C. Liu, C. Kroeze, A. Y. Hoekstra, W. Gerbens-Leenes, Past and future trends in grey water footprints of anthropogenic nitrogen and phosphorus inputs to major world rivers. *Ecol. Indic.* **18**, 42–49 (2012). doi: 10.1016/j.ecolind.2011.10.005
96. CO2Now.org; co2now.org/Current-CO2/CO2-Now/global-carbon-emissions.html (2014).
97. T. O. Wiedmann *et al*., The material footprint of nations. *Proc. Natl. Acad. Sci. U.S.A.* 10.1073/pnas.1220362110 (2013).
98. F. Bingham, B. Perkins, Trade Competitiveness & Advocacy Branch, Australia's coal and iron ore exports—2001–2011 (2012).
99. T. W. Hertel *et al*., Effects of US maize ethanol on global land use and greenhouse gas emissions: Estimating market-mediated responses. *Bioscience* **60**, 223–231 (2010). doi: 10.1525/bio.2010.60.3.8
100. J. Liu *et al*., Ecological degradation in protected areas: The case of Wolong Nature Reserve for giant pandas. *Science* **292**, 98–101 (2001). doi: 10.1126/science.1058104; pmid: 11292872
101. J. Phelps, L. R. Carrasco, E. L. Webb, L. P. Koh, U. Pascual, Agricultural intensification escalates future conservation costs. *Proc. Natl. Acad. Sci. U.S.A.* **110**, 7601–7606 (2013). doi: 10.1073/pnas.1220070110; pmid: 23589860
102. J. Rogelj, D. L. McCollum, A. Reisinger, M. Meinshausen, K. Riahi, Probabilistic cost estimates for climate change mitigation. *Nature* **493**, 79–83 (2013). doi: 10.1038/nature11787; pmid: 23282364
103. D. Shindell *et al*., Simultaneously mitigating near-term climate change and improving human health and food security. *Science* **335**, 183–189 (2012). doi: 10.1126/science.1210026; pmid: 22246768
104. J. Reis, T. Stojanovic, H. Smith, Relevance of systems approaches for implementing Integrated Coastal Zone Management principles in Europe. *Mar. Policy* **43**, 3–12 (2014). doi: 10.1016/j.marpol.2013.03.013
105. R. Biggs, F. R. Westley, S. R. Carpenter, Navigating the back loop: Fostering social innovation and transformation in ecosystem management. *Ecol. Soc.* **15**, 9 (2010).
106. T. A. Spies *et al*., Examining fire-prone forest landscapes as coupled human and natural systems. *Ecol. Soc.* **19**, art9 (2014). doi: 10.5751/ES-06584-190309
107. T. C. Coverdale, N. C. Herrmann, A. H. Altieri, M. D. Bertness, Latent impacts: The role of historical human activity in coastal habitat loss. *Front. Ecol. Environ* **11**, 69–74 (2013). doi: 10.1890/120130
108. X. Chen *et al*., Producing more grain with lower environmental costs. *Nature* **514**, 486–489 (2014). doi: 10.1038/nature13609; pmid: 25186728

ACKNOWLEDGMENTS

We thank the U.S. National Science Foundation, the International Network of Research on Coupled Human and Natural Systems, Michigan State University, and Michigan AgBioResearch for financial support. We are grateful to J. Broderick, W. McConnell, J. McCoy, S. Nichols, and W. Yang for assistance and to two anonymous reviewers for helpful comments.

10.1126/science.1258832

REPORTS

OPTICS

Observation of optical polarization Möbius strips

Thomas Bauer,[1,2] Peter Banzer,[1,2,3] Ebrahim Karimi,[3]* Sergej Orlov,[1,2] Andrea Rubano,[4,5] Lorenzo Marrucci,[4,5] Enrico Santamato,[4] Robert W. Boyd,[3,6] Gerd Leuchs[1,2]

Möbius strips are three-dimensional geometrical structures, fascinating for their peculiar property of being surfaces with only one "side"—or, more technically, being "nonorientable" surfaces. Despite being easily realized artificially, the spontaneous emergence of these structures in nature is exceedingly rare. Here, we generate Möbius strips of optical polarization by tightly focusing the light beam emerging from a *q*-plate, a liquid crystal device that modifies the polarization of light in a space-variant manner. Using a recently developed method for the three-dimensional nanotomography of optical vector fields, we fully reconstruct the light polarization structure in the focal region, confirming the appearance of Möbius polarization structures. The preparation of such structured light modes may be important for complex light beam engineering and optical micro- and nanofabrication.

Interference is one of the most intriguing features of the wave nature of light. This phenomenon can give rise to points or lines of zero intensity, when three or more plane waves are superimposed. Around these "nodes," the phase of the optical beam undergoes a dislocation, determined by the beam's wavelength as well as the geometry of the optical system (*1*). The phase variation around these points is described by a topological charge ℓ, an integer that determines the number of 2π phase cycles along a path around these nodes (*2*). The phase of the optical field is undefined at these nodes, and thus, such points are called phase singularities (*3*). Complex superpositions of optical beams result in rich topological structures of phase and intensity. For instance, elaborate beams designed by a computer-generated hologram form dark lines and knots in 3-dimensional (3D) space upon propagation (*4*, *5*). In addition, the vectorial features of multibeam interference lead to interesting polarization topologies (*6*–*8*). Three main polarization topologies—"lemon," "star," and "monstar"—are invoked in the paraxial regime to describe the vectorial patterns in the plane transverse to the beam propagation direction (*9*, *10*). A general polarization topology can be generated by a coherent superposition of two nonplanar circularly polarized beams with opposite handedness, copropagating paraxially and possessing nonidentical topological charges:

$$\mathbf{E}(\mathbf{r}) = \cos\left(\frac{\Theta}{2}\right) \mathrm{LG}_{p_1,\ell_1}(\mathbf{r})\mathbf{e}_\mathrm{L} + \sin\left(\frac{\Theta}{2}\right) e^{i\chi} \mathrm{LG}_{p_2,\ell_2}(\mathbf{r})\mathbf{e}_\mathrm{R} \qquad (1)$$

where Θ and χ respectively define amplitude coefficients and the relative phase between the two different polarization states; $\mathbf{e}_\mathrm{L}$ and $\mathbf{e}_\mathrm{R}$, are unit vectors of left- and right-hand circular polarization; and $\mathrm{LG}_{p,\ell}(\mathbf{r})$ are Laguerre-Gaussian (LG) modes with radial and azimuthal indices p and ℓ (*11*). The polarization of these beams in the transverse plane samples the entire Poincaré sphere, and the beams are thus called Poincaré beams (*12*). Two main polarization singularities, C-points and L-lines, respectively denoting points of circular and lines of linear polarization, are used to describe the beams' polarization topology (*13*, *14*).

In 2005, a beam configuration was proposed that consists of a pair of noncoaxial circularly

[1]Max Planck Institute for the Science of Light, Guenther-Scharowsky-Strasse 1, D-91058 Erlangen, Germany. [2]Institute of Optics, Information and Photonics, Friedrich-Alexander-University Erlangen-Nuremberg, Staudtstrasse 7/B2, D-91058 Erlangen, Germany. [3]Department of Physics, University of Ottawa, 25 Templeton Street, Ottawa, Ontario K1N 6N5, Canada. [4]Dipartimento di Fisica, Università di Napoli Federico II, Complesso Universitario di Monte Sant'Angelo, via Cintia, 80126 Napoli, Italy. [5]Consiglio Nazionale delle Ricerche (CNR)–SPIN, Complesso Universitario di Monte Sant'Angelo, via Cintia, Napoli, Italy. [6]Institute of Optics, University of Rochester, Rochester, NY 14627, USA.
*Corresponding author. E-mail: ekarimi@uottawa.ca

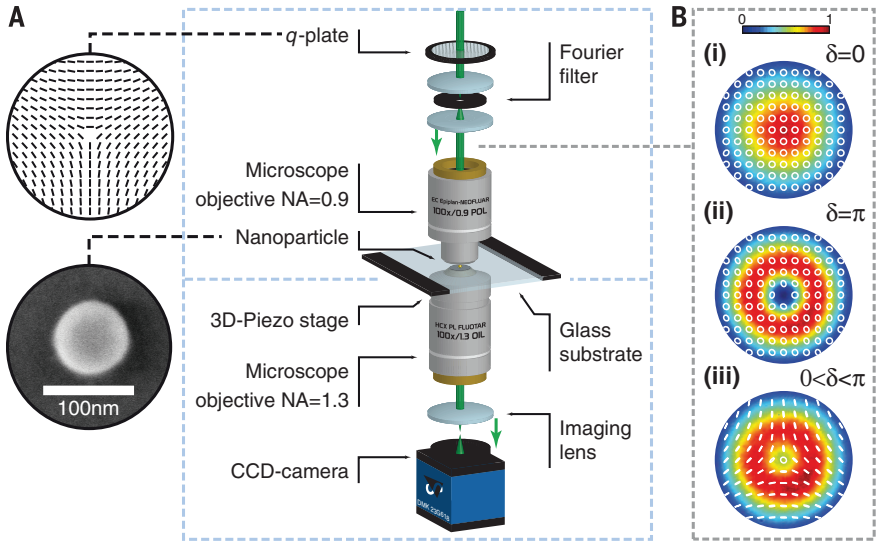

Fig. 1. Schematic of the experimental apparatus, and the intensity and polarization patterns of the generated beams. (**A**) A mode-cleaned right-hand circularly polarized TEM_{00} mode laser beam at a wavelength of 530 nm is sent through a $q = -1/2$-plate (QP). A spatial Fourier filter, made of two lenses and a pinhole, is used to filter unwanted higher-order radial modes of the generated beam after the QP. This beam is a superposition of a right-hand circularly polarized TEM_{00} mode and a left-hand circularly polarized $\mathrm{LG}_{0,1}$ mode, in which the superposition ratio was carefully adjusted by means of an external voltage applied to the QP. The composite beam is tightly focused by a microscope objective with a NA of 0.9 onto a single spherical gold nanoparticle with a diameter of 82 nm, sitting on a glass substrate. A 3D piezo stage is used to scan the sphere within the focal plane. The transmitted light is collected by an oil-immersion objective with NA = 1.3. A camera combined with an imaging system is used to image the back focal plane of the lower microscope objective for each position of the nanoparticle in the focal plane. Top and bottom insets respectively show the orientation of liquid crystal molecules in the $q = -1/2$-plate and a scanning electron microscope image of the gold nanoparticle. (**B**) Measured intensity and polarization distributions of the optical beam emerging from the QP. The local polarization ellipse is superimposed onto the intensity distribution in white color. The three cases (i) to (iii) correspond to different optical retardations, realized by applying different voltages to the QP: (i) a pure right-hand circularly polarized TEM_{00} beam, (ii) a pure left-hand circularly polarized $\mathrm{LG}_{0,1}$ beam, and (iii) a superposition of (i) and (ii). In the latter case, however, the beam possesses a polarization topology of –1/2 in the form of a star with a C-point on the optical axis.

polarized beams of opposite handedness with different scalar topological charges. In this scheme, a nonparaxial 3D polarization topology is generated at the beams' intersection plane (*15*). Analytical calculations revealed spectacular 3D-polarization topologies in the form of twisted ribbons and Möbius strips (*16*). Möbius strips are 3D objects that possess only a single surface and a single boundary component (*17*, *18*) and have been observed in chemistry, biology (*19*), particle physics (*20*), and materials science (*21*–*23*). In our experiment, these 3D objects are created by the tight focusing of individual Poincaré beams, as given by Eq. 1, by exploiting the longitudinal field component appearing in the focal region. In order to visualize the polarization Möbius strip, we reconstructed the amplitudes and relative phases of the individual components of the electric field and traced the polarization ellipse around the optical axis in the focal plane.

The optical element we used to generate the Poincaré beam is a *q*-plate, a patterned, birefringent plate with optical retardation δ and made of nematic liquid crystal. The orientation of the principal axis of the liquid crystal molecules comprising the *q*-plate varies with the azimuthal coordinate, so that the structure possesses a topological charge q (*24*). When $\delta = \pi$, the *q*-plate flips the handedness of the spin of an incoming beam and adds an orbital angular momentum (OAM) of $|2q|$ to the outgoing beam. For a non-π retardation, the *q*-plate generates a Poincaré beam from a circularly polarized Gaussian input beam. The generated beam is a coherent superposition of the fundamental TEM_{00} ($LG_{0,0}$) and $LG_{0,\pm 2q}$ modes with opposite circular polarizations, as described by Eq. 1 for $p_1 = p_2 = \ell_1 = 0$ and $\ell_2 = \pm 2q$. The optical retardation of the *q*-plate and its orientation determine the amplitude of the superposition coefficients, Θ, and relative phase between the two beams, χ, respectively (*10*). Our experiment involves a Poincaré beam with a polarization topology of $q = -1/2$ (or $q = -3/2$), and we tune the mode ratio between the two aforementioned modes by varying δ using an applied voltage (*25*). The intensity and polarization distributions of the output beam in the near-field of a *q*-plate with $q = -1/2$ are presented in Fig. 1B, for different optical retardations.

A star-shaped Poincaré beam with a polarization topology of −1/2 (Fig. 1B, iii), produced by the *q*-plate, is tightly focused by a microscope objective with a numerical aperture (NA) of 0.9, producing a complex focal field distribution, with a spot size comparable with the wavelength of the light beam. The paraxial approximation does not hold under tight focusing conditions, and the beam in general is no longer transverse as a strong longitudinal component of the electric field is created (*26*). We hence have $\mathbf{E} = E_x\hat{\mathbf{x}} + E_y\hat{\mathbf{y}} + E_z\hat{\mathbf{z}}$, where E_i are the components of electric field, and $\hat{\mathbf{x}}$, $\hat{\mathbf{y}}$, and $\hat{\mathbf{z}}$ are the unit vectors in a Cartesian coordinate frame in which z is oriented as the beam axis. In the present case, the strengths of the electric field components $|E_i|$ are almost the same. Furthermore, the intensity distribution close to the focus is highly asymmetric, and the initial cylindrical symmetry is broken into one of its subgroups—namely, the dihedral D_3 group. The symmetry-breaking observed in the beam intensity arises from the preexisting threefold symmetry of the initial beam's transverse polarization distribution. Shown in Fig. 2A are the theoretically calculated electric energy density and phase distributions of individual components of the electric field E_x, E_y, and E_z of the tightly focused Poincaré beam and the total electric energy density distribution at the focus (*26*).

We used a nanoprobe-based reconstruction technique to experimentally probe and reconstruct the electric field distributions generated in the focal plane, allowing the optical polarization Möbius strips hidden in this complex field structure to be observed (*27*). For this technique, we used a spherical gold nanoparticle on a glass substrate and scanned it through the field under study (Fig. 1A). The scattered and transmitted light was collected and angularly resolved for each position of the nanoprobe relative to the field distribution by using an immersion-type microscope objective with NA = 1.3. This procedure allows for the reconstruction of both amplitude and phase distributions from the data recorded for each nanoprobe position relative to the beam in the focal plane and different effective observation directions (*10*, *27*). The experimentally reconstructed intensity and relative phase distributions of the three individual electric field components of the tightly focused beam are shown in Fig. 2B. Because of the spin-to-OAM conversion, the longitudinal z-component of the field gains additional OAM of ±1, with the sign depending on the helicity of the input beam polarization (*28*). The beam is highly asymmetric because of its nonparaxiality.

We used the approach introduced in (*29*) to trace out the 3D orientation of the polarization

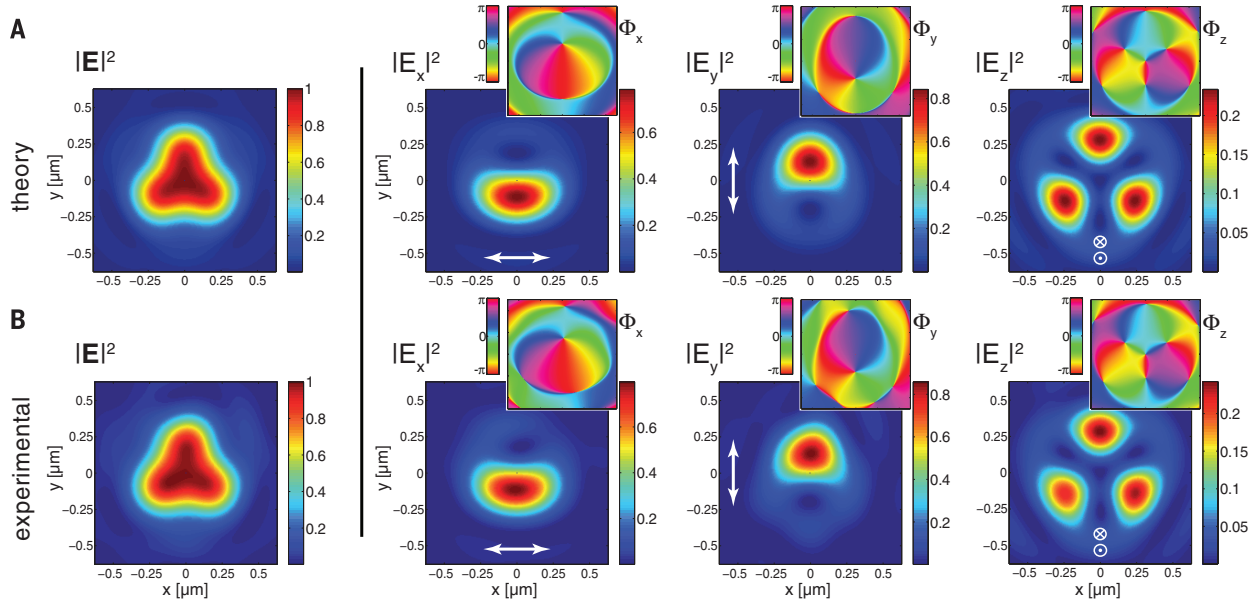

Fig. 2. Numerically calculated and experimentally observed electric energy density distributions of a tightly focused Poincaré beam. (**A**) and (**B**) show the numerically calculated and experimentally measured total electric energy density distribution as well as the electric energy densities and phase distributions of the individual field components of the tightly focused Poincaré beam shown in Fig. 1B, iii, in the focal plane of the high-numerical-aperture objective. Under tight-focusing conditions, the beam loses its cylindrical symmetry. Moreover, a longitudinal component of the field is generated. Top-right insets show the corresponding phase patterns for each field component, Φ_x, Φ_y, and Φ_z. Because of spin-to-OAM conversion, the longitudinal field component gains a helical phase-front of $\exp(\pm i\varphi)$, with a sign that depends on the input beam polarization. Three separated phase vortices can be seen surrounding the beam axis, generated by the interference of the two constituent input beams.

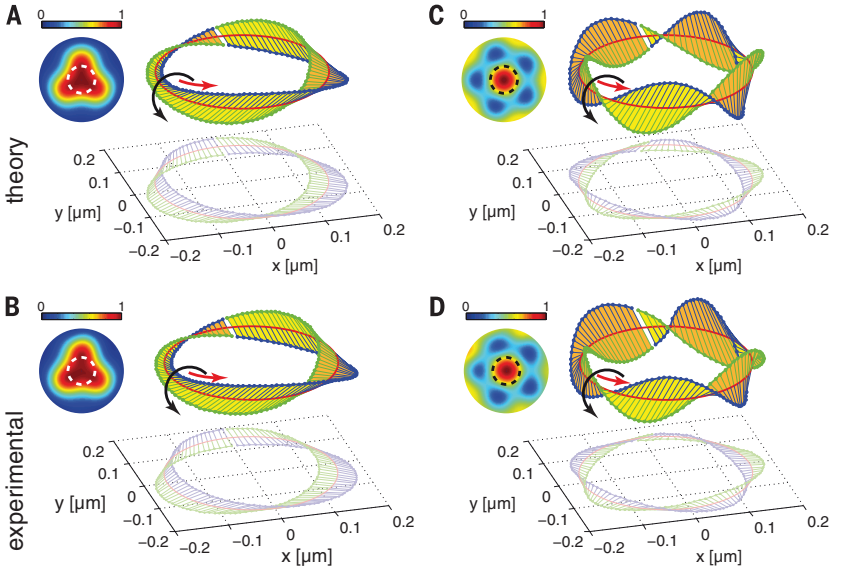

Fig. 3. Polarization topology of a highly nonparaxial Poincaré beam with topological charges of −1/2 and −3/2. (**A** and **C**) The numerically calculated polarization topologies in the focal plane of the beam. (**B** and **D**) The experimentally observed polarization topologies in the focal plane of the beam. Our experiment was performed under tight-focusing (nonparaxial) conditions, which accentuates the 3D topology of these Poincaré beams. In these plots, the major axis of the 3D polarization ellipse is represented as a function of position on a circle of 150 nm radius centered on the beam axis. This circle is shown as a dashed white or black line in the top-left insets superimposed to the scanned intensity image. In order to make the twist of the Möbius strip more noticeable, one half of the major axis of the local polarization ellipse is colored blue, and the other half is colored green. For a charge of −1/2 [(A) and (B)], we observe three half twists; for a charge of −3/2 (C and D), we observe five half twists. At the bottom of (A) to (D), the projection of the polarization major axis onto a plane (the *x*–*y* plane) transverse to the propagation direction *z* is shown.

ellipse around the optical axis (C-point). In this notation, the major and minor axes of the polarization ellipse and the normal to the polarization ellipse in the complex representation of the electric field are described by the vectors

$$\alpha = \frac{1}{\left|\sqrt{\mathbf{E}\cdot\mathbf{E}}\right|}\Re(\mathbf{E}^*\sqrt{\mathbf{E}\cdot\mathbf{E}})$$
$$\beta = \frac{1}{\left|\sqrt{\mathbf{E}\cdot\mathbf{E}}\right|}\Im(\mathbf{E}^*\sqrt{\mathbf{E}\cdot\mathbf{E}}) \quad , \qquad (2)$$
$$\gamma = \Im(\mathbf{E}^*\times\mathbf{E})$$

where $\Re(\mathbf{E})$, $\Im(\mathbf{E})$, and $\mathbf{E}^*$ represent the real and imaginary parts of $\mathbf{E}$ and its complex conjugate, respectively. In this representation, a C-line is a trajectory of $\mathbf{r}$ upon propagation in which the major and minor axes of the ellipse become degenerate, $\boldsymbol{\alpha}(\mathbf{r}) = \boldsymbol{\beta}(\mathbf{r}) = 0$. In our case, as the beam propagates, the polarization ellipses change in the transverse plane because TEM_{00} and $LG_{0,\pm1}$ possess different Gouy phases (*8*). The polarization topology of the beam remains unchanged but undergoes a global rotation that depends on the propagation distance. Furthermore, the C-line coincides with the optical axis in this case. In order to visualize and plot the polarization topology in 3D space, we considered only the polarization configuration in a plane orthogonal to the C-line, which is known as the principal plane. In particular, we considered first the focal plane, where the field's *z*-component is largest. We then calculated the major and minor ($\boldsymbol{\alpha}$, $\boldsymbol{\beta}$) axes of the polarization ellipses at all points lying on a circle in the principal plane, with the C-point in its center.

Because a strong longitudinal component of the electric field is generated, the major axis $\boldsymbol{\alpha}$ of the polarization ellipse undergoes a twist out of the focal plane in 3D space and forms a Möbius strip. The twisting direction for the specific topology under study is clockwise, which indicates a positive polarization topological charge of 3/2, or three half-twists. We show the corresponding theoretically calculated and experimentally observed Möbius strips with 3/2-twists for a Poincaré beam with $q = -1/2$ under tight focusing in Fig. 3, A and B, respectively. A Möbius strip of 5/2-twists is created and also observed by replacing the *q*-plate of $q = -1/2$ with one of $q = -3/2$. The corresponding theoretically expected and experimentally measured Möbius strips are shown in Fig. 3, C and D, whereas the focal field distributions are presented in the supplementary materials (*10*). Our measurements were performed in the focal plane, but the Möbius structure extends outside of the focal plane and for a variety of radii; additional results are given in the supplementary materials (*10*).

Our results reveal a hidden polarization topology under tight focusing that has not previously been reported in literature. These results are relevant to fundamental studies of optics and physics, light coupling to nanostructures, light-matter interactions, and nano-optics (*30*–*32*). Optical patterns such as those we demonstrate here could, for example, be used to optically fabricate material microstructures with nontrivial topology for new functional media—for example, metamaterials with exotic optical properties or molecular-shape–selective membranes or substrates.

REFERENCES AND NOTES

1. J. F. Nye, M. V. Berry, *Proc. R. Soc. Lond., Math. Phys. Sci.* **336**, 165–190 (1974).
2. J. F. Nye, *Natural Focusing and Fine Structure of Light: Caustics and Wave Dislocations* (CRC Press, Boca Raton, FL, 1999).
3. I. V. Basistiy, M. S. Soskin, M. V. Vasnetsov, *Opt. Commun.* **119**, 604–612 (1995).
4. J. Leach, M. R. Dennis, J. Courtial, M. J. Padgett, *Nature* **432**, 165 (2004).
5. M. R. Dennis, R. P. King, B. Jack, K. O'Holleran, M. J. Padgett, *Nat. Phys.* **6**, 118–121 (2010).
6. F. Flossmann, K. O'Holleran, M. R. Dennis, M. J. Padgett, *Phys. Rev. Lett.* **100**, 203902 (2008).
7. E. J. Galvez, S. Khadka, W. H. Schubert, S. Nomoto, *Appl. Opt.* **51**, 2925–2934 (2012).
8. F. Cardano, E. Karimi, L. Marrucci, C. de Lisio, E. Santamato, *Opt. Express* **21**, 8815–8820 (2013).
9. M. V. Berry, J. H. Hannay, *J. Phys. Math. Gen.* **10**, 1809–1821 (1977).
10. More details on 2D polarization topologies, *q*-plate output beams, and mode analysis, as well as the reconstruction technique and 3D polarization distribution through the focal volume, can be found in the supplementary materials.
11. A. E. Siegman, *Lasers* (University Science Books, Herndon, VA, 1986).
12. A. M. Beckley, T. G. Brown, M. A. Alonso, *Opt. Express* **18**, 10777–10785 (2010).
13. M. R. Dennis, K. O'Holleran, M. J. Padgett, *Prog. Opt.* **53**, 293–363 (2009).
14. I. Freund, *Opt. Commun.* **283**, 1–15 (2010).
15. I. Freund, *Opt. Commun.* **249**, 7–22 (2005).
16. I. Freund, *Opt. Lett.* **35**, 148–150 (2010).
17. C. A. Pickover, *The Möbius Strip: Dr. August Möbius's Marvelous Band in Mathematics, Games, Literature, Art, Technology, and Cosmology* (Thunder's Mouth Press, New York, 2005).
18. E. L. Starostin, G. H. M. van der Heijden, *Nat. Mater.* **6**, 563–567 (2007).
19. D. J. Craik, *Toxicon* **39**, 1809–1813 (2001).
20. A. Ynnerman, S. C. Chapman, P. Ljung, N. Andersson, *IEEE Trans. Plasma Sci.* **30**, 18–19 (2002).
21. C.-W. Chang *et al.*, *Phys. Rev. Lett.* **105**, 259903 (2010).
22. S. Tanda *et al.*, *Nature* **417**, 397–398 (2002).
23. T. Machon, G. P. Alexander, *Proc. Natl. Acad. Sci. U.S.A.* **110**, 14174–14179 (2013).
24. L. Marrucci, C. Manzo, D. Paparo, *Phys. Rev. Lett.* **96**, 163905 (2006).
25. S. Slussarenko *et al.*, *Opt. Express* **19**, 4085–4090 (2011).
26. B. Richards, E. Wolf, *Proc. R. Soc. London Ser. A* **253**, 358–379 (1959).
27. T. Bauer, S. Orlov, U. Peschel, P. Banzer, G. Leuchs, *Nat. Photonics* **8**, 23–27 (2014).
28. Y. Zhao, J. S. Edgar, G. D. M. Jeffries, D. McGloin, D. T. Chiu, *Phys. Rev. Lett.* **99**, 073901 (2007).
29. M. V. Berry, *J. Opt. A, Pure Appl. Opt.* **6**, 675–678 (2004).
30. A. Ambrosio, L. Marrucci, F. Borbone, A. Roviello, P. Maddalena, *Nat. Commun.* **3**, 989 (2012).
31. K. Toyoda, K. Miyamoto, N. Aoki, R. Morita, T. Omatsu, *Nano Lett.* **12**, 3645–3649 (2012).
32. K. Sugioka, Y. Cheng, *Light Sci. Appl.* **3**, e149 (2014).

ACKNOWLEDGMENTS

The authors thank C. Marquardt for fruitful discussions. E.K. and R.W.B. acknowledge the support of the Canada Excellence Research Chairs (CERC) Program.

SUPPLEMENTARY MATERIALS

www.sciencemag.org/content/347/6225/964/suppl/DC1
Materials and Methods
Supplementary Text
Figs. S1 to S6
References (*33*–*35*)

1 September 2014; accepted 16 January 2015
Published online 29 January 2015;
10.1126/science.1260635

is removed from solution. Our recent density functional theory calculation verified that the Pb^{2+} clusters on the $MAPbI_3$ surface tend to form charge traps (*6*). The internal quantum efficiency (IQE) of the 3-mm MSC device (derived by dividing EQE by the transmittance of the Au electrode; see Fig. 2D and fig. S2) was near unity (95 ± 7%).

The electrons generated in the very thin perovskite layer near the Au anode must traverse the whole crystal to be collected by the Ga cathode, indicating that the electron diffusion length in MSCs is greater than the crystal thickness (~3 mm). We also replaced Ga by a semitransparent Au (25 nm)/C_{60} (25 nm) layer as the cathode so that photogenerated charges would be located at the cathode side. Again, the value of J_{SC} measured at 0.1% sun was comparable with incident light from both sides, which indicates that the hole diffusion length in MSCs is also longer than the MSC thickness.

The dependence of responsivity (R) and J_{SC} on light intensity (I_L) for thick devices is summarized in Fig. 2, E and F, respectively [see fig. S3 for photocurrent density–voltage (J_{ph}-V) curves]. Under 1 sun, the open-circuit voltage V_{oc} was 0.62 V, versus ~1.00 V in optimized MPC thin-film devices, again indicating a strong charge recombination in the MSC devices under strong illumination. For thick MSC devices, R decreased from 35 mA W^{-1} to 0.19 mA W^{-1} when the intensity of white illuminated light increased from 0.003 mW cm^{-2} to 100 mW cm^{-2} because of increased charge recombination for higher I_L. Fitting of J_{sc} with I_L as $J_{sc} \propto I_L^{\beta}$ gave a value of β (recombination parameter) of 0.5 ± 0.01, which suggests that second-order charge recombination dominated in the thick MSC devices for $I_L >$ 0.003 mW cm^{-2}, as seen previously (*12*, *13*). Reducing the MSC thickness to 200 μm recovered large R (Fig. 2E) at 1 sun and increased β to 0.88, which indicates that the carrier diffusion length of MSCs is near 200 μm for 1 sun illumination.

We could characterize the carrier mobility μ and carrier lifetime τ_r because the carrier diffusion length L_D is determined by $L_D = (k_B T \mu \tau_r / e)^{1/2}$, where k_B, T, and e are the Boltzmann constant, absolute temperature, and elementary charge, respectively. The device dark current (J_D) was measured to derive the trap density and carrier mobilities. The MSCs were sandwiched by two Au electrodes deposited by thermal evaporation to form hole-only devices. As shown in Fig. 3A, the linear J_D-V relation (green line) indicates an ohmic response at the low bias (< 2.1 V). A trap-filling process was identified by the marked increase of the current injection at a bias range of 2.1 to 10.7 V. The voltage at which all the traps are filled (trap-filled limit voltage V_{TFL}) was determined by the trap density (*14*):

$$V_{TFL} = \frac{e n_t L^2}{2\varepsilon\varepsilon_0} \quad (1)$$

where L is the thickness of the MSCs, ε (= 32) is relative dielectric constant of $MAPbI_3$, and ε_0 is the vacuum permittivity. The trap density n_t in MSCs was calculated to be 3.6 × 10^{10} cm^{-3}. For comparison, the hole-only devices with MPC thin films were also fabricated with PEDOT:PSS and Au as the hole injection electrodes (fig. S4). The calculated hole trap density in the MPC thin films was 2.0 × 10^{15} cm^{-3}, which is almost five orders of magnitude greater than in the MSCs. Thermal admittance spectroscopy (fig. S5) confirmed the reduction in trap density by two to three orders of magnitude in MSCs. Thus, the extraordinary carrier diffusion length in the MSCs is the result of largely suppressed trap density. When operating in the trap-free space charge limit current (SCLC) regime above 10.7 V, the dark current of the MSC was well fitted (Fig. 3A, green line) by the Mott-Gurney law:

$$J_D = \frac{9\varepsilon\varepsilon_0 \mu V_b^2}{8L^3} \quad (2)$$

where V_b is applied voltage. A large hole mobility of 164 ± 25 cm^2 V^{-1} s^{-1} was derived from the curve fitting. The uncertainties we reported represent a single standard deviation in the measurements on 10 nominally identical devices. Hall effect measurements revealed that the MSC was slightly p-doped, with a low free hole concentration of 9 (±2) × 10^9 cm^{-3} (see supplementary materials). The hole mobility from Hall effect measurement was 105 ± 35 cm^2 V^{-1} s^{-1}, in agreement with the SCLC results. Similarly, the electron trap density and electron mobility of MSCs were measured with the electron-only devices, which had phenyl-C_{61}-butyric acid methyl (PCBM):C_{60}/Ga as both electrodes. A low electron trap density of 4.5 × 10^{10} cm^{-3} was derived (Fig. 3B), comparable to the hole trap density, and the electron mobility was 24.8 ± 4.1 cm^2 V^{-1} s^{-1}. Finally, we used time-of-flight (ToF) to verify the high electron mobilities of 24.0 ± 6.8 cm^2 V^{-1} s^{-1} (Fig. 3, C and D). The electron and hole mobilities in MSCs are several times the intrinsic band transport mobility in MPC thin films (*10*) and polycrystals (*15*) measured by the Hall effect method

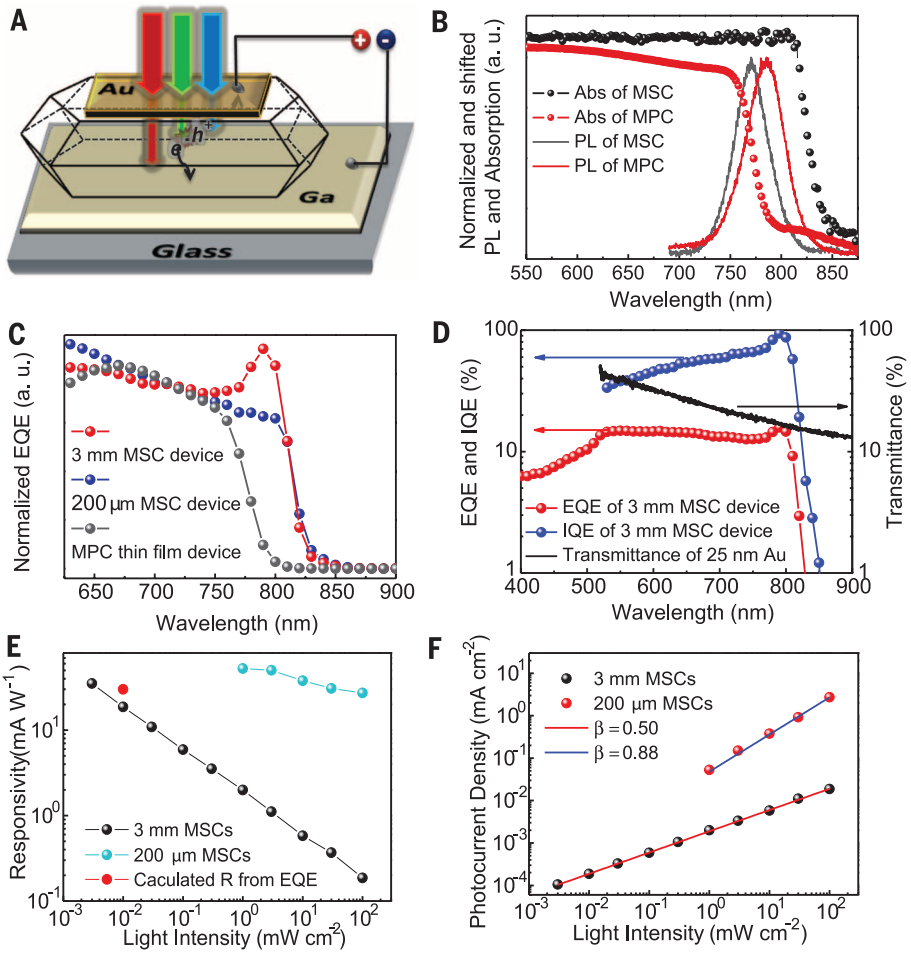

Fig. 2. Device structure and electrical and optical characterization of the MSC devices and MPC thin films. (**A**) Schematic device structure of the $MAPbI_3$ single-crystal devices. (**B**) Normalized PL and absorption spectra of the MSCs and MPC thin films. (**C**) Normalized EQEs of 3-mm-thick and 200-μm-thick MSC photovoltaic devices and a MPC thin-film device. (**D**) EQE of a 3-mm-thick MSC device, average transmittance of a 25-nm Au electrode, and calculated average IQE of the same MSC device. (**E**) Responsivity of the 3-mm-thick and 200-μm-thick MSC devices and responsivity calculated from the EQE of the 3-mm-thick MSC device. (**F**) Current density J_{sc} versus light intensity I_L fitted by $J_{SC} \propto I_L^{\beta}$ for the 3-mm-thick and 200-μm-thick MSC devices.

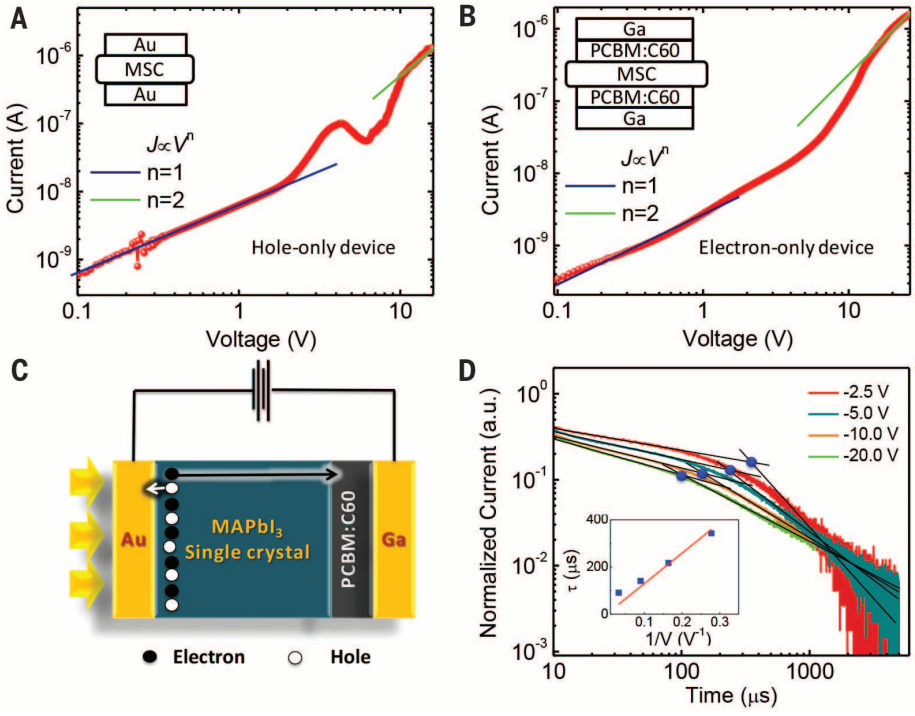

Fig. 3. Carrier mobility characterization of MSCs. (**A** and **B**) Current-voltage curve for a hole-only MSC device (A) and an electron-only MSC device (B). The insets show the device structure of hole-only and electron-only MSC devices, respectively. Three regions can be identified according to different values of the exponent *n*: *n* = 1 is the ohmic region, *n* = 2 is the SCLC region, and in between is the trap-filled limited region. (**C**) Schematic illustration of the device for the time-of-flight measurement. (**D**) The transient current curves of the MSC device show the normalized transient photocurrent under various reverse biases. The carrier transit time is determined by the intercept of the pretransit and posttransit asymptotes of the photocurrent, marked by solid blue circles. Inset shows the charge transit time versus the reciprocal of bias; the solid line is a linear fit to the data.

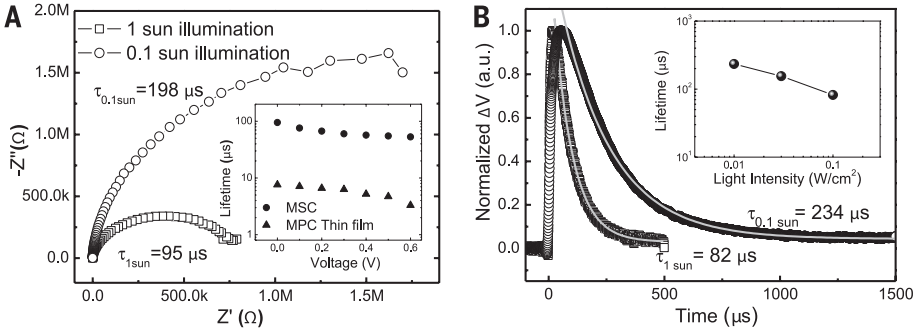

Fig. 4. Carrier recombination lifetime characterization of MSCs. (**A** and **B**) Impedance spectroscopies (A) and transient photovoltaic curves (B) of the MSC devices under 1 sun and 0.1 sun illumination, respectively, with incident light from the semitransparent Au anode. The TPV decay curves were fitted by a single-exponential decay function. The inset of (A) is the extracted charge recombination lifetime from IS measurement of the MSC device and the MPC thin film at various applied voltage biases under 1 sun illumination. The inset of (B) is the extracted charge recombination lifetime from TPV measurement of the MSC device under various light bias intensities.

and those measured by transient terahertz spectroscopy (*16*), both of which measure band transport mobility. However, ToF and SCLC mobilities are sensitive to the presence of charge traps in the materials. The excellent agreement of Hall mobility with ToF and SCLC mobilities in the single-crystal $MAPbI_3$ devices indicates that the band-tail states in the organolead trihalide perovskite single crystals are negligible.

We measured τ_r in MSCs with transient photovoltaic (TPV) and impedance spectroscopy (IS) at different values of I_L (Fig. 4); at 1 sun, the TPV and IS values of τ_r were 82 ± 5 μs and 95 ± 8 μs, respectively, more than 10 times the τ_r values in the best thin-film devices with sophisticated surface passivation (*10*). Combining the measured mobility and lifetime of MSCs, the hole diffusion length is 175 ± 25 μm under 1 sun. The measured bulk carrier lifetime can be underestimated because of the presence of surface charge recombination, so the bulk carrier diffusion length should exceed this value. Reducing the bias light intensity to 0.1 sun increased τ_r to 234 and 198 μs by TPV and IS measurements, respectively, indicating a longer carrier diffusion length under weaker light intensity.

The long carrier diffusion length of $MAPbI_3$ can find direct application in x-ray and gamma-ray sensing and in radiation energy harvesting. Radiation is generally much weaker than 1 sun but should penetrate the entire device. Details pertaining to the carrier diffusion length extrapolation under weak light, radiation measurement, simulation, and estimation of gammavoltaic efficiency can be found in the supplementary materials. We extrapolated a carrier recombination lifetime of 2.6 ± 0.2 s and carrier diffusion length sum of 33 ± 5 mm under a light intensity of 0.003 mW cm^{-2} from our 1 sun data. The presence of surface recombination should reduce the carrier diffusion length, and the measured >3 mm electron and hole diffusion length under weak light is thus reasonable. We exposed the 3-mm MSC device to intense gamma radiation and measured the electric current generation. A cesium-137 gamma irradiator of 102 Ci yielded a persistent current of 36.3 ± 0.3 nA, which corresponds to a photon-to-electron conversion efficiency of 3.9% and agrees with the theoretic estimation.

The demonstrated high carrier mobility, carrier lifetime, and diffusion length of the MSCs described above point to several new directions for the application of $MAPbI_3$ materials in printable electronics, lasers, and solar cells (*4*). The high PL quantum yield of $MAPbI_3$ and the excellent overlap of the PL spectra with the absorption spectrum of the single crystal allow photon recycling in thick perovskite crystals by reabsorbing the emission (*4*, *5*). The demonstration of a charge diffusion length that greatly exceeds the absorption depth of photons with energy larger than the band gap of perovskites implies that IQEs of essentially 100% can be achieved under the low internal electric fields at device working condition.

REFERENCES AND NOTES

1. S. D. Stranks *et al.*, *Science* **342**, 341–344 (2013).
2. M. M. Lee, J. Teuscher, T. Miyasaka, T. N. Murakami, H. J. Snaith, *Science* **338**, 643–647 (2012).
3. A. Mei *et al.*, *Science* **345**, 295–298 (2014).
4. G. Xing *et al.*, *Nat. Mater.* **13**, 476–480 (2014).
5. Z. K. Tan *et al.*, *Nat. Nanotechnol.* **9**, 687–692 (2014).
6. R. Dong *et al.*, *Adv. Mater.* 10.1002/adma.201405116 (2015).
7. J. Kim, S. H. Lee, J. H. Lee, K. H. Hong, *J. Phys. Chem. Lett.* **5**, 1312–1317 (2014).
8. N. K. Noel *et al.*, *ACS Nano* **8**, 9815–9821 (2014).
9. I. A. Shkrob, T. W. Marin, *J. Phys. Chem. Lett.* **5**, 1066–1071 (2014).
10. Z. Xiao *et al.*, *Adv. Mater.* **26**, 6503–6509 (2014).
11. T. Baikie *et al.*, *J. Mater. Chem. A* **1**, 5628–5641 (2013).
12. J. S. Manser, P. V. Kamat, *Nat. Photonics* **8**, 737–743 (2014).
13. S. D. Stranks *et al.*, *Phys. Rev. A* **2**, 034007 (2014).
14. R. H. Bube, *J. Appl. Phys.* **33**, 1733–1737 (1962).
15. C. C. Stoumpos, C. D. Malliakas, M. G. Kanatzidis, *Inorg. Chem.* **52**, 9019–9038 (2013).
16. C. Wehrenfennig, G. E. Eperon, M. B. Johnston, H. J. Snaith, L. M. Herz, *Adv. Mater.* **26**, 1584–1589 (2014).

ACKNOWLEDGMENTS

Supported by U.S. Department of Energy award DE-EE0006709 (solar cell) and Defense Threat Reduction Agency award HDTRA1-14-1-0030 (radiation detector). J.H. conceived the idea and supervised the project; Q.D. grew the single crystals and fabricated the devices; Q.D., Y.F., and Y.S. conducted the electric and optical characterization of the devices; P.M., J.Q., and L.C. measured the devices under gamma ray irradiation and did the simulation; and J.H. wrote the paper.

SUPPLEMENTARY MATERIALS

www.sciencemag.org/content/347/6225/967/suppl/DC1
Materials and Methods
Figs. S1 to S11
Tables S1 and S2
References (*17*–*21*)

27 December 2014; accepted 20 January 2015
Published online 29 January 2015;
10.1126/science.aaa5760

WATER SPLITTING

Metal-free efficient photocatalyst for stable visible water splitting via a two-electron pathway

Juan Liu,[1] Yang Liu,[1] Naiyun Liu,[1] Yuzhi Han,[1] Xing Zhang,[1] Hui Huang,[1] Yeshayahu Lifshitz,[1,2]* Shuit-Tong Lee,[1]* Jun Zhong,[1] Zhenhui Kang[1]*

The use of solar energy to produce molecular hydrogen and oxygen (H_2 and O_2) from overall water splitting is a promising means of renewable energy storage. In the past 40 years, various inorganic and organic systems have been developed as photocatalysts for water splitting driven by visible light. These photocatalysts, however, still suffer from low quantum efficiency and/or poor stability. We report the design and fabrication of a metal-free carbon nanodot–carbon nitride (C_3N_4) nanocomposite and demonstrate its impressive performance for photocatalytic solar water splitting. We measured quantum efficiencies of 16% for wavelength λ = 420 ± 20 nanometers, 6.29% for λ = 580 ± 15 nanometers, and 4.42% for λ = 600 ± 10 nanometers, and determined an overall solar energy conversion efficiency of 2.0%. The catalyst comprises low-cost, Earth-abundant, environmentally friendly materials and shows excellent stability.

Production of hydrogen and oxygen from water is a promising means of storing solar energy in a way that compensates for the intermittency of sunlight as a primary source of power (*1*, *2*). It can be realized by applying a hybrid system in which a solar cell powers an electrolyzer [photovoltaic (PV) electrolysis]. Photoelectrolysis (PE) uses photocatalyst electrodes with additional electrical power provided by a photovoltaic element. Photocatalysis (PC) involves light-irradiated catalysts (typically catalyst powders suspended in water) for water splitting (*3*). Recently reported "solar-to-hydrogen" (STH) efficiencies for PV electrolysis systems exceed 10% (*4*–*6*). State-of-the-art PE systems yield STH values of 2 to 3% (*7*) but are believed to provide a cheaper solution for H_2 production. PC is the simplest water-splitting approach, more amenable to cheap, large-scale applications of H_2 generation. Unfortunately, despite intense efforts during the past 40 years (*8*–*15*), current direct photocatalysts for water splitting still face several challenging issues: (i) Currently reported catalysts suffer from low quantum efficiency (QE) in the visible range, with STH efficiencies less than 0.1% (*16*–*18*); (ii) many photocatalysts are made of rare and expensive materials; (iii) various photocatalysts show poor stability [e.g., inorganic sulfide and (oxy)nitride-based photocatalysts are less stable and more susceptible to oxidation than water]; (iv) O_2 release from semiconductor catalysts is difficult, so that the use of sacrificial reagents is required; (v) the overall four-electron water oxidation to O_2 encounters a large overpotential; and (vi) the kinetically competing two-electron reaction to H_2O_2 often poisons the photocatalysts (*19*).

Overall water splitting to H_2 and O_2 requires a high free energy of 113.38 kcal/mol (*20*, *21*). The challenge lies mainly in the release of diatomic O_2, which involves four electron and four proton transfers for the eventual formation of an O-O bond. The concerted four-electron process for oxygen evolution (1.23 eV) is thermodynamically more favorable than the two-electron process for H_2O_2 formation (1.78 eV). However, detailed analysis (see supplementary text) shows that a higher reaction rate may be achieved in a system where water is first oxidized via a two-electron reaction to H_2O_2 and H_2, followed by H_2O_2 decomposition to O_2 and H_2O. For this stepwise two-electron/two-electron water splitting to H_2 and O_2 to be viable and practical, the photocatalyst applied should be capable of promoting generation as well as subsequent decomposition of H_2O_2 with high efficiencies and low overpotentials, so as to allow considerable reduction in the energy cost for production of H_2 and O_2 via overall water splitting. Here, we report that nanocomposites of carbon nanodots embedded in a C_3N_4 matrix perform as an excellent photocatalyst fulfilling the above requirements.

C_3N_4 is commercially available (e.g., from Carbodeon) and can be easily fabricated (e.g., from urea) (*19*). It is an Earth-abundant and low-cost photocatalyst capable of generating H_2 and H_2O_2 from water even in the absence of catalytic metals, albeit with a low QE (*19*, *22*–*26*). C_3N_4 belongs to the oldest reported polymer materials prepared by chemists (by Berzelius in ~1830) and first termed "Melon" (*27*). In 2006 it was determined that the visible light activity of TiO_2 after treatment with urea was due to "Melon" (*28*). In 2009, Antonietti and colleagues described in detail the optical properties, electronic structure, and photocatalytic activity of C_3N_4 (*29*). Following this work, many groups attempted to optimize the catalytic properties of C_3N_4, motivated by its relatively low band gap energy E_g of 2.7 eV, and high valence band and conduction band positions (*29*) [1.8 and −0.9 eV versus reversible hydrogen electrode (RHE)]. Many heterojunction composites with oxide semiconductors as well as photocatalyst systems were investigated. The latter included systems with a variety of oxides (*30*) and sulfides (*31*) along with pure metals (*19*) and even graphene (*32*) and carbon nanotubes (*33*). Different preparation methods were studied in an effort to increase the surface area of C_3N_4 and to improve its catalytic activity. The QE values obtained using C_3N_4 as a catalyst for water splitting to H_2 and O_2 have been low (maximum 3.75% at 420 nm and less than 0.5% for 500 nm), and generally the use of a sacrificial reagent has been necessary (*19*, *24*, *26*, *30*–*32*, *34*). The efficiency at 700 nm can be largely increased by applying dye molecules, but again a sacrificial reagent is a must (*35*). During water splitting C_3N_4 suffers from poisoning by the produced H_2O_2, which is difficult to remove from the C_3N_4 surface (*19*). Different methods including stirring, bubbling, and/or addition of chemical agents have been attempted for regeneration of the poisoned C_3N_4 catalyst (*19*).

Carbon nanodots (CDots; monodisperse graphite particles less than 10 nm in diameter) exhibit unique photo-induced electron transfer, photoluminescence, and electron reservoir properties (*36*). In particular, CDots possess high catalytic activity (by chemical catalysis; no light is needed) for H_2O_2 decomposition (*37*). Given the photocatalytic properties of CDots and C_3N_4, we hypothesized that a combination of CDots and C_3N_4 could constitute a high-performance composite photocatalyst for water splitting via the stepwise two-electron/two-electron process: (i) $2H_2O \rightarrow H_2O_2 + H_2$; (ii) $2H_2O_2 \rightarrow 2H_2O + O_2$.

[1]Jiangsu Key Laboratory for Carbon-based Functional Materials and Devices, Institute of Functional Nano and Soft Materials (FUNSOM), Soochow University, Suzhou 215123, China. [2]Department of Materials Science and Engineering, Technion, Israel Institute of Technology, Haifa 3200003, Israel.
*Corresponding authors. E-mail: zhkang@suda.edu.cn (Z.K.); apannale@suda.edu.cn (S.-T.L.); shayli@tx.technion.ac.il (Y.L.)

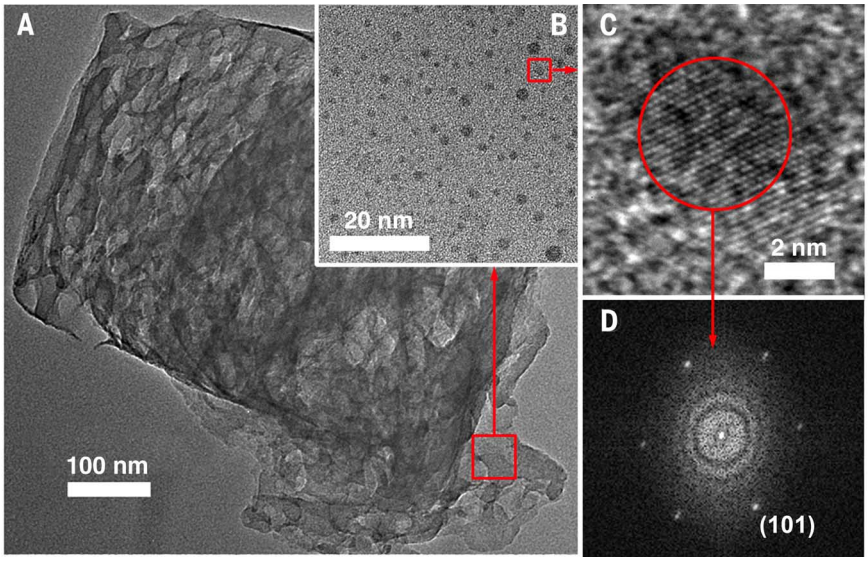

Fig. 1. Characterization of the physical structure of the composite catalyst. (**A**) TEM image of a grain of the CDots-C_3N_4 composite. (**B**) A magnified TEM image of the CDots-C_3N_4 region of (A) marked in red. (**C**) HRTEM image of a single CDot embedded in C_3N_4. (**D**) Corresponding FFT pattern of the crystallite in (C), indicating hexagonal symmetry. In all panels, the CDots concentration of the sample was 1.6 × 10^{-5} $g_{CDots}/g_{catalyst}$.

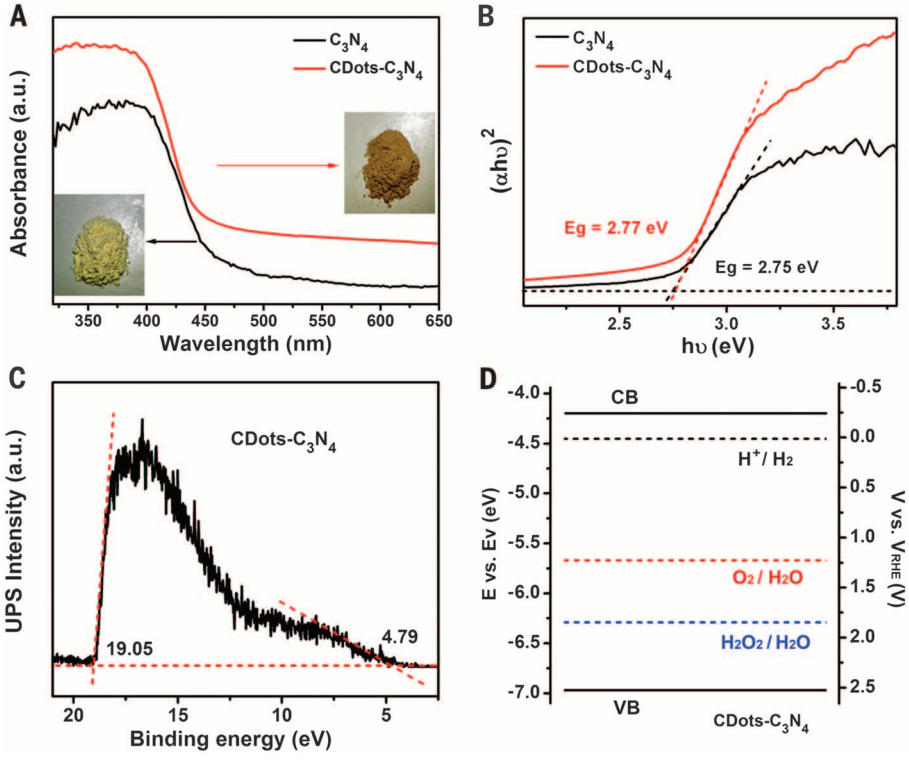

Fig. 2. Characterization of the electronic structure of the composite catalyst. (**A**) UV-vis absorption spectra of C_3N_4 (black curve) and CDots-C_3N_4 (red curve) catalysts. Inset: Digital photograph of catalyst grains. The actual size of the digital photo is 4 cm × 4.3 cm. (**B**) $(\alpha h\nu)^2$ versus $h\nu$ curve of C_3N_4 (black curve) and CDots-C_3N_4 (red curve). The horizontal dashed black line marks the baseline; the other dashed lines are the tangents of the curves. The intersection value is the band gap. (**C**) UPS spectra of CDots-C_3N_4 (black curve). The dashed red lines mark the baseline and the tangents of the curve. The intersections of the tangents with the baseline give the edges of the UPS spectra from which the UPS width is determined. (**D**) Band structure diagram for CDots-C_3N_4. In all panels, the CDots concentration in the CDots-C_3N_4 sample analyzed was 1.6 × 10^{-5} $g_{CDots}/g_{catalyst}$. VB, valence band; CB, conduction band.

CDots were synthesized by a typical electrochemical method followed by hydrothermal treatment with ammonia (*37*). CDots-C_3N_4 composites were then prepared by heating a mixture of ammonia-treated CDots and urea powder at 550°C for 3 hours (see supplementary material). Characterization of the as-produced CDots-C_3N_4 composites by transmission electron microscopy (TEM) showed highly porous grains (Fig. 1A) consisting of CDots (2 to 10 nm in diameter) embedded in a porous C_3N_4 matrix (Fig. 1B). The CDots were nonuniformly distributed, with apparent regions of dots denser by one order of magnitude than the average concentration in the C_3N_4 matrix. A high-resolution TEM (HRTEM) image of a CDot crystallite (Fig. 1C) showed an interplanar spacing of 0.202 nm, which corresponds to the ⟨101⟩ spacing of graphitic carbon. The corresponding 2D fast Fourier transform (FFT) pattern (Fig. 1D) exhibits the hexagonal crystalline structure of the CDots. Linewidth analysis of x-ray powder diffraction patterns (fig. S1) of the grains of the CDots-C_3N_4 composite suggests that the C_3N_4 matrix comprises nanocrystallites with an average diameter of ~4 nm (*29*, *38*, *39*). The diameter of the grains of the CDots-C_3N_4 composite deduced from atomic force microscopy (fig. S2) ranges between 90 and 400 nm (fig. S3).

The incorporation of CDots into the C_3N_4 matrix leads to an increase in the ultraviolet-visible (UV-vis) absorption over the entire wavelength range investigated (Fig. 2A). The optical band gap of a semiconductor can be estimated from the Tauc plot [i.e., the curve of converted $(\alpha h\nu)^r$ versus $h\nu$ from the UV-vis spectrum, in which α, h, and ν are the absorption coefficient, Planck constant, and light frequency, respectively, and r = 2 for a direct band gap material and r = 1/2 for an indirect band gap material]. Figure 2B shows a good linear fit when using r = 2, in accord with previous work (*25*) claiming C_3N_4 to be a direct band gap material (no good linear fit is obtained for r = 1/2). The E_g value of CDots-C_3N_4 (CDots concentration of 1.6 × 10^{-5} $g_{CDots}/g_{catalyst}$) was thus determined to be 2.77 eV by measuring the x-axis intercept of an extrapolated line from the linear regime of the curve (Fig. 2B, red curve), which is almost identical to that of pure C_3N_4 (Fig. 2B, 2.75 eV, black curve) within experimental error. The Tauc plot curve (Fig. 2B, red curve) of CDots-C_3N_4 shows an apparent tail between 2.0 and 2.7 eV, which is helpful for improving the light absorbance and the photocatalytic efficiency. Aside from an appropriate band gap, the proper matching of conduction band and valence band levels of a photocatalyst with the redox potentials of the photocatalytic reactions is also important for water splitting. We used ultraviolet photoelectron spectroscopy (UPS) to determine the ionization potential [equivalent to the valence band energy (E_v)] of CDots-C_3N_4, which was calculated to be 6.96 eV by subtracting the width of the He I UPS spectra (Fig. 2C) from the excitation energy (21.22 eV). The conduction band energy E_c is thus estimated at 4.19 eV from $E_v - E_g$. The E_g, E_v, and E_c values of

CDots-C_3N_4 in electron volts are converted to electrochemical energy potentials in volts according to the reference standard for which 0 V versus RHE (reversible hydrogen electrode) equals −4.44 eV versus evac (vacuum level). Figure 2D further shows that the reduction level for H_2 is positioned below the conduction band of CDots-C_3N_4, and the oxidation level for H_2O to H_2O_2 or O_2 is above the valence band; these bands are properly positioned to permit transfer of electrons and holes, respectively, for water splitting, thus corroborating the potential of CDots-C_3N_4 as a photocatalyst for overall water splitting. Additional characterization of the CDots-C_3N_4 composites included Raman spectroscopy (fig. S4), Fourier transform infrared spectroscopy (FTIR, fig. S5), energy-dispersive spectra (EDS, fig. S6), x-ray photoelectron spectroscopy (XPS, fig. S7), and x-ray absorption near edge structure (XANES, fig. S8).

Figure 3A shows the evolution of H_2 and O_2 from 150 ml of water containing 0.08 g of nonoptimized CDots-C_3N_4 composite under visible light irradiation. H_2 and O_2 were both quantified by gas chromatography (GC); a typical sample curve (GC signal) is shown in fig. S9. H_2 and O_2 evolution proceeded continuously in a molar ratio of H_2/O_2 of 2.02, effectively identical to the theoretical value of 2 for overall water splitting, but ceased immediately when the light was turned off. The constant H_2 evolution rate was ~8.4 μmol/hour and that of O_2 ~4.1 μmol/hour, and no other gases than H_2 and O_2 (e.g., CO_2 or N_2) were detected by GC. Control experiments showed that no O_2 evolution was detected by gas chromatography when pure CDots, pure C_3N_4, or a macroscopic mixture of the two was used as photocatalyst over a 24-hour reaction period. This indicates (see supplementary material) that proximity between the CDots and the generation sites of H_2O_2 (achieved in the composite CDots-C_3N_4 structure) is necessary for the CDots to decompose H_2O_2 and generate O_2.

We further verified that the detected O_2 was indeed generated by water splitting. When we used $H_2{}^{18}O$ as reagent under the same water-splitting conditions described earlier, $^{18}O_2$ (mass 36) was the only product detected by GC-MS (gas chromatography–mass spectrometry). We next measured the QE of overall water splitting by CDots-C_3N_4 as a function of the incident light wavelength λ_0 (Fig. 3B). QE decreased with increasing wavelength, and the longest wavelength capable of inducing water-splitting coincided with the red absorption edge of the CDots-C_3N_4 composite, suggesting the reaction proceeds via photoabsorption by the catalyst. We proceeded to optimize the catalyst composition by measuring QE for different concentrations of CDots in a fixed mass of composite (Fig. 3C). With increasing CDots concentration, the QE increased to a maximum value of 16% around 4.8×10^{-3} $g_{CDots}/g_{catalyst}$, after which it decreased upon addition of more CDots. Next, we optimized the amount of composite catalyst added to water at the optimum CDots/C_3N_4 ratio of 4.8×10^{-3} $g_{CDots}/g_{catalyst}$ (Fig. 3D). We found that the QE increased to a maximum value of 16% as the catalyst was added, and then stayed the same upon further addition.

We interpret the dependence of QE on CDots concentration to an enhancement of the decomposition rate of H_2O_2 until the rate is sufficient to remove all the generated H_2O_2 (by the photocatalytic effect of C_3N_4). Afterward, further increase of the CDots concentration could enhance the light absorption by introducing subband states, thus raising the QE to a maximum, after which addition of more CDots seems to increase energy losses (light absorbed in CDots and not in C_3N_4, e^-/h^+ recombination, lower catalytic efficiency of C_3N_4 due to CDots, etc.), thus decreasing the QE. On the other hand, the initial increase (Fig. 3D) of the composite catalyst load (keeping the CDots concentration constant) increases the generation rate of H_2 (more catalyst → more light absorbance) until reaching a maximum. Additional increase of the composite CDots-C_3N_4 load cannot further increase the light absorbance (all incident light is absorbed), so that the QE remains unchanged (Fig. 3D). We believe that the large values of QE obtained by the CDots-C_3N_4 composite relate to the highly porous structure of the C_3N_4 grains (resulting from the preparation method of the catalyst), which yields a large water-catalyst interface area [97 m^2/g as measured by the Brunauer-Emmett-Teller (BET) method]. Our further studies systematically confirmed that water-splitting photocatalysis by CDots-C_3N_4 indeed proceeds via the stepwise $2e^-/2e^-$ two-step process, in which H_2O oxidation to H_2O_2 is the first and rate-limiting step, followed by the second and fast step of H_2O_2 disproportionation to O_2, which is chemically catalyzed by CDots (detailed experiments and analysis are given in the supplementary material).

The experiments above focused on catalytic properties at λ = 420 nm; however, solar water splitting in the vicinity of the solar spectrum peak (λ = 550 to 650 nm) region is more relevant to efficient harvesting of solar energy. The QE of the standard CDots-C_3N_4 catalyst (i.e., CDots concentration of 1.6×10^{-5} $g_{CDots}/g_{catalyst}$, catalyst load 0.53 g/liter) at λ = 580 nm was relatively low

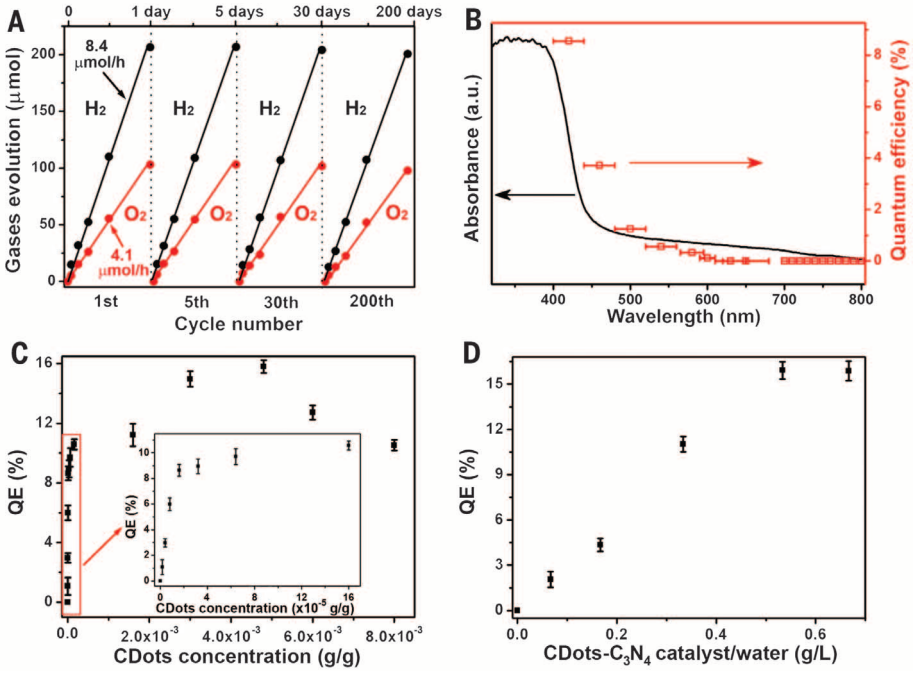

Fig. 3. Photocatalytic water-splitting performance of the composite catalyst. (**A**) Typical time course of H_2 and O_2 production from water under visible light irradiation (by a 300-W Xe lamp using a long-pass cutoff filter allowing λ > 420 nm) catalyzed by CDots-C_3N_4 (CDots concentration, 1.6×10^{-5} $g_{CDots}/g_{catalyst}$). (**B**) Wavelength-dependent QE (red dots) of water splitting by CDots-C_3N_4 (irradiated by a 300-W Xe lamp using a bandpass filter of λ ± 20 nm for 420, 460, 500, 540, and 630 nm; a bandpass filter of λ ± 15 nm for 580 nm; a bandpass filter of λ ± 10 nm for 600 nm; a bandpass filter of λ ± 30 nm for 650 nm; and a long-pass cutoff filter for λ > 700 nm). The UV-vis absorption spectrum (black) of the CDots-C_3N_4 catalyst is superimposed for comparison. The data were derived using a nonoptimized CDots-C_3N_4 catalyst (CDots concentration, 1.6×10^{-5} $g_{CDots}/g_{catalyst}$). (**C**) QE for different concentrations of CDots ($g_{CDots}/g_{catalyst}$) in a fixed mass of composite catalyst. Experimental conditions: 0.080 g of catalyst, 150 ml of ultrapure water, 300-W Xe lamp irradiation for 24 hours with a 420 ± 20 nm bandpass filter. The inset shows an enlarged curve of the low CDots concentration in the region marked in the figure. (**D**) QE for different catalyst loads with a constant CDots concentration of 4.8×10^{-3} $g_{CDots}/g_{catalyst}$) in 150 ml of ultrapure water. The experiments were carried out under the same light irradiation conditions as in (C). For (B), the horizontal bars indicate the width of the wavelength band of the filters used. For (C) and (D), the vertical error bars indicate the maximum and minimum values obtained; the dot represents the average value.

(~0.3%). Upon optimization, we succeeded in preparing catalysts with a high QE = 16% at $\lambda = 420 \pm 20$ nm by increasing the quantity of CDots in the C_3N_4. The higher CDots concentration and the associated larger total C fraction in the composite (Fig. 4A) concurrently increased the absorbance in the solar spectrum peak region (black versus red curve in Fig. 4B). This is most likely due to the effect of C addition leading to the formation of more subband states in the band gap. Figure 4C shows that the H_2 generation rate at our standard conditions (80 mg of catalyst in 150 ml of water; 300-W Xe light radiation with a long-pass cutoff filter allowing $\lambda > 420$ nm) increased by a factor of 5.4 for CDots-C_3N_4 with a higher CDots concentration. The QE of the catalyst with the optimum amount of CDots (4.8×10^{-3} $g_{CDots}/g_{catalyst}$) remarkably increased (Fig. 4D, black) relative to the QE of the catalyst with a CDots concentration of 1.6×10^{-5} $g_{CDots}/g_{catalyst}$ (Fig. 4D, red). It reached 6.29% at $\lambda = 580 \pm 15$ nm (20 times the QE for the 1.6×10^{-5} $g_{CDots}/g_{catalyst}$ catalyst) and 4.42% at $\lambda = 600 \pm 10$ nm. For irradiation wavelengths $\lambda > 650$ nm, both catalyst systems showed zero QE (Fig. 4D).

The solar energy conversion was evaluated in the following studies by using an AM 1.5G (air mass 1.5 global conditions) solar simulator as the light source (see fig. S10 for ~output spectral distribution) and CDots-C_3N_4 (4.8×10^{-3} $g_{CDots}/g_{catalyst}$) as the catalyst (80 mg catalyst in 150 ml of water). After 6 hours of illumination, the total incident power over the irradiation area of 9 cm^2 was 0.63 W, so that the total input energy was 1.36×10^4 J. During the photocatalytic reaction, 1150 μmol of H_2 was detected by GC, which indicated that the energy generated by water splitting is E_F = 274 J. The STH value of CDots-C_3N_4 with the higher concentration of CDots was determined to be 2.0%, which is at least one order of magnitude larger than previously reported values (*40*, *41*). Indeed, the STH values were very low (0.3% for 1.6×10^{-5} $g_{CDots}/g_{catalyst}$) for low CDots concentration and reached 2% only at the optimum CDots concentration (fig. S11). An independent alternative STH calculation based on the CDots-C_3N_4 (4.8×10^{-3} $g_{CDots}/g_{catalyst}$) QE curve (Fig. 4D, black curve) and the spectral irradiance of the AM 1.5G solar simulator (fig. S10) was also carried out, yielding a STH value of 1.78%, in good agreement (89%) with the direct solar simulator value of 2% (see supplementary material for detailed calculations).

A recent work (*40*) claimed a STH efficiency of 5.1% for CoO nanoparticles, but the catalyst system was unstable and corroded after 1 hour of operation. In striking contrast, the CDots-C_3N_4 composite of 1.6×10^{-5} $g_{CDots}/g_{catalyst}$ exhibited long-term stability of at least 200 days for a catalyst dried and reused 200 times (Fig. 3A), whereas the catalyst with the larger CDots concentration of 4.8×10^{-3} $g_{CDots}/g_{catalyst}$ has shown no obvious decay of QE after 50 1-day cycles of reuse (fig. S12). The stability of the CDots-C_3N_4 catalyst system was further studied from several different vantage points: (i) the structural stability of the catalyst over time, (ii) the catalytic functionality (generation rate of H_2 and O_2) over time, (iii) the mass loss or gain after long-term operation, and (iv) the gases released during operation (to detect possible degradation by-products). These factors were probed for two CDots concentrations (1.6×10^{-5} and 4.8×10^{-3} $g_{CDots}/g_{catalyst}$) and two catalyst loads (80 mg/150 ml and 10 mg/150 ml). All photocatalytic water-splitting experiments conducted under different conditions for a variety of reaction times manifested the same H_2 and O_2 generation rates and QEs, within experimental error (Fig. 3A and figs. S12 to S15). These different experiments included (i) 45 days of continuous operation (figs. S13 and S14), (ii) 200 cycles of 24 hours each (Fig. 3A), (iii) 50 cycles of 24 hours each (fig. S12), and (iv) 15 cycles of 24 hours (fig. S15). Raman, FTIR, and XPS spectra (figs. S16 to S18) of CDots-C_3N_4 catalysts before and after 50 24-hour cycled reactions show no obvious differences, confirming the structural stability of the CDots-C_3N_4 catalyst under water-splitting conditions. No CO_2 or N_2 gas could be detected in the reaction system by GC, which suggests that the CDots-C_3N_4 catalyst is stable and did not decompose during the photocatalytic process. There was only negligible mass loss or gain in all the experiments in which the catalyst was weighed before and after use (tables S1 and S2).

A recent U.S. Department of Energy (DOE)–solicited technoeconomical analysis of H_2 generation by solar water splitting (*3*) suggested that PC systems with STH = 5% (not far away from the 2% efficiency reported above) would allow a H_2 production cost of $2.30/kg, which meets the DOE target of $2 to $4/kg H_2. The cheapest PE configuration with STH = 10%, in comparison, allows a H_2 production cost of $5.60/kg H_2, more than twice the cost of the PC system (although the efficiency of the PE system is twice the efficiency of the PC system). The present PC catalyst thus offers a simpler and cheaper approach to extract H_2 from water in large scale. The main disadvantage of PC systems is the generation of a potentially explosive gas mixture of oxygen and hydrogen, which requires separation to ensure safety. Modern industrial technology offers a variety of mature methods for realization of large-scale hydrogen separation and extraction from other gases (nitrogen, argon, oxygen). This point is considered and is part of the above H_2 production cost evaluation of the DOE-solicited work. The separation systems evaluated (*3*) include pressure swing adsorption (PSA), temperature swing adsorption (TSA), palladium membrane separation, nanoporous membrane separation, and electrochemical pumps (*42*).

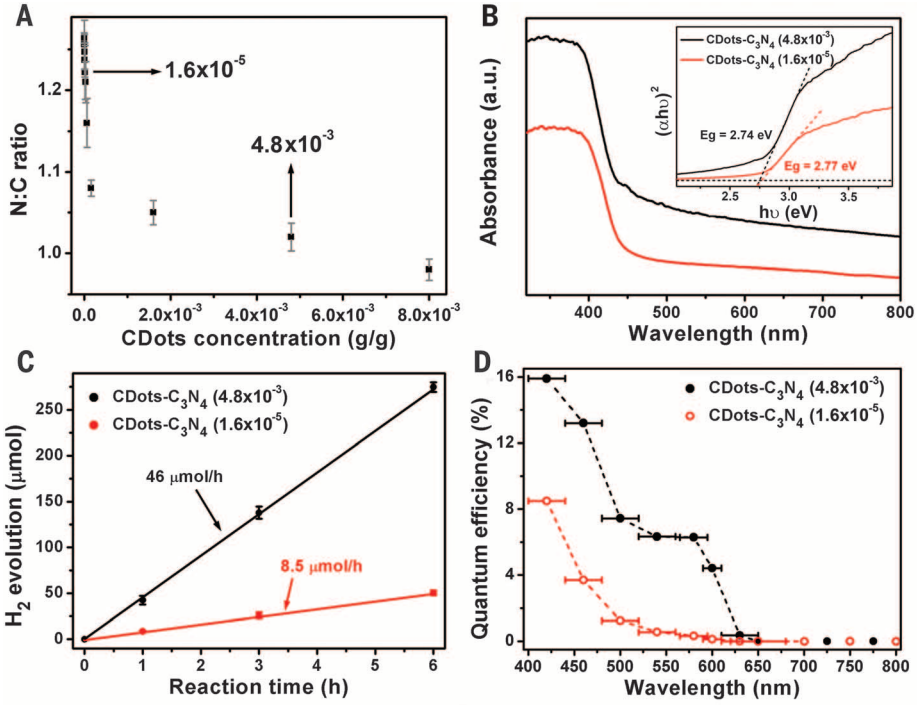

Fig. 4. Catalyst optimization for longer-wavelength absorption. (**A**) Ratio of nitrogen to carbon (N:C) for different concentrations of CDots ($g_{CDots}/g_{catalyst}$) in the composite catalyst from the average value of the EDS test. (**B**) Wavelength-dependent absorbance and derived Tauc plots of two different concentrations of CDots in the CDots-C_3N_4 composite (red: 1.6×10^{-5} $g_{CDots}/g_{catalyst}$; black: 4.8×10^{-3} $g_{CDots}/g_{catalyst}$). (**C**) H_2 generation rate from composites with two different concentrations of CDots (300-W Xe lamp, $\lambda > 420$ nm), showing considerable rate increase for higher CDots concentration. (**D**) Wavelength-dependent QE of water splitting by catalysts with two different concentrations of CDots applying several bandpass filters (for $\lambda < 680$ nm). A long-pass cutoff filter was used to attain $\lambda > 700$ nm light from a 300-W Xe lamp. For (A) and (C), the vertical error bars indicate the maximum and minimum values obtained; the dot represents the average value. For (D), the horizontal bars indicate the width of the wavelength band of the filters used.

The active wavelength region of CDots-C_3N_4, $\lambda < 620$ nm, would allow a theoretical STH efficiency of ~15% for sunlight (AM 1.5G), which thus leaves substantial room for technical optimization. Our catalyst is also mildly active for the overall seawater photocatalytic splitting. Using CDots-C_3N_4 (4.8×10^{-3} $g_{CDots}/g_{catalyst}$) in seawater, we obtained QE (420 nm) of 3.86% and STH = 0.45% (fig. S19). This is a preliminary result, and future studies should probe the reason for the reduction of water-splitting efficiency of sea water versus pure water [QE (420 nm) = 16%, STH = 2%].

We have shown that CDots-C_3N_4 composites can be made of low-cost, environmentally benign materials and can split water into H_2 and O_2 with QEs of 16% for $\lambda = 420 \pm 20$ nm and 6.3% for $\lambda = 580 \pm 15$ nm. The 2.0% STH efficiency obtained is at least one order of magnitude larger than that previously reported for any stable water-splitting photocatalysts (*41*). It is close to 5% STH, which allows achievement of the DOE price target for H_2 generation. In contrast to the conventional one-step four-electron reaction, CDots-C_3N_4 catalyzes water splitting to hydrogen and oxygen via the stepwise two-electron/two-electron two-step pathway under visible light irradiation. C_3N_4 is responsible for the first step (photocatalysis), and CDots are responsible for the second step (chemical catalysis). CDots also increase the light absorbance and thus the values of QE and STH. The composite nature of the catalyst provides sufficient proximity between the H_2O_2 generation sites on the C_3N_4 surface and the Cdots so that H_2O_2 decomposition and O_2 generation in the second stage become efficient. Moreover, CDots-C_3N_4 maintains a high rate of hydrogen and oxygen production (for $\lambda > 420$ nm) with robust stability in 200 runs of recycling use over 200 days. The results demonstrate CDots-C_3N_4 as a highly efficient and stable photocatalyst for visible light–driven water splitting.

REFERENCES AND NOTES

1. A. Kudo, Y. Miseki, *Chem. Soc. Rev.* **38**, 253–278 (2009).
2. A. Iwase, Y. H. Ng, Y. Ishiguro, A. Kudo, R. Amal, *J. Am. Chem. Soc.* **133**, 11054–11057 (2011).
3. B. A. Pinaud *et al.*, *Energy Environ. Sci.* **6**, 1983–2002 (2013).
4. T. J. Jacobsson, V. Fjällström, M. Sahlberg, M. Edoff, T. Edvinsson, *Energy Environ. Sci.* **6**, 3676–3683 (2013).
5. J. Luo *et al.*, *Science* **345**, 1593–1596 (2014).
6. S. Licht, *J. Phys. Chem. B* **105**, 6281–6294 (2001).
7. M. S. Prévot, K. Sivula, *J. Phys. Chem. C* **117**, 17879–17893 (2013).
8. K. Domen, S. Naito, M. Soma, T. Onishi, K. J. Tamaru, *J. Chem. Soc. Chem. Commun.* **12**, 543–544 (1980).
9. A. Kudo, Y. Miseki, *Chem. Soc. Rev.* **38**, 253–278 (2009).
10. W. J. Youngblood, S. H. A. Lee, K. Maeda, T. E. Mallouk, *Acc. Chem. Res.* **42**, 1966–1973 (2009).
11. K. Maeda, K. Domen, *J. Phys. Chem. Lett.* **1**, 2655–2661 (2010).
12. X. Chen, S. Shen, L. Guo, S. S. Mao, *Chem. Rev.* **110**, 6503–6570 (2010).
13. K. Maeda, *ACS Catal.* **3**, 1486–1503 (2013).
14. K. Maeda *et al.*, *J. Phys. Chem. B* **110**, 13753–13758 (2006).
15. K. Maeda *et al.*, *Nature* **440**, 295 (2006).
16. V. Balzani, A. Credi, M. Venturi, *ChemSusChem* **1**, 26–58 (2008).
17. H. B. Gray, *Nat. Chem.* **1**, 7 (2009).
18. I. Tsuji, H. Kato, A. Kudo, *Angew. Chem. Int. Ed.* **44**, 3565–3568 (2005).
19. J. Liu, Y. Zhang, L. Lu, G. Wu, W. Chen, *Chem. Commun.* **48**, 8826–8828 (2012).
20. F. Rappaport, M. Guergova-Kuras, P. J. Nixon, B. A. Diner, J. Lavergne, *Biochemistry* **41**, 8518–8527 (2002).
21. G. Ananyev, G. C. Dismukes, *Photosynth. Res.* **84**, 355–365 (2005).
22. D. J. Martin, P. J. Reardon, S. J. Moniz, J. Tang, *J. Am. Chem. Soc.* **136**, 12568–12571 (2014).
23. F. He *et al.*, *ACS Appl. Mater. Interfaces* **6**, 7171–7179 (2014).
24. X. Zhang *et al.*, *ACS Catal.* **4**, 162–170 (2014).
25. K. Schwinghammer *et al.*, *J. Am. Chem. Soc.* **136**, 1730–1733 (2014).
26. R. Marschall, *Adv. Mater.* **24**, 2421–2440 (2014).
27. J. Liebig, *Ann. Pharm.* **10**, 10 (1834).
28. S. Yin, Y. Aita, M. Komatsu, T. Sato, *J. Eur. Ceram. Soc.* **26**, 2735–2742 (2006).
29. X. Wang *et al.*, *Nat. Mater.* **8**, 76–80 (2009).
30. B. Chai, T. Peng, J. Mao, K. Li, L. Zan, *Phys. Chem. Chem. Phys.* **14**, 16745–16752 (2012).
31. J. Hong, Y. Wang, Y. Wang, W. Zhang, R. Xu, *ChemSusChem* **6**, 2263–2268 (2013).
32. Q. J. Xiang, J. G. Yu, M. Jaroniec, *J. Phys. Chem. C* **115**, 7355–7363 (2011).
33. A. Suryawanshi *et al.*, *Int. J. Hydrogen Energy* **37**, 9584–9589 (2012).
34. S. Yang *et al.*, *Adv. Mater.* **25**, 2452–2456 (2013).
35. L. Yu *et al.*, *Phys. Chem. Chem. Phys.* **16**, 4106–4114 (2014).
36. H. T. Li, Z. H. Kang, Y. Liu, S. T. Lee, *J. Mater. Chem.* **22**, 24230–24253 (2012).
37. H. Ming *et al.*, *Dalton Trans.* **41**, 9526–9531 (2012).
38. X. Wang *et al.*, *J. Am. Chem. Soc.* **131**, 1680–1681 (2009).
39. M. Yang, Q. Huang, X. Q. Jin, *Mater. Sci. Eng. B* **177**, 600–605 (2012).
40. L. Liao *et al.*, *Nat. Nanotechnol.* **9**, 69–73 (2014).
41. S. Mubeen *et al.*, *Nat. Nanotechnol.* **8**, 247–251 (2013).
42. R. W. Baker, *Ind. Eng. Chem. Res.* **41**, 1393–1411 (2002).

ACKNOWLEDGMENTS

We thank A. Rothschild for helpful discussions. We thank Beijing and Shanghai synchrotron radiation facility for XANES and EXAFS data collection. Supported by Collaborative Innovation Center of Suzhou Nano Science and Technology, the National Basic Research Program of China (973 Program) (2012CB825803, 2013CB932702), the National Natural Science Foundation of China (51422207, 51132006, 21471106), the Specialized Research Fund for the Doctoral Program of Higher Education (20123201110018), a Suzhou Planning Project of Science and Technology (ZXG2012028), and a project funded by the Priority Academic Program Development of Jiangsu Higher Education Institutions (PAPD).

SUPPLEMENTARY MATERIALS

www.sciencemag.org/content/347/6225/970/suppl/DC1
Materials and Methods
Figs. S1 to S36
Tables S1 to S3
References (*43*–*54*)

17 November 2014; accepted 26 January 2015
10.1126/science.aaa3145

PLASMA PHYSICS

Stochastic electron acceleration during spontaneous turbulent reconnection in a strong shock wave

Y. Matsumoto,[1]* T. Amano,[2] T. N. Kato,[3] M. Hoshino[2]

Explosive phenomena such as supernova remnant shocks and solar flares have demonstrated evidence for the production of relativistic particles. Interest has therefore been renewed in collisionless shock waves and magnetic reconnection as a means to achieve such energies. Although ions can be energized during such phenomena, the relativistic energy of the electrons remains a puzzle for theory. We present supercomputer simulations showing that efficient electron energization can occur during turbulent magnetic reconnection arising from a strong collisionless shock. Upstream electrons undergo first-order Fermi acceleration by colliding with reconnection jets and magnetic islands, giving rise to a nonthermal relativistic population downstream. These results shed new light on magnetic reconnection as an agent of energy dissipation and particle acceleration in strong shock waves.

The acceleration of charged particles is a fundamental topic in astrophysical, space, and laboratory plasma research. Very high-energy particles are commonly found in astrophysical and planetary shocks (*1*–*3*) and in the energy releases of solar flares and terrestrial substorms (*4*–*7*). Collisionless shock waves and magnetic reconnection, respectively, have been considered to be the ultimate plasma energization mechanisms responsible for relativistic particles found in such phenomena. Although ions can be energized efficiently during the energy conversions, plasma kinetic processes in a localized region must be invoked to explain the observed electron heating and acceleration (*8*–*11*). In this Report, we show that efficient electron energization can occur during turbulent magnetic reconnection that arises over an entire region of a strong shock wave.

Magnetized collisionless shocks are characterized by the Alfvén Mach number M_A, which is the ratio of the flow speed to the Alfvén speed. When the Alfvén Mach number becomes larger than a critical value ($M_A^* \sim 3$), the upstream (low-entropy) plasma cannot be fully dissipated across the shock (*12*). In such supercritical collisionless shocks, ions are partly reflected by the shock front and then counterflow in the upstream region. The motion of these particles serves to dissipate the plasma further by exciting multiple kinetic instabilities (*13*). The reflected ions are the key

[1]Department of Physics, Chiba University 1-33 Yayoi-cho, Inage-ku, Chiba 263-8522, Japan. [2]Department of Earth and Planetary Science, The University of Tokyo, 7-3-1 Hongo, Bunkyo-ku, Tokyo 113-0033, Japan. [3]Center for Computational Astrophysics, National Astronomical Observatory of Japan, 2-21-1 Osawa, Mitaka, Tokyo 181-8588, Japan.
*Corresponding author. E-mail: ymatumot@chiba-u.jp

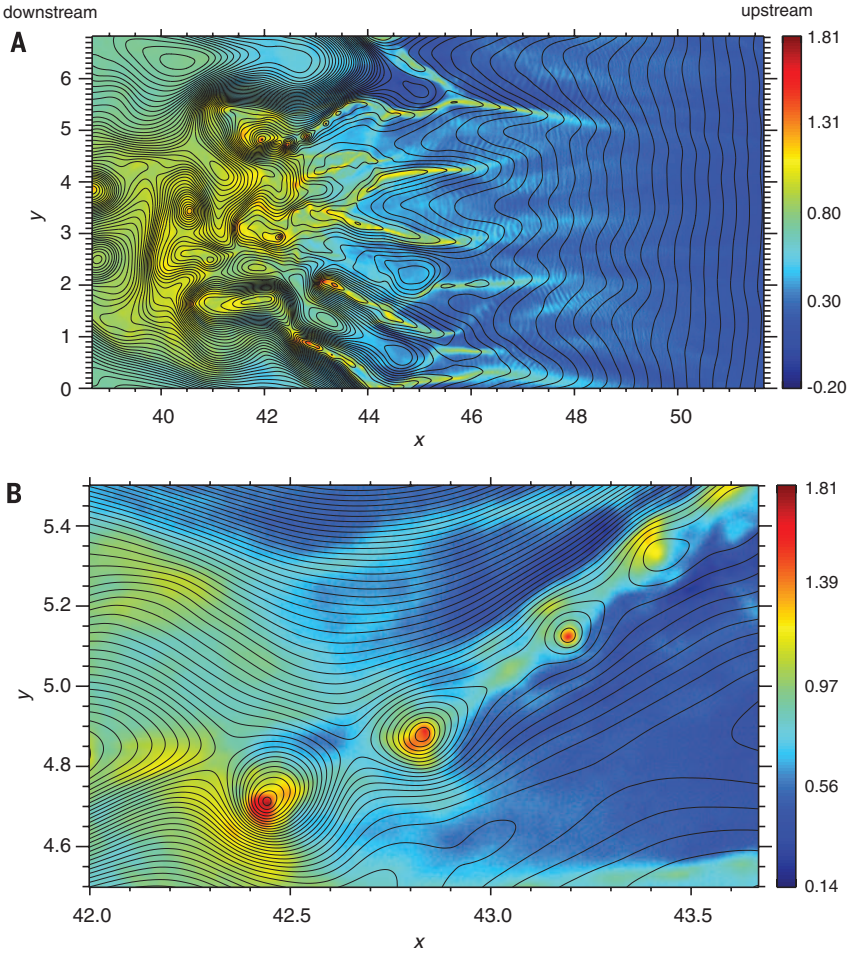

Fig. 1. Supercomputer simulations of a strong collisionless shock revealing spontaneous turbulent reconnection. (**A**) Electron number density profile with magnetic field lines in the *x*-*y* plane (solid line) around the shock front. The *z* component of the vector potential was used to represent the in-plane magnetic field components. Each axis was normalized to the upstream ion inertia length λ_i, and the number density was normalized to the upstream value and color-coded on a logarithmic scale. This snapshot was taken at time $T = 1125\ \Omega_{ge}^{-1}$, where Ω_{ge} is the electron gyro frequency in the upstream region. (**B**) Enlarged view of the region at $42.0 \le x \le 43.7$ and $4.5 \le y \le 5.5$.

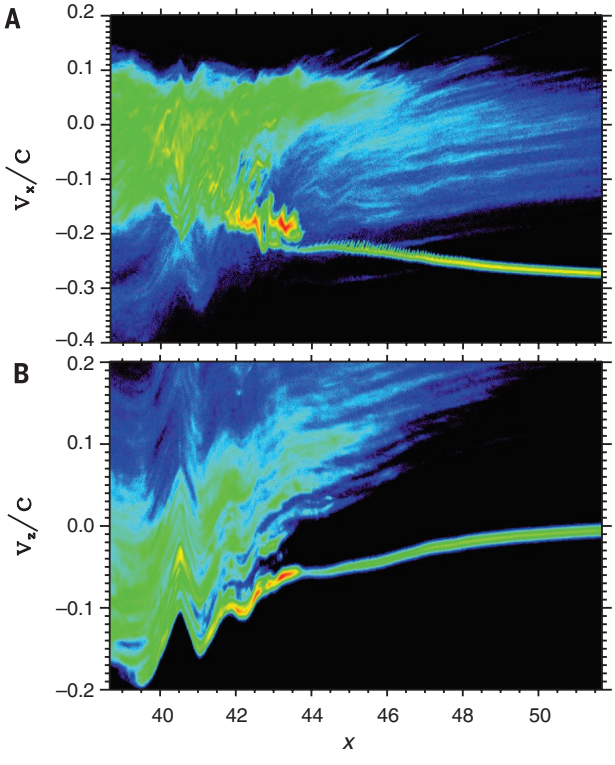

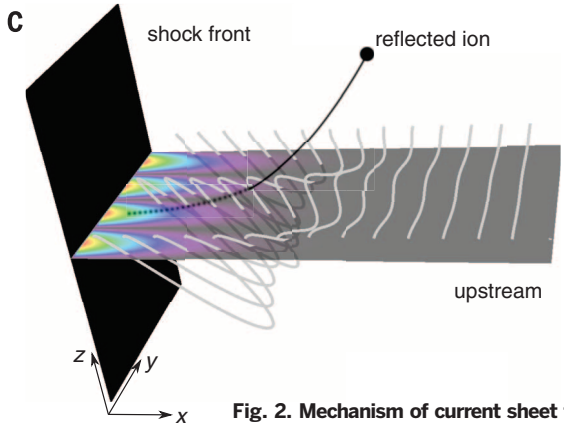

Fig. 2. Mechanism of current sheet formation. (**A**) Ion phase space ($x - v_x$) density around the shock front in the shock-rest frame along $y = 3.4$. The number of particles in each bin is color-coded using a logarithmic scale. The population departing from the shock front ($x \sim 42$) toward the upstream region ($v_x > 0$) is the reflected ions. (**B**) Ion phase space density for v_z, using the same format as in (A). There also exists a large dispersion in the velocity space, owing to the gyrating reflected ions. (**C**) Illustration of the current sheet formation mechanism via the ion beam Weibel instability. The B_x and B_z components of the magnetic field were generated and saturated at amplitudes much larger than the upstream field strength (B_{y0}). Folded field lines in the shock transition region are depicted with gray lines, and the field strength in the *x*-*y* plane is color-coded in arbitrary units.

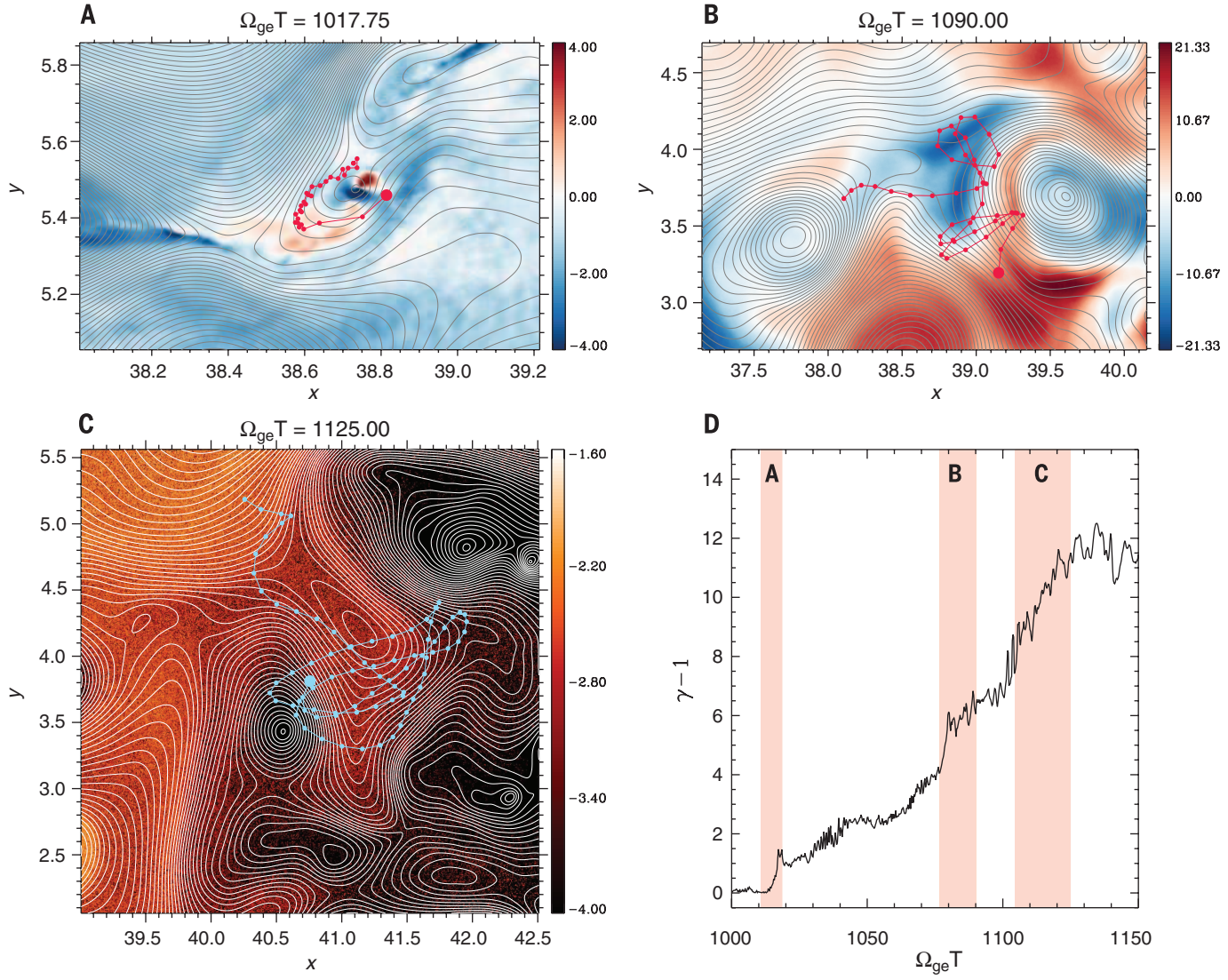

Fig. 3. Electron acceleration from multiple reconnection jets and magnetic islands. (**A**) Accelerated electron's orbit (red) in the *x*-*y* plane. The large red circle denotes the position of the particle at $T = 1017.75\ \Omega_{ge}^{-1}$, following a trajectory back for $7\ \Omega_{ge}^{-1}$ [colored time interval in (D)]. This was superimposed on the magnetic field lines (gray), and the *x* component of $\boldsymbol{E} \times \boldsymbol{B}$ drift speed ($\boldsymbol{V_E} = c\boldsymbol{E} \times \boldsymbol{B}/B^2$) in the shock-rest frame normalized to the local Alfvén speed $V_A = |B|/\sqrt{4\pi Mn}$, where $|B| = 30\ B_0$, $n = 10\ n_0$ were adopted and *M* is the ion mass. (**B**) The particle's orbit with the magnetic field lines at $T = 1090\ \Omega_{ge}^{-1}$. These were superimposed on the *z* component of the magnetic field normalized to the upstream value. (**C**) The number density ratio of the energetic electrons to the local population at $T = 1125\ \Omega_{ge}^{-1}$ in the downstream region. The energetic particle density was calculated for electrons whose energy was larger than a Lorentz factor of $\gamma = 4.5$, which corresponds to the upstream ion kinetic energy. A small value of 10^{-4} was added to the logarithmic representation. The field lines (white) and the particle's orbit (cyan) were superimposed using the same format as in (A) and (B). (**D**) History of an electron's kinetic energy $\gamma - 1$ as a function of time normalized to the upstream electron gyro frequency. The times for which the particle's orbit were drawn in (A) to (C) are indicated by the shaded areas.

to understanding the energy redistribution in supercritical collisionless shocks.

In shocks with sufficiently high Alfvén Mach number (say $M_A > 10$), theoretical works have predicted that electron-scale instabilities can be excited to a large amplitude in the upstream region, and electrons are strongly heated by the resulting electric fields (*14*, *15*). Numerical simulations have not only confirmed this strong heating but have also found electron acceleration mechanisms that produce a long tail in the energy distribution (*8*, *9*, *16*–*18*). The underlying mechanism of the proposed accelerations can be understood from resonant interactions with coherent electrostatic or electromagnetic waves, whereby a charged particle continuously gains energy while it interacts with the same phase of the wave.

We present here a different type of acceleration mechanism by examining computer simulations of a high–Alfvén Mach number collisionless shock. We explored the shock evolution using ab initio particle-in-cell (PIC) simulations in two dimensions. The high computational capability of the K computer at RIKEN helped us to conduct large-scale PIC simulations to reveal electron energizations in multiscale shock structures. To create a collisionless shock, we injected ions and electrons continuously from one boundary on the righthand side of the simulation domain at a supersonic (super-Alvénic) speed toward the other end, where they were reflected back. Therefore, the simulations were conducted in the shock-downstream frame, in which the shock front propagated upstream. In the present case, we dealt with a perpendicular shock in which the

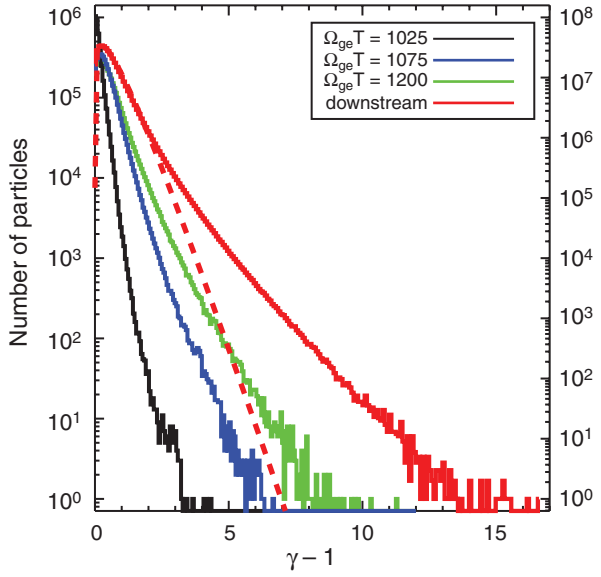

Fig. 4. Energy distribution of the sampled electrons (black, blue, and green) and in the downstream region (red). The temporal evolution is shown for the energy distributions of the sampled electrons taken at different times of 1025 Ω_{ge}^{-1} (black), 1075 Ω_{ge}^{-1} (blue), and 1200 Ω_{ge}^{-1} (green). The energy distribution of particles in the downstream region ($39 < x < 41$) at T = 1125 Ω_{ge}^{-1} refers to the right axis (red).

upstream magnetic field lies in the plane orthogonal to the shock normal. The resulting sonic and Alfvén Mach numbers reached $M_s \sim 45.7$ and $M_A \sim 41.7$, respectively. These very high Mach numbers with a nonrelativistic shock speed (28% of the speed of light c) were achieved by adopting a large ion-to-electron mass ratio of $M/m = 225$ and an upstream electron thermal speed of $v_{the}/c = 7.1 \times 10^{-2}$. The simulation domain size in the x direction was expanded as the shock wave propagated with time. The domain size in the y direction was fixed to 6.8 times the upstream ion inertia length ($L_y = 6.8\ \lambda_i$), using the periodic boundary condition. In the later stages, about 10^{10} particle movements were followed in 24,000 × 2048 computational cells.

Between the upstream region ($x > 51$) and the downstream region ($x < 39$), there is a transition region characterized by tangled magnetic field lines (Fig. 1A). These are so turbulent that the shock front cannot be visibly identified. It is also of interest that filamentary structures are created, as can be seen in the density profile in the transition region. Because these are associated with folded magnetic field lines, the enhanced-density regions contain current sheets. We observe that magnetic reconnection takes place at multiple sites (Fig. 1B), and as a result, magnetic islands are formed along the current sheet. Similar evidence for the magnetic reconnection is found in other current sheets in the transition and the downstream regions.

Figure 2 demonstrates how the current sheets form spontaneously. In the supercritical shock, a portion of the upstream ions (~20%) is reflected specularly by the shock front and gyrates in the transition region (Fig. 2, A and B). The large dispersion both in the x and z (out-of-plane) velocity components between the incident and reflected ions is the free energy for exciting the ion beam Weibel instability (*19*–*23*). This instability, which is destabilized on the ion inertia scale λ_i and has a wave vector perpendicular to the beam direction, is fed by a positive feedback from the perturbed current density in the x and z directions; it then generates the B_x and B_z components of the magnetic field. The amplitude of the generated magnetic fields finally exceeded 20 times the upstream field strength (B_{y0}). Incoming magnetic field lines were strongly deformed through the instability and spontaneously created thin current sheets (filaments) in the transition region (Fig. 2C). Therefore, the number of current sheets corresponds to the mode number of the ion beam Weibel instability in the y direction.

We sampled ~4 ×10^6 electrons in the upstream region at a time T = 900 Ω_{ge}^{-1} (Ω_{ge}, electron gyro frequency in the upstream region) to understand the electron acceleration mechanisms, and their motion was recorded during the simulation runs until they were transmitted downstream. From their orbits, we found that a part of the upstream electrons encountered the reconnection sites. The "luckiest" particle that ultimately acquired the highest energy among the sampled electrons indeed traveled through the reconnection regions many times (Fig. 3 and movie S1). The first major acceleration occurred when it interacted with a reconnection region in the shock transition region. The particle abruptly turned and moved in the opposite direction as it elastically collided with a jet ejected at the local Alfvén speed from the x point (Fig. 3A). Then it passed through the turbulent magnetic field structure. The second major acceleration occurred when the particle skimmed the x point and then experienced collisions with magnetic islands residing in the outflow region (Fig. 3B). A similar process likewise contributed to the energy increase in the downstream region (Fig. 3C). The energy of the particle (Lorentz factor γ) finally reached $\gamma \sim 13$ over a time scale of 100 times the upstream electron gyro period Ω_{ge}^{-1} (Fig. 3D).

The energy history shows that the acceleration mechanism has two components: a rapid acceleration when the particle encounters a jet from the x point, and a gradual increase during collisions with the magnetic islands surrounding the outflow region. The overall process manifests a first-order Fermi acceleration, in which head-on collisions are incurred by multiple reconnection outflows and magnetic islands filled with thermal plasmas (*24*). The acceleration discussed is not found only for this most accelerated particle. Such energetic electrons tend to reside near the x point and between the magnetic islands (Fig. 3C), which indicates that all other relativistic electrons are produced in the same manner as that represented by the particle's orbit.

The accelerated relativistic electrons constitute a high-energy tail in the energy distribution (Fig. 4). In the upstream region, the distribution is very narrow: $\Delta\gamma = 2.5 \times 10^{-3}$, where $\Delta\gamma$ corresponds to the temperature in units of the electron rest mass energy. At the time of the initial major acceleration shown in Fig. 3, a nonthermal component has already appeared, accompanying the hot thermal component. This evolves with time, both increasing the number of nonthermal particles and heating the main thermal component associated with the magnetic field dissipation via turbulent reconnection. In the downstream region, whereas the thermal component fit by a relativistic Maxwellian gave $\Delta\gamma$ = 0.31 (red dashed line), the high-energy tail exceeds three times the upstream ion kinetic energy (γ = 13.5). The number of the energetic particles ($\gamma >$ 4.5) accounts for 0.3% of the total population.

Magnetic reconnection, which has been individually discussed as a plasma energization process in different contexts (*10*, *11*, *24*, *25*), is here revealed as an intrinsic aspect of high–Alfvén Mach number shocks. Reconnection may be triggered if the ion beam Weibel instability generates large-amplitude magnetic fields. The saturation level of the generated field energy $B_{iw}^2/8\pi$, which is about 1% of the ion beam energy (*21*), should be much larger than the upstream magnetic field energy, $B_0^2/8\pi$, in order to generate thin current sheets, i.e.

$$B_{iw} \sim 0.1\sqrt{4\pi\rho_0 V_0^2} \quad (1)$$

where ρ_0 and V_0 denote the upstream (beam) ion mass density and speed, respectively, and

$$B_{iw} \gg B_0 \quad (2)$$

This leads to a condition in terms of the Alfvén Mach number as

$$M_A \gg 10 \quad (3)$$

In three dimensions, shocks satisfying this condition must involve more enhanced magnetic turbulence than we found in our simulations, in which homogeneity in one dimension (the z direction) has been assumed. The acceleration efficiency may be different in three dimensions during turbulent reconnection (*26*). We await the next-generation, exascale computing for verification.

Strong shock waves have been ubiquitously found in space and astrophysical objects; the Alfvén Mach nubmers are usually much higher

than 10 in supernova remnant shocks, and M_A > 20 have been observed at Saturn's bow shock (*3*, *27*). The present results indicate that, in such strong shock waves, the upstream (ion) kinetic energy can be converted to magnetic energy, which will be further dissipated efficiently via turbulent reconnection. The resulting reconnection jets and magnetic islands work as scattering bodies, akin to the role played by Alfvén waves in the cosmic-ray transport theory (*28*, *29*).

REFERENCES AND NOTES

1. A. Bamba, R. Yamazaki, M. Ueno, K. Koyama, *Astrophys. J.* **589**, 827–837 (2003).
2. F. Acero *et al.*, *Astron. Astrophys.* **516**, A62 (2010).
3. A. Masters *et al.*, *Nat. Phys.* **9**, 164–167 (2013).
4. S. Masuda, T. Kosugi, H. Hara, S. Tsuneta, Y. Ogawara, *Nature* **371**, 495–497 (1994).
5. R. P. Lin *et al.*, *Astrophys. J.* **595**, L69–L76 (2003).
6. M. Øieroset, R. P. Lin, T. D. Phan, D. E. Larson, S. D. Bale, *Phys. Rev. Lett.* **89**, 195001 (2002).
7. S. Imada *et al.*, *J. Geophys. Res.* **112**, A03202 (2007).
8. K. G. McClements, M. E. Dieckmann, A. Ynnerman, S. C. Chapman, R. O. Dendy, *Phys. Rev. Lett.* **87**, 255002 (2001).
9. M. Hoshino, N. Shimada, *Astrophys. J.* **572**, 880–887 (2002).
10. J. F. Drake *et al.*, *Science* **299**, 873–877 (2003).
11. J. Egedal, W. Daughton, A. Le, *Nat. Phys.* **8**, 321–324 (2012).
12. M. M. Leroy, *Phys. Fluids* **26**, 2742 (1983).
13. C. Wu *et al.*, *Space Sci. Rev.* **37**, 63 (1984).
14. K. Papadopoulos, *Astrophys. Space Sci.* **144**, 535 (1988).
15. P. J. Cargill, K. Papadopoulos, *Astrophys. J.* **329**, L29 (1988).
16. T. Amano, M. Hoshino, *Astrophys. J.* **690**, 244–251 (2009).
17. M. A. Riquelme, A. Spitkovsky, *Astrophys. J.* **733**, 63 (2011).
18. Y. Matsumoto, T. Amano, M. Hoshino, *Astrophys. J.* **755**, 109 (2012).
19. B. D. Fried, *Phys. Fluids* **2**, 337 (1959).
20. J. T. Frederiksen, C. B. Hededal, T. Haugbølle, Å. Nordlund, *Astrophys. J.* **608**, L13–L16 (2004).
21. T. N. Kato, H. Takabe, *Astrophys. J.* **681**, L93–L96 (2008).
22. T. N. Kato, H. Takabe, *Astrophys. J.* **721**, 828–842 (2010).
23. Y. Matsumoto, T. Amano, M. Hoshino, *Phys. Rev. Lett.* **111**, 215003 (2013).
24. M. Hoshino, *Phys. Rev. Lett.* **108**, 135003 (2012).
25. J. F. Drake, M. Swisdak, H. Che, M. A. Shay, *Nature* **443**, 553–556 (2006).
26. G. Kowal, E. M. de Gouveia Dal Pino, A. Lazarian, *Astrophys. J.* **735**, 102 (2011).
27. A. Masters *et al.*, *J. Geophys. Res.* **116**, A10107 (2011).
28. E. Fermi, *Phys. Rev.* **75**, 1169–1174 (1949).
29. J. Skilling, *Mon. Not. R. Astron. Soc.* **172**, 557–566 (1975).

ACKNOWLEDGMENTS

This research used the computational resources of the K computer provided by the RIKEN Advanced Institute for Computational Science through the High Performance Computing Infrastructure System Research project (project identification nos. hp120222 and hp120287) and was supported in part by a Japan Society for the Promotion of Science KAKENHI Grant-in-Aid for Scientific Research (C) 26400266, Ministry of Education, Culture, Sports, Science and Technology Strategic Programs for Innovative Research and the Joint Institute for Computational Fundamental Science.

SUPPLEMENTARY MATERIALS

www.sciencemag.org/content/347/6225/974/suppl/DC1
Movie S1

19 August 2014; accepted 3 February 2015
10.1126/science.1260168

SURFACE CHEMISTRY

Probing the transition state region in catalytic CO oxidation on Ru

H. Öström,[1] H. Öberg,[1] H. Xin,[2] J. LaRue,[2,3] M. Beye,[2,4] M. Dell'Angela,[5] J. Gladh,[1] M. L. Ng,[2] J. A. Sellberg,[1,2] S. Kaya,[2] G. Mercurio,[5] D. Nordlund,[6] M. Hantschmann,[4] F. Hieke,[5] D. Kühn,[4] W. F. Schlotter,[7] G. L. Dakovski,[7] J. J. Turner,[7] M. P. Minitti,[7] A. Mitra,[7] S. P. Moeller,[7] A. Föhlisch,[4,8] M. Wolf,[9] W. Wurth,[5,10] M. Persson,[11] J. K. Nørskov,[2,3] F. Abild-Pedersen,[2] H. Ogasawara,[6] L. G. M Pettersson,[1] A. Nilsson[1,2,6]*

Femtosecond x-ray laser pulses are used to probe the carbon monoxide (CO) oxidation reaction on ruthenium (Ru) initiated by an optical laser pulse. On a time scale of a few hundred femtoseconds, the optical laser pulse excites motions of CO and oxygen (O) on the surface, allowing the reactants to collide, and, with a transient close to a picosecond (ps), new electronic states appear in the O K-edge x-ray absorption spectrum. Density functional theory calculations indicate that these result from changes in the adsorption site and bond formation between CO and O with a distribution of OC–O bond lengths close to the transition state (TS). After 1 ps, 10% of the CO populate the TS region, which is consistent with predictions based on a quantum oscillator model.

The transition state (TS) is the key to understanding chemical reactivity (*1*). It separates reactants from products, and the free energy required to reach it determines the kinetics of an elementary chemical reaction. Molecules in the TS are hard to capture or observe because the short lifetime leads to a near-zero TS population at steady-state conditions. Ultrafast pump-probe techniques have, however, opened up opportunities for probing molecular structures near the TS region by promoting a sufficient population of molecules to allow detection on short time scales (*1*, *2*). In particular, a number of dissociation and isomerization processes of single molecular units have been probed with visible and infrared laser pulses (*1*). Much of chemistry, however, involves bimolecular reactions where new chemical bonds are formed. Previous pump-probe experiments have been performed in cases where reactants in the gas phase are brought together as a van der Waals complex or in liquid phase reactions between solute and solvent. These experiments could follow the bimolecular reaction dynamics and detect intermediates, but a direct spectroscopic probing of the TS region has proved a challenge (*3*–*5*). We take the next step and probe the TS region through time-resolved snapshots of the valence electronic structure in a surface-catalyzed bimolecular reaction.

A catalyst modifies the TS substantially, opening new reaction pathways that can lead to higher reactivity and selectivity (*6*, *7*). Furthermore, the surface in heterogeneous catalysis and the metal center in homogeneous catalysis both facilitate the reaction by bonding the reacting molecular fragments in close proximity. This opens up the prospect of probing bimolecular reactions on ultrafast time scales where the reacting adsorbed species are present at neighboring sites and are brought to collide rapidly by optical excitation. Optical lasers can drive surface reactions on ultrafast time scales (*8*–*14*) and, in particular, the reaction between adsorbed CO and O to form CO_2 on metal surfaces, which occurs within a few picoseconds (ps) (*11*, *12*, *14*). The ability to probe species on surfaces on ultrafast time scales has recently taken a major leap forward with the development of free-electron x-ray lasers delivering ultrashort pulses combined with atom-specific spectroscopic tools to monitor the electronic structure (*15*–*17*). In a first exploitation of this technique, a short-lived intermediate precursor state was detected in CO desorption from Ru using x-ray emission spectroscopy (XES) and x-ray absorption spectroscopy (XAS) (*16*).

We demonstrate that ultrafast pump-probe x-ray spectroscopy based on the Linac Coherent Light Source (LCLS) x-ray free-electron laser (*18*) can be used to probe the electronic structure of molecular species in the TS region during CO oxidation on a Ru surface. With an optical laser pump pulse, we excited the electrons in the substrate. Subsequent energy transfer to the adsorbate

[1]Department of Physics, AlbaNova University Center, Stockholm University, SE-10691, Sweden. [2]SUNCAT Center for Interface Science and Catalysis, SLAC National Accelerator Laboratory, 2575 Sand Hill Road, Menlo Park, CA 94025, USA. [3]SUNCAT Center for Interface Science and Catalysis, Department of Chemical Engineering, Stanford University, Stanford, CA 95305, USA. [4]Helmholtz Zentrum Berlin für Materialien und Energie GmbH, Albert-Einstein-Strasse 15, D-12489 Berlin, Germany. [5]Physics Department and Center for Free Electron Laser Science, University of Hamburg, Luruper Chausse 149, D-22761 Hamburg, Germany. [6]Stanford Synchrotron Radiation Lightsource, SLAC National Accelerator Laboratory, 2575 Sand Hill Road, Menlo Park, CA 94025, USA. [7]Linac Coherent Light Source, SLAC National Accelerator Laboratory, 2575 Sand Hill Road, Menlo Park, CA 94025, USA. [8]Fakultät für Physik und Astronomie, Universität Potsdam, Karl-Liebknecht-Strasse 24-25, 14476 Potsdam, Germany. [9]Fritz-Haber Institute of the Max-Planck-Society, Faradayweg 4-6, D-14195 Berlin, Germany. [10]Deutsches Elektronen-Synchrotron, Photon Science, Notkestrasse 85, D-22607 Hamburg, Germany. [11]Surface Science Research Centre and Department of Chemistry, The University of Liverpool, Liverpool, L69 3BX, UK.
***Corresponding author. E-mail: nilsson@slac.stanford.edu**

system led to a rapid increase in adsorbate-substrate vibrational excitations, which then drove the CO oxidation reaction on ultrafast time scales. Using O K-edge XAS, we followed the time evolution of the unoccupied valence electronic structure around the adsorbed O and CO in an element-specific way during the oxidation process. Both the O and CO adsorbed species were activated within a few hundred femtoseconds upon laser excitation. This result suggests an ultrafast energy transfer to the adsorbed species from surface electrons excited by the laser pulse. After a delay on the order of 800 fs, new electronic states appeared, indicating the existence of new adsorbed species that do not resemble the separate systems in terms of CO molecules or O atoms adsorbed on the Ru surface. By comparing the experimental data to calculations of XAS spectra, these new resonances are identified as due to CO shifted from on-top toward hollow sites, O from hollow sites toward bridge sites, and the formation of a bond between CO and O that is substantially elongated in comparison to the CO_2 final product. From the computed potential energy surface for the reaction, these fragments can be identified as molecular species being in the TS region while attempting to form CO_2. Based on a simple quantum mechanical picture, we provide a probability analysis that rationalizes the ~10% population of species in the TS region during the first few ps as indicated by the experiment.

The black curve in Fig. 1A shows the initial (t < 0 ps) unpumped XAS O K-edge spectrum of atomic O and CO coadsorbed on Ru(0001) (*17*, *19*). The resonance at 530.8 eV is the signature of the adsorbed O atom as an O 2*p*-Ru 4*d* antibonding state, here denoted O 2*p**, that resides just above the Fermi level (*20*). The spectral feature at 533.8 eV is the 2π* resonance of adsorbed CO (*16*, *21*), and the broad structure at 542 eV is related to adsorbed O as an O 2*p*-Ru 5*sp* shape resonance (*22*).

With a delay of ~1 ps after excitation by a 400-nm laser pulse, the XAS spectrum changed dramatically, as shown in red in Fig. 1A. We observed four distinct major spectral changes with respect to the unpumped spectrum. These changes were visualized in more detail after curve-fitting the pumped spectrum with four new spectral components, together with 90% of the unpumped spectrum; to account for the increased translational, nonreactive motion, the position of the CO 2π* level was let free and shifted to lower energy, similar to the case of pure CO on Ru(0001) after 400-nm laser excitation (*15*). We observed a low-energy component at 529.8 eV in the O-related O 2*p** feature, indicating activation of the O atoms. Additional intensity appeared between the O 2*p** and CO 2π* resonances at 532 eV that was neither present upon laser excitation of CO adsorbed separately on Ru(0001) (*15*) nor seen in spectrum calculations of O displacement toward lower coordination in the coadsorbate system. We saw a shoulder on the high-energy side of the 2π* resonance distinguished more clearly in the curve fitting as a broad resonance at 535.6 eV, and there was additional intensity appearing at higher energies that could be approximated as a broad feature centered at 539 eV. The intensity in this region was fitted with two separate Gaussians in order to incorporate the features predicted from our spectrum calculations.

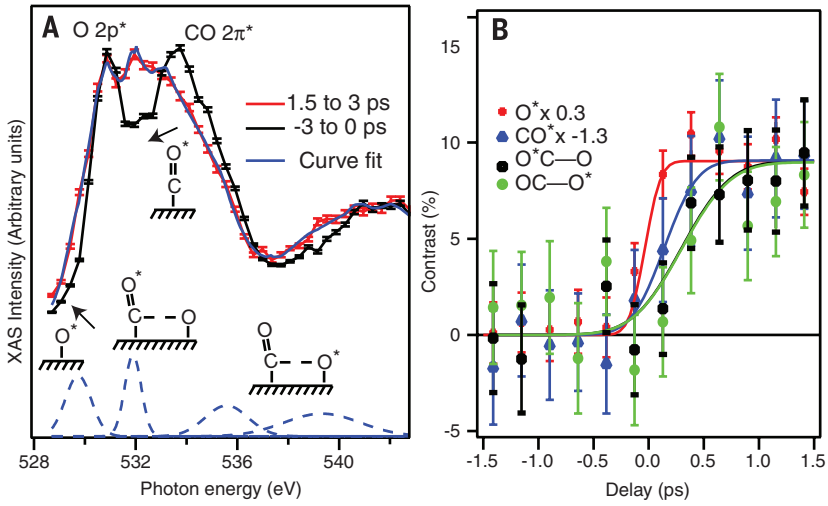

Fig. 1. Measured x-ray absorption spectra with time-dependent changes. (**A**) Pump-probe O K-edge XAS spectrum of CO/O/Ru(0001). The black line and markers show as reference the spectrum averaged over the 3 ps right before the arrival of the pump pulse, and the red line and markers show the spectrum averaged over the interval between 1.5 and 3 ps after the arrival of the laser pump. Averaging is performed to reduce noise. The solid blue line shows a curve fit obtained from a weighted sum of the unpumped XAS spectrum and the four Gaussians plotted with dashed blue lines in the bottom of the figure, with a red shift of the CO 2π* due to external vibrational motion taken into account. The insets schematically depict the microscopic interpretation of the laser-induced spectral changes, and the arrows indicate the direction of spectral shifts as the O and CO species move out from their equilibrium sites. (**B**) Time development of the spectral intensities in four different spectral regions plotted as the contrast [difference between the pumped and unpumped experimental data normalized to the sum of the intensities and scaled to have the same asymptotes (*19*)]. The red dots (O*) show the contrast on the low-energy side of the O 2*p** that corresponds to activation of adsorbed O. Note the very fast (280 fs) change in contrast following the pump laser. The blue triangles (CO*) show the contrast on the CO 2π* resonance, where a negative contrast appears on a 550-fs time scale [reversed in the figure for easy comparison of slopes (*19*)], corresponding to a loss of intensity after laser irradiation due to activation of external vibrations in the adsorbed CO. The black squares (O*C–O) and green circles (OC–O*) show the contrast around the O–CO π* and O–CO σ*, respectively. Both show a transient increase in the contrast on a time scale of 800 fs. The Poisson error bars are shown.

Figure 1B shows the transient changes of these spectral features in terms of delay from the laser pump (*19*). Despite the shot-by-shot statistical uncertainties in the x-ray spectra with spurious effects already before the optical pulse, significant and systematic changes are evident in Fig. 1B. The O 2*p** intensity shows a rapid increase on a 280 ± 100 fs time scale (*19*), which can be regarded as almost instantaneous within our time resolution. This time scale is similar to the thermalization time of femtosecond laser-excited electrons in Ru (*23*), such that both thermalized and nonthermalized electrons may contribute (*8*, *11*). The shift in the CO 2π* occurs on a time scale of 550 ± 120 fs, and the new state between the O 2*p** and CO 2π* appears on the same 800 ± 250 fs time scale as the additional intensity in the region 536 to 539 eV (*19*).

To shed more light on the molecular species that give rise to these additional spectral features, we turn to density functional theory calculations of XAS spectra (*19*, *24*) based on structures found along the minimum energy reaction path. Figure 2A shows the calculated pathway from the initial state (IS), where the CO is adsorbed at an on-top site and O in a hollow site, to the highest TS (TS1), where O and CO have come into chemical contact with the O atom in the bridge site and CO in a near-hollow site with a small 16° tilt from the surface normal. Beyond TS1, we find a rather flat descending region that ends with an abrupt change in energy, giving a small barrier (TS2), which corresponds to a bent, weakly chemisorbed CO_2 species that has a 34° tilt and where, along the CO–O reaction coordinate, there is still a bond elongation in comparison to the expected final state (FS), with CO_2 released into gas phase with substantial kinetic energy (*25*). To analyze the reaction further, we compute the potential of mean force (*16*), including contributions from entropy, as a function of the reaction coordinate. Figure 2A shows that TS1 and TS2 become stabilized relative to the IS at higher temperatures, but otherwise there are no dramatic changes.

Figure 2, B and C, show the calculated O K-edge spectra of O and CO along the reaction path. In Fig. 2C, we observe a red-shifted O 2*p** peak for O in a near–bridge position, which we relate to the intensity at 529.8 eV in the experiment. Focusing

on the changes between IS and TS1, Fig. 2B shows a shift of 1 eV in the CO 2π* position toward lower energy, into the region between the O and CO resonances, where we observed an increase in intensity in the experimental data. Such a shift has been established previously for CO on Ni(100), where coadsorbed hydrogen generates a mixed on-top and hollow phase where the experimental XAS spectrum shows a shift of 2 eV between the two adsorption sites (*26*). This result is similar to the O 1*s* binding energy shift observed with x-ray photoelectron spectroscopy (*27*). The computed shift is consistent with the present experimental data but seems to be underestimated. The CO 2π* shift is similar for TS2. We denote this spectral component O*C–O, because it is the O atom in the CO molecule that mostly contributes the spectral intensity.

In TS1, a weak OC–O bond is formed with an elongated bond distance of 1.7 Å, compared with 1.2 Å in the CO_2 molecule. The sigma bond within a molecule gives rise to an antibonding shape resonance whose energy position is sensitive to the bond length (*28*). In Fig. 2C, we note that the computed OC–O* shape resonance, mostly located on the O atom, is at 535.5 eV, which nicely corresponds to the intensity appearing on the high-energy side of the CO 2π* resonance after the laser pump. Figure 2C shows that this resonance shifts to higher energy at 540 eV in the TS2 state because of a shorter OC–O bond length. There is not much contribution in the pumped experimental data at 540 eV indicating less population of TS2, but, as discussed above, there is substantial intensity around 538 to 539 eV indicating species with bond lengths between TS1 and TS2. Figure 2D shows a nearly linear dependence between bond length and resonance position in the computed OC–O shape resonance energy position until the bond length becomes similar to the other internal C–O bond and the two resonances delocalize (*28*), as seen in CO_2. Because the pumped spectra from Fig. 1 can be fit with two broad OC–O resonances, there are species of various bond lengths contributing to the experimental data. This corresponds to the population of several points around TS1 and on the path toward TS2 as the activated species undergo several attempts to react, where the majority does not pass over the barrier, however, but dissociate back to O and CO.

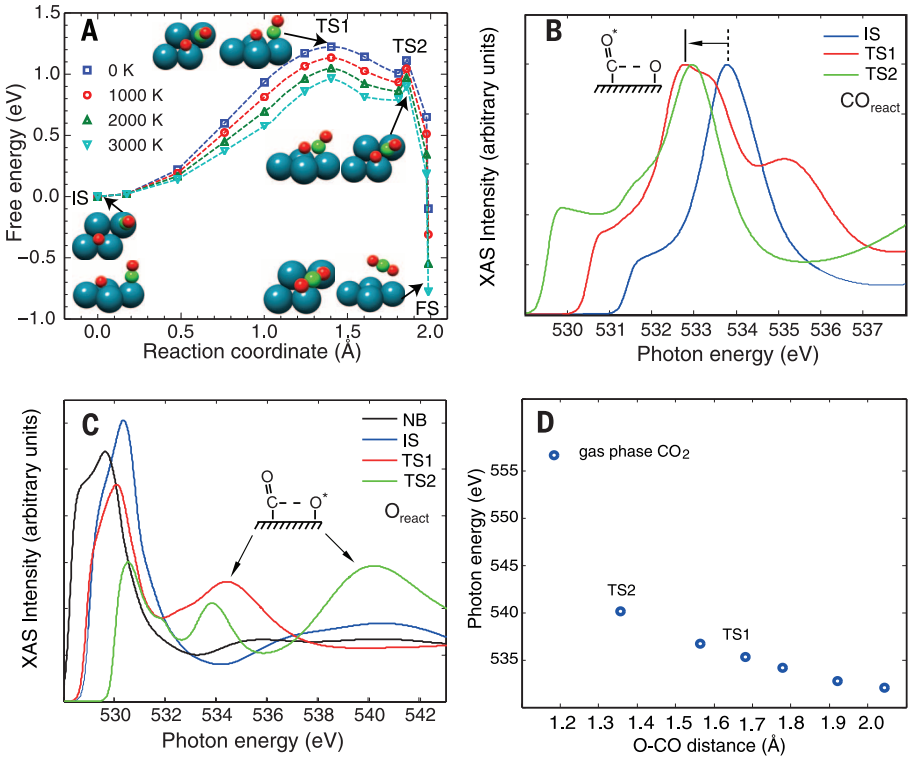

Fig. 2. Computed reaction path and x-ray spectra. (**A**) The free energy for CO oxidation on Ru(0001) at 0 K (minimum energy path), 1000 K, 2000 K, and 3000 K. To put the initial state (IS) structure at the origin, the reaction coordinate is defined as $d_{O\text{-}CO}(IS) - d_{O\text{-}CO}(X)$, where $d_{O\text{-}CO}$ is the distance between the reacting O atom and the C atom in the adsorbed CO molecule, and X is the position along the reaction path, from the IS to the final state (FS). The surface structures (top and side view) of the IS, TS1, TS2, and FS are shown. (**B** and **C**) Computed XAS O K-edge spectra of selected geometries projected on the reacting CO (B) or O (C). In (C), the XAS spectrum for a separate configuration denoted NB (near-bridge) in which atomic O is situated close to a bridge site in the coadsorbate system is also shown. (**D**) The computed energy of the shape resonance (see Fig. 2C, where it is mainly located on the O atom at ~540 eV in TS2) arising from OC–O bond formation is plotted against the OC–O bond length for a number of different geometries along the reaction path. The linear trend is broken as the resonance position of gas phase CO_2 is included at ~557 eV.

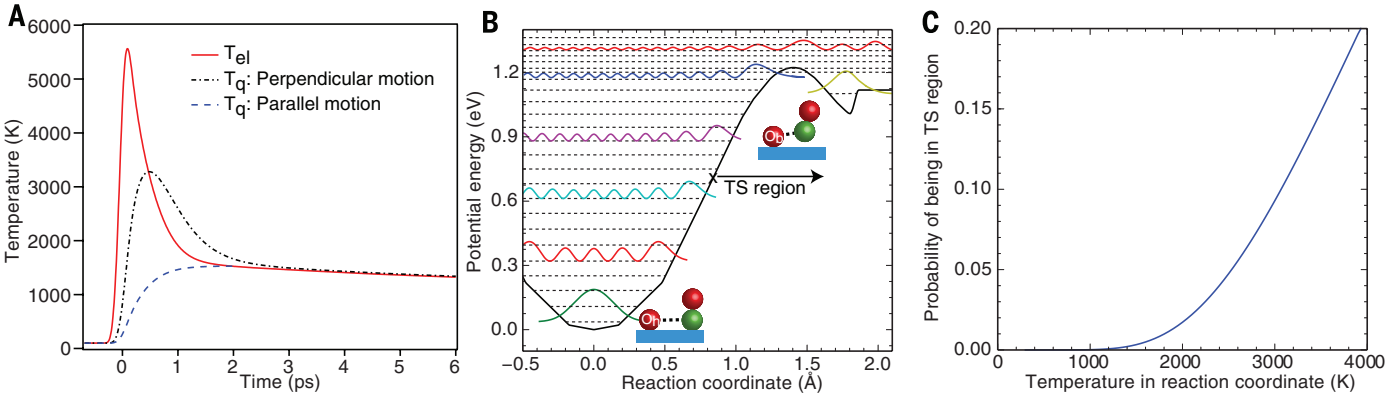

Fig. 3. Time evolution of the temperature and probability analysis for forming O–CO near-TS complexes on Ru(0001). (**A**) Based on the two-temperature model and ab initio electronic friction of O atoms on Ru(0001) (*19*), the peak values of the adsorbate temperature in the relevant O–Ru vibrational modes perpendicular and parallel to the surface are estimated to be 1500 to 3300 K in the time range between 0.5 and 3 ps after the laser excitation. (**B**) Minimum energy path for CO oxidation where the left side, approaching a different O atom, is not shown for simplicity (*19*). Dashed lines are energy eigenvalues, and solid lines represent the corresponding probability density distribution at selected energy levels. The TS region is defined from the inflection point (arrow) of the minimum energy path out to 2 Å. (**C**) Probability of finding O–CO complexes within the TS region as a function of the adsorbate temperature in the reaction coordinate. The peak values of the adsorbate temperature lead to a potential population of the TS region of up to ~10%.

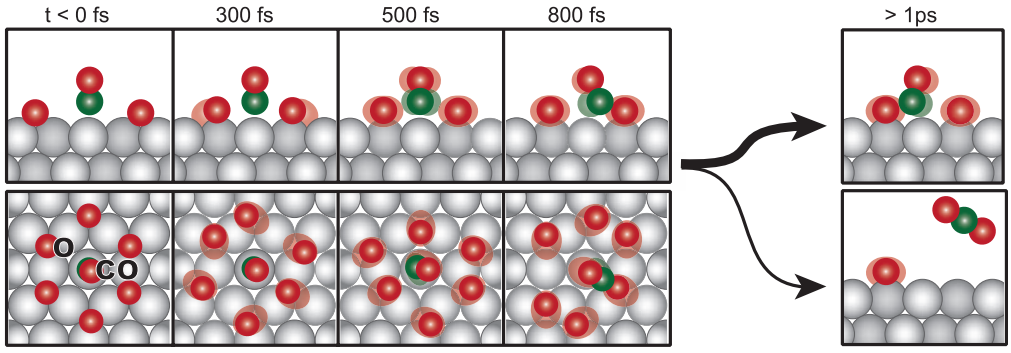

Fig. 4. Pictorial side and top views of the reaction sequence with the corresponding time scales for oxygen activation, CO translation, collisions that lead to form the TS and either dissociation back to reactants and further collisions into the TS or, with lower probability, to the final CO_2 reaction product.

Let us now address the transient populations as a function of delay time between the optical and x-ray laser pulses. Within the time resolution of the experiment, Fig. 1B shows an almost instantaneous O 1*s* shift to lower energy consistent with O moving from the hollow site toward the bridge site (Fig. 2C). The activation of CO is somewhat slower, where the 500 fs transient is within the time resolution of previous measurements of pure CO on Ru(0001) (*15*). These studies concluded that excitation of frustrated rotations (*29*) leads to translational motion on the surface (*15*).

Femtosecond laser-induced reactions are typically explained in terms of photoexcitation of substrate electrons leading to thermalized electrons at a high temperature and subsequent heating of the substrate phonons (Fig. 3A), which on ruthenium takes place on a time scale of ~1 to 2 ps (*13*). The reaction is thus driven via energy transfer from the electron or phonon systems to the adsorbates. The observed subpicosecond time scale is consistent with a dominating excitation process involving electrons in the substrate (*13*, *15*, *30*), with weaker coupling for the CO molecule than for O, leading to a slower response. The spectral changes associated with TS1 and the region between TS1 and TS2 in terms of the O*C–O and OC–O* resonances both have the same transient of 800 fs, suggesting a population of the same class of configurations. These spectral components reach a maximum in intensity after around 1 ps, as shown in Fig. 1B. Because most of the energy to reach the TS is related to the activation of the oxygen atom, we followed the contrast at the low-energy side of the spectra that decays on a time scale of a few ps (*19*). This indicates vibrationally excited atomic motions as in a thermal process, making the species undergo several attempts to react. The two broad overlapping components between 535 and 541 eV in the fit of the experimental spectrum indicate that there is a distribution of transient species of various OC–O bond lengths. This is further corroborated by the rather constant intensity of all observed transient species between 1 and 3 ps.

In the fit of the experimental data in Fig. 1A, there is roughly a 10% population of species in the TS region between 1.5 and 3 ps. Figure 3 demonstrates that this is consistent with a sufficiently highly excited vibrational state. Figure 3B shows the vibrational wave function probability distribution for different quantum states in the CO and O potential well up to TS1 from Fig. 2A. Highly excited vibrational states clearly have large amplitude at the turning points where, in a classical picture, the motion slows down. We estimate the probability (*19*) of finding O and CO in the CO_2 TS region as indicated in Fig. 3B based on an elevated adsorbate temperature obtained from ultrafast energy transfer from transiently excited substrate electrons (*19*). With an estimated peak adsorbate temperature of 1500 to 3300 K (Fig. 3A), we find a transient population of the TS region up to ~10% (Fig. 3C). The majority of these species are reflected back to O and CO at the barrier but still have a significant probability of populating the vicinity of the classical turning point in the TS region. We note that CO_2 molecules formed from reactants passing over the barrier are expected to desorb with excess translational energy from a hot state rather than forming an intermediate chemisorbed state (*25*). The origin of the low transmission coefficient over the barrier to the CO_2 final product is an open question where friction leading to nonadiabatic processes could play an important role and will require further theoretical work.

From the above observations, we summarize the findings based on a simple picture as depicted in Fig. 4. The O becomes activated with motions parallel to the surface on a time scale below 300 fs, whereas CO is activated on a 500-fs time scale. They will start to collide on the surface because the CO is caged by O atoms in neighboring sites in the coadsorbed honeycomb structure (*19*). These collisions generate a transient population of species around the TS region that appears on time scales slightly longer than the initial motion of the CO and O species. Most collisions lead to dissociation back to CO and O, with subsequent further collisions into TS, and only a small fraction of the events result in the formation of CO_2 as seen in the low reaction yield (*11*).

We thus experimentally observe species near and beyond the rate-determining barrier at TS1, i.e., also in the rather flat region between TS1 and TS2, as shown in Fig. 2A. Although unexpected, this is not surprising given that, both classically and quantum mechanically, transit over a potential energy barrier entails a deceleration as kinetic energy is converted to potential energy. The ability to probe transient species close to the TS opens completely new insights into the electronic states of reacting molecules at surfaces, and it provides theory with an unprecedented benchmark in the description of surface-catalyzed processes. We anticipate that this will provide an essential tool to underpin our fundamental understanding of surface chemical processes in heterogeneous catalysis.

REFERENCES AND NOTES

1. J. C. Polanyi, A. H. Zewail, *Acc. Chem. Res.* **28**, 119–132 (1995).
2. A. Stolow, A. E. Bragg, D. M. Neumark, *Chem. Rev.* **104**, 1719–1758 (2004).
3. P. I. Ionov, S. I. Ionov, C. Wittig, *J. Chem. Phys.* **107**, 9457–9463 (1997).
4. A. J. Orr-Ewing, *J. Chem. Phys.* **140**, 090901 (2014).
5. N. F. Scherer, C. Sipes, R. B. Bernstein, A. H. Zewail, *J. Chem. Phys.* **92**, 5239–5259 (1990).
6. G. Ertl, *Reactions at Solid Surfaces* (Wiley, Hoboken, NJ, 2009).
7. J. K. Nørskov, F. Studt, F. Abild-Pedersen, T. Bligaard, *Fundamental Concepts in Heterogeneous Catalysis* (Wiley, 2014).
8. H. Petek, *J. Chem. Phys.* **137**, 091704 (2012).
9. J. A. Prybyla, T. F. Heinz, J. A. Misewich, M. M. T. Loy, J. H. Glownia, *Phys. Rev. Lett.* **64**, 1537–1540 (1990).
10. F. Kao, D. G. Busch, D. Cohen, D. Gomes da Costa, W. Ho, *Phys. Rev. Lett.* **71**, 2094–2097 (1993).
11. T.-H. Her, R. J. Finlay, C. Wu, E. Mazur, *J. Chem. Phys.* **108**, 8595 (1998).
12. M. Bonn *et al.*, *Science* **285**, 1042–1045 (1999).
13. C. Frischkorn, M. Wolf, *Chem. Rev.* **106**, 4207–4233 (2006).
14. P. Szymanski, A. L. Harris, N. Camillone III, *J. Phys. Chem. C* **112**, 15802–15808 (2008).
15. M. Beye *et al.*, *Phys. Rev. Lett.* **110**, 186101 (2013).
16. M. Dell'Angela *et al.*, *Science* **339**, 1302–1305 (2013).
17. T. Katayama *et al.*, *J. El. Spec. Rel. Phen.* **187**, 9–14 (2013).
18. W. F. Schlotter *et al.*, *Rev. Sci. Instrum.* **83**, 043107 (2012).
19. Details of the materials and methods, and supporting analysis of the experimental and theoretical data, are available as supplementary materials at *Science* Online.
20. A. Nilsson *et al.*, *Catal. Lett.* **100**, 111–114 (2005).
21. C. Keller *et al.*, *Phys. Rev. B* **57**, 11951–11954 (1998).
22. E. O. F. Zdansky *et al.*, *Phys. Rev. B* **48**, 2632–2641 (1993).
23. M. Lisowski *et al.*, *Appl. Phys., A Mater. Sci. Process.* **78**, 165–176 (2004).
24. L. Triguero, L. G. M. Pettersson, H. Ågren, *Phys. Rev. B* **58**, 8097–8110 (1998).
25. C. Hess *et al.*, *Appl. Phys., A Mater. Sci. Process.* **71**, 477–483 (2000).
26. H. Tillborg, A. Nilsson, N. Mårtensson, J. N. Andersen, *Phys. Rev. B* **47**, 1699–1702 (1993).
27. H. Tillborg, A. Nilsson, N. Mårtensson, *Surf. Sci.* **273**, 47–60 (1992).
28. J. Stöhr, *NEXAFS Spectroscopy*, G. Ertl, R. Gomer, D. L. Mills, Eds., Springer Series in Surface Science (Springer-Verlag, Berlin-Heidelberg, 1992).
29. M. Bonn *et al.*, *Phys. Rev. Lett.* **84**, 4653–4656 (2000).
30. A. C. Luntz, in *Chemical Bonding at Surfaces and Interfaces*, A. Nilsson, L. G. M. Pettersson, J. K. Nørskov, Eds. (Elsevier, 2008).

ACKNOWLEDGMENTS

This work is supported by the U.S. Department of Energy, Basic Energy Science through the SUNCAT Center for Interface Science and Catalysis, the Swedish Research Council,

the Knut and Alice Wallenberg foundation, the U.S. Department of Energy through the SLAC Laboratory Directed Research and Development program under contract DE-AC02-76SF00515, the Volkswagen Stiftung, and the Deutsche Forschungsgemeinschaft within the excellence cluster "Center for Ultrafast Imaging (CUI)." The spectrum calculations were performed on resources provided by the Swedish National Infrastructure for Computing (SNIC) at the HPC2N center. Portions of this research were carried out on the SXR Instrument at the Linac Coherent Light Source (LCLS), a division of SLAC National Accelerator Laboratory, and an Office of Science user facility operated by Stanford University for the U.S. Department of Energy. The SXR Instrument is funded by a consortium whose membership includes the LCLS, Stanford University through the Stanford Institute for Materials Energy Sciences (SIMES), Lawrence Berkeley National Laboratory (LBNL), University of Hamburg through the Bundesministerium für Bildung, Wissenschaft, Forschung und Technologie priority program FSP 301, and the Center for Free Electron Laser Science (CFEL). The experimental and theoretical data are available in the supplementary materials.

SUPPLEMENTARY MATERIALS

www.sciencemag.org/content/347/6225/978/suppl/DC1
Materials and Methods
Figs. S1 to S7
Table S1
Structures and Data
References (*31*–*46*)

26 September 2014; accepted 28 January 2015
Published online 12 February 2015;
10.1126/science.1261747

ACTUATING MATERIALS

Voxelated liquid crystal elastomers

Taylor H. Ware,[1,2] Michael E. McConney,[1] Jeong Jae Wie,[1,2] Vincent P. Tondiglia,[1,3] Timothy J. White[1]*

Dynamic control of shape can bring multifunctionality to devices. Soft materials capable of programmable shape change require localized control of the magnitude and directionality of a mechanical response. We report the preparation of soft, ordered materials referred to as liquid crystal elastomers. The direction of molecular order, known as the director, is written within local volume elements (voxels) as small as 0.0005 cubic millimeters. Locally, the director controls the inherent mechanical response (55% strain) within the material. In monoliths with spatially patterned director, thermal or chemical stimuli transform flat sheets into three-dimensional objects through controlled bending and stretching. The programmable mechanical response of these materials could yield monolithic multifunctional devices or serve as reconfigurable substrates for flexible devices in aerospace, medicine, or consumer goods.

The dexterity, reversibility, and reconfigurability of complex shape or surface adaptivity within soft materials may enable enhancement and miniaturization of devices in medicine, robotics, and aerospace (*1*). Complex shape change and actuation has been reported in patterned hydrogels and through mechanical programming of carefully designed semicrystalline polymer networks (*2*, *3*). The implementation of programmable shape change in applications in aerospace and other outlets requires the further development of soft materials that exhibit large stimuli-induced responses while affording local control of the magnitudes and directionality of the strain. Once realized, these shape-programmable materials could enable and extend the functionality of devices in applications from as simple as packaging to as complex as deployable and tunable antennas.

Liquid crystal elastomers (LCEs) are lightly cross-linked, ordered polymers that exhibit a reversible shape change in response to heat, light, or solvent. The alignment of LCEs into so-called monodomain or single-crystal orientations has primarily used stretching [analogous to the training of shape memory metals (*4*)] or magnetic fields. Uniaxially aligned LCEs exhibit dimensional changes (tensile strain) that can exceed 300% along the alignment direction in response to temperature changes (*5*). However, these alignment methods are limited in spatial control of orientation as well as resolution. Complex director profiles within LCEs are necessary to realize monolithic devices or functional substrates capable of nontrivial, programmable, reversible shape change (*6*–*8*). Such methods exist and have been used to generate complex and spatial variations in the director orientations of low-molar-mass liquid crystals as well as glassy liquid crystalline polymer networks (*9*, *10*). However, the materials chemistries and procedures used to synthesize aligned LCEs have proven insensitive to these techniques. Here, we report on the development of a facile materials chemistry platform that is conducive to the surface alignment of liquid crystals. The sensitivity of the materials chemistry to surface alignment is combined with photoalignment of volumetric elements (also known as "voxels") containing discrete domains of aligned LCEs. Enabled by the large strain inherent to LCEs, the sensitivity of the materials chemistry to surface alignment, and the optical patterning methods, we demonstrate programmable shape change and actuation in monolithic elements derived from a variety of complex director profiles.

To prepare spatially heterogeneous LCEs, we developed an optical patterning system in which

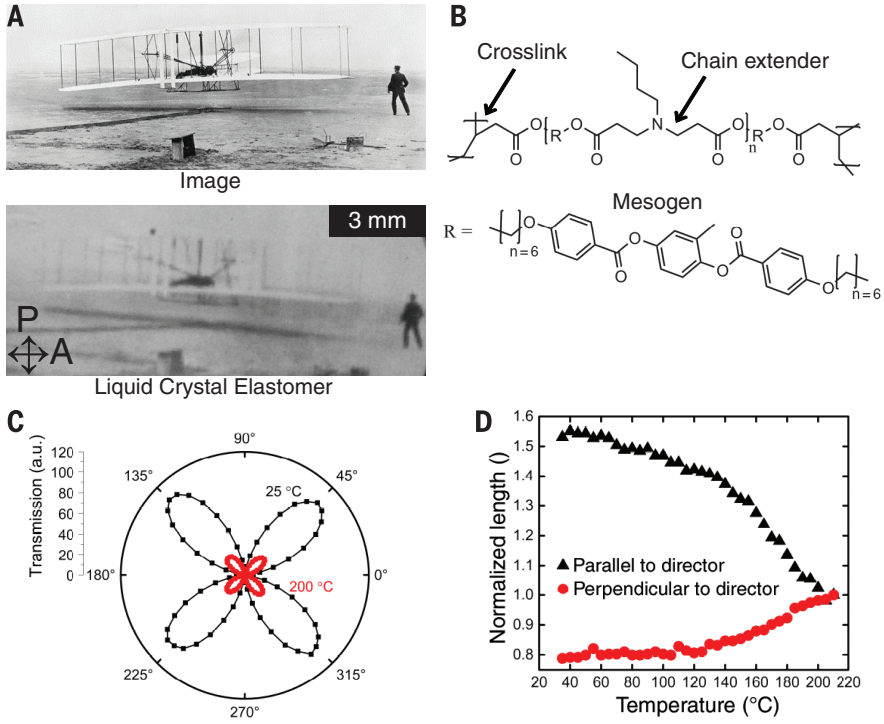

Fig. 1. Digital patterning of LCEs. (**A**) Liquid crystals can be aligned point-by-point by altering surface conditions. (Top) An image (*29*) is digitized, and the grayscale value is converted to an alignment condition. Between crossed polarizers, the programmed optical rotation of the liquid crystal introduces light and dark regions. (**B**) Schematic of chemical structure of the main-chain LCE that can be surface-aligned. (**C**) Transmission of light through an LCE between crossed polarizers in the room-temperature nematic state and high-temperature paranematic state. (**D**) Biaxial actuation of homogeneously aligned LCE in the absence of mechanical load.

[1]Air Force Research Laboratory, Materials and Manufacturing Directorate, Wright-Patterson Air Force Base, OH, USA. [2]Azimuth Corporation, Dayton, OH, USA. [3]Leidos, Dayton, OH, USA.
***Corresponding author. E-mail: timothy.white.24@us.af.mil**

the polarization of an irradiating 445-nm laser is dynamically controlled over an area as small as 0.01 mm^2 (fig. S1). The optical setup was purposed to manipulate the local surface alignment of liquid crystalline cells prepared with commercially available, azobenzene-based photoalignment materials. The azobenzene dyes in the photoalignment material orient normal to the electric field vector of the linearly polarized light. Upon filling the cell with a nematic mixture of monomers, the director of the liquid crystal aligns to the local surface orientation of the photoalignment layer, which is translated through the sample thickness. Arbitrary and spatially complex patterns can be written into alignment cells with the system described in fig. S1 as illustrated in Fig. 1A, which presents a patterned liquid crystal cell that replicates the grayscale image of the first powered flight of the Wright brothers. The grayscale pixel values of the image are converted to the orientation angle of the surface-alignment pixels between 0° (dark) and 45° (bright). Upon filling the cell, the liquid crystalline monomers interact with the orientation of the pixelated surface-alignment layer to form oriented voxels. After polymerization, the grayscale image is retained and visible between crossed polarizers. In this example, 226 distinct director orientations are patterned into 21,350 voxels of material, each 100 by 100 μm in area and 0.0005 mm^3 in volume. Each of these voxels can be thought of as local domain with a specific director orientation.

Seeking to enable both high actuation strain and complex surface alignment in a monolith, we prepared LCEs via a two-step synthetic procedure to produce poly(β-amino ester) networks (*11*, *12*). Whereas the "Finkelmann method" to produce LCEs uses mechanical stretching to align the liquid crystal polymer and limits the complexity of alignment (*13*), this method allows for self-assembly to patterned surfaces. To enable surface alignment, we used a solvent-free, one-pot reaction that begins with low-viscosity precursors. After alignment, these monomers undergo a chain-extension reaction, forming main-chain nematic macromers that can be subsequently cross-linked, as schematized in fig. S2 (*14*). Cross-linking traps the alignment as dictated by the surface patterning into a low modulus and elastic solid. The resulting network structure is shown in Fig. 1B, in which the mesogen lies in the main chain of the polymer. After cross-linking, the birefringence of a surface-aligned uniaxially ordered elastomer is evident by monitoring light transmission between crossed polarizers (Fig. 1C) and through wide-angle x-ray scattering (fig. S3). At 200°C, the material is still birefringent (anisotropic), although the magnitude of the light transmission is greatly reduced at all angles. This remnant order is characteristic of a low-order paranematic state that arises from the constraint of cross-links within the network of certain LCEs (*15*). As evident in Fig. 1D, a spontaneous and reversible contraction on heating and expansion of 55% on cooling along the director is observed. Deformation of the LCEs is expected to be nearly volume-conserving, and as such, the two directions perpendicular to the director exhibit contraction upon cooling and expansion upon heating (*16*).

Here, we demonstrate that topological defects can also be imprinted in LCEs. A photograph between crossed polarizers of a voxelated LCE containing nine defects in a square array is shown in Fig. 2A. As depicted in the inset schematic to Fig. 2A, each +1 defect is a point around which the director varies azimuthally by 360°. Macroscopic azimuthal contraction (along the director) and radial expansion around each defect center lead to the emergence of cones. Remarkably, these features are more than 100 times taller than the initial film thickness of 50 μm, as seen in Fig. 2B. The apex of the cone is centered on the topological defect and is tipped with a stretched hemispherical cap with a radius less than three times the film thickness. The original patterned director profile is maintained in the film over many actuation cycles. This result suggests that recent theoretical and experimental results on highly cross-linked, liquid crystalline networks are also applicable to LCEs (*17*, *18*).

Despite their highly compliant nature, the actuation of voxelated LCEs is not limited to an unloaded state (fig. S4). A representative photograph of an array of four defects lifting a load 147 times heavier than the weight of the actuator with a stroke of ~3000% is shown in Fig. 2C. This giant stroke arises from the amplification of the intrinsic shape change (~55% contraction) through a combination of localized stretching and delocalized bending. The performance of a single +1 defect as an actuator (along the axis of the cone) is quantified in Fig. 2D as a function of resisting load. Maximum specific work capacities of 2.6 J/kg and volumetric work capacities of 3.6 kJ/m^3 were measured. As a point of reference, the specific

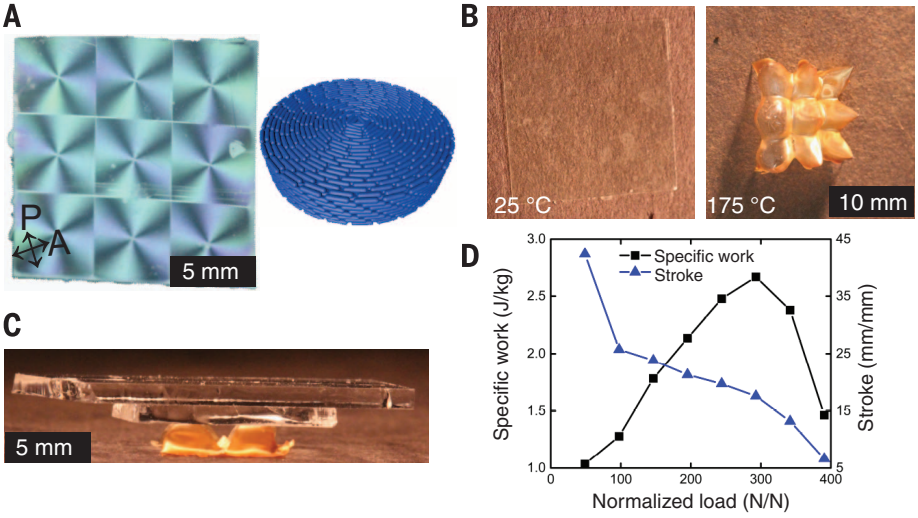

Fig. 2. Topological defects, conical actuators. (**A**) Representative photograph of LCE film with nine +1 topological defects between crossed polarizers. As indicated in the inset schematic, the director orientation varies azimuthally around the defect. (**B**) Upon heating, nine cones arise from the LCE film that reversibly flatten upon cooling. (**C**) Actuation occurs in the presence of loads tens of times larger than the actuator weight. (**D**) Quantification of specific work and stroke of a single actuating +1 defect.

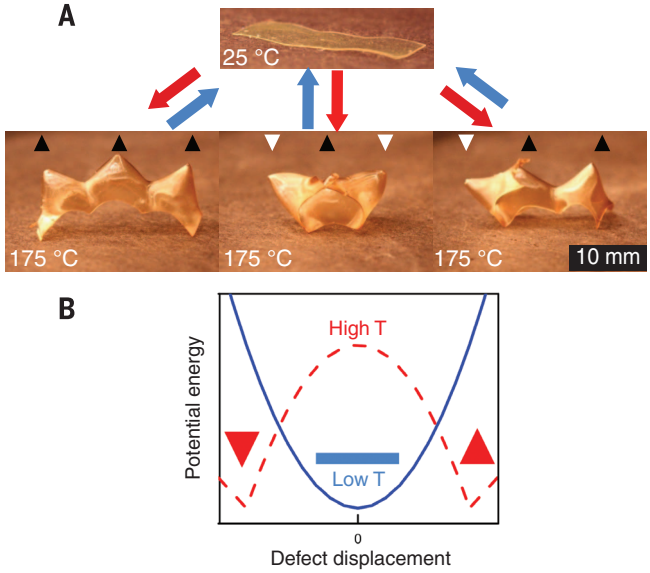

Fig. 3. Mechanical multistability. (**A**) Each individual defect can actuate either up or down, leading to three distinct shapes from a single actuator with three defects. The orientation of the defect is indicated with black and white triangles (**B**) The potential energy diagram illustrates the presence of two metastable states on heating a single actuating defect.

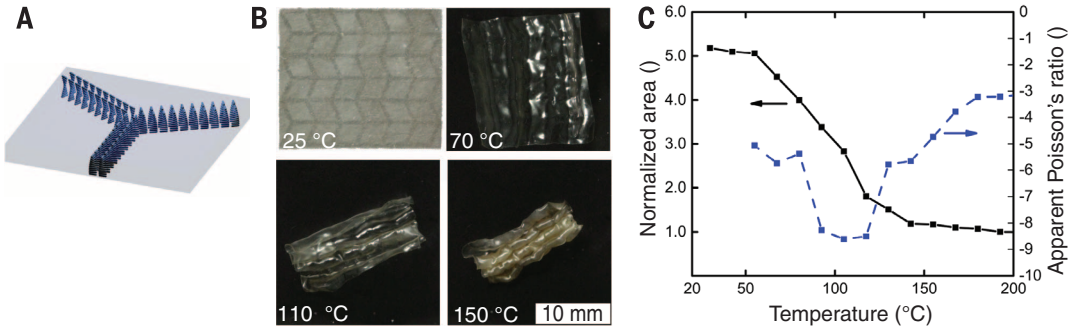

Fig. 4. Origami-inspired actuators. (**A**) Schematic of an edge portion of the Miura-ori pattern with a localized twisted nematic region bounded by unordered regions. (**B**) At room temperature, the LCE film is flat and upon heating above 150°C collapses in a way reminiscent of Miura-ori. (**C**) A reversible 5× reduction in area is observed with a negative in-plane Poisson's ratio.

work capacity is similar to some low-stroke, high-stress linear actuators, such as piezoelectric ceramic stacks (*19*). This work capacity can be attributed to the high energetic cost of preventing the emergence of Gaussian curvature at the center of the defect, which is equivalent to introducing stretch in a flat film (*20*). When normalizing to the 25-mm^2 area of the defect (fig. S5), the actuation stress of a single +1 defect under the maximum applied load was 260 Pa. This value is not the blocking stress because the corresponding stroke is still >650%. The observed specific work capacities are far from the maximum reported values for organic tensile actuators. For example, coiled high-performance polymer and carbon nanotube fibers can generate >10^3 J/kg of work (*21*, *22*). Despite these limitations in pure work capacity and stress generated, the voxelated LCEs are distinguished in the combination of moderate work capacity, the ease of shape programmability, and large stroke. These shape changes are not limited to thermal stimulus but can also be triggered by using chemical stimulus. Exposure to good solvents leads to the reduction of order in LCEs and also triggers complex reversible shape changes (fig. S6.). This feature may be particularly useful in active fluidics in which both linear displacement and shape of the active surface are critical to performance and could be controlled in situ.

Programming of shape can be extended further by taking advantage of the mechanical multistability of stretched and bent polymer films. Because of the constant director pattern through the thickness of the film, each topological defect possesses inversion symmetry. On activation, the defect must break this symmetry and spontaneously choose an orientation, upward or downward. In Fig. 3A, we examine a strip of three +1 defects tiled into a rectangle. Assuming that each defect can independently be identified and assigned either an up or down configuration, a total of 2^3 shapes could arise from a single monolithic element. We observed that each defect can be directed by mechanically pressing on the vertex until the defect snaps through to the opposite orientation. The potential energy associated with the tip of the cone displacement is schematized in Fig. 3B. Temperature cycling does not alter the orientation of the defect once "programmed." As a result, the actuator reversibly forms the selected state in subsequent temperature cycles. This memory is likely imparted by a small irreversible strain bias that can be seen in the room-temperature actuator after cooling (Fig. 3A, top). In the particular case of this actuator design, symmetry reduces the actual number of distinct shapes to three, each of which is shown in Fig. 3A. This is a singular route to multistable shapes and is distinct from the variety of methods used to prepare multiple temporary shapes in shape memory polymers, in that the shape change is reversible and only requires simple up/down mechanical training (*23*, *24*).

Three-dimensional displacement can also be generated by introducing nonuniform director profiles through the thickness, as demonstrated in Fig. 4. By patterning a 500-μm-wide twisted nematic [in which the orientation of the nematic director rotates by 90° across the sample thickness (Fig. 4A)] region (hinge) across an otherwise unpatterned cantilever, reversible bending of over 150° is demonstrated in fig. S7. Over the course of 100 temperature cycles, the performance of the hinge does not appreciably change (fig. S7). Localized bending is caused by a gradient in strain through the material thickness associated with the variation in the orientation of the nematic director, which is analogous to a bimetallic strip used in household thermostats (*25*, *26*). The facets of the film are composed of unpatterned regions that do not exhibit a preferential actuation direction. When arrays of these hinges are combined, origami-like actuators can be fabricated. The Miura-ori pattern describes a series of mountain and valley folds that can be simultaneously folded or unfolded with a mechanical stimulus (*27*). The resulting structure is an example of a planar auxetic structure. This pattern arises naturally in the leaves of certain plants and has been used in deploying solar cells (*28*). As shown in Fig. 4B, we mimic this pattern using 84 twisted nematic hinges, as schematized in fig. S8. Heating the initially flat film (318 mm^2) results in cooperative folding at the localized hinges, which correspondingly reduces the macroscopic area by five (Fig. 4C). Although inherently the material has a Poisson's ratio of ~0.5, the Poisson's ratio of the structure is negative throughout the actuation, with a final value of –3.

A facile one-pot synthesis of a poly(β-amino ester) allows for the preparation of LCE sensitive to directed self-assembly of local alignment with voxel-by-voxel–level control of actuation direction and magnitude. The resulting film can be programmed to exhibit localized bending or stretching in response to an order-reducing stimulus. These localized actuations can be combined to generate monolithic actuators with giant stroke or shape deployment.

REFERENCES AND NOTES

1. C. Liu, H. Qin, P. T. Mather, *J. Mater. Chem.* **17**, 1543–1558 (2007).
2. J. Kim, J. A. Hanna, M. Byun, C. D. Santangelo, R. C. Hayward, *Science* **335**, 1201–1205 (2012).
3. M. Behl, K. Kratz, U. Noechel, T. Sauter, A. Lendlein, *Proc. Natl. Acad. Sci. U.S.A.* **110**, 12555–12559 (2013).
4. C. Ohm, M. Brehmer, R. Zentel, *Adv. Mater.* **22**, 3366–3387 (2010).
5. H. Wermter, H. Finkelmann, *e-Polymers* **1**, 111–123 (2001).
6. Z. Pei *et al.*, *Nat. Mater.* **13**, 36–41 (2014).
7. A. Agrawal, T. Yun, S. L. Pesek, W. G. Chapman, R. Verduzco, *Soft Matter* **10**, 1411–1415 (2014).
8. A. Buguin, M.-H. Li, P. Silberzan, B. Ladoux, P. Keller, *J. Am. Chem. Soc.* **128**, 1088–1089 (2006).
9. L. T. de Haan *et al.*, *Adv. Funct. Mater.* **24**, 1251–1258 (2014).
10. M. E. McConney *et al.*, *Adv. Mater.* **25**, 5880–5885 (2013).
11. D. M. Lynn, R. Langer, *J. Am. Chem. Soc.* **122**, 10761–10768 (2000).
12. D. L. Safranski, M. A. Lesniewski, B. S. Caspersen, V. M. Uriarte, K. Gall, *Polymer (Guildf.)* **51**, 3130–3138 (2010).
13. J. Küpfer, H. Finkelmann, *Makromol. Chem., Rapid Commun.* **12**, 717–726 (1991).
14. Materials and methods are available as supplementary materials on *Science* Online.
15. S. Disch, C. Schmidt, H. Finkelmann, *Macromol. Rapid Commun.* **15**, 303–310 (1994).
16. R. H. Pritchard, P. Lava, D. Debruyne, E. M. Terentjev, *Soft Matter* **9**, 6037–6045 (2013).
17. C. D. Modes, K. Bhattacharya, M. Warner, *Proc. R. Soc. A Math. Phys. Eng. Sci.* **467**, 1121–1140 (2011).
18. L. T. de Haan, C. Sánchez-Somolinos, C. M. W. Bastiaansen, A. P. H. J. Schenning, D. J. Broer, *Angew. Chem. Int. Ed. Engl.* **51**, 12469–12472 (2012).
19. V. Giurgiutiu, C. A. Rogers, *J. Intell. Mater. Syst. Struct.* **7**, 656–667 (1996).
20. C. D. Modes, K. Bhattacharya, M. Warner, *Phys. Rev. E Stat. Nonlin. Soft Matter Phys.* **81**, 060701 (2010).
21. C. S. Haines *et al.*, *Science* **343**, 868–872 (2014).
22. M. D. Lima *et al.*, *Science* **338**, 928–932 (2012).
23. T. Xie, *Nature* **464**, 267–270 (2010).
24. J. Zotzmann, M. Behl, D. Hofmann, A. Lendlein, *Adv. Mater.* **22**, 3424–3429 (2010).
25. K. M. Lee *et al.*, *Adv. Funct. Mater.* **21**, 2913–2918 (2011).
26. Y. Sawa *et al.*, *Proc. Natl. Acad. Sci. U.S.A.* **108**, 6364–6368 (2011).
27. M. Schenk, S. D. Guest, *Proc. Natl. Acad. Sci. U.S.A.* **110**, 3276–3281 (2013).
28. D. S. A. De Focatiis, S. D. Guest, *Philos. Trans. A Math Phys. Eng. Sci.* **360**, 227–238 (2002).
29. 1860–1952 Records of the War Department General and Special Staffs, Photograph No. 165-WW-7B-6, "Wright Brothers' 1903 Aeroplane Kitty Hawk in First Flight," National Archives at College Park.

ACKNOWLEDGMENTS

This research was completed at Wright-Patterson Air Force base with the support of the Air Force Research Laboratory and the Air Force Office of Scientific Research. The authors thank A. Harbach for experimental assistance and K. M. Lee for helpful discussions. Additional information is available in the supplementary materials and from the authors.

SUPPLEMENTARY MATERIALS

www.sciencemag.org/content/347/6225/982/suppl/DC1
Materials and Methods
Supplementary Text
Figs. S1 to S8
Reference (*30*)

9 September 2014; accepted 30 December 2014
10.1126/science.1261019

MOSQUITO BIOLOGY

Evolution of sexual traits influencing vectorial capacity in anopheline mosquitoes

Sara N. Mitchell,[1]* Evdoxia G. Kakani,[1,2]* Adam South,[1]* Paul I. Howell,[3] Robert M. Waterhouse,[4,5,6,7] Flaminia Catteruccia[1,2]†

The availability of genome sequences from 16 anopheline species provides unprecedented opportunities to study the evolution of reproductive traits relevant for malaria transmission. In *Anopheles gambiae,* a likely candidate for sexual selection is male 20-hydroxyecdysone (20E). Sexual transfer of this steroid hormone as part of a mating plug dramatically changes female physiological processes intimately tied to vectorial capacity. By combining phenotypic studies with ancestral state reconstructions and phylogenetic analyses, we show that mating plug transfer and male 20E synthesis are both derived characters that have coevolved in anophelines, driving the adaptation of a female 20E-interacting protein that promotes oogenesis via mechanisms also favoring *Plasmodium* survival. Our data reveal coevolutionary dynamics of reproductive traits between the sexes likely to have shaped the ability of anophelines to transmit malaria.

Anophelines are the only mosquitoes capable of transmitting human malaria, a disease that affects hundreds of millions of people and causes approximately 600,000 fatalities annually (*1*). The vectorial capacity of different anopheline species, a metric of their ability to transmit the *Plasmodium* parasites that cause malaria, is governed by multiple elements of mosquito biology. These include longevity, blood-feeding preferences, immune responses to the parasites, and mosquito population densities, the latter largely determined by the mosquito's reproductive success (*2*). Across most anopheline species, females are monandrous, with reproduction relying on a single mating event that generally occurs in swarms (*3*). Our knowledge on the reproductive biology of this mosquito genus derives principally from studies in *Anopheles gambiae*, the primary malaria vector. In this species, males coagulate seminal secretions produced by the male accessory glands (MAGs) into a mating plug that is transferred to females during mating, delivering also large titers of the steroid hormone 20-hydroxyecdysone (20E) (*4*, *5*). Sexual transfer of 20E has profound effects on female physiology as it induces a cascade of events that render *A. gambiae* females refractory to further copulation while increasing egg production and triggering egg laying (*5*, *6*). The mating-induced increase in oogenesis is mediated by vitellogenic lipid transporters that are also regulated by lower levels of 20E produced by the female after a blood meal (*7*). Interestingly, these lipid transporters facilitate *Plasmodium* development by reducing the parasite-killing ability of the mosquito immune system, providing a link between reproductive and immune processes (*8*). Additionally, the 20E-regulated monandrous mating system positively affects female longevity—a key feature of malaria transmission given the lengthy *Plasmodium* cycle within the mosquito—by decreasing predation risks associated with swarming behavior (*3*) and avoiding the fitness costs associated with multiple matings in other insects (*9*–*11*). Therefore, 20E in *A. gambiae* modulates multiple physiological processes that are highly relevant to the mosquito's competence to transmit malaria: reproductive success, parasite development, and longevity.

Mating plug formation and 20E synthesis in the MAGs are not observed in other mosquito genera or in the fruit fly *Drosophila melanogaster* (*3*, *5*, *12*), suggesting that these traits are potential targets of sexual selection that have either been lost by other insects or gained in anophelines. Given their fundamental relation to fitness, ejaculate characters are often subject to rapid change driven by coevolutionary interactions between the sexes (*13*, *14*). Importantly, the evolution of novel reproductive traits in males that induce adaptive changes in female physiology may also affect pathogen transmission in insect vectors of disease (*15*). Phylogenetic analyses of relevant sexual traits can therefore offer insights into how male-female coevolutionary dynamics influence the vectorial capacity of different species.

To determine how selection has shaped the macroevolution of reproductive traits that also impact malaria transmission, we set out to establish the evolutionary trajectories of the mating plug and male 20E in anophelines, taking advantage of the recent completion of genome assemblies for 16 *Anopheles* species (*16*). We first characterized the occurrence of mating plug formation among nine geographically dispersed species, which span the three subgenera (*Cellia*, *Anopheles*, and *Nyssorhynchus*) that include the most relevant malaria vectors and comprise a range of evolutionary distances from *A. gambiae* (*16*). We performed mating experiments on laboratory-reared colonies, dissected female reproductive tracts from each of the nine selected species, and assessed whether females had received a mating plug. We observed considerable divergence in plug phenotypes (Fig. 1). Three African species (the previously characterized *A. gambiae,* plus *A. arabiensis* and *A. funestus*) and one Indian species (*A. stephensi*) had a solid, highly coagulated plug; three east and southeast Asian species (*A. farauti*, *A. dirus*, and *A. sinensis*) and one European species (*A. atroparvus*) exhibited a less compact, more amorphous structure—likely reflecting reduced levels of coagulation—whereas no plug was detected in the New World species *A. albimanus*.

We next assessed whether 20E is produced in the MAGs of the same species and identified significantly different hormone levels through an enzyme immunoassay on MAGs from virgin males ($P < 0.0001$) (Fig. 2A). Although all species with a fully coagulated plug produced high titers of 20E (above 200 pg/MAGs), two species with partial plug coagulation, *A. dirus* and *A. farauti,* had intermediate hormone levels (<100 pg/MAGs), and negligible amounts (<20 pg/MAGs) were found in *A. sinensis* and *A. atroparvus* (intermediate plugs) and in the plugless *A. albimanus*. Sexual transfer of 20E was determined in five species for which we could reliably isolate mating events and dissect females shortly after copulation (Fig. 2B). All species transferred approximately half of the 20E content from their MAGs, with the exception of *A. arabiensis*, which invested the full 20E complement, suggesting a possible divergence of mating strategy in this important vector. This observed variation in hormone sexual transfer led us to assess the role of 20E in inducing postmating responses in other anophelines. Similar to results previously obtained in *A. gambiae* (*6*), 20E injections in virgin *A. arabiensis* females, a species with high levels of male-transferred 20E, triggered both oviposition and refractoriness to mating (Fig. 2, C and D). Conversely, these postmating responses were not induced in *A. albimanus,* as expected given the lack of 20E transfer by males (Fig. 2, C and D). Consistent with these findings, a mating-induced increase in egg development was observed in *A. arabiensis* and *A. stephensi* but not in *A. albimanus* (fig. S1).

To determine whether mating plug transfer and 20E synthesis in the MAGs are ancestral or derived traits within the anophelines, we next performed ancestral state reconstructions using maximum parsimony. As outgroups, we selected two related dipterans, *D. melanogaster* and *Aedes*

[1]Department of Immunology and Infectious Diseases, Harvard T. H. Chan School of Public Health, Boston, MA 02115, USA. [2]Dipartimento di Medicina Sperimentale, Università degli Studi di Perugia, Perugia 06100, Italy. [3]Centers for Disease Control and Prevention, Atlanta, GA 30329, USA. [4]Department of Genetic Medicine and Development, University of Geneva Medical School, Geneva 1211, Switzerland. [5]Swiss Institute of Bioinformatics, Geneva 1211, Switzerland. [6]Computer Science and Artificial Intelligence Laboratory, Massachusetts Institute of Technology, Cambridge, MA 02139, USA. [7]The Broad Institute of MIT and Harvard, Cambridge, MA 02142, USA. *These authors contributed equally to this work. †Corresponding author. E-mail: fcatter@hsph.harvard.edu

aegypti, for which sufficient genomic information is available to build our phylogeny (fig. S2). Phylogenetic hypotheses about species relatedness were based on maximum likelihood analysis of 4829 single-copy orthologs. Parsimony reconstructions indicated that the most recent common ancestor of the species included in our phylogeny was likely one in which males were incapable of coagulating seminal secretions and did not

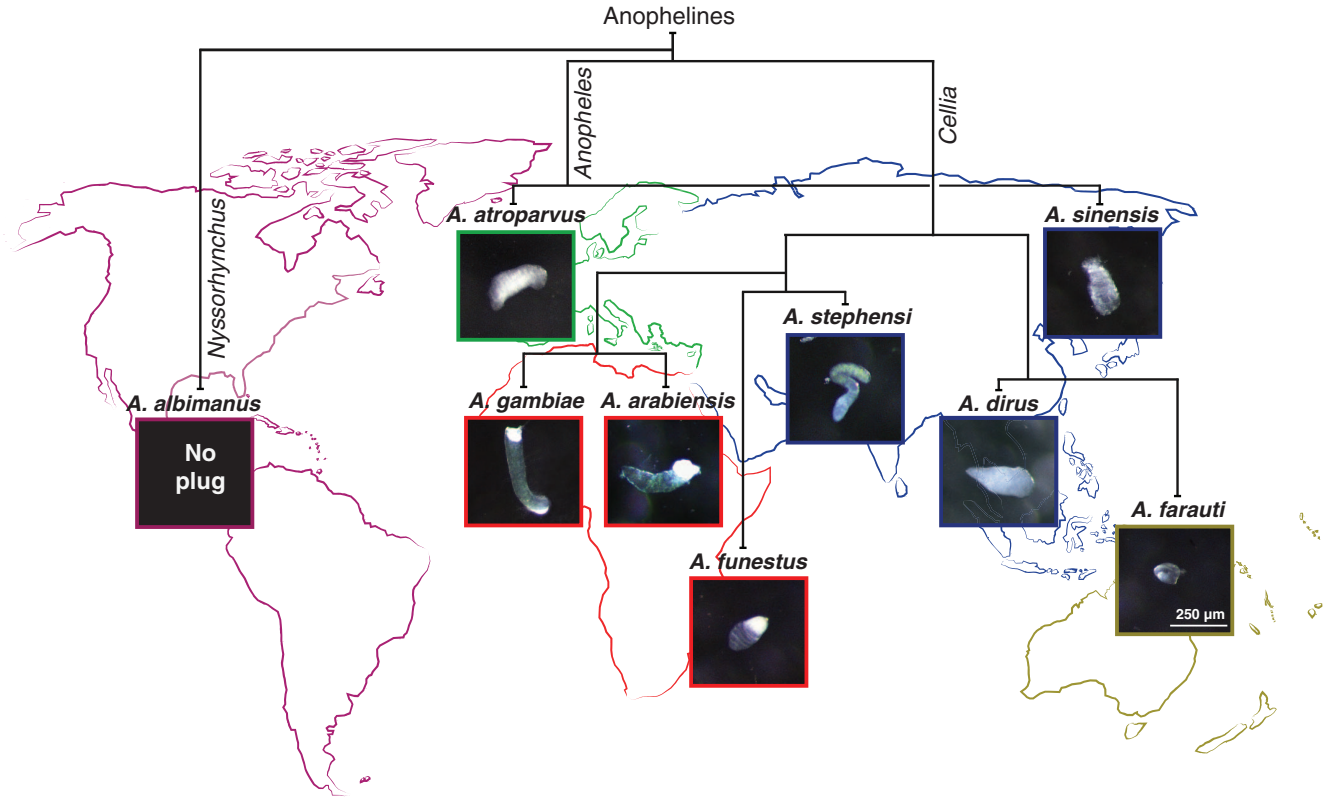

Fig. 1. Mating plug phenotypes across anophelines. Considerable divergence in mating plug phenotypes is observed across nine geographically dispersed anopheline species that span three major subgenera (vertical branch labels). The African *A. gambiae*, *A. arabiensis*, and *A. funestus* and the Indian *A. stephensi* species transfer a structured, fully coagulated plug, whereas the east and southeast Asian species *A. farauti*, *A. dirus*, and *A. sinensis*, along with the European species *A. atroparvus*, present a less coagulated, amorphous plug phenotype. No mating plug transfer was recorded in the New World species *A. albimanus*. Species are placed according to their approximate geographical distribution, and the scale bar present in *A. farauti* applies to all. For accurate branch lengths, see fig. S2.

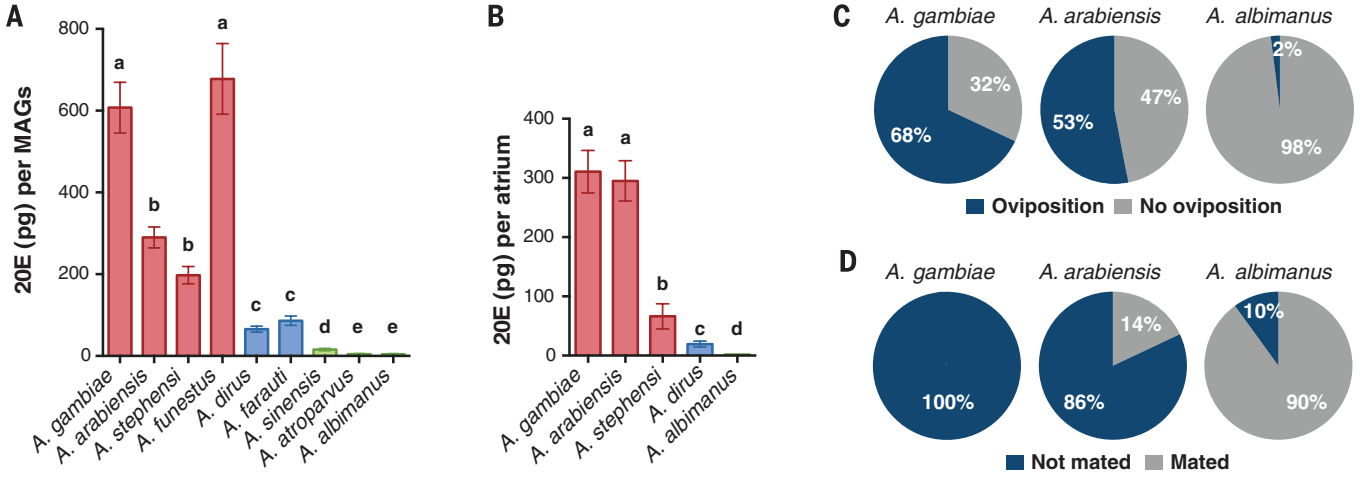

Fig. 2. Synthesis and transfer of 20-hydroxyecdysone (20E) and its effect on oviposition and refractoriness to mating. (**A**) 20E levels in male accessory glands (MAGs) differ significantly across the nine anophelines [analysis of variance (ANOVA) $F_{8,73}$ = 227.8, P < 0.0001]. Species are color-coded according to 20E levels (high, red; intermediate, blue; negligible, green). (**B**) 20E levels in the female atrium from five selected species dissected 1 hour postmating. *A. gambiae* and *A. arabiensis* receive significantly higher levels of 20E from males compared with the other species analyzed (ANOVA $F_{4,32}$ = 80.52, P < 0.0001). In both (A) and (B), results are presented as mean values ± SEM, and letters indicate post hoc significance (Tukey's post hoc test). (**C** and **D**) 20E injections in virgin females induce oviposition after blood feeding (C) and refractoriness to mating (D) in a species that sexually transfers 20E (*A. arabiensis*, P < 0.0001), but not in 20E-less *A. albimanus* (P = ns) when compared with ethanol-injected controls (Fisher's exact test). *A. gambiae* results are taken from previously published data (*6*). Both oviposition and refractoriness data are presented as percentage relative to control females.

synthesize the steroid hormone 20E in their MAGs (Fig. 3). From this ancestor, the ability to form a plug did not evolve until after the *A. albimanus* lineage split from the remainder of the *Anopheles* (node A). Our analysis indicates that plug formation began as a partially coagulated structure, with subsequent elaboration into a fully coagulated plug occurring at node B, the common ancestor of *A. gambiae*, *A. arabiensis*, *A. stephensi*, and *A. funestus*. The production of 20E was not likely to start until node C (where all states are equally parsimonious), suggesting that 20E synthesis in the MAGs evolved shortly after plug coagulation. High titers of 20E occurred at node D, representing the same common ancestor in which full plug coagulation arose. No reversions to the plugless and 20E-less states have occurred in these extant species. The remarkable congruence in ancestral state reconstructions of plug coagulation and 20E levels was confirmed with character correlation and independent contrast analysis, which indicates strong support for a model of correlated evolution between these two characters (independent contrasts, $r = 0.86$, $F_{1,10} = 26.65$, $P = 0.0006$).

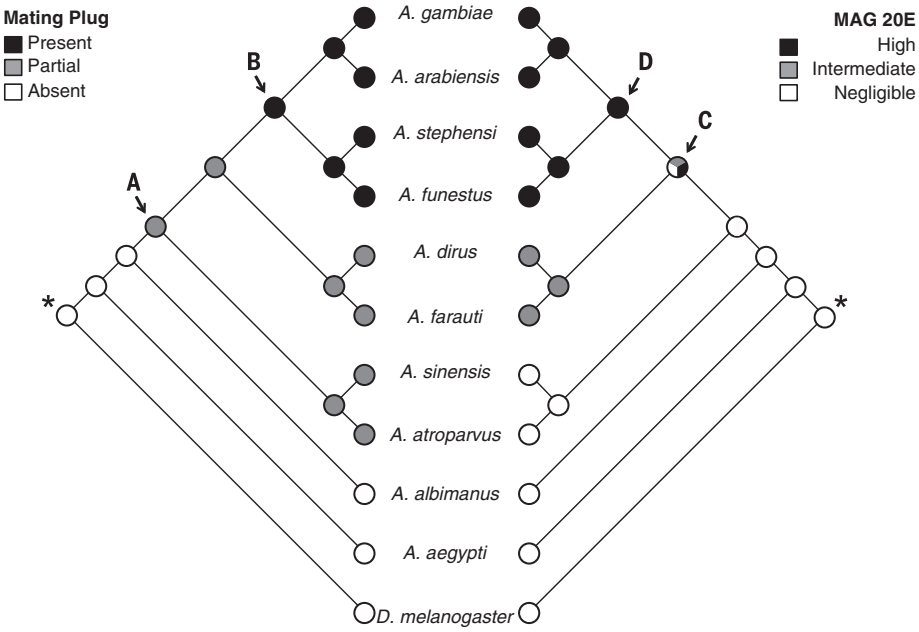

Fig. 3. Maximum parsimony multistate ancestral state reconstructions of mating plug and 20-hydroxyecdysone (20E) characters. Mating plug phenotypes (left) and 20E titers (right) from nine anopheline species and two related dipteran species (*A. aegypti* and *D. melanogaster*) were each coded as multistate categorical characters. Reconstructions reveal that the most common ancestor to all species (indicated by *) was one that lacked a mating plug and did not produce 20E in their male accessory glands (MAGs). Labeled nodes (A to D) are discussed in the text.

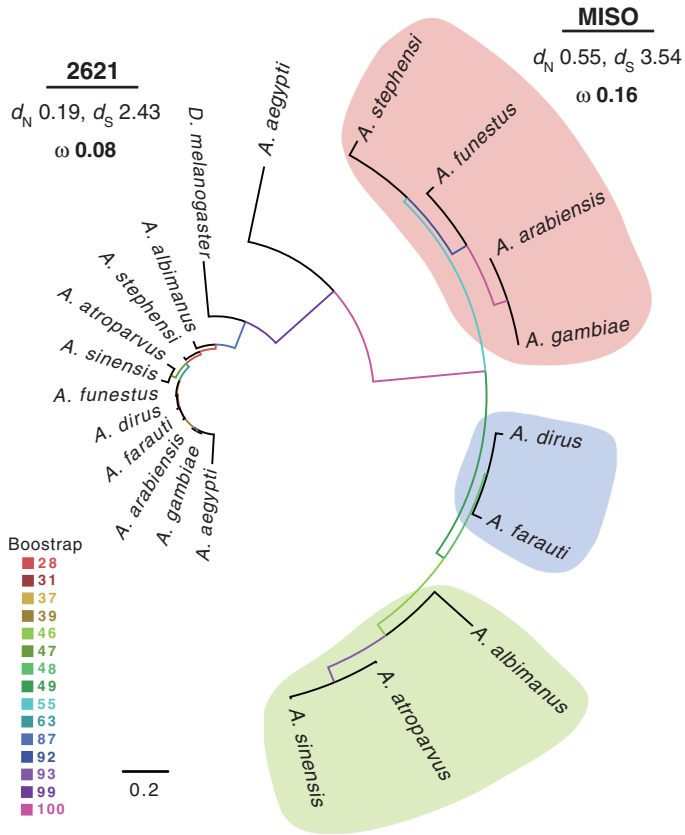

Fig. 4. Phylogenetic analysis of MISO and AGAP002621. A maximum likelihood phylogeny of protein sequences from nine anophelines and two outgroup dipteran species (*D. melanogaster* and *A. aegypti*) using randomized axelerated maximum likelihood (RaxML). Across the anophelines, high sequence conservation (shorter branch lengths) is seen in the MISO paralog AGAP002621 (2621), whereas greater divergence, reflected in a higher d_N and ω ratio, is exhibited by MISO. Colors are coded according to 20E levels in Fig. 2A.

Given our finding of correlated evolution between male ejaculate characters and the observed cross-species increase in egg development as a consequence of 20E transfer, females are predicted to exhibit a pattern of parallel (or reciprocal) evolution of the reproductive traits that translate male 20E into such a fitness benefit (*17*–*19*). To explore this prediction, we performed an evolutionary analysis of the female reproductive protein Mating-Induced Stimulator of Oogenesis (MISO), which to date is the only fitness-increasing female factor known to interact with sexually transferred 20E (*5*). *MISO* in *A. gambiae* is strongly induced by 20E specifically in the atrium (uterus) (*5*). Upon induction, the interaction of MISO with 20E leads to an increase in the expression of vitellogenic lipid transporters after blood feeding, causing a boost in oogenesis by a mechanism also known to promote *Plasmodium* development (*5*, *8*). We created a maximum likelihood protein phylogeny using the orthologs of MISO (AGAP002620) and its adjacent paralog (AGAP002621) in the anopheline species and the *Aedes* and *Drosophila* outgroups studied above. Although the paralog AGAP002621 was considerably conserved, MISO was highly divergent and evolved more rapidly than AGAP002621 [phylogenetic analysis by maximum likelihood (PAML) analysis: ratio of the number of nonsynonymous to synonymous substitutions (d_N/d_S) *MISO*, 0.16; d_N/d_S *AGAP002621*, 0.08] (Fig. 4). Interestingly, among the species producing high titers of 20E, *A. funestus* showed a greater degree of sequence similarity to *A. gambiae* than to *A. stephensi* (Fig. 4), more consistent with 20E levels (Fig. 2A) than with phylogenetic distance across these species (fig. S2). Moreover, *A. albimanus*, which diverged some 100 million years ago from the rest of the anophelines (*16*) (fig. S2), surprisingly grouped with *A. sinensis* and *A. atroparvus* (Fig. 4), the other two species with negligible 20E levels (Fig. 2A). Taken together, these data indicate that *MISO* may be the product of gene duplication from its ancestral paralog and thus subject to relaxed evolutionary constraints promoting acquisition of novel functions (*20*), potentially driven by divergence in male 20E levels. Additional elements of female physiology

are likely to have evolved in response to these substantial changes in ejaculate characteristics. As an example, *A. gambiae* females synthesize significantly lower levels of 20E after blood feeding compared with *A. albimanus* (*7*, *21*), indicating a possible adaptation of female 20E to levels transferred by the male. The observed effects of the male 20E-MISO interaction in regulating egg development suggest that the evolution of sexually transferred 20E will have influenced other blood-feeding–induced processes, with possible consequences for parasite transmission. Notably, a role for ecdysone in mediating protozoan parasite development has been reported in a number of insect species [reviewed in (*22*)], including other vectors of human disease (*23*).

Our phylogenetic approaches combined with phenotypic analyses of multiple reproductive traits provide considerable insight into a group of important disease vectors. Multiple key entomological parameters that directly affect malaria transmission are influenced by the diverse functions of sexually transferred 20E: mosquito densities via MISO-mediated increased oogenesis (*5*); parasite development through the expression of lipid transporters that protect *Plasmodium* from the mosquito immune system (*8*); and longevity due to reduced mating-associated fitness costs (*9*–*11*). Consequently, divergent sexual transfer of 20E across anophelines may have shaped their ability to transmit this deadly disease, and, intriguingly, all four species that transfer large levels of 20E are major malaria vectors originating from Africa and India, the regions of highest malaria burden (*1*). By demonstrating correlated evolution in male ejaculate characters and parallel changes in female physiology implicated in vectorial capacity, we reveal coevolutionary dynamics likely to have fundamentally influenced disease transmission to humans.

REFERENCES AND NOTES

1. World Health Organization, *World Malaria Report 2014* (WHO, Geneva, 2014).
2. G. MacDonald, *Bull. World Health Organ.* **15**, 613–626 (1956).
3. B. Yuval, *Annu. Rev. Entomol.* **51**, 413–440 (2006).
4. E. Pondeville, A. Maria, J. C. Jacques, C. Bourgouin, C. Dauphin-Villemant, *Proc. Natl. Acad. Sci. U.S.A.* **105**, 19631–19636 (2008).
5. F. Baldini *et al.*, *PLOS Biol.* **11**, e1001695 (2013).
6. P. Gabrieli *et al.*, *Proc. Natl. Acad. Sci. U.S.A.* **111**, 16353–16358 (2014).
7. H. Bai, D. B. Gelman, S. R. Palli, *Pest Manag. Sci.* **66**, 936–943 (2010).
8. M. K. Rono, M. M. Whitten, M. Oulad-Abdelghani, E. A. Levashina, E. Marois, *PLOS Biol.* **8**, e1000434 (2010).
9. T. Chapman, L. F. Liddle, J. M. Kalb, M. F. Wolfner, L. Partridge, *Nature* **373**, 241–244 (1995).
10. S. Wigby, T. Chapman, *Curr. Biol.* **15**, 316–321 (2005).
11. A. Dao *et al.*, *J. Med. Entomol.* **47**, 769–777 (2010).
12. M. Bownes, A. Dubendorfer, T. Smith, *J. Insect Physiol.* **30**, 823–830 (1984).
13. J. C. Perry, L. Sirot, S. Wigby, *Trends Ecol. Evol.* **28**, 414–422 (2013).
14. S. M. Lewis, A. South, *Adv. Stud. Behav.* **44**, 53–97 (2012).
15. M. K. Lawniczak *et al.*, *Trends Ecol. Evol.* **22**, 48–55 (2007).
16. D. E. Neafsey *et al.*, *Science* **347**, 1258522 (2015).
17. S. H. Alonzo, T. Pizzari, *Am. Nat.* **175**, 174–185 (2010).
18. S. H. Alonzo, T. Pizzari, *Philos. Trans. R. Soc. Lond. B Biol. Sci.* **368**, 20120044 (2013).
19. S. A. West, A. S. Griffin, A. Gardner, *Curr. Biol.* **17**, R661–R672 (2007).
20. B. Walsh, *Genetica* **118**, 279–294 (2003).
21. Y. H. Lu, H. H. Hagedorn, *Int. J. Inver. Reprod. Develop.* **9**, 79–94 (1986).
22. P. O. Lawrence, *In Vitro Cell. Dev. Biol.* **27**, 487–496 (1991).
23. M. R. Cortez *et al.*, *Exp. Parasitol.* **131**, 363–371 (2012).

ACKNOWLEDGMENTS

We thank E. Lund and D. Clarke for help with mosquito rearing and insectary procedures and M. Bernardi for assistance with artwork. We are grateful to D. Neafsey and N. Besansky for numerous helpful discussions and to S. Lewis, D. Neafsey, M. Mota, and members of the Catteruccia laboratory for careful reading of the manuscript. This work was sponsored in part by the following grants awarded to F.C.: a European Research Council FP7 ERC Starting Grant (grant Anorep, ID: 260897), a William F. Milton Fund grant (Harvard Medical School 2013), and an NIH grant (grant ID: NIH 1R01AI104956-01A1). S.N.M., E.G.K., A.S., and F.C. designed the experiments. P.I.H. provided experimental material, and S.N.M., E.G.K, and P.I.H. performed the experiments. S.N.M., E.G.K, A.S., and R.M.W. analyzed the data. S.N.M., E.G.K., A.S., and F.C. wrote the manuscript. S.N.M., E.G.K., and A.S. contributed equally to this study. All gene sequences are freely available via given gene identifiers from VectorBase (www.vectorbase.org). The single-copy ortholog sequences used to produce the species phylogeny are available via OrthoDB (http://cegg.unige.ch/orthodbmoz2). Protein sequence alignments employed for the species and MISO-AGAP002621 phylogenies are available via DRYAD: doi:10.5061/dryad.6f576.

SUPPLEMENTARY MATERIALS

www.sciencemag.org/content/347/6225/985/suppl/DC1
Materials and Methods
Figs. S1 and S2
References (*24*–*32*)

31 July 2014; accepted 16 January 2015
10.1126/science.1259435

CLIMATE CHANGE

Atlantic and Pacific multidecadal oscillations and Northern Hemisphere temperatures

Byron A. Steinman,[1]* Michael E. Mann,[2] Sonya K. Miller[2]

The recent slowdown in global warming has brought into question the reliability of climate model projections of future temperature change and has led to a vigorous debate over whether this slowdown is the result of naturally occurring, internal variability or forcing external to Earth's climate system. To address these issues, we applied a semi-empirical approach that combines climate observations and model simulations to estimate Atlantic- and Pacific-based internal multidecadal variability (termed "AMO" and "PMO," respectively). Using this method, the AMO and PMO are found to explain a large proportion of internal variability in Northern Hemisphere mean temperatures. Competition between a modest positive peak in the AMO and a substantially negative-trending PMO are seen to produce a slowdown or "false pause" in warming of the past decade.

Distinguishing between forced and unforced variability in climate is critical for assessing the impact of anthropogenic forcing on temperature, drought, hurricane activity, weather extremes, and other climate phenomena. The North Atlantic and North Pacific oceans are the key drivers of internal variability in Northern Hemisphere temperatures on multidecadal time scales, but there is substantial uncertainty in their relative contributions to the observed variability. We applied a new semi-empirical method that uses a combination of observational data and a large ensemble of coupled climate model simulations to assess the relative roles of both forced and internal variability in the Northern Hemisphere over the historical period.

The Atlantic Multidecadal Oscillation (AMO) (*1*) is the leading mode of internal variability in North Atlantic sea surface temperature (SST) on multidecadal (~50 to 70 years) time scales (*2*–*4*). The Pacific Decadal Oscillation (PDO) (*5*, *6*) is the leading mode of North Pacific internal SST variability but, as defined, consists of at least two distinct signals, one roughly bidecadal with a ~16- to 20-year period and the other multidecadal with a ~50- to 70-year period (*4*, *7*–*9*). The PDO and AMO time series typically are defined in terms of the temporal pattern of temperature change in the north-central Pacific and North Atlantic, respectively. The multidecadal component of the PDO may in part be related to the AMO [although centered in the Atlantic, it appears (*2*, *3*) to project at least weakly onto the Pacific] and in part reflective of low-frequency variability related to the El Niño–Southern Oscillation (ENSO) and its extratropical response (*10*–*16*). We distinguish the multidecadal component from the conventionally defined PDO by terming it the "PMO," and we term the multidecadal component of internal Northern Hemisphere mean temperature variability the "NMO."

Prior methods used to define these internal variability components and their influence on Northern Hemisphere temperature include (i) a simple linear detrending of the mean North Atlantic SST time series (*17*–*21*), (ii) estimating the forced trend based on regression of North Atlantic SST against global mean SST and

[1]Large Lakes Observatory and Department of Earth and Environmental Sciences, University of Minnesota Duluth, Duluth, MN, USA. [2]Department of Meteorology and Earth and Environmental Systems Institute, Pennsylvania State University, University Park, PA, USA.
*Corresponding author. E-mail: bsteinma@d.umn.edu

removing the forced trend to yield an estimate of the internal variability (*16*, *22*, *23*), and (iii) defining the forced component as the mean of North Atlantic SST in an ensemble of climate model simulations and defining the internal variability component as the difference between the observed SST series and the multimodel mean (*24*, *25*). These methods, as shown below, do not in general yield correct results. We estimated the Atlantic and Pacific-basin multidecadal internal variability components and their contribution to Northern Hemisphere temperature change on the basis of a new target region regression approach.

Our method is based on the principle that internal variability is uncorrelated among distinct realizations of a large ensemble. We therefore used the mean of the Coupled Model Intercomparison Project Phase 5 (CMIP5) ensemble (*26*) as an initial estimate of the forced component of surface temperature for the North Atlantic, North Pacific, and the entire (land + ocean) Northern Hemisphere region (Fig. 1). The estimated forced series is rescaled via linear regression against the actual temperature series so as to accommodate potential differences in the amplitude of the true forced response relative to the multimodel mean response (for example, because of disparities in climate sensitivity). We define the AMO, PMO, and NMO as the difference between the observations and estimated, regional forced temperature series for each of the three respective regions, low-pass filtered at a frequency of 40 years in order to isolate multidecadal variability (*27*).

We analyzed both the subensemble of simulations (n = 24) of the GISS-E2-R model (*28*) (henceforth "CMIP5-GISS"); the subensemble of simulations (n = 45) of models (M = 15) with aerosol indirect effects ("CMIP5-AIE"); and the larger, full (n = 170 total realizations) ensemble of all (M = 44) models ("CMIP5-All") (Fig. 1, fig. S1, and table S1). The three ensembles are complementary in their characteristics. The GISS-E2-R simulations (which comprise the largest CMIP5 ensemble for an individual model) are consistent in their forcings and include representation of the first aerosol indirect effect (cloud albedo). The CMIP5-AIE models all have full representations of both the first and second (cloud lifetime) indirect aerosol effects, which are potentially important contributions to the net radiative forcing (*29*). The CMIP5-All ensemble provides a much larger sample, but individual simulations vary in the forcings that were used and how they were implemented. Recent work (*30*) has explored the hypothesis that at least some of the difference between modeled and observed temperature changes arises from errors in the forcing estimates (for example, the accumulated effects of small volcanic eruptions over the past decade are not accounted for in the vast majority of CMIP5 simulations). Our assumption is that these three different ensembles mean estimates of the forced temperature signal span a representative range of uncertainty in the underlying forcing.

In defining the AMO, PMO, and NMO, we considered target regions spanning the equator to 60° north over the Atlantic (0° to 80°W) and Pacific (120°E to 100°W) oceans (the areal mean over all SST gridboxes in each basin), and the full Northern Hemisphere (ocean + land). The CMIP5-All multimodel ensemble mean series (latitude weighted) for each of the target regions, along with the ensemble of individual simulations, were compared with the actual historical observations over the interval 1854–2012 C.E. (Fig. 1 and fig. S1) (*27*). We used Goddard Institute for Space Studies (GISS) Surface Temperature (GISTEMP) (*31*) for the observational NH mean (ocean + land) series, owing to recent evidence (*32*) that other products may underestimate recent warming by undersampling the Arctic. For the regional observational SST estimates, we used the mean of the Hadley Centre Global Sea Ice and Sea Surface Temperature (HadISST) (*33*), National Oceanic and Atmospheric Administration (NOAA) Extended Reconstructed Sea Surface Temperature (ERSST) (*34*, *35*), and Kaplan (*36*–*38*) products.

The results of the target-region regression analysis show for each of the three model ensembles that the estimated internal variability components derived from the various realizations are statistically independent, as they should be if the method is performing correctly, contrasting with what we find for the other previously used methods (Fig. 2, figs. S2 to S4, and table S2) (*27*). We next applied the methods in a semi-empirical setting in order to estimate the actual historical AMO, PMO, and NMO series. Under the assumption that the observational temperature series are the sum of a forced component and the real-word realization of internal variability, we estimate the true historical internal variability component as the residual series after the forced components are removed.

Our approach gives similar results whether CMIP5-All, CMIP5-GISS, CMIP5-AIE [or even individual models with a minimum of $n \geq 10$ realizations (fig. S6)] ensemble means are used (*39*). The root mean square amplitude of the AMO and PMO are similar for all three ensembles (0.10/0.11/0.09°C for AMO and 0.09/0.09/0.11°C for PMO, for CMIP5-All/CMIP5-GISS/CMIP5-AIE, respectively). Unlike with the linear detrending approach, the PMO and AMO are not found to be significantly correlated. An analysis of the full multimodel ensemble reveals any putative correlation between the AMO and PMO [and arguments of a "stadium wave" climate signal (*40*)] to be an artifact of the linear detrending approach (fig. S7) (*27*). Shown also (Fig. 3) are the results of a simple bivariate regression demonstrating that the NMO can be very closely approximated [coefficient of determination (R^2) = 0.86/0.88/0.91 for CMIP5-All/CMIP5-GISS/CMIP5-AIE, respectively] by a weighted combination of the AMO and PMO series (*41*). The amplitude of the NMO (0.07°C using either CMIP5-All or CMIP5-GISS, and 0.08°C using CMIP5-AIE) is consistent with results from long model control runs (*3*).

Our analysis shows the NMO to be decreasing at the end of the series (Fig. 3 and figs. S5 and S6). Mann *et al.* (*42*) assessed the recent decrease in the NMO in terms of a negative-trending AMO contribution. However, we reach a somewhat different conclusion in the present study, finding that the recent decrease in the NMO is instead a result of a sharply decreasing PMO (with a relatively flat AMO contribution). That observation is consistent with recent findings that the anomalous slowing of warming over the past decade

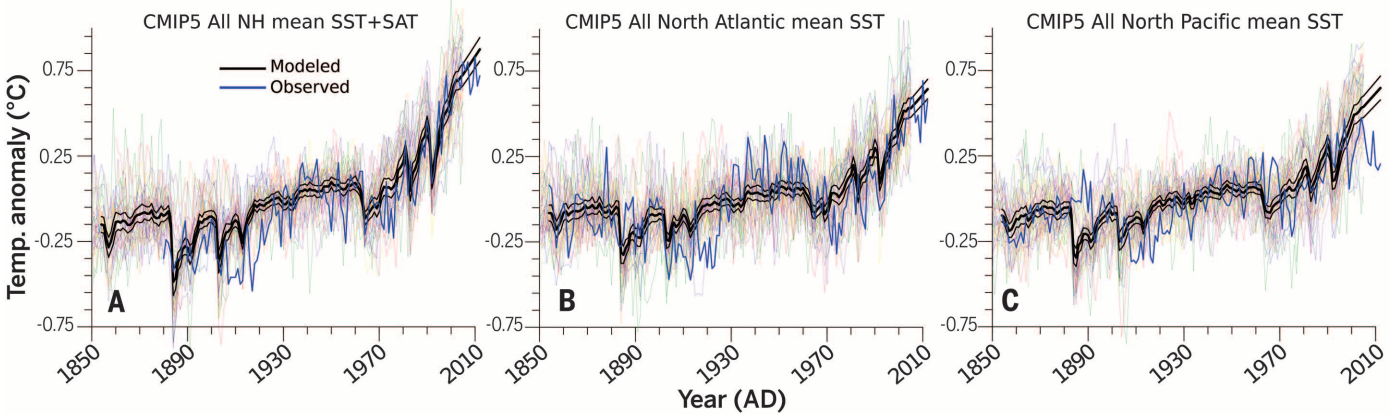

Fig. 1. CMIP5-All ensemble means shown with individual model means. (**A**) Northern Hemisphere SST+SAT. (**B**) North Atlantic SST. (**C**) North Pacific SST. Ensemble mean, black curves; individual model means, colored curves. Thin black line depicts the 95% confidence limits of the model mean determined via bootstrap resampling. Blue line depicts observed temperatures.

is tied to subsurface heat burial in the tropical Pacific and a tendency for persistent "La Niña"–like conditions (*43*–*46*). Our analysis attributes this trend to internal variability as a consequence of the failure of the CMIP5 models to identify a recent forced trend of this nature. However, there is paleoclimate evidence suggesting that a La Niña–like response might arise from positive radiative forcing (*47*), and the possibility remains that state-of-the-art climate models fail to capture such a dynamical response to anthropogenic radiative forcing.

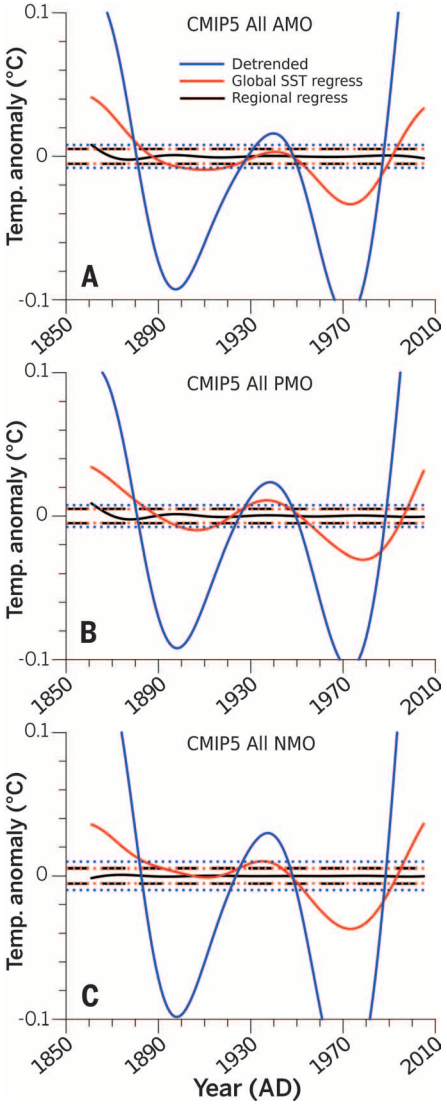

Fig. 2. CMIP5-All mean series and estimated 1-σ bounds for mean series under the assumption of statistical independence of internal variability among ensemble members. (**A**) AMO. (**B**) PMO. (**C**) NMO. Solid lines indicate mean of all realizations; dashed lines indicate estimated 1-σ bounds. Determined by using detrending (blue), global SST regression (red), and target region regression (black). Individual realizations of CMIP5-All internal variability as well as results for target region differencing are shown in the supplementary materials (fig. S2).

Some recent work (*18*, *19*, *21*, *22*, *25*) has attributed a potentially large proportion of observed regional and hemispheric temperature changes to multidecadal internal variability related to the so-called "AMO" and/or "PDO." Using the CMIP5 multimodel historical climate simulations, we have established that the methods used in these studies tend to inflate and distort the estimated internal variability owing to an incorrect partition of internal and forced variability. We have demonstrated that our target-region regression method correctly isolates the internal variability components.

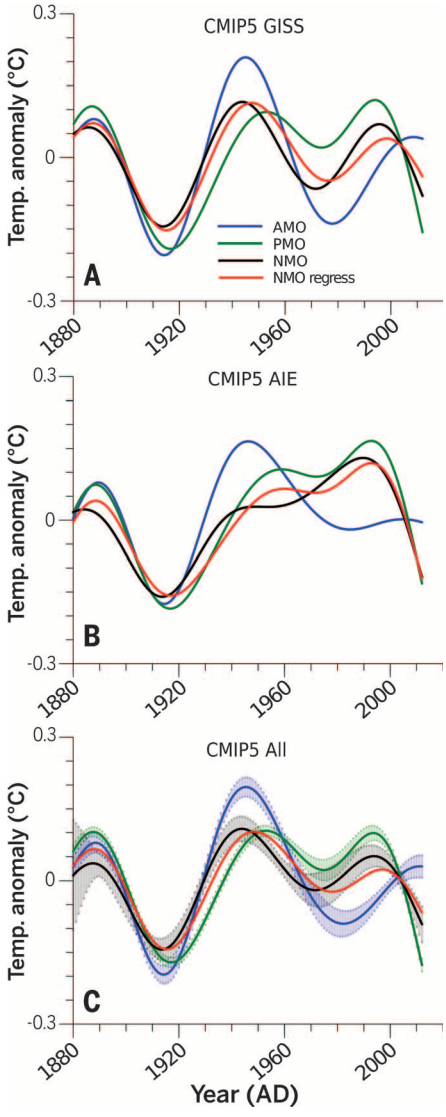

Fig. 3. Semi-empirical estimate of AMO, PMO, and NMO based on target region regression using historical climate model realizations. (**A**) CMIP5-GISS. (**B**) CMIP5-AIE. (**C**) CMIP-All. In (A) to (C), blue, AMO; green, PMO; and black, NMO. Bivariate regression-based approximation of NMO (red) strongly correlates (R^2 = 0.86/0.88/0.91 for CMIP5-All/CMIP5-GISS, CMIP5-AIE, respectively) with semi-empirical NMO estimate (black). 95% confidence limits of the AMO, PMO, and NMO CMIP5-All means were determined by using the ensemble of target region mean series resulting from bootstrap resampling (Fig. 1) and are shown as colored shading.

Applying our method to observational surface temperature data, we find that internal variability is likely to have had a substantial influence on multidecadal Northern Hemisphere temperature changes over the historical period, contributing up to 0.15°C peak warming/cooling. The AMO appears to have been influential in the early and middle 20th century, but the PMO has played a more dominant role in recent decades. This result is consistent across the three ensembles (GISS, AIE, and All) (Fig. 3). Our findings (the AIE experiments, especially) suggest that natural internal variability has had a modest influence on Atlantic SST over the past half century and that multidecadal climate variability attributed to Atlantic SST changes (such as variations in tropical storm frequency and strength and Sahel and Midwestern North American drought) (*48*–*51*) was largely driven by external forcing (as concluded in other recent work) (*52*). Our results also highlight the substantial uncertainties associated with the role of anthropogenic aerosol forcing in recent decades because the greatest discrepancies using the three different ensembles occur during that time period.

Our findings have strong implications for the attribution of recent climate changes. We find that internal multidecadal variability in Northern Hemisphere temperatures (the NMO), rather than having contributed to recent warming, likely offset anthropogenic warming over the past decade. This natural cooling trend appears to reflect a combination of a relatively flat, modestly positive AMO and a sharply negative-trending PMO. Given the pattern of past historical variation, this trend will likely reverse with internal variability instead, adding to anthropogenic warming in the coming decades.

REFERENCES AND NOTES

1. R. A. Kerr, *Science* **288**, 1984–1985 (2000).
2. T. L. Delworth, M. E. Mann, *Clim. Dyn.* **16**, 661–676 (2000).
3. J. R. Knight, R. J. Allan, C. K. Folland, M. Vellinga, M. E. Mann, *Geophys. Res. Lett.* **32**, L20708 (2005).
4. M. E. Mann, J. Park, *J. Geophys. Res.* **99** (D12), 25819 (1994).
5. N. J. Mantua, S. R. Hare, Y. Zhang, J. M. Wallace, R. C. Francis, *Bull. Am. Meteorol. Soc.* **78**, 1069–1079 (1997).
6. N. J. Mantua, S. R. Hare, *J. Oceanogr.* **58**, 35–44 (2002).
7. M. E. Mann, J. Park, *J. Clim.* **9**, 2137–2162 (1996).
8. M. E. Mann, J. Park, *Adv. Geophys.* **41**, 1–131 (1999).
9. S. Minobe, *Geophys. Res. Lett.* **24**, 683–686 (1997).
10. M. A. Alexander *et al.*, *J. Clim.* **15**, 2205–2231 (2002).
11. D. J. Vimont, *J. Clim.* **18**, 2080–2092 (2005).
12. W. Chen, B. Dong, R. Lu, *J. Geophys. Res.* **115** (D17), D17109 (2010).
13. B. Dong, R. T. Sutton, A. A. Scaife, *Geophys. Res. Lett.* **33**, L08705 (2006).
14. B. Guan, S. Nigam, *J. Clim.* **22**, 4228–4240 (2009).
15. G. J. van Oldenborgh, L. A. te Raa, H. A. Dijkstra, S. Y. Philip, *Ocean Sci.* **5**, 293–301 (2009).
16. C. Marini, C. Frankignoul, *Clim. Dyn.* **43**, 607–625 (2013).
17. S. B. Goldenberg, C. W. Landsea, A. M. Mestas-Nunez, W. M. Gray, *Science* **293**, 474–479 (2001).
18. M. G. Wyatt, S. Kravtsov, A. A. Tsonis, *Clim. Dyn.* **38**, 929–949 (2011).
19. M. G. Wyatt, J. A. Curry, *Clim. Dyn.* **42**, 2763–2782 (2013).

20. R. Zhang, T. L. Delworth, *Geophys. Res. Lett.* **34**, n/a (2007).
21. P. Chylek, J. D. Klett, G. Lesins, M. K. Dubey, N. Hengartner, *Geophys. Res. Lett.* **41**, 1689–1697 (2014).
22. M. Ting, Y. Kushnir, R. Seager, C. Li, *J. Clim.* **22**, 1469–1481 (2009).
23. K. E. Trenberth, D. J. Shea, *Geophys. Res. Lett.* **33**, L12704 (2006).
24. J. R. Knight, *J. Clim.* **22**, 1610–1625 (2009).
25. L. Terray, *Geophys. Res. Lett.* **39**, L19712 (2012).
26. K. E. Taylor, R. J. Stouffer, G. A. Meehl, *Bull. Am. Meteorol. Soc.* **93**, 485–498 (2012).
27. Materials and methods are available as supplementary materials on *Science* Online.
28. R. L. Miller *et al.*, *J. Adv. Model. Earth Syst.* **6**, 441–477 (2014).
29. M. Collins *et al.*, *Long-Term Climate Change: Projections, Commitments and Irreversibility*, T. F. Stocker *et al.*, Eds. (Cambridge Univ. Press, Cambridge, 2013), pp. 1029–1136.
30. G. A. Schmidt, D. T. Shindell, K. Tsigaridis, *Nat. Geosci.* **7**, 158–160 (2014).
31. J. Hansen, R. Ruedy, M. Sato, K. Lo, *Rev. Geophys.* **48**, RG4004 (2010).
32. K. Cowtan, R. G. Way, *Q. J. R. Meteorol. Soc.* **140**, 1935–1944 (2014).
33. N. A. Rayner, *J. Geophys. Res.* **108** (D14), 4407 (2003).
34. T. M. Smith, R. W. Reynolds, T. C. Peterson, J. Lawrimore, *J. Clim.* **21**, 2283–2296 (2008).
35. Y. Xue, T. M. Smith, R. W. Reynolds, *J. Clim.* **16**, 1601–1612 (2003).
36. A. Kaplan *et al.*, *J. Geophys. Res.* **103** (C9), 18,567–18,589 (1998).
37. D. E. Parker, P. D. Jones, C. K. Folland, A. Bevan, *J. Geophys. Res.* **99** (D7), 14373 (1994).
38. R. W. Reynolds, T. M. Smith, *J. Clim.* **7**, 929–948 (1994).
39. The regression analyses applied to the full CMIP5 multimodel mean yields a scaling factor ("beta") for Northern Hemisphere temperature changes that slightly exceeds unity (beta = 1.053 ± 0.0169), implying a real-world forced response that is slightly greater than that estimated by the CMIP5 multimodel mean. In contrast, North Atlantic mean temperatures yields a scaling factor slightly below unity (beta = 0.916 ± 0.0155), and North Pacific mean temperatures yield a scaling factor substantially below unity (beta = 0.629 ± 0.0182), suggesting that the CMIP5 multimodel mean substantially overestimates the amplitude of forced temperature changes over the North Pacific. Further details, including results for the two subensembles (CMIP5-A1E and CMIP5-GISS), are available in the supplementary materials (table S3).
40. S. Kravtsov, M. G. Wyatt, J. A. Curry, A. A. Tsonis, *Geophys. Res. Lett.* **41**, 6881–6888 (2014).
41. NMO = 0.35 AMO + 0.43 PMO for CMIP5-All; NMO = 0.42 AMO + 0.36 PMO for CMIP5-GISS; NMO = −0.06 AMO + 0.85 PMO for CMIP5-AIE; AMO and PMO regression coefficients are significant at the $P << 0.05$ level based on a one-sided test.
42. M. E. Mann, B. A. Steinman, S. K. Miller, *Geophys. Res. Lett.* **41**, 3211–3219 (2014).
43. K. E. Trenberth, J. T. Fasullo, *Earth's Future* **1**, 19–32 (2013).
44. M. H. England *et al.*, *Nature Clim. Change* **4**, 222–227 (2014).
45. Y. Kosaka, S.-P. Xie, *Nature* **501**, 403–407 (2013).
46. S. McGregor *et al.*, *Nature Clim. Change* **4**, 888–892 (2014).
47. M. E. Mann *et al.*, *Science* **326**, 1256–1260 (2009).
48. M. E. Mann, K. A. Emanuel, *Eos Trans. AGU* **87**, 233 (2006).
49. E. R. Martin, C. Thorncroft, *Geophys. Res. Lett.* **41**, 2169–2175 (2014).
50. J. R. Knight, C. K. Folland, A. A. Scaife, *Geophys. Res. Lett.* **33**, L17706 (2006).
51. Y. Kushnir, R. Seager, M. Ting, N. Naik, J. Nakamura, *J. Clim.* **23**, 5610–5628 (2010).
52. B. B. B. Booth, N. J. Dunstone, P. R. Halloran, T. Andrews, N. Bellouin, *Nature* **484**, 228–232 (2012).

ACKNOWLEDGMENTS

All raw data, Matlab code, and results from our analysis are available at the supplementary website: www.meteo.psu.edu/holocene/public_html/supplements/Science2015. We acknowledge the World Climate Research Programme's Working Group on Coupled Modeling, which is responsible for CMIP, and we thank the climate modeling groups for producing and making available their model output. We thank K. Emanuel and G. Schmidt for helpful comments on earlier versions of the manuscript. B.A.S. acknowledges support by the U.S. National Science Foundation Atmospheric and Geospace Sciences–Postdoctoral Research Fellowships (AGS-PRF) (AGS-1137750). Kaplan SST V2 data were provided by the NOAA/Office of Oceanic and Atmospheric Research/Earth System Research Laboratory Physical Sciences Division, Boulder, Colorado, USA: www.esrl.noaa.gov/psd. HadISST data were provided by the Met Office Hadley Centre: www.metoffice.gov.uk/hadobs. ERSST data were provided by NOAA: www.ncdc.noaa.gov/data-access/marineocean-data/extended-reconstructed-sea-surface-temperature-ersst-v3b.

SUPPLEMENTARY MATERIALS

www.sciencemag.org/content/347/6225/988/suppl/DC1
Materials and Methods
Supplementary Text
Figs. S1 to S7
Tables S1 to S3
References (*53*–*58*)

24 June 2014; accepted 26 January 2015
10.1126/science.1257856

PEST CONTROL

Full crop protection from an insect pest by expression of long double-stranded RNAs in plastids

Jiang Zhang,[1] Sher Afzal Khan,[2] Claudia Hasse,[1] Stephanie Ruf,[1] David G. Heckel,[2] Ralph Bock[1]*

Double-stranded RNAs (dsRNAs) targeted against essential genes can trigger a lethal RNA interference (RNAi) response in insect pests. The application of this concept in plant protection is hampered by the presence of an endogenous plant RNAi pathway that processes dsRNAs into short interfering RNAs. We found that long dsRNAs can be stably produced in chloroplasts, a cellular compartment that appears to lack an RNAi machinery. When expressed from the chloroplast genome, dsRNAs accumulated to as much as 0.4% of the total cellular RNA. Transplastomic potato plants producing dsRNAs targeted against the β-actin gene of the Colorado potato beetle, a notorious agricultural pest, were protected from herbivory and were lethal to its larvae. Thus, chloroplast expression of long dsRNAs can provide crop protection without chemical pesticides.

Double-stranded RNA (dsRNA) fed to insects can be taken up by midgut cells and processed into small interfering RNAs (siRNAs) by the insect's Dicer endoribonuclease (*1*–*3*). If the sequence of the fed dsRNA matches that of an insect gene, gene silencing by RNA interference (RNAi) disrupts expression of the insect's gene (*3*, *4*). By targeting essential insect genes, dsRNAs can be developed into highly species-specific insecticides (*4*). However, although expression of dsRNAs targeted against insect genes in transgenic plants (*1*, *2*, *5*–*8*) has impaired growth and development, complete protection of the plants and efficient killing of the insects have not been achieved. dsRNAs at least 60 base pairs (bp) in length are required for efficient uptake and biological activity in the target insect (*3*), but the plant's own system for producing small RNAs (*9*) prevents the accumulation of high amounts of long dsRNA. The major processing products of dsRNA cleavage by Dicer are 21-bp siRNAs, but these had little (*10*) or no effect when fed to insects (*3*). Thus, rapid turnover of dsRNAs in the plant limits the efficacy of transgenic RNAi-based anti-insect strategies.

The plastids (chloroplasts) of plant cells are derived from formerly free-living cyanobacteria, a group of prokaryotes that lack an RNAi pathway. We reasoned that chloroplasts might be capable of stably accumulating long dsRNAs, in which case dsRNA expression from the plastid genome could provide better protection against insect pests than dsRNA expression from the nuclear genome. To test the feasibility of stable dsRNA expression in plastids, we transformed the tobacco (*Nicotiana tabacum*) plastid genome with three different types of dsRNA constructs (Fig. 1A and fig. S1). In ptDP constructs, the dsRNA is generated by transcription from two convergent (dual) promoters. In ptSL constructs, the dsRNA is also produced from two convergent promoters, but each strand is additionally flanked by sequences forming stem-loop–type secondary structures, which increase RNA stability in plastids (*11*). In ptHP constructs, hairpin-type dsRNA (hpRNA) is produced by transcription of two transgene copies arranged as an inverted repeat (Fig. 1A). We targeted the Colorado potato beetle (*Leptinotarsa decemlineata*; CPB), a notorious insect pest of potato and other solanaceous crops (e.g., tomato and eggplant). Both larvae and adults feed on foliage, skeletonize the leaves, and, if left uncontrolled, completely destroy the crop. In many areas of the world, the beetle has no natural enemies, and chemical pesticides are the main method of CPB control. However, since the middle of the 20th century, CPB has developed resistance to all major insecticide classes (and therefore has been branded an "international superpest") (*12*).

[1]Max-Planck-Institut für Molekulare Pflanzenphysiologie, D-14476 Potsdam-Golm, Germany. [2]Max-Planck-Institut für Chemische Ökologie, D-07745 Jena, Germany.
*Corresponding author. E-mail: rbock@mpimp-golm.mpg.de

As essential target genes, the CPB *ACT* and *SHR* genes were chosen. *ACT* encodes β-actin, an essential cytoskeletal protein, and *SHR* encodes Shrub (also known as Vps32 or Snf7), an essential subunit of a protein complex involved in membrane remodeling for vesicle transport. Disruption of these genes when the insects are fed in vitro synthesized dsRNAs induces mortality with high efficacy (*3*, *13*). To test longer dsRNAs and test for a possible synergistic action, we also produced an *ACT+SHR* fusion gene. To confirm the activity of these dsRNAs in the beetles, we synthesized the dsRNAs (*ACT*, *SHR*, *ACT+SHR* fusion, and *GFP* as a control) by in vitro transcription, painted them onto young potato leaves, and fed the leaves to second-instar CPB larvae. All three insect gene–derived dsRNAs reduced larval growth (fig. S2). The *ACT* dsRNA was more effective than the *SHR* dsRNA, and the *ACT+SHR* dsRNA was the least effective dsRNA (fig. S2), indicating that targeting two insect genes with the same dsRNA does not necessarily enhance insecticidal activity.

We first evaluated the three strategies for in vivo dsRNA production (ptDP, ptSL, and ptHP constructs; Fig. 1A and fig. S1C) with the *ACT+SHR* fusion gene in tobacco plants, because chloroplast transformation is relatively routine in this species. Transplastomic tobacco lines were produced by particle gun–mediated chloroplast transformation and purified to homoplasmy by additional rounds of regeneration and selection. Transgene integration into the plastid genome by homologous recombination and elimination of all wild-type copies of the highly polyploid plastid genome were confirmed by restriction fragment length polymorphism analyses and inheritance assays (figs. S1E and S3A). All transplastomic lines (referred to as Nt-ptDP-ACT+SHR, Nt-ptSL-ACT+SHR, and Nt-ptHP-ACT+ SHR) displayed no visible phenotype and were indistinguishable from wild-type plants, both under in vitro culture conditions and upon growth in the greenhouse (fig. S3, B and D), indicating that dsRNA expression in the chloroplast is phenotypically neutral.

To test whether dsRNAs stably accumulate in chloroplasts, we performed Northern blot analyses. The results revealed that all three types of expression constructs triggered production of substantial amounts of long dsRNAs (Fig. 1B), suggesting the absence of efficient dsRNA-degrading mechanisms from plastids. dsRNA accumulation levels in Nt-ptDP and Nt-ptSL plants were very similar, indicating that the terminal stem-loop structures added to the ptSL constructs do not increase dsRNA stability (Fig. 1, A and B). dsRNA accumulation levels in Nt-ptHP lines were even higher but included shorter-than-expected transcripts (Fig. 1B), possibly because the plastid RNA polymerase encounters difficulties transcribing sequences containing large inverted repeats. Therefore, we used the convergent promoter approach (ptDP constructs) for dsRNA expression in all subsequent experiments.

We next introduced the three target gene constructs (*ACT*, *SHR*, and *ACT+SHR*, integrated into the ptDP cassette; Fig. 1A) into the plastid genome of potato (*14*) (see supplementary materials), the main host of CPB, and isolated homoplasmic transplastomic lines (St-ptDP-ACT, St-ptDP-SHR, and

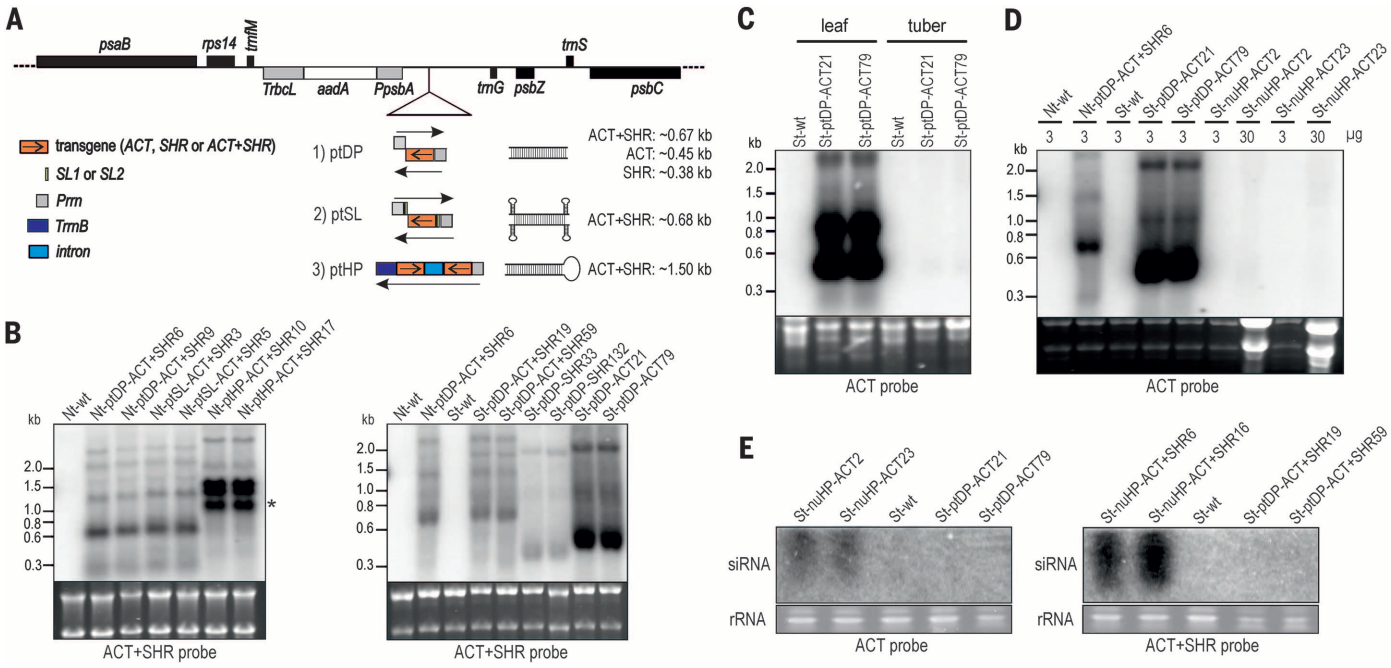

Fig. 1. Expression of dsRNAs in plastids. (**A**) Map of transformation vectors for dsRNA expression from the plastid genome. The cassettes designed to produce the three different types of dsRNAs (ptDP, ptSL, and ptHP) are schematically depicted below the map, along with the expected structures and sizes of the dsRNAs. The selectable marker gene *aadA* is driven by the *psbA* promoter (*PpsbA*) and the 3′ untranslated region (3′ UTR) of the *rbcL* gene (*TrbcL*) from *Chlamydomonas reinhardtii*. DNA sequences from CPB target genes are shown in orange. *SL1* and *SL2*, stem-loop–encoding sequences; *Prrn*, tobacco rRNA operon promoter; *TrrnB*, *rrnB* terminator from *E. coli*; intron, first intron from the potato GA20 oxidase gene. (**B**) Northern blot analysis of dsRNA accumulation in transplastomic tobacco and potato lines; 5 μg of total RNA was loaded in each lane, and the band sizes of the RNA marker are given at the left. The ethidium bromide–stained gel prior to blotting is shown below each blot. The asterisk indicates a shorter-than-expected transcript present in Nt-ptHP-ACT+SHR lines. Accumulation of some larger RNA species is likely due to read-through transcription, which is common in plastids (*22*, *23*). Note that transplastomic lines generated with the same construct show identical transgene expression levels due to targeting by homologous recombination. (**C**) Comparison of dsRNA accumulation levels in leaves and tubers of transplastomic potato lines expressing *ACT* dsRNA; 5 μg of total cellular RNA was loaded per lane. The ethidium bromide–stained gel prior to blotting is shown below the blot. (**D**) Analysis of *ACT* dsRNA accumulation by Northern blotting. The amount of total RNA loaded in each lane is given (in μg). The ethidium bromide–stained gel prior to blotting is shown below the blot as a loading control. Note that 10 times as much RNA was loaded for the nuclear transgenic lines. (**E**) Analysis of siRNA accumulation by Northern blotting. Note that siRNAs accumulate only in the nuclear transgenic plants but not in the transplastomic plants, confirming that the dsRNAs produced in the plastid stay put. Thus, although the CPB *ACT* sequence used has some similarity to the potato *ACT* gene (66% over a stretch of 226 nucleotides), it cannot even theoretically silence the plant's endogenous *ACT* gene because the chloroplast-produced dsRNAs do not leak out into the cytosol.

St-ptDP-ACT+SHR; fig. S1, B and F). To be able to compare the level of protection from herbivory in transplastomic and nuclear transgenic plants, we introduced the identical transgenes (as hairpin constructs containing a spliceosomal intron that is posttranscriptionally removed) (*15*) into the nuclear genome by *Agrobacterium*-mediated transformation (St-nuHP; fig. S1D). Phenotypic analyses showed that all transplastomic and nuclear transgenic potato plants were indistinguishable from wild-type plants with regard to growth and tuber production (fig. S3, C and E, and figs. S4 and S5).

Northern blot analyses of transplastomic potato lines revealed that the accumulation levels of *ACT* dsRNAs were higher than those of *SHR* and *ACT+SHR* dsRNAs (Fig. 1B). Comparison to a dilution series of in vitro synthesized RNA revealed dsRNA accumulation levels in leaves of ~0.4% of the total cellular RNA for *ACT*, ~0.05% for *SHR*, and ~0.1% for *ACT+SHR* (fig. S6). By contrast, hybridization signals in the nuclear transgenic

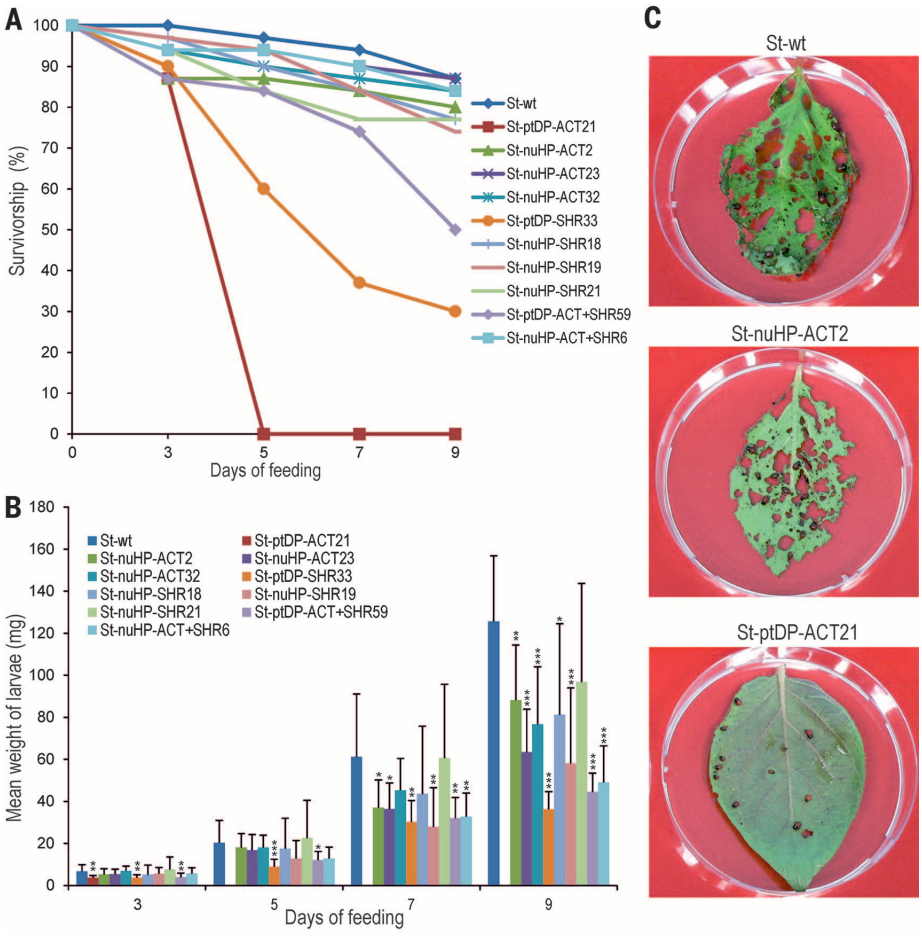

Fig. 2. Feeding assays of CPB larvae on transplastomic and nuclear transgenic potato plants. (**A**) Survivorship of first-instar larvae upon feeding on detached leaves of wild-type, transplastomic, and nuclear transgenic potato plants. (**B**) Growth of surviving larvae. The weight of survivors was determined after 3, 5, 7, and 9 days of feeding. Data are means ± SD (n = 30). Significant differences to the wild-type control were identified by analysis of variance. *P < 0.05, **P < 0.01, ***P < 0.001. The best-performing nuclear transgenic lines were included in the assay (see figs. S7 to S10). For assays with additional transplastomic lines, see fig. S9. Note that the weight of survivors in the assays with the transplastomic plants expressing *ACT* dsRNA (St-ptDP-ACT21) could only be measured until day 3, because all larvae were already dead at day 5 [see (A)]. (**C**) Example of a bioassay with detached leaves of wild-type potato plants and nuclear transgenic and transplastomic leaves expressing *ACT* dsRNA. Leaves were exposed to first-instar CPB larvae, replaced with fresh young leaves every day, and the photograph was taken at day 3. Note that almost no visible damage is seen in St-ptDP-ACT21 leaves.

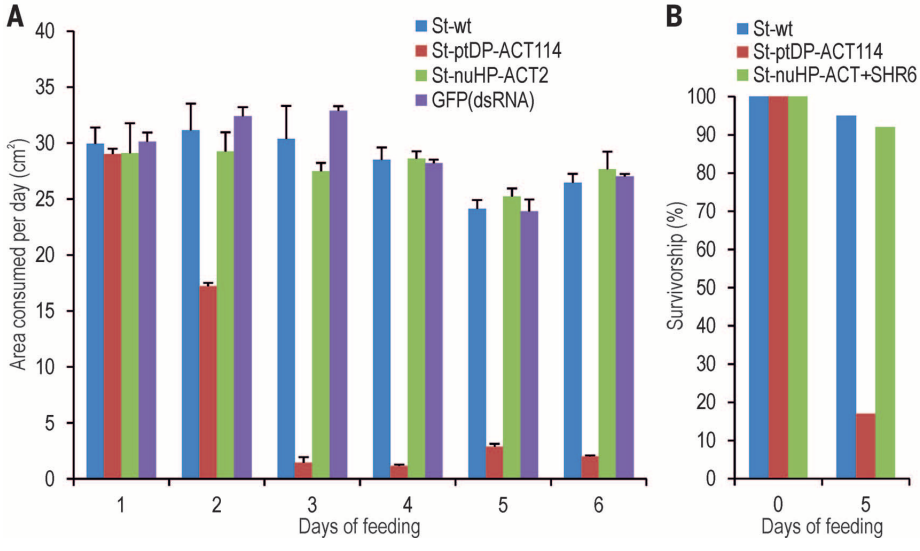

Fig. 3. Consumption of detached leaves of potato plants by adult beetles, and survivorship of larvae upon feeding on whole plants. (**A**) Leaf area consumed by freshly emerged adult beetles fed on leaves of wild-type potato plants, nuclear transgenic plants, and transplastomic plants expressing *ACT* dsRNA. As an additional control, leaves painted with in vitro synthesized *GFP*-derived dsRNA were included. Data are mean ± SD (n = 24 for St-wt, n = 12 for all other lines). (**B**) Survivorship of second-instar CPB larvae after feeding on whole plants at day 5 (see fig. S12).

plants could be detected only upon overloading of the gels and/or overexposure of the blots, consistent with efficient degradation of dsRNAs into siRNAs by the plant's endogenous RNAi machinery (Fig. 1D and figs. S7 and S8A). The presence of siRNAs in nuclear transgenic plants and their absence from transplastomic plants were directly confirmed by Northern blot analyses (Fig. 1E).

Because CPB larvae and adults feed on leaves but not on belowground potato tubers, only the leaves need to be protected from herbivory. Nonphotosynthetic tissues, such as tubers, express plastid to much lower levels than photosynthetic tissues, such as leaves (*16*, *17*). Thus, despite whole-plant transformation, dsRNA production in tubers, where accumulation of transgene-derived RNA is unnecessary and perhaps undesired by the consumer, was below or near the detection limit (Fig. 1C and fig. S8B).

Having established that long dsRNAs accumulate to high levels in leaves of transplastomic potato lines, we next tested whether dsRNA production in the chloroplast offers protection against CPB. To this end, the mortality of first-instar CPB larvae was determined upon feeding on detached leaves from wild-type, transplastomic, and nuclear transgenic potato plants for 9 consecutive days (Fig. 2A and fig. S9A). In addition, the weight of all surviving larvae was measured to follow their growth (Fig. 2, B and C; fig. S9, B to D; and fig. S10). The bioassays revealed that all transplastomic potato plants induced high mortality (Fig. 2, A and C, and fig. S9A). Consistent with the high expression level of *ACT* dsRNA (Fig. 1B and fig. S6) and the high efficacy of in vitro synthesized *ACT* dsRNA (fig. S2), the most potent insecticidal activity was conferred by the *ACT* dsRNA–expressing transplastomic plants that caused 100% mortality within 5 days. By contrast, none of the nuclear transgenic potato plants conferred any larval mortality (Fig. 2A and fig. S9A), in line with the earlier finding that short siRNAs fed to insects have only small effects or do not induce an RNAi response at all (*3*). However, all nuclear transgenic lines caused reduced growth of CPB larvae (Fig. 2B), presumably due to the small amounts of dsRNAs the plants accumulate (Fig. 1D and figs. S7 and S8). While none of the CPB larvae survived feeding on transplastomic St-ptDP-ACT plants, some of the larvae survived for 9 days on St-ptDP-SHR and St-ptDP-ACT+SHR leaves. However, these survivors suffered from very strong growth retardation (Fig. 2B and fig. S9, C and D).

To confirm that the killing of the CPB larvae by the transplastomic plants was due to induction of RNAi, we determined expression of the target genes in the larval gut after 3 days of feeding (i.e., when the larvae fed on the transplastomic plants were still alive). Already at this early stage, expression of β-actin and Shrub was suppressed in the insects (fig. S11, A and B). As expected on the basis of the mortality data (Fig. 2A), target gene suppression was strongest in larvae fed on St-ptDP-ACT plants. Moreover, accumulation of *ACT*-derived siRNAs was detected in gut tissue of larvae fed with transplastomic leaves, whereas accumulation in larvae fed with nuclear transgenic leaves was below the limit of reliable detection (fig. S11C).

CPB resistance of transplastomic potato plants was further assessed by determining the leaf area consumed by CPB larvae and adult beetles. Almost no visible consumption of leaf biomass occurred in St-ptDP-ACT leaves (Fig. 2C and fig. S12A), due to complete cessation of larval feeding after 24 hours, even prior to mortality (Fig. 2A). Similarly, adult beetles caused very little additional damage to St-ptDP-ACT leaves after 2 days (Fig. 3A). Finally, we exposed whole plants to second-instar larvae (which are generally less sensitive to insecticidal agents than first-instar larvae) and scored survival. This test resulted in 17% survival of the larvae after 5 days of feeding on St-ptDP-ACT plants (and 63% survival upon feeding on St-ptDP-SHR plants after 6 days; Fig. 3B, fig. S12, B to D, and fig. S13), presumably due to the initial larval growth and development on wild-type leaves. However, the larvae grew very poorly after transfer to the transplastomic plants, and the damage they caused to the leaves was very small (fig. S12, B to D). In nature, CPB larvae typically hatch and feed on the same plant, and therefore they would not enjoy a wild-type diet before feeding on the transplastomic plant.

To ultimately confirm that the plastid-expressed *ACT* dsRNA silences the actin gene in CPB larvae, we examined actin filaments in the larval midgut, hindgut, and Malpighian tubules by staining with fluorescein isothiocyanate (FITC)–labeled phalloidin. Already after 1 to 2 days of feeding on transplastomic leaves, the larvae displayed disorganized actin filaments, which were particularly obvious in the columnar cells of the midgut (fig. S14). Also, the intensity of phalloidin-FITC labeling progressively decreased with the time of feeding (fig. S14), which suggests that actin deficiency is the cause of death. RNA-dependent RNA polymerase (RdRP) genes are absent from the genomes of insects (*18*). Therefore, silencing signals are not amplified at the RNA level, and RNAi effects remain restricted to those cells that have taken up (or produced) silencing-inducing dsRNAs. Consequently, a continuous input of dsRNAs is required for efficient gene silencing in insects. Because of the low stability of dsRNAs expressed from the nuclear genome and their efficient processing by the plant's own Dicer endoribonucleases, complete protection of plants from insect pests has not been accomplished (*1*, *2*). Our findings underscore the importance of producing large amounts of long dsRNAs to achieve efficient protection. Whereas transplastomic *ACT* dsRNA–expressing plants cause 100% lethality to CPB larvae, *SHR* dsRNA–expressing plants are somewhat less efficient (70% mortality after 9 days; Fig. 2A). This correlates with the factor of ~8 lower accumulation levels of the *SHR* dsRNA. Because both constructs are driven by the same expression signals, we conclude that the *SHR* sequence chosen is less stable in potato plastids than the *ACT* sequence. Consequently, testing other fragments of the *SHR* gene seems an appropriate future strategy to improve the insecticidal efficiency of *SHR* dsRNA–expressing transplastomic plants.

As insect pests are developing increasing resistance to chemical insecticides and Bt toxins (*12*, *19*–*21*), RNAi technology is becoming a promising future strategy for plant protection. RNAi-activating dsRNAs can be chosen from a vast number of potential target genes. Moreover, the dsRNA approach provides plant protection without chemicals and without synthesis of foreign proteins in the plant. We have shown that plastids can be engineered to produce the quantities of dsRNA needed to control a major agricultural pest, the Colorado potato beetle. Shifting the target of transgenesis from the nucleus to the plastid removes the major hurdle on the way to exploiting transgenically delivered RNAi for efficient plant protection in the field (*18*).

REFERENCES AND NOTES

1. J. A. Baum *et al.*, *Nat. Biotechnol.* **25**, 1322–1326 (2007).
2. Y.-B. Mao *et al.*, *Nat. Biotechnol.* **25**, 1307–1313 (2007).
3. R. Bolognesi *et al.*, *PLOS ONE* **7**, e47534 (2012).
4. S. Whyard, A. D. Singh, S. Wong, *Insect Biochem. Mol. Biol.* **39**, 824–832 (2009).
5. W. Zha *et al.*, *PLOS ONE* **6**, e20504 (2011).
6. M. Pitino, A. D. Coleman, M. E. Maffei, C. J. Ridout, S. A. Hogenhout, *PLOS ONE* **6**, e25709 (2011).
7. P. Kumar, S. S. Pandit, I. T. Baldwin, *PLOS ONE* **7**, e31347 (2012).
8. J.-Q. Zhu *et al.*, *PLOS ONE* **7**, e38572 (2012).
9. F. Vazquez, S. Legrand, D. Windels, *Trends Plant Sci.* **15**, 337–345 (2010).
10. M. Kumar, G. P. Gupta, M. V. Rajam, *J. Insect Physiol.* **55**, 273–278 (2009).
11. D. B. Stern, W. Gruissem, *Cell* **51**, 1145–1157 (1987).
12. A. Alyokhin, M. Baker, D. Mota-Sanchez, G. Dively, E. Grafius, *Am. J. Potato Res.* **85**, 395–413 (2008).
13. F. Zhu, J. Xu, R. Palli, J. Ferguson, S. R. Palli, *Pest Manag. Sci.* **67**, 175–182 (2011).
14. V. T. Valkov *et al.*, *Transgenic Res.* **20**, 137–151 (2011).
15. N. A. Smith *et al.*, *Nature* **407**, 319–320 (2000).
16. S. Kahlau, R. Bock, *Plant Cell* **20**, 856–874 (2008).
17. V. T. Valkov *et al.*, *Plant Physiol.* **150**, 2030–2044 (2009).
18. D. R. Price, J. A. Gatehouse, *Trends Biotechnol.* **26**, 393–400 (2008).
19. L. J. Gahan, F. Gould, D. G. Heckel, *Science* **293**, 857–860 (2001).
20. J. S. Griffitts, J. L. Whitacre, D. E. Stevens, R. V. Aroian, *Science* **293**, 860–864 (2001).
21. A. J. Gassmann *et al.*, *Proc. Natl. Acad. Sci. U.S.A.* **111**, 5141–5146 (2014).
22. F. Zhou, D. Karcher, R. Bock, *Plant J.* **52**, 961–972 (2007).
23. M. Oey, M. Lohse, B. Kreikemeyer, R. Bock, *Plant J.* **57**, 436–445 (2009).

ACKNOWLEDGMENTS

We thank P. Endries for help with plant transformation, E. Maximova for help with microscopy, Y. Zhang for providing phalloidin-FITC, the MPI-MP Greenteam for plant cultivation, M. Kaltenpoth and B. Weiss for help in insect tissue preparation, and T. Krügel and the MPI-CE greenhouse team. This research was financed by the Max Planck Society. Plastid transformation vectors and transplastomic plants are available under a material transfer agreement. J.Z., S.A.K., D.G.H., R.B., and the Max Planck Society (MPG) have filed a patent application (EP14199415) that relates to the transplastomic production of dsRNAs for plant protection. Supplement contains additional data.

SUPPLEMENTARY MATERIALS

www.sciencemag.org/content/347/6225/991/suppl/DC1
Materials and Methods
Figs. S1 to S14
Table S1
References (*24*–*37*)

24 September 2014; accepted 12 January 2015
10.1126/science.1261680

EBOLA VIRUS

Two-pore channels control Ebola virus host cell entry and are drug targets for disease treatment

Yasuteru Sakurai,[1] Andrey A. Kolokoltsov,[2] Cheng-Chang Chen,[3] Michael W. Tidwell,[4] William E. Bauta,[4] Norbert Klugbauer,[5] Christian Grimm,[3] Christian Wahl-Schott,[3] Martin Biel,[3] Robert A. Davey[1]*

Ebola virus causes sporadic outbreaks of lethal hemorrhagic fever in humans, but there is no currently approved therapy. Cells take up Ebola virus by macropinocytosis, followed by trafficking through endosomal vesicles. However, few factors controlling endosomal virus movement are known. Here we find that Ebola virus entry into host cells requires the endosomal calcium channels called two-pore channels (TPCs). Disrupting TPC function by gene knockout, small interfering RNAs, or small-molecule inhibitors halted virus trafficking and prevented infection. Tetrandrine, the most potent small molecule that we tested, inhibited infection of human macrophages, the primary target of Ebola virus in vivo, and also showed therapeutic efficacy in mice. Therefore, TPC proteins play a key role in Ebola virus infection and may be effective targets for antiviral therapy.

Ebola viruses (EBOVs), together with Marburgvirus, are a highly diverse group of viruses that constitute the *Filoviridae*. Almost all of them, including the strain responsible for the latest outbreak in West Africa, cause a highly lethal, rapidly progressing hemorrhagic fever in humans and nonhuman primates (*1*, *2*). However, there is currently no licensed drug treatment or broadly active vaccine (*3*), making them important public health threats and potential biothreat agents. Because, like most viruses, EBOV depends on host cell factors to complete its life cycle (*4*), blocking such interactions may have a large impact on infection and disease outcome. Recent successes in cell culture and some animal models suggest that this approach holds promise for rapidly bringing new drugs to the clinic (*5*).

EBOV binds to several types of cell surface proteins to initiate host cell entry (*6*–*8*), after which it is internalized by macropinocytosis and follows an endosomal route to reach acidic compartments (*9*, *10*). There, host proteases such as cathepsins cleave the viral glycoproteins (GPs) (*11*), which bind to the endosomal membrane protein, NPC1, and eventually facilitate the release of the viral core to the cell cytoplasm, where replication begins (*12*, *13*). Previously, we showed that host calcium signaling proteins were important for EBOV host cell entry but were unable to identify the functional mechanism nor address whether they could be therapeutic targets (*14*).

To identify and characterize upstream effectors regulating calcium signaling in the context of EBOV infection, we tested the importance of calcium channels using antagonists for each of the four common channel types (Fig. 1, A to C, and fig. S1). Only compounds blocking L-type channels inhibited EBOV infection in HeLa cells, which is consistent with previous reports (*15*, *16*). Verapamil, a drug approved by the U.S. Food and Drug Administration (FDA) to treat cardiovascular diseases, efficiently inhibited EBOV infection with a half-maximal inhibitory concentration (IC_{50}) of 4 μM (Fig. 1A). Similarly, two other structurally distinct L-type channel antagonists, nimodipine and diltiazem, also reduced EBOV infection efficiency (fig. S1, A and B). Tetrandrine, originally isolated from Chinese and Japanese herbs but now produced synthetically, was especially potent, with an IC_{50} of 55 nM (Fig. 1B). By contrast, gabapentin, representing a fifth distinct class of L-type channel inhibitor, had no effect, even at high concentrations (Fig. 1C). This finding suggested that classical L-type channels were not the upstream factor in EBOV calcium-channel dependence. Recently, verapamil, nimodipine, and diltiazem were shown to also

[1]Texas Biomedical Research Institute, San Antonio, TX, USA. [2]The University of Texas Medical Branch, Galveston, TX, USA. [3]Center for Integrated Protein Science Munich (CIPSM) at the Department of Pharmacy–Center for Drug Research, Ludwig-Maximilians-Universität München, Munich, Germany. [4]Southwest Research Institute, San Antonio, TX, USA. [5]Institute for Experimental and Clinical Pharmacology and Toxicology, Albert-Ludwigs-Universität Freiburg, Freiburg, Germany.
*Corresponding author. E-mail: rdavey@txbiomed.org

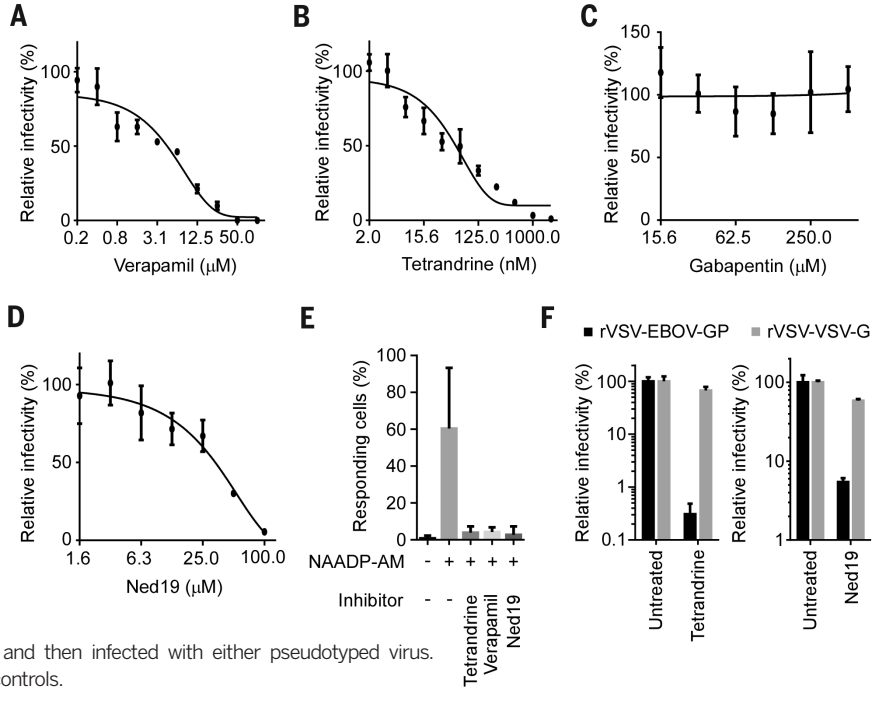

Fig. 1. Inhibitors of NAADP signaling block EBOV infection. Dose-response curves for verapamil (**A**), tetrandrine (**B**), gabapentin (**C**), and Ned19 (**D**) were determined by pretreating HeLa cells with the indicated doses of each compound and then infecting the cells with a recombinant EBOV encoding green fluorescent protein (GFP) as a marker of infection (EBOV-GFP). Infection efficiencies were calculated by dividing the numbers of GFP-positive cells by those of total cells and normalizing the infectivity to untreated cells (mean ± SD, n = 3). Each data set is representative of three independent experiments. (**E**) The effect of the indicated compounds on NAADP-stimulated calcium release was measured by stimulating cells with 1 μM NAADP-AM (*30*, *31*) or control dimethyl sulfoxide and imaging cell fluorescence after addition of the calcium-sensitive dye Fluo-4. Cells showing $F_{max}/F_0 > 2$ (F_{max}: maximum fluorescence intensity; F_0: mean fluorescence intensity before stimulation) were counted as responsive cells. At least 800 cells were analyzed for each treatment, and data averaged over three experiments ± SD. (**F**) Pseudotyped viruses bearing the glycoproteins of EBOV (rVSV-EBOV-GP) or VSV (rVSV-VSV-G) and encoding firefly luciferase as an infection marker were used to show entry dependence of EBOV on NAADP signaling. Cells were treated with tetrandrine (2 μM) or Ned19 (100 μM) and then infected with either pseudotyped virus. Luciferase activities were normalized to those of untreated controls.

inhibit calcium signaling triggered by nicotinic acid adenine dinucleotide phosphate (NAADP) (*17*). NAADP is a highly potent intracellular calcium–mobilizing agent and stimulates intracellular calcium channels to release Ca^{2+} from endosomes and lysosomes (*18*). This pathway is specifically blocked by the small-molecule antagonist Ned19 (*19*). We found that Ned19 also blocked EBOV infection (Fig. 1D). All inhibitors tested showed

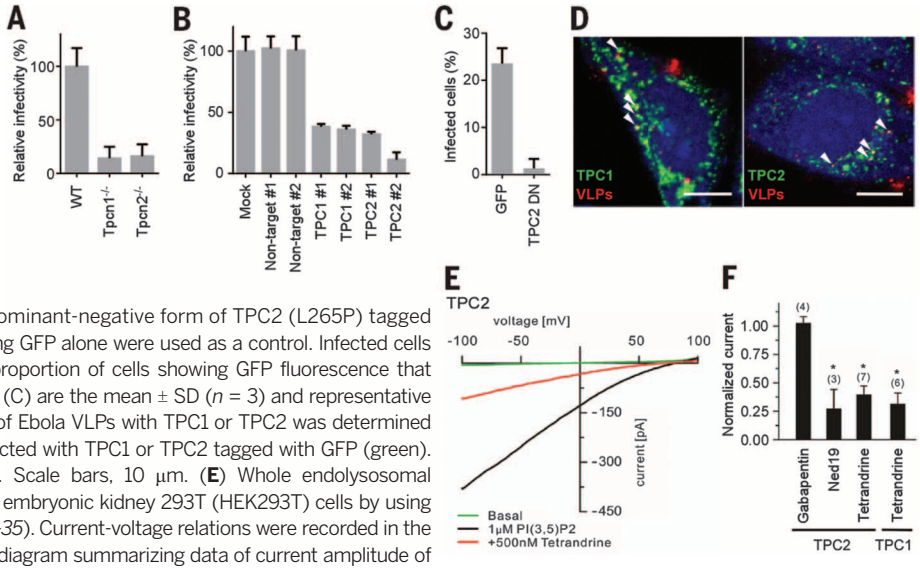

Fig. 2. The endosomal calcium channels TPC1 and TPC2 are necessary for EBOV infection. (**A**) MEFs from wild-type (WT), *Tpcn1*$^{-/-}$, or *Tpcn2*$^{-/-}$ mice (*25*, *32*) were infected with EBOV-GFP. The frequency of GFP-positive cells in the total cell population was normalized to that of total cells. (**B**) HeLa cells were transfected with either two independent nontargeting, TPC1-specific, or TPC2-specific siRNAs and infected with EBOV-GFP. The frequency of GFP-positive cells in the total cell population was normalized to that of mock-transfected cells. (**C**) HeLa cells overexpressing a dominant-negative form of TPC2 (L265P) tagged with GFP were infected with WT EBOV. Cells expressing GFP alone were used as a control. Infected cells were detected with antibody against EBOV GP. The proportion of cells showing GFP fluorescence that were infected was calculated. All data for (A), (B), and (C) are the mean ± SD (n = 3) and representative of three independent experiments. (**D**) Colocalization of Ebola VLPs with TPC1 or TPC2 was determined by incubating VLPs (red) for 2 hours with cells transfected with TPC1 or TPC2 tagged with GFP (green). Colocalized particles were indicated by arrowheads. Scale bars, 10 μm. (**E**) Whole endolysosomal currents were recorded from TPC2-expressing human embryonic kidney 293T (HEK293T) cells by using modified conventional patch-clamp with $PI(3,5)P_2$ (*33*–*35*). Current-voltage relations were recorded in the presence or absence of tetrandrine (500 nM). (**F**) Bar diagram summarizing data of current amplitude of TPC2 or TPC1 in the presence of gabapentin (100 μM), Ned19 (200 μM), or tetrandrine (500 nM), normalized to those before drug application. *P < 0.001 using analysis of variance, compared to current in the presence of gabapentin for TPC2 or without inhibitors for TPC1. Data are the mean ± SEM.

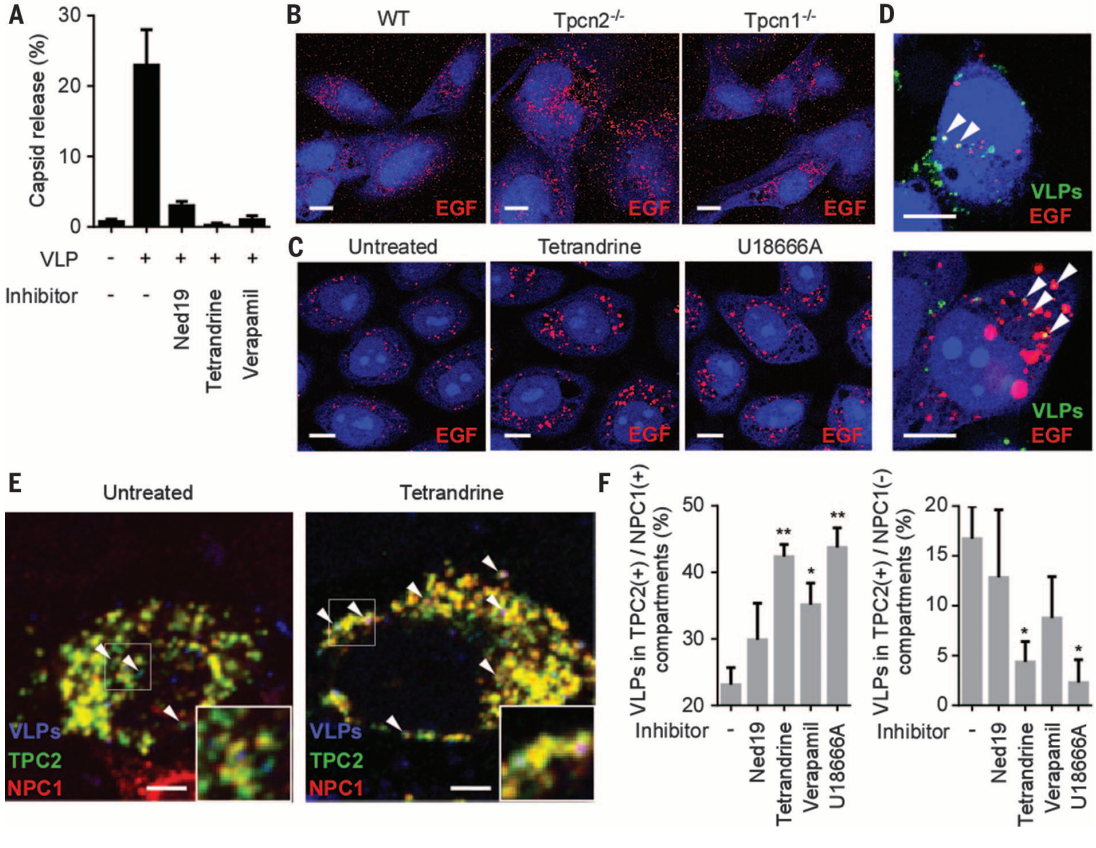

Fig. 3. Blocking TPC function affects EBOV entry through endosomal compartments. (**A**) VLPs loaded with β-lactamase were used to measure membrane fusion and virus capsid release into the cytoplasm after each treatment (as for fig. S10). The number of cells showing signal was divided by the number of total cells. (**B**) Evaluation of EGF trafficking in TPC knockout cells. Representative confocal images of WT, *Tpcn2*$^{-/-}$, and *Tpcn1*$^{-/-}$ MEFs incubated with AlexaFluor555-EGF. (**C**) Evaluation of EGF trafficking in tetrandrine or U18666A-treated cells. Representative confocal images of HeLa cells incubated with AlexaFluor555-EGF (red) in the presence or absence of tetrandrine or U18666A. (**D**) Colocalization of Ebola VLPs and EGF. HeLa cells were incubated with AlexaFluor555-EGF (red) for 30 min followed by Ebola VLPs (green) for 3.5 hours in the presence of tetrandrine. VLPs were stained with a GP-specific antibody. Examples of colocalized particles are indicated by arrowheads. Scale bars (B to D): 10 μm. (**E**) Effect of tetrandrine on colocalization of Ebola VLPs with TPC2- and/or NPC1-positive endosomes was measured. HeLa cells overexpressing GFP-tagged TPC2 (green) and Myc-tagged NPC1 (red) were pretreated with inhibitors and incubated with VLPs (blue) for 4 hours. Insets show magnified areas of the image, and arrowheads indicate examples of VLPs that are associated with the TPC2(+)/NPC1(−) compartment (left panel) or the TPC2(+)/NPC1(+) compartment (right panel). Scale bars, 5 μm. (**F**) In the presence of the indicated inhibitors, the ratio of VLPs colocalizing with the TPC2(+)/NPC1(+) compartment (left) or the TPC2 (+)/NPC1(−) compartment (right) was calculated. *P < 0.05 and **P < 0.005, using unpaired Student's t test to compare treated to untreated cells. Data are the mean ± SEM (n = 3 or 4).

no cytotoxicity at the highest concentration used (fig. S2). Like verapamil and Ned19, tetrandrine was also a potent inhibitor of NAADP-stimulated calcium release (Fig. 1E and fig. S3). These results suggested a role for NAADP-stimulated calcium channels in EBOV infection and that tetrandrine could block this host factor.

NAADP has been suggested to regulate endosome maturation through vesicular fusion and trafficking (*20*). This would suggest a role in virus entry into cells, which was tested with pseudotyped viruses. Infection of cells by recombinant vesicular stomatitis virus bearing the glycoprotein of EBOV (rVSV-EBOV-GP) was highly sensitive to tetrandrine, verapamil, or Ned19 (Fig. 1F and fig. S4A). This suggests that NAADP-stimulated channel activity specifically affects the GP-mediated entry step of EBOV. Moreover, tetrandrine and verapamil potently inhibited infection of recombinant VSV bearing Marburgvirus glycoprotein, but inhibited infection only weakly for VSV, Lassa virus, Venezuelan equine encephalitis virus, or Rabies virus (Fig. 1F and fig. S4, B and C), suggesting that filoviruses are much more dependent on this pathway than are other virus types.

To gain further insight into the connection between the NAADP-mediated pathway and EBOV infection, we sought to identify the effector calcium channel required for the infection. Recent studies have shown that two-pore channels (TPCs) are the major calcium channels activated by NAADP (*21*). They are also activated by the phosphatidylinositol 3,5-bisphosphate [$PI(3,5)P_2$] and are highly conserved proteins with both TPC1 and TPC2 present in humans, mice, and other animals (*22*). We found that mouse embryonic fibroblasts (MEFs) lacking TPC1 or TPC2 expression ($Tpcn1^{-/-}$ or $Tpcn2^{-/-}$) resisted EBOV infection (Fig. 2A). Overexpression of human TPCs in the mutant cells significantly recovered the infectivity (fig. S5), suggesting the specific effects of gene knockout. Similarly, even though suppression of TPC expression by small interfering RNAs (siRNAs) was incomplete (fig. S6), EBOV infection was reduced in HeLa cells transfected with either TPC1 or TPC2 siRNAs (Fig. 2B). In addition, overexpression of a dominant-negative form of TPC2, which was reported to efficiently block NAADP-stimulated calcium release (*23*), inhibited EBOV infection (Fig. 2C). Furthermore, Ebola virus-like particles (VLPs) incubated with cells localized to TPC1- and TPC2-positive endosomal compartments (Fig. 2D). Whole endolysosomal patch-clamp analyses showed that tetrandrine blocked both TPC1- and TPC2-mediated current elicited by $PI(3,5)P_2$ as well as NAADP (Fig. 2, E and F, and fig. S7). In contrast, gabapentin, which did not inhibit virus infection, had no effect on TPC2 function. Together, our data showed that TPCs, the effector channels of NAADP and $PI(3,5)P_2$-mediated signaling, are important for EBOV infection, probably while virus is inside endosomes. Calcium channel inhibitors targeted TPCs, with tetrandrine being the most potent.

During host cell entry, EBOV is transported to acidic endosomes, which express lysosomal-associated membrane protein 1 (LAMP1) (*9*). We found that VLPs still localized to LAMP1-positive vesicles in $Tpcn1^{-/-}$ and $Tpcn2^{-/-}$ MEFs, as well as inhibitor-treated cells (fig. S8), indicating that this step was unaffected. The EBOV GP is then cleaved by endosomal cysteine proteases before virus-endosome membrane fusion can occur (*11*), and so we next examined whether precleaved GPs could overcome the action of the inhibitory drugs using rVSV-EBOV-GP pretreated with the protease thermolysin. Treatment with Ned19, tetrandrine, or verapamil still efficiently blocked precleaved virus infection, but a control cysteine protease inhibitor, E-64-D, did not (fig. S9), indicating that the calcium channel inhibitors affect a late entry step after GP proteolysis in endosomes. When membrane fusion was evaluated, with a virus contents release assay (*24*), these inhibitors significantly reduced the contents mixing signal (Fig. 3A and fig. S10), indicating that virus-endosome membrane fusion and virus capsid release into the cell cytoplasm were arrested.

A recent study showed that blocking TPC2 function resulted in accumulation of epidermal growth factor (EGF) in LAMP1-positive endosomal compartments, suggesting a block of endosomal trafficking in these acidic compartments (*25*). We found that tetrandrine-treated HeLa cells showed a similar accumulation of EGF, as well as $Tpcn2^{-/-}$ MEFs, whereas $Tpcn1^{-/-}$ MEFs showed less EGF accumulation (Fig. 3, B and C). Moreover, Ebola VLPs and EGF colocalized in tetrandrine-treated cells (Fig. 3D), suggesting that both use or converge upon a common endosomal trafficking route that is regulated by TPCs. Previously, EBOV entry was shown to be dependent on another endosomal protein, NPC1 (*12*, *13*). The small molecule U18666A induces a phenotype that mimics NPC1 deficiency, leading to cholesterol accumulation in endosomes. When cells were treated with U18666A, the pattern of EGF accumulation was similar to that seen after treatment with tetrandrine (Fig. 3C). Moreover, treatment of rVSV-EBOV-GP–infected cells with verapamil or U18666A revealed similar inhibitory kinetics, with each becoming ineffective when the drug was added 1.5 to 2 hours after infection (fig. S11), suggesting that each affected virus infection close to the same time. To further study this relationship and characterize the infection step affected by TPCs, we investigated viral colocalization with NPC1 or TPC2 (Fig. 3E). In untreated cells, VLPs were found in compartments containing both NPC1 and TPC2, as well as a distinct compartment containing only TPC2. However, treatment with tetrandrine significantly (and with other channel inhibitors less potently) increased accumulation of VLPs in the TPC2(+)/NPC1(+) compartment while proportionately decreasing TPC2(+)/NPC1(–) compartment colocalization (Fig. 3F). These results suggest that disrupting endosomal trafficking with tetrandrine potently alters viral distribution such that VLPs are retained in the NPC1(+) compartment.

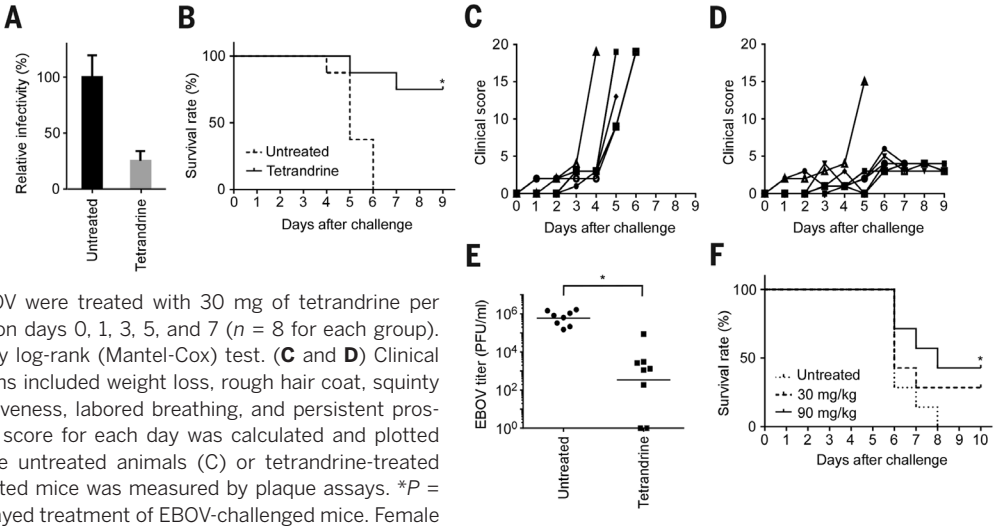

Fig. 4. Tetrandrine inhibits EBOV infection both in vitro and in vivo. (**A**) Macrophages were treated with tetrandrine (8 μM) and then infected with EBOV-GFP. After 48 hours, the frequency of GFP-positive cells was calculated and normalized to that of untreated controls. The data are the mean ± SD (n = 3) and representative of two independent experiments. (**B**) Female Balb/c mice injected intraperitoneally with mouse-adapted EBOV were treated with 30 mg of tetrandrine per kilogram of body weight or control saline on days 0, 1, 3, 5, and 7 (n = 8 for each group). Survival curves are shown. *P = 0.0008 by log-rank (Mantel-Cox) test. (**C** and **D**) Clinical scores of EBOV-infected mice. Disease signs included weight loss, rough hair coat, squinty eyes, hunched back, moderate unresponsiveness, labored breathing, and persistent prostration. Based on these criteria, a clinical score for each day was calculated and plotted (individually indicated by symbols) for the untreated animals (C) or tetrandrine-treated animals (D). (**E**) Virus titer in sera of infected mice was measured by plaque assays. *P = 0.006 by unpaired Student's t test. (**F**) Delayed treatment of EBOV-challenged mice. Female Balb/c mice injected intraperitoneally with mouse-adapted EBOV were treated with tetrandrine (30 or 90 mg/kg) or control saline on days 1, 3, 5, and 7 (n = 7 for each group). Survival curves are shown. *P = 0.04 by log-rank (Mantel-Cox) test comparing treated to untreated animals.

Because decreased colocalization with the TPC2 (+)/NPC1(−) compartment correlated with reduced infectivity, EBOV likely uses this compartment to enter host cells. Treatment with U18666A again resulted in VLP localization similar to that seen with calcium channel inhibitors (Fig. 3F). This may be explained by a recent report showing that U18666A treatment caused endosomal calcium depletion. Moreover, cells carrying a defective NPC1 were shown to have a loss of NAADP response, suggesting a close association of TPCs and NPC1 in host cells, which may affect EBOV infection (*26*).

Finally, we addressed whether TPC function could be targeted for anti-EBOV therapy. First, primary macrophages, an initial target of virus infection in humans and other animals, were evaluated. Similar to its effect in HeLa cells, tetrandrine potently blocked EBOV infection in human monocyte-derived macrophages, with verapamil and Ned19 being effective but requiring high doses (Fig. 4A and fig. S12) that did not show cytotoxicity. Of these, tetrandrine was the best candidate for animal testing because of its high potency and low cytotoxicity in culture. Moreover, the dose of tetrandrine needed to inhibit virus infection (IC_{50} = 55 nM) was at least a factor of 40 less than safe plasma concentrations achieved in mice and was reported to have good pharmacological properties, being well tolerated and having a long circulatory time (*27*). We therefore assessed therapeutic efficacy in the mouse model of EBOV disease (*28*). Mice were challenged with mouse-adapted EBOV and then given tetrandrine or saline every 2 days for 1 week. Starting tetrandrine treatment soon after infection significantly enhanced the survival of mice without any detectable side effects (Fig. 4B). Clinical scores in treated mice remained low compared to the control group (Fig. 4, C and D, and fig. S13). Virus titers in sera measured at day 3 after inoculation showed a factor of 1000 decrease (Fig. 4E), and by day 9 virus was undetectable. Furthermore, when the treatment was started 1 day after virus challenge, half the mice survived (Fig. 4F). These results indicate that tetrandrine is highly effective against disease in mice.

Taken together, we identified a role for TPCs in EBOV infection. These calcium channels appear responsible for controlling movement of endosomes containing virus particles. By disrupting TPC function, we prevented EBOV from escaping the endosomal network into the cell cytoplasm, halting infection. TPCs proved effective targets for existing drugs, with the bisbenzylisoquinoline alkaloid, tetrandrine, being the most potent. This may be due to its ability to block both TPC1 and TPC2, which regulate different stages of endosomal trafficking (*22*). Tetrandrine is one representative from this drug class; other members are found in plants around the world (*29*) and may also block EBOV infection. Because the entry of Marburgvirus, a distantly related filovirus, was also affected, it is likely that all filoviruses require TPC function to infect cells and that tetrandrine is a broad-spectrum filovirus inhibitor.

REFERENCES AND NOTES

1. H. Feldmann, T. W. Geisbert, *Lancet* **377**, 849–862 (2011).
2. S. Baize *et al.*, *N. Engl. J. Med.* **371**, 1418–1425 (2014).
3. B. M. Friedrich *et al.*, *Viruses* **4**, 1619–1650 (2012).
4. O. Dolnik, L. Kolesnikova, S. Becker, *Cell. Mol. Life Sci.* **65**, 756–776 (2008).
5. M. S. Boguski, K. D. Mandl, V. P. Sukhatme, *Science* **324**, 1394–1395 (2009).
6. C. P. Alvarez *et al.*, *J. Virol.* **76**, 6841–6844 (2002).
7. A. Takada *et al.*, *J. Virol.* **78**, 2943–2947 (2004).
8. A. S. Kondratowicz *et al.*, *Proc. Natl. Acad. Sci. U.S.A.* **108**, 8426–8431 (2011).
9. M. F. Saeed, A. A. Kolokoltsov, T. Albrecht, R. A. Davey, *PLOS Pathog.* **6**, e1001110 (2010).
10. A. Nanbo *et al.*, *PLOS Pathog.* **6**, e1001121 (2010).
11. K. Chandran, N. J. Sullivan, U. Felbor, S. P. Whelan, J. M. Cunningham, *Science* **308**, 1643–1645 (2005).
12. M. Côté *et al.*, *Nature* **477**, 344–348 (2011).
13. J. E. Carette *et al.*, *Nature* **477**, 340–343 (2011).
14. A. A. Kolokoltsov, M. F. Saeed, A. N. Freiberg, M. R. Holbrook, R. A. Davey, *Drug Dev. Res.* **70**, 255–265 (2009).
15. P. B. Madrid *et al.*, *PLOS ONE* **8**, e60579 (2013).
16. G. Gehring *et al.*, *J. Antimicrob. Chemother.* **69**, 2123–2131 (2014).
17. A. A. Genazzani *et al.*, *Br. J. Pharmacol.* **121**, 1489–1495 (1997).
18. A. Galione, *Cold Spring Harb. Perspect. Biol.* **3**, a004036 (2011).
19. E. Naylor *et al.*, *Nat. Chem. Biol.* **5**, 220–226 (2009).
20. M. Ruas *et al.*, *Curr. Biol.* **20**, 703–709 (2010).
21. P. J. Calcraft *et al.*, *Nature* **459**, 596–600 (2009).
22. M. X. Zhu *et al.*, *Am. J. Physiol. Cell Physiol.* **298**, C430–C441 (2010).
23. E. Brailoiu *et al.*, *J. Biol. Chem.* **285**, 38511–38516 (2010).
24. O. Martinez *et al.*, *Cell. Microbiol.* **12**, 148–157 (2010).
25. C. Grimm *et al.*, *Nat. Commun.* **5**, 4699 (2014).
26. E. Lloyd-Evans *et al.*, *Nat. Med.* **14**, 1247–1255 (2008).
27. C. L. Dai *et al.*, *Cancer Chemother. Pharmacol.* **60**, 741–750 (2007).
28. M. Bray, K. Davis, T. Geisbert, C. Schmaljohn, J. Huggins, *J. Infect. Dis.* **179** (suppl. 1), S248–S258 (1999).
29. C. Y. Kwan, F. I. Achike, *Acta Pharmacol. Sin.* **23**, 1057–1068 (2002).
30. R. Aarhus, R. M. Graeff, D. M. Dickey, T. F. Walseth, C. L. Hon, *J. Biol. Chem.* **270**, 30327–30333 (1995).
31. R. Parkesh *et al.*, *Cell Calcium* **43**, 531–538 (2008).
32. L. Arndt *et al.*, *Mol. Biol. Cell* **25**, 948–964 (2014).
33. X. Wang *et al.*, *Cell* **151**, 372–383 (2012).
34. C. Cang *et al.*, *Cell* **152**, 778–790 (2013).
35. C. Cang, B. Bekele, D. Ren, *Nat. Chem. Biol.* **10**, 463–469 (2014).

ACKNOWLEDGMENTS

All BSL4 work was performed at Texas Biomedical Research Institute by Y.S. and veterinary staff. For advice about preparation of NAADP-AM, we thank G. Churchill. For guidance and use of their high-performance liquid chromatography system, we thank A. Hayhurst and L. Sherwood. We thank D. Ren (University of Pennsylvania) for guidance in using the modified patch clamp. A. Reyes and J. Bentz provided technical support. O. Shtanko and M. Anantpadma gave helpful discussions and advice. We also thank all those cited in Materials and Methods for reagents. The data presented in this manuscript are tabulated in the main paper and in the supplementary materials. R.A.D and A.A.K. are inventors on U.S. patent 8,889,743, issued 28 November 2014, entitled "Inhibition of filovirus entry into cells and uses thereof." This work was supported by NIH R01AI063513, DOD/DTRA HDTRA1-12-1-0002, Project FRBAA09-6H-2-0043, the Ewing Halsell Foundation, and SFB TRR 152 TP04, TP05, TP06, and TP12.

SUPPLEMENTARY MATERIALS

www.sciencemag.org/content/347/6225/995/suppl/DC1
Materials and methods
Figs. S1 to S13

15 July 2014; accepted 20 January 2015
10.1126/science.1258758

ARCHAEOLOGY

Sedimentary DNA from a submerged site reveals wheat in the British Isles 8000 years ago

Oliver Smith,[1] Garry Momber,[2] Richard Bates,[3] Paul Garwood,[4] Simon Fitch,[5] Mark Pallen,[6]* Vincent Gaffney,[7]* Robin G. Allaby[1]*†

The Mesolithic-to-Neolithic transition marked the time when a hunter-gatherer economy gave way to agriculture, coinciding with rising sea levels. Bouldnor Cliff, is a submarine archaeological site off the Isle of Wight in the United Kingdom that has a well-preserved Mesolithic paleosol dated to 8000 years before the present. We analyzed a core obtained from sealed sediments, combining evidence from microgeomorphology and microfossils with sedimentary ancient DNA (sedaDNA) analyses to reconstruct floral and faunal changes during the occupation of this site, before it was submerged. In agreement with palynological analyses, the sedaDNA sequences suggest a mixed habitat of oak forest and herbaceous plants. However, they also provide evidence of wheat 2000 years earlier than mainland Britain and 400 years earlier than proximate European sites. These results suggest that sophisticated social networks linked the Neolithic front in southern Europe to the Mesolithic peoples of northern Europe.

The Mesolithic-to-Neolithic transition is associated with the replacement of a hunter-gatherer economy by arable farming of crops such as einkorn, emmer, and barley. Although it is generally accepted that the Neolithic had arrived by 6000 years before the present (yr B.P.) on the British mainland, controversy surrounds the timing and mode of Neolithization in the British Isles (*1*). It also remains unclear whether the arrival of Neolithic technologies on the mainland was rapid, facilitated by the arrival of migrating farmers, who displaced or acculturated existing hunter-gatherers (*2*); or whether hunter-gatherers gradually transitioned to

a Neolithic economy, with increasing dependency on cereals over millennia (*3*).

The Neolithic arrived on the British mainland during a warming period in which sea levels rose and inundated land between Britain and Europe, forming the English Channel and much of the North Sea (*3*–*7*). We hypothesized that the earliest stages of Neolithization in the British Isles occurred in these lowland regions.

Some Mesolithic paleosols, representing the old land surface, have been preserved under marine sediments, including a paleosol from Bouldnor Cliff, off the Isle of Wight in the Western Solent. The site has been dated to 8030 to 7980 calendar (cal) yr B.P. (*8*) (Fig. 1 and table S1), placing it in the late Mesolithic of the British Isles, a period that is represented by few assemblages and is still little understood. This paleosol formed along the edge of an ancient valley that was dissected by a river and fed by tributaries from the surrounding hills. The area then became wetter, orming a peat bog, before eventual marine inundation over a period of about 30 to 100 years, followed by the deposition of marine sediments (*9*). Archaeological artifacts from this paleosol include worked and burnt flint, corded fiber, worked wood, and burnt hazelnut shells (*10*). Many of these artefacts represent early instances of such technologies and suggest that the Mesolithic peoples of Bouldnor Cliff were connected to more-advanced groups from Europe relative to those on mainland Britain (*11*). We thus analyzed sedimentary ancient DNA (sedaDNA) from sediment cores from the Bouldnor Cliff site. The sedaDNA approach has been applied to a range of terrestrial and marine sediments and has been shown to be highly informative in environmental contexts, providing more information than macrofossil assemblages (*12*–*14*)

Before taking samples for DNA analysis, microgeomorphological and microfossil analyses were undertaken on four sediment cores [MS-04, MS-05, MS-07, and MS-08 (*9*) (fig. S2)]. The sediment layers were of low porosity, with the paleosol and peat layers sealed beneath dense silty-clay marine alluvial sediments. We found a sharp boundary between the paleosol and the overlying peat, with no evidence of mixing of particles. Diatom and foraminifera analysis revealed a range of species in the superficial marine alluvial sediments. However, these did not penetrate into the underlying peat layer, indicating a lack of vertical movement in the sediment column. Given the absence of evidence of soil erosion (as might be revealed by illuviation or podsolization), we concluded that the archaeological artifacts had been deposited in situ on a pristine land surface rather than entered the samples through alluvial deposition from another site. Radiocarbon dates obtained from 21 samples of wood and plant macrofossils from the sediment cores (*9*) (table S1 and figs. S1 and S2) allow an inference of marine inundation beginning 8020 to 7980 cal yr B.P., which represents the latest date for human activity at the site, with inundation complete by 7990 to 7900 cal yr B.P.

We took four paleosol sediment samples (S308, 0 to 2 cm; S308, 2 to 4 cm; S308, 4 to 6 cm; and S308, 6 to 8 cm) from a location at the site associated with Mesolithic food debris (burnt hazelnut shells) (*9*). The samples were taken at successive 2-cm intervals from the top of the stratum, each roughly representing the period of a decade. Samples were taken on site (*15*), examined for macrofossils, and subjected to ancient DNA extraction in a dedicated laboratory (*16*). Samples were found to be devoid of macrofossils, apart from a few *Alnus glutinosa* (common alder) twigs.

We made Illumina libraries from the sediment cores and generated 71,856,199 256–base pair (bp) single-end reads on the MiSeq platform (table S2). To overcome the problem of bias resulting from

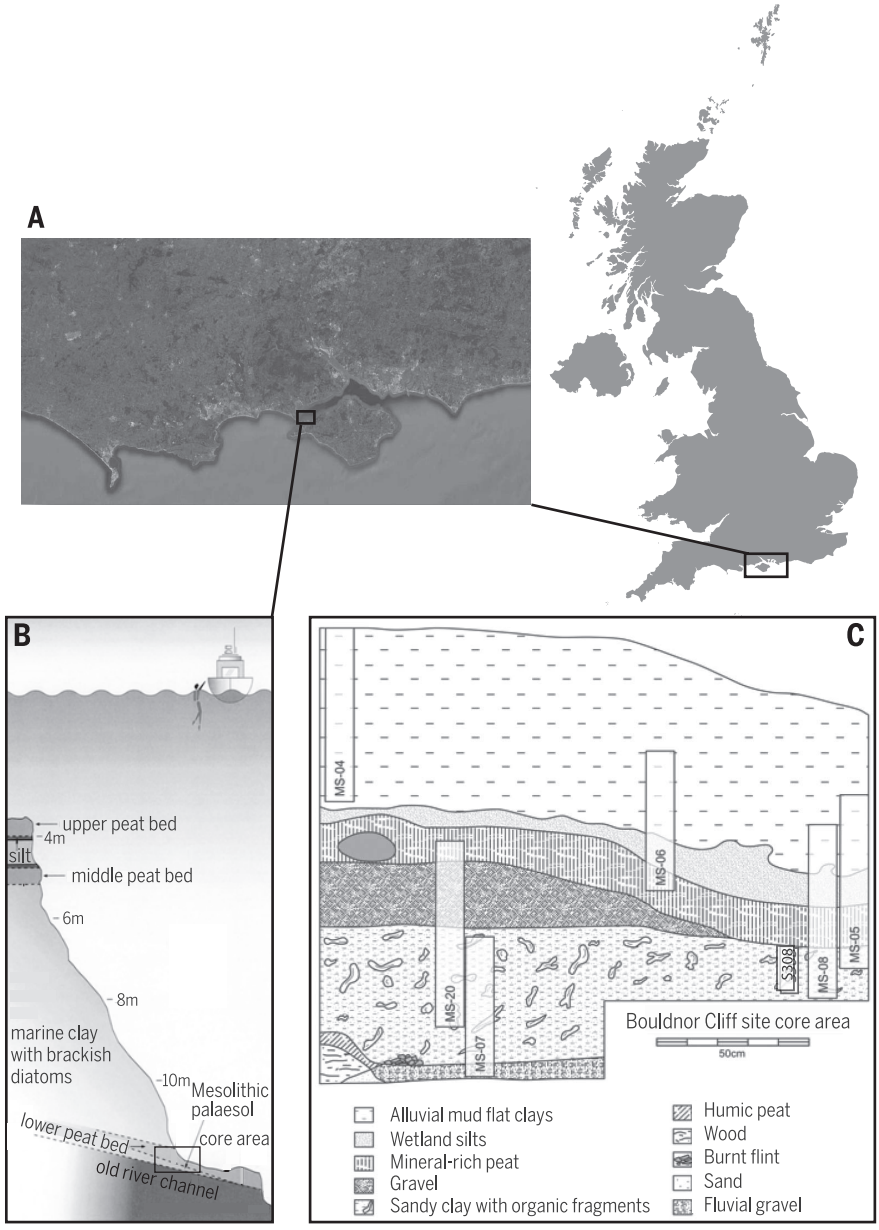

Fig. 1. Sampling location of sedaDNA from Bouldnor Cliff. (**A**) Location of the Bouldnor Cliff site in the Solent on the coast of the Isle of Wight. (**B**) Large-scale stratigraphic profile of the site, indicating the depth and location of the Mesolithic palaeosol and the location of the area from which cores were taken. (**C**) Core area in detail, stratigraphic profile of the site indicating core sites (MS-04-8, and MS-20), and approximate location of the sediment sample taken for sedaDNA analysis (S308).

[1]School of Life Sciences, University of Warwick, Coventry CV4 7AL, UK. [2]Maritime Archaeology Trust, Room W1/95, National Oceanography Centre, Empress Dock, Southampton SO14 3ZH, UK. [3]Department of Earth Sciences, University of St Andrews, St Andrews, Fife KY16 9AL, Scotland. [4]Department of Classics, Ancient History and Archaeology, University of Birmingham, Edgbaston, Birmingham B15 2TT, UK. [5]School of History and Cultures, University of Birmingham, IBM VISTA ERI Building, Pritchatts Road, Birmingham B15 2TT, UK. [6]Warwick Medical School, University of Warwick, Coventry CV4 7AL, UK. [7]Division of Archaeological, Geographical and Environmental Sciences, University of Bradford, Bradford, West Yorkshire BD7 1DP, UK.
*These authors contributed equally to this work. **†Corresponding author. E-mail: r.g.allaby@warwick.ac.uk**

partial representation of species in the publicly available sequence databases, we designed a phylogenetic intersection analysis for phylogenetic assignation of sedaDNA (*15*) that we estimate has an accuracy of 81% (*15*). sedaDNA sequences were sorted into major taxonomic groups in a preliminary phylogenetic clustering stage (*17*), and phylogenetic intersection analysis on major tetrapod groups (except for primates) and flowering plants (Magnoliophytes) (table S3) was performed under high-stringency conditions (≥99% of read length aligning to database entries, with ≥3 taxa on which to base the phylogenetic intersection analysis). Reads that met the stringency criteria were used to construct a paleoenvironmental profile (Fig. 2 and tables S4 and S5). It was not necessary to reject any data, post hoc (*15*), allowing us to avoid imposing any a priori assumptions about the past environment.

The sedaDNA profile revealed a wooded landscape that included oak, poplar, apple, and beech family members, with grasses and a few herbs present. Oak and poplar were also detected in the pollen profile (*9*, *18*), whereas oak, apple, and alder have been reported in archaeological worked wood remains at the site (*9*, *10*).

Palynological analysis shows an abundance of true grass species (Poaceae) at the site, which is reflected in more detail in the sedaDNA profile (figs. S3 to S6). There is a marked difference in the profile of grasses and fauna between the top half (0 to 4 cm) and bottom half (4 to 8 cm) of the paleosol. The lower strata contain a varied and abundant representation of major clades of grasses. We also found sequences assigned to Triticeae, which is the grass tribe within the Pooideae that encompasses genera with many domesticated species of cereal crop in the lower strata, albeit at relatively low levels (4% of the sedaDNA signal for flowering plants). However, reads assigned to Triticeae grow to dominate the plant profile in the upper strata (81% of the signal for flowering plants). The Poaceae type pollen from this zone 1b does not indicate the presence of larger cereal-type pollen (*9*), suggesting that the source of the *Triticum* signal is unlikely to be from wheat that was grown on site.

We specifically examined the possibility that the *Triticum* signal could be due to a false positive or may have been caused by the members of the Triticeae that are known to be native to the British Isles (*Leymus, Elymus*, *Agropyron*, and *Hordelymus*). All instances in which these species were detected in the analysis showed them to be less similar to the sedaDNA than the *Triticum*/*Aegilops* group. Many sedaDNA sequences showed 100% nucleotide identity with sequences from *Triticum*, particularly *Triticum monococcum* (einkorn), with decreasing similarity next to its sister genus *Aegilops* (table S5). The British Triticeae all occur outside this taxonomic group and thus were excluded as a possible source of the signal. Because both the *Triticum* and *Aegilops* are Near Eastern genera with no known wild members in northern Europe, we conclude that these are genuine wheat sequences. We considered the possibility that the sequences could be due to modern contamination, but discounted this because wheat has not been studied in the ancient DNA facility used. Furthermore, the sediment samples were taken during the winter months and sealed underwater, and the stratified sedaDNA signal would not be expected from contamination. We also tested for the presence of wheat DNA in both our reagents and the core samples by preparing blank libraries from the same reagent batch, which we sequenced on the MiSeq platform. No sequences of wheat, or indeed of any higher plant, were found in these control libraries. We thus conclude that the *Triticum* sequences derive from the core itself and therefore are associated with Mesolithic human activity at the site.

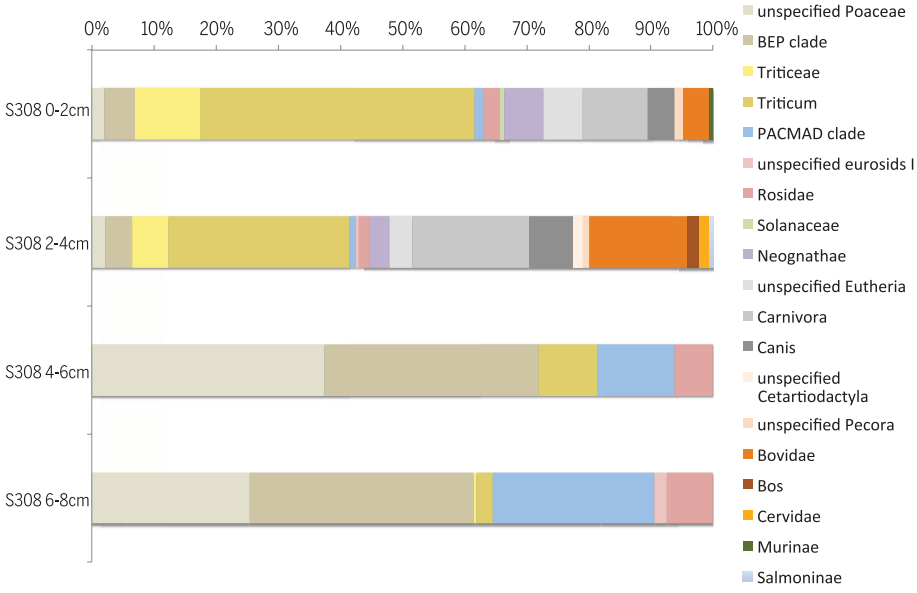

Fig. 2. Floral and faunal composition of the Mesolithic palaeosol. Depths are measured from the top of the stratum. Compositions are based on read assignations detailed in table S3.

SedaDNA analysis of the upper strata further revealed a faunal profile compatible with human activity, with an abundant presence of *Canis* and Bovidae. *Canis* may be interpreted as either dogs or wolves. Two of the bovid reads sat at the intersection of *Bos* with the sister genus *Bison*, which we interpreted as most likely *Bos* and which was supported by a subsequent find of an auroch bone at the site (fig. S8). We also detected the presence of deer, members of the grouse family, and rodents: all compatible with the contents of a Mesolithic diet shared by humans and dogs.

The occurrence of wheat 8000 years ago on the British continental shelf appears early, given its later establishment on the UK mainland. Neolithic assemblages first appear in northwest Europe in the 8th millennium B.P., from 7500 B.P. in the central Rhineland (*19*), 7300 B.P. in the Rhine/Maas delta and adjacent areas (*20*, *21*), and 7400 B.P. in western France (*22*). These developments were driven by the spread of the Linear Pottery (LBK) culture from trans-Danubia into central Europe around 7600 B.P. (*19*) and the Cardial culture from the Mediterranean into Western France around 7600 to 7400 B.P. (*23*). These dates suggest only a 400-year gap between Bouldnor Cliff and the earliest known presence of farming in proximate European sites. However, the spread of the Cardial culture is still incompletely understood, with dates of 8000 B.P. in southern France a recurring theme (*24*, *25*). Given the littoral route of the Cardial spread, it is possible that earlier sites may also be submerged in southern Europe. Such dates are contemporaneous with the Mesolithic site at Bouldnor cliff, and given the high mobility of Mesolithic communities, it is plausible that communication occurred over such distances. It has been suggested that agricultural products moved ahead of the front of Neolithization into Mesolithic zones (*26*).

In the absence of significant environmental barriers to the dissemination of agriculture across Europe, there is no a priori reason why the spread of farming products from the Balkans to the Atlantic zone could not have been swift: The only constraints were the scale, intensity, and spatial and temporal articulation of social and demographic networks. It is possible that the isolation of Britain from mainland Europe by the sea represented an environmental barrier. Although sea levels clearly rose during the early Holocene, the identification of coastlines within the North Sea during the early Holocene are complex (*27*), and estimates of coastline have been speculative (*28*). We explored the plausibility of a direct connection between Britain and Europe at the time of the paleosol by plotting a generalized map on the basis of C^{14} and optically stimulated luminescence (OSL)–dated marine cores of early Holocene sediments taken from the east coast of the United Kingdom (*29*) (Fig. 3). This map represents an estimate of coastal extent around southern Britain from dated evidence. These data support two possible points of direct contact with northern France and the Netherlands,

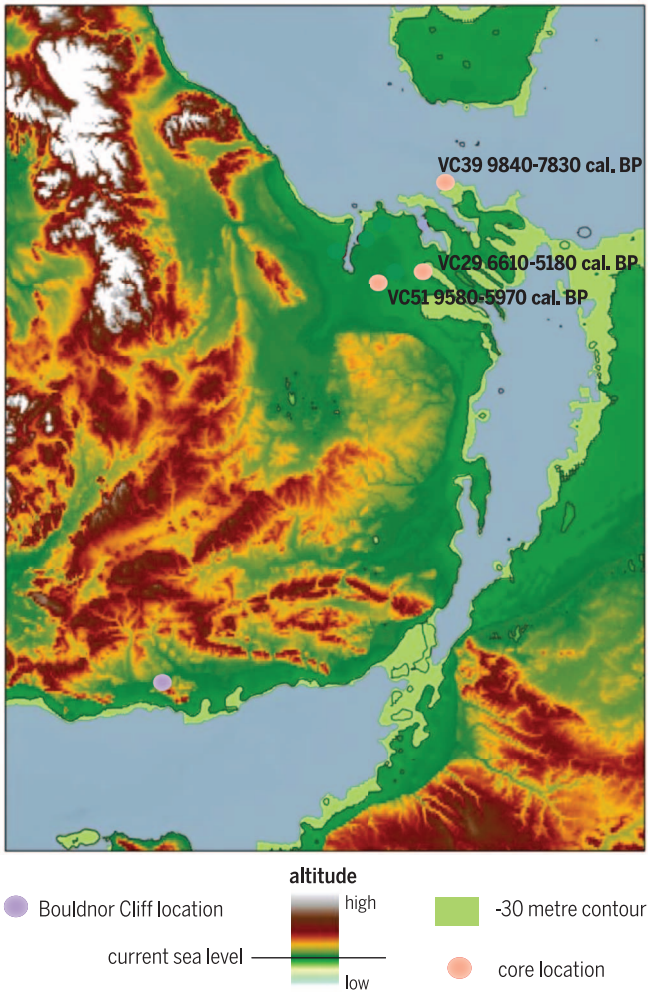

Fig. 3. Generalized map of potential coastal extent around southern Britain 9840 to 7830 cal yr B.P. Vibrocores through submersed old land surfaces off the coast of Britain at depths of 31.68 m (VC39), 24.01 m (VC51), and 23.9 0m (VC29) were OSL-dated (*32*). The map extrapolates the contour of the VC29 vibrocore site.

respectively, supporting the possibility of contact between the Mesolithic peoples of the British area with both LBK and Cardial cultures.

Our sedaDNA analysis has revealed the presence of wheat, a domesticated plant associated with the Neolithic, at a site on the British continental shelf 2000 years earlier than would be expected from the known archaeology of the British mainland and 400 years earlier than at proximate European sites. We obtained no archaeological evidence suggesting cultivation at this site. The Poaceae pollen profile does not show an expansion indicating an open environment suitable for farming until higher strata above the peat zone overlaying the paleosol (*15*) (pollen zone 2). Therefore, in the absence of direct evidence, we suspect that this wheat represents foodstuffs imported from the continent rather than the cultivation of this cereal crop at this locale. The presence of wheat, along with pioneering technological artifacts at the site, provides evidence for a social network between well-developed Mesolithic peoples of northwest Europe and the advancing Neolithic front. In this light, recent debates concerning the chronology of the spread of farming to northwest Europe during the late 8th and 7th millennia B.P. (*2*, *30*, *31*), as well as the respective contributions of migration, colonization, and acculturation, may have focused only on the latter part of the time frame during which these events occurred.

REFERENCES AND NOTES

1. C. J. Stevens, D. Q. Fuller, *Antiquity* **86**, 707–722 (2012).
2. P. Rowley-Conwy, *Curr. Anthropol.* **52**, S431–S451 (2011).
3. A. Whittle, F. Healy, A. Bayliss, *Gathering Time: Dating the Early Neolithic Enclosures of Southern Britain and Ireland* (Oxbow Books, Oxford, 2011), pp. 207, 348–350.
4. V. Gaffney, S. Fitch, D. Smith, *Europe's Lost World, the Rediscovery of Doggerland* [Council for British Archaeology (CBA) Research Report 160, CBA, York, UK, 2009], pp. 30–31.
5. G. Momber, in *Prehistoric Archaeology of the Continental Shelf: A Global Review*, A. Evans, J. Flatman, N. C. Flemming, Eds. (Springer, New York, 2014), pp. 194–212.
6. J. H. M. Peeters, G. Momber, *J. Geosci. (Prague)* **93**, 55–70 (2014).
7. V. Gaffney, K. Thomson, S. Fitch, *Mapping Doggerland* (Archaeopress, Oxford, 2007), pp. 1–6.
8. D. Tomalin, G. Momber, N. Nayling, in *Mesolithic Occupation at Bouldnor Cliff and the Submerged Prehistoric Landscapes of the Solent*, G. Momber, D. Tomalin, R. Scaife, J. Satchell, J. Gillespie, Eds. (CBA Research Report 164, CBA, York, UK, 2011], pp. 3–14.
9. G. Momber *et al*., in *Mesolithic Occupation at Bouldnor Cliff and the Submerged Prehistoric Landscapes of the Solent*, G. Momber, D. Tomalin, R. Scaife, J. Satchell, J. Gillespie, Eds. (CBA Research Report 164, CBA, York, UK, 2011), pp. 19–65.
10. G. Momber *et al*., in *Mesolithic Occupation at Bouldnor Cliff and the Submerged Prehistoric Landscapes of the Solent*, G. Momber, D. Tomalin, R. Scaife, J. Satchell, J. Gillespie, Eds. (CBA Research Report 164, CBA, York, UK, 2011), pp. 66–93.
11. D. Tomalin, in *Mesolithic Occupation at Bouldnor Cliff and the Submerged Prehistoric Landscapes of the Solent*, G. Momber, D. Tomalin, R. Scaife, J. Satchell, J. Gillespie, Eds. (CBA Research Report 164, CBA, York, UK, 2011), pp. 155–163.
12. E. Willerslev *et al*., *Science* **317**, 111–114 (2007).
13. F. Lejzerowicz *et al*., *Biol. Lett.* **9**, 20130283 (2013).
14. J. Haile *et al*., *Mol. Biol. Evol.* **24**, 982–989 (2007).
15. See the supplementary materials for methods.
16. M. T. Gilbert, H. J. Bandelt, M. Hofreiter, I. Barnes, *Trends Ecol. Evol.* **20**, 541–544 (2005).
17. D. H. Huson, A. F. Auch, J. Qi, S. C. Schuster, *Genome Res.* **17**, 377–386 (2007).
18. G. Momber *et al*., in *Mesolithic Occupation at Bouldnor Cliff and the Submerged Prehistoric Landscapes of the Solent*, G. Momber, D. Tomalin, R. Scaife, J. Satchell, J. Gillespie, Eds. (CBA Research Report 164, CBA, York, UK, 2011), pp. 105–119.
19. J. Robb, *Curr. Anthropol.* **54**, 657–683 (2013).
20. L. P. Louwe Kooijmans, *Proc. Br. Acad.* **144**, 287–309 (2007).
21. P. Crombé, B. Vanmontfort, *Proc. Br. Acad.* **144**, 263–285 (2007).
22. G. March and, *Proc. Br. Acad.* **144**, 225–242 (2007).
23. A. Tresset, J.-D. Vigne, *Proc. Br. Acad.* **144**, 189–210 (2007).
24. J. Guilane, C. Manen, *Proc. Br. Acad.* **144**, 21–51 (2007).
25. C. Joly, L. Visset, *Rev. Palaeobot. Palynol.* **154**, 124–179 (2009).
26. C. Jeunesse, *Rev. Alsace* **129**, 97–112 (2003).
27. T. Bell, A. O' Sullivan, R. Quinn, *Archaeol. Ireland* **20**, 12–17 (2006).
28. B. J. Coles, *Proc. Prehist. Soc.* **64**, 45–81 (1998).
29. D. R. Tappin *et al*., *The Humber Regional Environmental Characterisation* (British Geological Survey Open Report OR/10/54, Marine Aggregate Levy Sustainability Fund, Lowestoft, UK, 2011), pp. 194–230.
30. M. Collard, K. Edinborough, S. Shennan, M. G. Thomas, *J. Archaeol. Sci.* **37**, 866–870 (2010).
31. J. Thomas, in *Prehistoric Britain*, J. Pollard, Ed. (Blackwell, Oxford, 2008), pp. 58–89.
32. G. Momber, in *Submerged Prehistory*, J. Benjamin, C. Bonsall, C. Pickard, A. Fischer, Eds. (Oxbow Books, Oxford, 2011), pp. 85–98.

ACKNOWLEDGMENTS

The authors thank A. Clapham for identification of *Alnus glutinosa* fragments, J. Z. M. Chan and G. L. Kay for assistance with operating the MiSeq platform, and the SplashCOS and Deucalion networks for continued support. O.S. was funded by Warwick Medical School. Sequence data were deposited at the European Molecular Biology Laboratory European Bioinformatics Institute, accession number PRJEB6766 (ERP006391). We acknowledge previous supporting work by J. Gillespie (Foram analysis), D. Tomalin (lithic analysis), J. Heathcote (micromorphology and depositional evidence), and in particular R. Scaife for his pollen analysis The cores are stored in the British Ocean Sediment Core Research Facility at the National Oceanography Centre, Southampton, UK. Access to the Bouldnor Cliff cores for further analysis is provided by the Maritime Archeology Trust.

SUPPLEMENTARY MATERIALS

www.sciencemag.org/content/347/6225/998/suppl/DC1
Materials and Methods
Figs. S1 to S12
Tables S1 to S4
References (*33*–*37*)

15 September 2014; accepted 22 January 2015
10.1126/science.1261278

STEM CELLS

m^{6}A mRNA methylation facilitates resolution of naïve pluripotency toward differentiation

Shay Geula,[1*] Sharon Moshitch-Moshkovitz,[2*] Dan Dominissini,[3*] Abed AlFatah Mansour,[1*] Nitzan Kol,[2] Mali Salmon-Divon,[2] Vera Hershkovitz,[2] Eyal Peer,[2] Nofar Mor,[1] Yair S. Manor,[1] Moshe Shay Ben-Haim,[2] Eran Eyal,[2] Sharon Yunger,[2] Yishay Pinto,[4] Diego Adhemar Jaitin,[5] Sergey Viukov,[1] Yoach Rais,[1] Vladislav Krupalnik,[1] Elad Chomsky,[1] Mirie Zerbib,[1] Itay Maza,[1] Yoav Rechavi,[1] Rada Massarwa,[1] Suhair Hanna,[1,6] Ido Amit,[5] Erez Y. Levanon,[4] Ninette Amariglio,[2,4] Noam Stern-Ginossar,[1] Noa Novershtern,[1]†‡ Gideon Rechavi,[2]†‡ Jacob H. Hanna[1]†‡

Naïve and primed pluripotent states retain distinct molecular properties, yet limited knowledge exists on how their state transitions are regulated. Here, we identify Mettl3, an *N*^{6}-methyladenosine (m^{6}A) transferase, as a regulator for terminating murine naïve pluripotency. Mettl3 knockout preimplantation epiblasts and naïve embryonic stem cells are depleted for m^{6}A in mRNAs, yet are viable. However, they fail to adequately terminate their naïve state and, subsequently, undergo aberrant and restricted lineage priming at the postimplantation stage, which leads to early embryonic lethality. m^{6}A predominantly and directly reduces mRNA stability, including that of key naïve pluripotency-promoting transcripts. This study highlights a critical role for an mRNA epigenetic modification in vivo and identifies regulatory modules that functionally influence naïve and primed pluripotency in an opposing manner.

Murine pluripotent embryonic stem cells (ESCs) reside in a "naïve" molecular state that largely resembles that of the preimplantation inner cell mass, whereas epiblast stem cells (EpiSCs), derived from the postimplantation epiblast, resemble an advanced developmental stage and are already "primed" for differentiation (*1, 2*). Limited knowledge exists with regard to the molecular regulators that are critical for transitioning toward or for exclusively maintaining primed pluripotent EpiSCs. Thus, we conducted a small interfering RNA (siRNA) screen against selected transcriptional and epigenetic regulators previously evaluated in the context of naïve pluripotency modulation (*1, 2*) and tested whether primed EpiSCs, harboring a green fluorescent protein (GFP) reporter knock-in allele under the control of endogenous Oct4 promoter (Oct4-GFP$^{+/+}$), might selectively rely on some of these factors (Fig. 1A and fig. S1). Regulators that specifically inhibited the stability and viability of Oct4-GFP$^+$ primed cells included the epigenetic repressors Dnmt1, Eed, and Suz12 Polycomb components; Mbd3; and *N*^{6}-adenosine methyltransferase Mettl3, a component of the *N*^{6}-methyladenosine (m^{6}A) mRNA methylating complex (*3*) (Fig. 1A and fig. S1).

We subsequently focused on the role of m^{6}A in pluripotency transitions, because the biological role of RNA modifications is only starting to be unveiled (*4*). m^{6}A is an RNA modification catalyzed by Mettl3 (methyl transferase–like 3) and Mettl14, components of a partially characterized multicomponent methyltransferase complex (*3*). This modification is removed by Fto and Alkbh5 demethylases. A role for m^{6}A was

[1]The Department of Molecular Genetics, Weizmann Institute of Science, Rehovot, Israel. [2]Cancer Research Center, Chaim Sheba Medical Center, Tel Hashomer, Israel, and Sackler School of Medicine, Tel Aviv University, Tel Aviv, Israel. [3]Department of Chemistry and Institute for Biophysical Dynamics, The University of Chicago, Chicago, IL 60637, USA. [4]Mina and Everard Goodman Faculty of Life Sciences, Bar-Ilan University, Ramat Gan, Israel. [5]The Department of Immunology, Weizmann Institute of Science, Rehovot, Israel. [6]The Department of Pediatrics and the Pediatric Immunology Unit, Rambam Medical Center, and the B. Rappaport Faculty of Medicine, Technion, Haifa, Israel.

*These authors contributed equally to this work. †These authors contributed equally to this work. ‡Corresponding author. E-mail: jacob.hanna@weizmann.ac.il (J.H.H.); noa.novershtern@weizmann.ac.il (N.N.); gidi.rechavi@sheba.health.gov.il (G.R.)

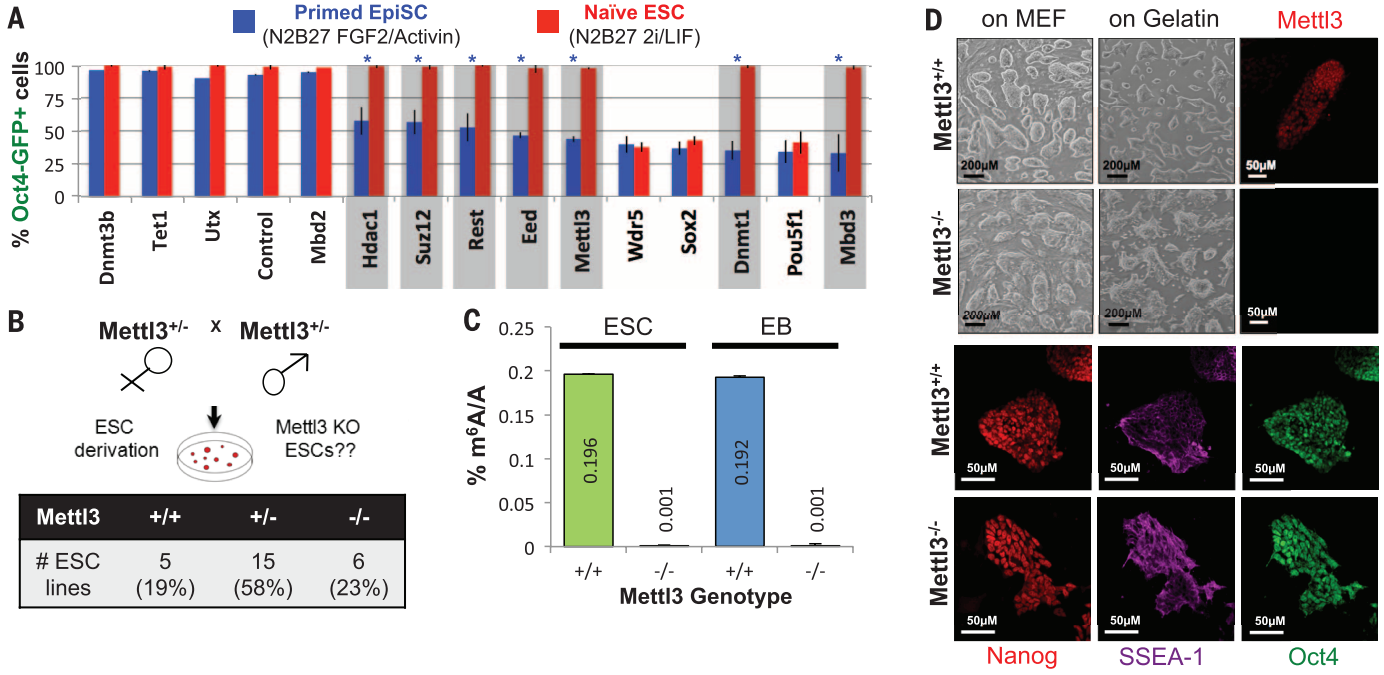

Mettl3	+/+	+/-	-/-
# ESC lines	5 (19%)	15 (58%)	6 (23%)

Fig. 1. Derivation and characterization of Mettl3 KO ESCs. (**A**) siRNA screen for regulators that destabilize Oct4-GFP+ mouse naïve or primed pluripotent cells. Error bars indicate SD (n = 3). Student's t test *P < 0.05 relative to scrambled control. Gray boxes highlight EpiSC-specific regulators. (**B**) ESC derivation efficiency after mating of Mettl3 heterozygote mice. (**C**) Liquid chromatography–tandem mass spectrometry analysis of m^{6}A percentage relative to adenosine in purified mRNA. Error bars indicate SD (n = 3). (**D**) ESC morphology and immunostaining.

demonstrated in regulation of gene expression through mRNA splicing, localization, and degradation, as well as in modulating the binding capacity of m^{6}A binding "reader" proteins such as Ythdf1-3 (*4*).

We targeted the endogenous *Mettl3* locus in mouse ESCs and generated a truncated out-of-frame allele (fig. S2). Mettl3$^{+/-}$ mice were obtained and used to derive embryonic day (E)3.5 blastocysts (Fig. 1B). Mettl3$^{-/-}$ knockout (KO) blastocysts retained normal morphology and expression of pluripotency markers (fig. S3, A and B) and yielded ESCs at the expected ratio (Fig. 1B and fig. S3, C and D). Quantitative mass spectrometry analysis (MS) of m^{6}A levels in purified mRNA from wild-type Mettl3$^{+/+}$ (WT) and KO cells showed that Mettl3 ablation leads to near-complete depletion of m^{6}A on mRNA (Fig. 1C).

Mettl3$^{-/-}$ ESCs preserve their naïve pluripotent identity, as evidenced by domed-shape colony morphology and expression of pluripotency markers (Fig. 1D and fig. S3, F to I). To test their differentiation ability, WT and KO cells were transferred to differentiation media for embryoid bodies (EBs) for 8 to 21 days. KO cells generated dense EB spheres but failed to undergo the characteristic cavitation observed in WT EBs (fig. S4, A and B). KO EBs failed to robustly up-regulate early developmental markers and to adequately repress pluripotent genes (Fig. 2A and fig. S4C). Twenty-one–day–old EBs were disaggregated and replated in ESC growth conditions, and only KO EBs efficiently regenerated stable ESCs (fig. S4, D and E). In vitro protocols did not efficiently differentiate Mettl3$^{-/-}$ ESCs into mature neurons (fig. S4F). Consistently, Mettl3 KO ESCs did not contribute to embryo chimera formation after blastocyst microinjection (fig. S5).

WT and KO ESCs were injected into immunodeficient mice to generate mature teratomas. Mettl3$^{-/-}$ ESCs generated larger tumors, and histological analysis showed that KO teratomas were poorly differentiated. However, mature structures were abundant in WT teratomas (fig. S6, A to C). Immunostaining showed that KO teratomas poorly expressed differentiation markers, such as Gata4/6 and troponin, and diffusely expressed pluripotent markers, such as Oct4 and Nanog, even 6 weeks after subcutaneous in vivo growth (Fig. 2B and fig. S6, D and E). Disaggregation of dissected KO tumors demonstrated that >75% of their cells still expressed Oct4-GFP pluripotency reporter (fig. S6F). Only KO teratomas contained pluripotent cells that could rapidly recover in culture and give rise to ESC colonies within 6 days and could form stable Oct4-GFP$^+$ ESC lines (fig. S6G). The resistance to differentiation could be rescued by reconstitution with a WT *Mettl3* transgenic allele (fig. S7). Deletion in ESCs of the other methyltransferase complex component, Mettl14 (*5*), showed an equivalent reduction in m^{6}A in mRNA and recapitulated in vitro resistance to differentiation as seen with Mettl3 KO ESCs (fig. S8).

We next wanted to test the ability of female Mettl3$^{-/-}$ ESCs to convert from naïve pluripotent state into primed epiblastlike state in vitro, by applying primed fibroblast growth factor 2 (FGF2)–activin conditions (*2*). WT colonies obtained a typical flat morphology (Fig. 2C); reduced expression of naïve markers (Nanog, Rex1, and Klf4); and induced primed pluripotency markers (Xist, Foxa2, Brachyury, and Fgf5) (fig. S9, A to D). Mettl3$^{-/-}$ colonies, however, kept their

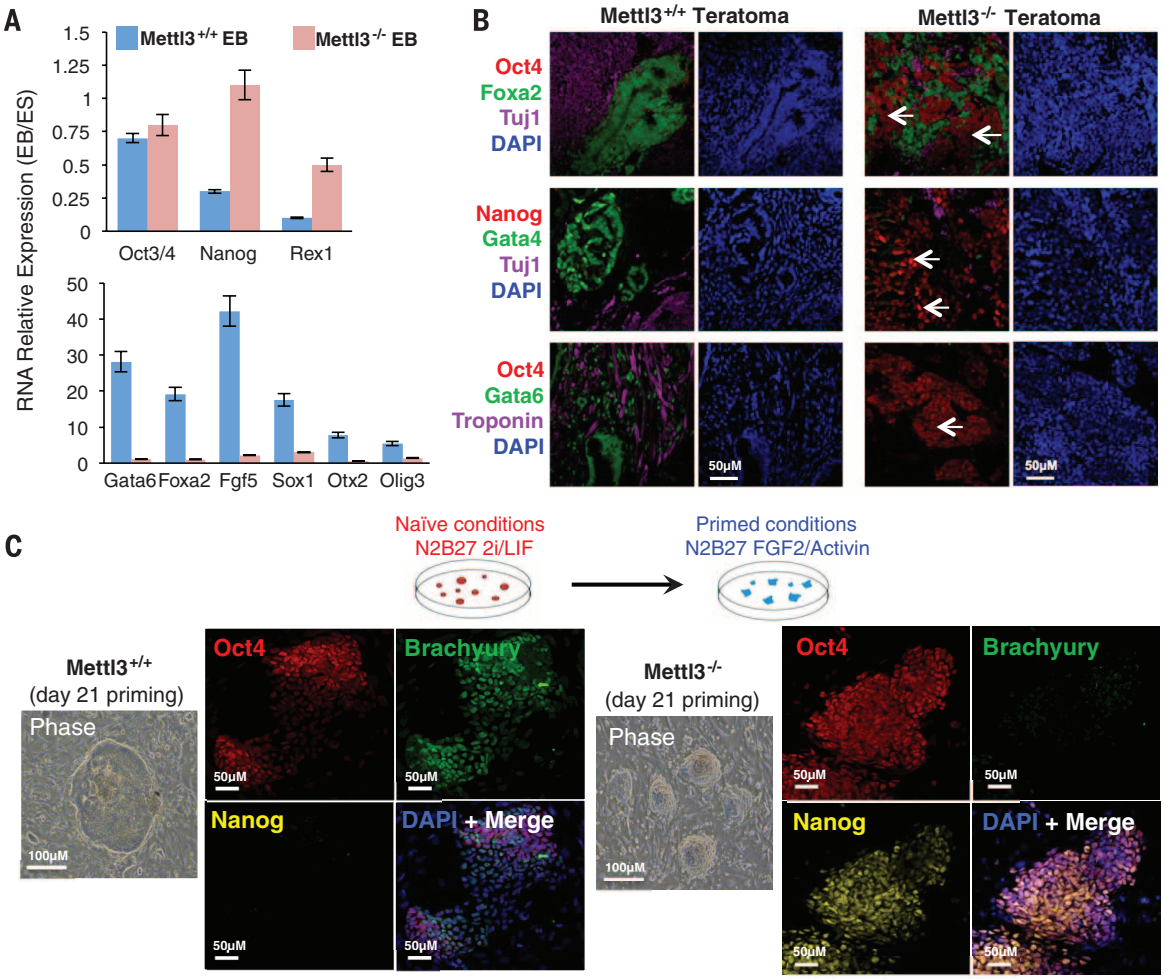

Fig. 2. Mettl3 KO ESCs resist termination of naïve pluripotency. (**A**) qPCR analysis for pluripotency (top) and differentiation markers (bottom) expression after 8 days of EB induction. Error bars indicate SD (n = 3). (**B**) Immunostaining of teratoma sections. DAPI, 4′,6-diamidino-2-phenylindole. (Arrows highlight regions with pluripotency marker expression.) (**C**) Morphology and immunostaining images of Mettl3 WT and KO ESCs transferred to primed conditions.

naïve-domed shape; failed to down-regulate naïve markers, such as Esrrb and Nanog; and up-regulated only Fgf5 but not Xist, Foxa2, or Brachyury (Fig. 2C and fig. S9, A to D). Other indicators for pluripotency priming, such as enriched cytoplasmic localization of Tfe3 upon pluripotency priming and X-chromosome inactivation (evident by formation of foci for histone H3 trimethylated at lysine 27), were observed only in WT cells (fig. S9, B and E). KO ESCs were also more resilient to differentiation in the absence of LIF (fig. S9F). In conclusion, depletion of m^{6}A in mRNA of Mettl3$^{-/-}$ ESCs hampers their priming and differentiation competence, which leads to a "hyper"-naïve pluripotency phenotype.

We next analyzed the effect of Mettl3 depletion on normally established WT EpiSC viability and stability, in comparison with WT naïve ESCs. Quantitative polymerase chain reaction (qPCR) analysis showed that, in naïve cells, Mettl3 depletion amplifies the already highly expressed naïve pluripotency transcripts, which further boosts naïve circuitry stability (fig. S10, A and B). The increase in minimally expressed lineage factors like Fgf5 is marginal, as their basal transcript levels are very low (fig. S10B). As naïve WT cells progress toward EpiSC stage, pluripotency genes are down-regulated, and lineage commitment markers become abundantly expressed (*2*) (fig. S10, C and D). At this stage, Mettl3 depletion leads to minimal amplification of pluripotency genes and further boosts the highly expressed lineage commitment markers, which leads to tipping the balance toward differentiation and compromises the stability of the primed state (fig. S11, A and B, and supplementary text). Consistently, we dissected a complex effect for Mettl3 depletion in different stages of cellular reprogramming toward naïve pluripotency (figs. S11 and S12).

To resolve the roles of m^{6}A in the onset of the "hyper"-naïve pluripotent phenotype, we applied m^{6}A sequencing (m^{6}Aseq) (*4*) on RNA purified from mouse naïve ESCs, 11-day-old EBs, and mouse embryonic fibroblasts (MEFs) (fig. S13). We identified 10,431, 8356, and 11,948 m^{6}A peaks within 6412, 5504, and 6427 expressed genes of ESCs, EBs, and MEFs, respectively, which constitute 44 to 52% of expressed genes (Fig. 3A, figs. S13 and S14, and tables S1 and S2). Functional enrichment analysis of methylated genes revealed statistically significant enrichment of genes involved in various basic cellular processes, as well as for targets of pluripotency regulators (e.g., Nanog) (false discovery rate <1%) (fig. S13G). Note that 28 out of 35 (80%) naïve pluripotency-promoting genes (*6*) were methylated for m^{6}A, including Nanog, Klf2, and Esrrb but not Oct4, which is expressed in both pluripotent states (Fig. 3A, fig. S15, and table S3) (*1*). Lineage priming transcripts expressed in WT EBs, like Foxa2 and Sox17, were also positive for m^{6}A (fig. S16, A to C).

Global transcriptional profiles of KO EB samples exhibit high correlation with those of WT

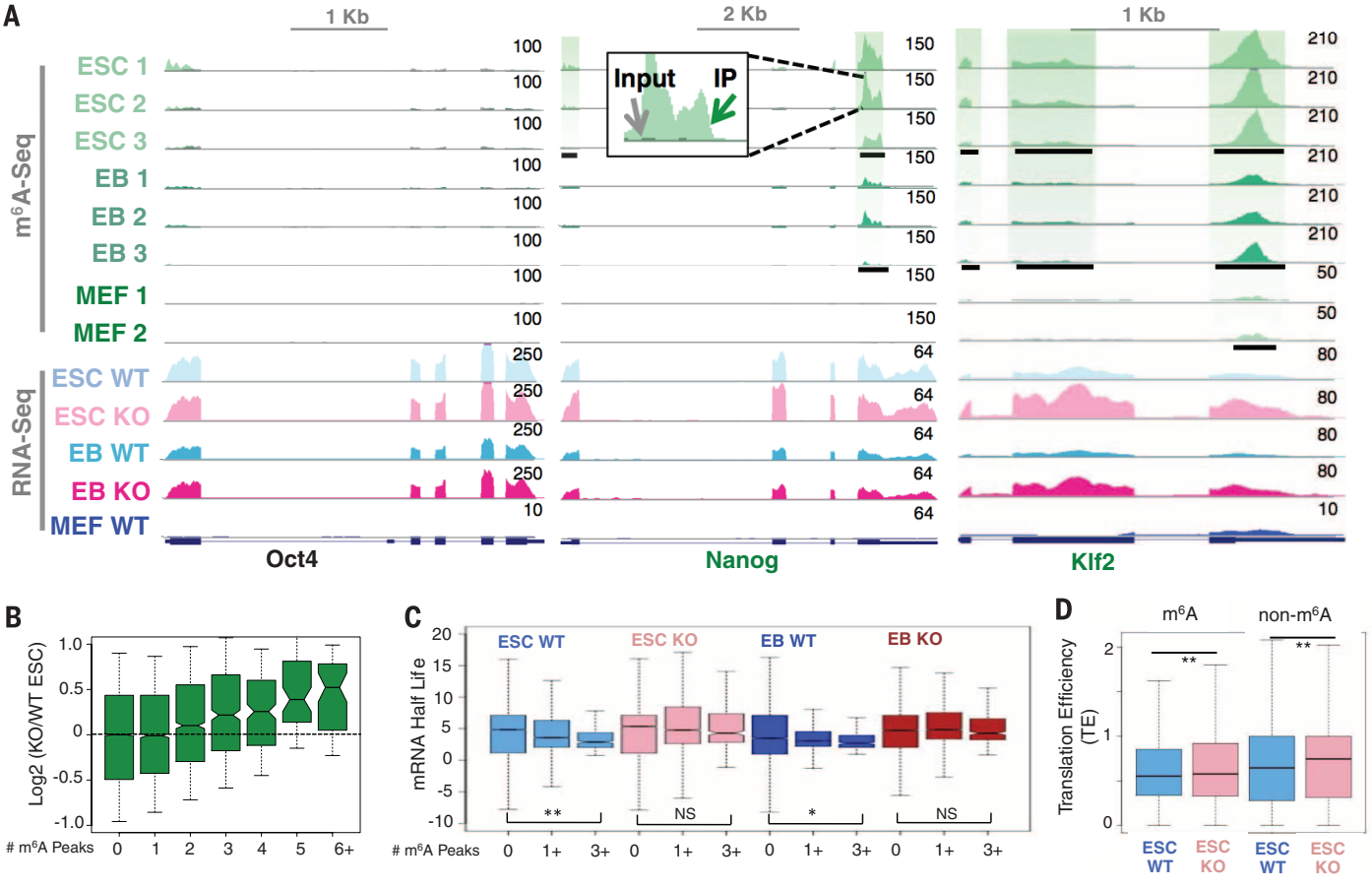

Fig. 3. Molecular characterization of Mettl3 KO cells. (**A**) The m^{6}A methylation and transcriptional landscape. Normalized read density (reads-per-million) levels are shown as green shades: m^{6}A-IP in WT ESC, EB, and MEF; gray shades: m^{6}A input in WT ESC, EB, and MEF; blue shades: RNAseq in WT ESC, EB, and and MEF; and pink shades: RNAseq in KO ESC and EB. In m^{6}A samples, all three biological replicates are shown (replicate number indicated on the left). The genome browser, range is shown at the right side of each track. Significant peaks are indicated in horizontal black rectangles and green highlight. Levels are normalized by the number of reads in each sample. (**B**) Transcript level changes in KO ESCs compared with WT ESCs, as a function of the number of m^{6}A peaks in each transcript. Box plots describe the distribution of fold-change; medians are indicated in the center of the boxes. (**C**) Distribution of transcripts' half-life (in hours) in ESCs (left) and EBs (right), for WT (blue shades) and KO (pink/red). Distributions are shown for genes without m^{6}A (12,461), genes with at least one m^{6}A peak in either condition (n = 7181), and genes with at least three peaks (427). Paired Wilcoxon *P < 0.05, **P < 0.00005. (**D**) Translation efficiency in WT and KO ESCs. Paired Wilcoxon **$P < 10^{-8}$.

and KO ESCs (fig. S17A), which validates our functional phenotypic observations (Fig. 2). Pluripotency regulators' transcript levels are increased in KO EBs compared with WT, and in several cases, this increase is evident already in ESCs (e.g., Klf2, Klf4, and Esrrb) (figs. S15 and S17, F and G). Notably, m^{6}A marked transcripts are significantly higher in KO than in WT ESCs (Fig. 3B and fig. S17, B and E), as well as known targets of Ythdf2 (*7*) and of Mettl3 in mouse ESCs (*8*) (fig. S17C). The change in expression level of a given gene in KO compared with WT is positively correlated with the number of m^{6}A peaks of that transcript in ESCs and EBs (Fig. 3B and fig. S17, B and D). Overall, these results suggest that m^{6}A depletion from mRNA by Mettl3 KO increases mRNA levels of methylated transcripts.

Changes in mRNA levels reflect the difference between transcription and degradation rates. A recent study showed that certain Ythdf proteins, abundantly expressed in ESCs and EBs (fig. S18A), mediate degradation of methylated mRNA (*7*). To measure mRNA degradation rates, we monitored mRNA levels after transcription inhibition with actinomycin-D (fig. S18B), followed by calculation of degradation and half-life rates. The half-life of methylated transcripts is significantly shorter than that of unmethylated transcripts in WT ESCs ($P < 3 \times 10^{-6}$) and WT EBs ($P < 0.005$) (Fig. 3C). Subsequently, in KO cells, the half-life of methylated transcripts increases significantly in ESCs and EBs ($P < 2 \times 10^{-16}$) (fig. S18). Previously identified mRNA bound targets of Ythdf2 and pluripotent gene transcripts also showed a significantly increased half-life that was prominent in KO samples (figs. S18D and S19). Transcript half-life was assessed by reverse transcription with qPCR (RT-qPCR) with and without actinomycin-D treatment in ESCs, and this procedure validated increased half-life rates (>twofold change) of Klf4, Nanog, Sox2, and Zfp42 but not Oct4 and Mta2, as those transcripts are unmethylated (fig. S20). Combined knockdown of Nanog, Klf4, and Esrrb in Mettl3 KO ESCs improved their ability to up-regulate lineage commitment markers upon in vitro priming (fig. S21). Overall, these results indicate that increased stability of methylated pluripotent mRNA transcripts, which resulted in matching alterations of protein levels (fig. S22), contributed to the "hyperpluripotent" phenotype induced by Mettl3 ablation.

Analysis of translation topology in WT and KO ESCs and EBs was conducted by using ribosome profiling [Riboseq (*9*)] (figs. S22C and S23). To identify whether differences in translation existed and were correlated with m^{6}A abundance, we calculated translation efficiency (TE; ribosome footprint reads per million reads (RPM)/mRNA RPM) (*9*). When we analyzed the TE in cells of KO compared with WT cells, we found a modest yet significantly increased TE in KO compared to WT ESCs (Fig. 3D and fig. S22D), including of pluripotency-promoting transcripts, such as Utf1, Lin28, and Gbx2 (fig. S22E). This effect was observed on methylated and unmethylated transcripts with significantly higher GC content,

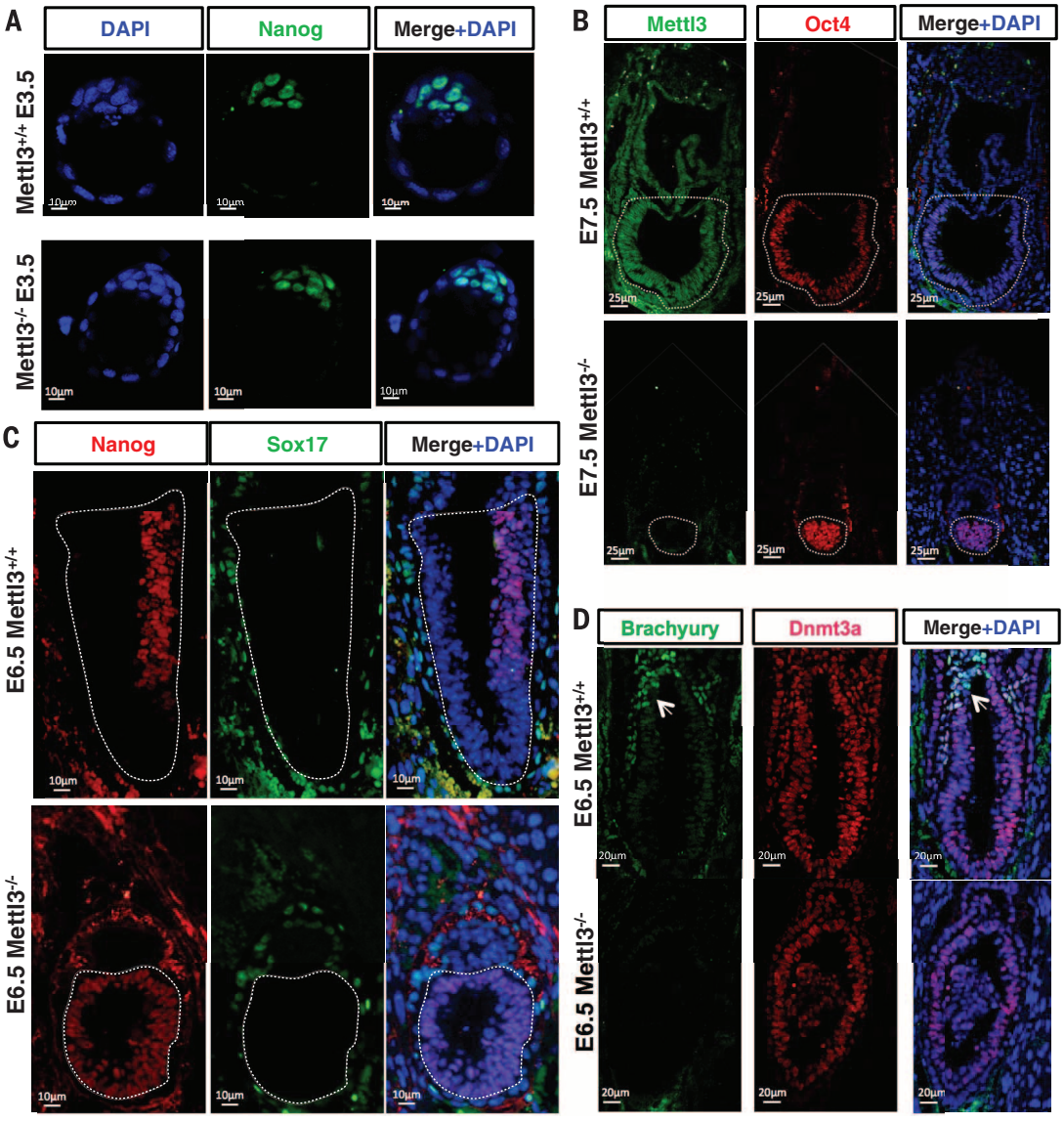

Fig. 4. Mettl3 regulates pluripotency priming and differentiation in vivo. (**A** to **D**) Representative immunostaining images of WT and KO histological sections at the indicated developmental stages. (Epiblasts are marked by dashed outline; arrows highlight Brachyury+ cells.)

yet independent of the length of the 3′ untranslated region or m^{6}A deposition (Fig. 3D and fig. S22, F to I). Collectively, absence of m^{6}A leads to an indirect increase in translation efficiency of GC-rich transcripts and a direct increase in mRNA stability of m^{6}A-decorated transcripts. This includes transcripts of prominent naïve pluripotency regulators that stabilize this state and shield its responsiveness to lineage priming cues. Upon depletion of Mettl3, we detected significant changes in splicing patterns that were directly dependent on m^{6}A and significant changes in adenosine-to-inosine RNA editing that were indirectly dependent on m^{6}A (figs. S24 and S25) (*10*). However, how and whether the latter changes alter Mettl3-KO pluripotency regulation remain to be defined (supplementary text).

We then determined the extent to which the in vitro observed phenotypes correlate with in vivo development and crossed heterozygote mice to obtain Mettl3$^{-/-}$ litters. KO of Mettl3 is embryonic lethal (fig. S26). Inspecting E12.5, E10.5, and E8.5 embryos, we saw that all KO embryos were already absorbed (fig. S26, B to G). Whereas E3.5 KO blastocysts retain normal characteristics (Fig. 4A and fig. S3, A and B), postimplantation E5.5 to E7.5 KO embryos were deformed and relatively deficient in adopting the typical postimplantation epiblast egg cylinder shape (fig. S26, E to G). Note that Oct4+ cells were readily detected at E5.5 to E7.5 in KO postimplantation epiblasts, which suggested that pluripotent cells existed in vivo and excluded precocious differentiation as the cause for embryonic lethality (Fig. 4B and fig. S27). However, the typical down-regulation and retraction in Nanog expression seen in WT embryos at E5 to E5.5 (*11*) was not observed in KO embryos (fig. S28A). Moreover, at E6.0 to E7.5, Nanog expression in WT embryos was reinitiated and restricted to the proximal posterior epiblast (Fig. 4C). On the contrary, Nanog was diffusely expressed throughout the entire Oct4+ epiblast in KO E6.0 to E7.5 embryos, (Fig. 4C and fig. S28, B and C). Notably, X-chromosome inactivation and Esrrb down-regulation were observed in both WT and KO postimplantation epiblasts (fig. S29), which indicated that some level of priming does occur and that the latter relative resistance to priming is less severe in some characteristics in vivo relative to that observed in vitro (Fig. 2). Nevertheless, reduced competence to undergo priming was also evident in vivo by the fact that early differentiation markers such as Brachyury+, Foxa2+ cells or early Oct4+/Blimp1+ primordial germ cells were not induced in KO postimplantation embryos (Fig. 4D and figs. S30 to S32). Further, E6.5 KO Oct4+ epiblasts expanded and maintained in primed FGF2-activin conditions yielded Oct4+/Esrrb+/Nanog+ naïve-like pluripotent lines (fig. S33). Collectively, the retention of widespread Nanog expression and maintenance of Oct4 expression without up-regulating lineage commitment genes in vivo are largely consistent with the in vitro observed phenotypes. Further, the latter reiterate relative resistance to terminate aspects of naïve pluripotency and the formation of an inadequately primed pluripotent epiblast in Mettl3 KO postimplantation embryos (fig. S34).

In summary, we identify m^{6}A mRNA methylation as a regulator acting at molecular switches, during resolution of murine naïve pluripotency, to safeguard an authentic and timely down-regulation of pluripotency factors, which is needed for proper lineage priming and differentiation (fig. S34). These findings set the stage for dissecting the role of m^{6}A in other developmental transitions (*12, 13*) and for exploring other potential regulatory roles for m^{6}A and its reader proteins.

REFERENCES AND NOTES

1. J. A. Hackett, M. A. Surani, *Cell Stem Cell* **15**, 416–430 (2014).
2. J. Hanna *et al.*, *Cell Stem Cell* **4**, 513–524 (2009).
3. J. Liu *et al.*, *Nat. Chem. Biol.* **10**, 93–95 (2014).
4. D. Dominissini *et al.*, *Nature* **485**, 201–206 (2012).
5. Y. Saletore, S. Chen-Kiang, C. E. Mason, *RNA Biol.* **10**, 342–346 (2013).
6. S. J. Dunn, G. Martello, B. Yordanov, S. Emmott, A. G. Smith, *Science* **344**, 1156–1160 (2014).
7. X. Wang *et al.*, *Nature* **505**, 117–120 (2014).
8. Y. Wang *et al.*, *Nat. Cell Biol.* **16**, 191–198 (2014).
9. N. Stern-Ginossar *et al.*, *Science* **338**, 1088–1093 (2012).
10. Y. Saletore *et al.*, *Genome Biol.* **13**, 175 (2012).
11. D. Acampora, L. G. Di Giovannantonio, A. Simeone, *Development* **140**, 43–55 (2013).
12. O. Gafni *et al.*, *Nature* **504**, 282–286 (2013).
13. Y. Rais *et al.*, *Nature* **502**, 65–70 (2013).

ACKNOWLEDGMENTS

G.R. is supported by grants from the Flight Attendant Medical Research Institute (FAMRI), the Israel Science Foundation (grant no. 1667/12), the Israeli Centers of Excellence (I-CORE) Program and The Israel Science Foundation (grants no. 41/11 and no. 1796/12), and the Ernest and Bonnie Beutler Research Program. G.R. is a member of the Sagol Neuroscience Network and holds the Djerassi Chair for Oncology (Sackler Faculty of Medicine, Tel-Aviv University, Israel). D.D. is supported by a Human Frontier Science Program long-term fellowship. J.H.H. is supported by a generous gift from Ilana and Pascal Mantoux; the New York Stem Cell Foundation; FAMRI; the Kimmel Innovator Research Award; the European Research Council starting grant (StG-2011-281906); the Leona M. and Harry B. Helmsley Charitable Trust; Britain Israel Research and Academic Exchange Partnership Regenerative Medicine Initiative; The Sir Charles Clore Research Prize; the Israel Science Foundation (Bikura, Morasha, ICORE, and Regular research programs); the Israel Cancer Research Fund; the Benoziyo endowment fund; the Helen and Martin Kimmel Institute for Stem Cell Research; Fritz Thyssen Stiftung; and Erica A. and Robert Drake. J.H.H. is a New York Stem Cell Foundation–Robertson Investigator. We thank Weizmann Institute management for providing critical financial and infrastructural support. DNA sequencing data have been deposited under National Center for Biotechnology Information, Gene Expression Omnibus submission GSE61998. All authors declare lack of conflict of interest.

SUPPLEMENTARY MATERIALS

www.sciencemag.org/content/347/6225/1002/suppl/DC1
Materials and Methods
Supplementary Text
Figures S1 to S34
Tables S1 to S6
References (*14–60*)

18 September 2014; accepted 18 December 2014
Published online 1 January 2015;
10.1126/science.1261417

CANCER

TERT promoter mutations and telomerase reactivation in urothelial cancer

Sumit Borah,[1,2]* Linghe Xi,[1,3]* Arthur J. Zaug,[1,2]* Natasha M. Powell,[1,3] Garrett M. Dancik,[4] Scott B. Cohen,[5] James C. Costello,[6,7] Dan Theodorescu,[6,7,8] Thomas R. Cech[1,2,3,6]†

Reactivation of telomerase, the chromosome end–replicating enzyme, drives human cell immortality and cancer. Point mutations in the telomerase reverse transcriptase (*TERT*) gene promoter occur at high frequency in multiple cancers, including urothelial cancer (UC), but their effect on telomerase function has been unclear. In a study of 23 human UC cell lines, we show that these promoter mutations correlate with higher levels of TERT messenger RNA (mRNA), TERT protein, telomerase enzymatic activity, and telomere length. Although previous studies found no relation between *TERT* promoter mutations and UC patient outcome, we find that elevated TERT mRNA expression strongly correlates with reduced disease-specific survival in two independent UC patient cohorts (n = 35; n = 87). These results suggest that high telomerase activity may be a better marker of aggressive UC tumors than *TERT* promoter mutations alone.

Telomerase activity is high in embryonic and stem cells but nearly undetectable in most somatic cells, due primarily to transcriptional down-regulation of telomerase reverse transcriptase (TERT), the catalytic subunit of the ribonucleoprotein particle (RNP) (*1*, *2*). Telomerase activity is up-regulated in 85 to 90% of cancers (*3*), and the recent identification of two highly recurrent point mutations in the *TERT* promoter in multiple cancer types suggests one probable mechanism for TERT reactivation. These mutations were first reported in melanoma (*4*, *5*) and

then quickly found in many other cancers such as urothelial cancer (UC), the fifth most common cancer in the Western world (*6*). For some cancers such as UC, these mutations occur more frequently than any other mutation, including *TP53*, and a recent report suggests that they may be the most prevalent of all noncoding mutations in cancer (*6*, *7*). The two mutations reside 124 and 146 base pairs upstream from the ATG translation start site (Fig. 1A) and are proposed to augment transcription by recruiting ETS transcription factors to newly generated GGA(A/T) motifs (*4*, *5*).

Though the frequency of the *TERT* promoter mutations suggests their importance for telomerase reactivation in cancer, fundamental questions remain. First, only modest increases in gene expression were seen upon introducing these mutations into heterologous luciferase reporter constructs: ~1.5- to ~4-fold increases, depending on the particular cell line used (*4*, *5*, *8*). Measurements of TERT mRNA levels in tumor tissues of many diverse cancer types have yielded similarly small differences with the promoter mutation (*9*–*12*), such as a ~1.4-fold increase for UC (*13*). However, one report of ~40-fold increased mRNA expression in cirrhotic preneoplastic lesions that harbor promoter mutations allows for the possibility of larger effects early in oncogenesis (*10*). Second, without evidence that these mutations have any consequence for telomerase activity and telomere length, their biological contribution to tumorigenesis is unclear. It is conceivable, for example, that *TERT* up-regulation promotes tumorigenesis primarily by telomerase-independent mechanisms, such as by perturbation of the c-MYC or WNT signaling pathways [(*14*); however, see (*15*)]. A third confounding observation is that roughly equal frequencies of these mutations are found across all stages and grades of UC and other cancers (*8*, *12*, *13*, *16*), which might suggest that telomerase up-regulation is not particularly important for tumor progression in these cases. One early study did find an association of telomerase activity level with pathological grade and clinical stage of bladder tumors (*17*); these authors were appropriately circumspect about their conclusions because they relied on a polymerase chain reaction (PCR)–based assay to measure telomerase activity instead of the more reliable direct enzymatic activity assay. Also, *TERT* promoter mutations have been associated with reduced survival of patients with glioblastoma multiforme (*6*) and with larger tumors and lymph node metastasis in the case of conventional papillary thyroid carcinomas (*12*).

To explore the effect of the *TERT* promoter mutations on telomerase activity in UC, we studied a panel of 23 UC cell lines (UC23) derived from tumors of a wide range of stages and grades, including both muscle-invasive and noninvasive tumors (tables S1 to S3). We genotyped the *TERT* promoter in each of the UC23 and found frequent incidence of the –124 C→T mutation and less frequent incidence of the –146 C→T mutation (Fig. 1B and fig. S1) (*16*). We also observed two instances of a –57 A→C mutation, previously identified in a family prone to melanoma but otherwise not frequently observed across cancer types (*7*, *18*), and several single-nucleotide polymorphisms (fig. S1).

Because amplification of the *TERT* gene has also been reported to be a mechanism of *TERT* reactivation in some cancers (*11*, *18*, *19*), we measured *TERT* copy number variation (CNV) in the UC23. Some variation was observed; the MGHU3 cell line was estimated to have ~six copies; the MGHU4 cell line was estimated to have ~three to four copies; and the HT1197, TCCSUP, and UMUC9 cell lines were estimated to have ~three copies each (Fig. 1B). As controls, our estimates of ~five *TERT* copies per HeLa genome and ~two per human embryonic kidney–293T genome agreed with previous reports (*20*, *21*).

We then examined TERT expression and telomerase activity in each of the UC23. We compared cell lines harboring either the –124 or –146 mutation to those without. Although the –57 mutation also generates a GGA(A/T) motif, it lies exactly at the major annotated transcriptional start site (TSS) for *TERT* and thus would probably affect transcription initiation by means other than simple up-regulation (*22*, *23*). Indeed, the –57 mutation resulted in the smallest of all changes observed in expression of a luciferase reporter (*4*). We hypothesized that all of the UC23 would show more or less similar levels of telomerase activity because virtually all cancers reactivate telomerase, whether by one mechanism (e.g., –124/–146 promoter mutation) or another (e.g., *TERT* CNV, up-regulation of ETS or c-MYC transcription factors, or down-regulation of repressive chromatin modifications), and because most reports had found no association between the promoter mutations and the severity of disease in UC (*1*–*3*, *8*, *19*, *24*).

Contrary to our hypothesis, we found that TERT mRNA levels were dramatically increased in those cancer cell lines harboring the –124 or –146 promoter mutations relative to the others, with an 18-fold increase in median value as measured by reverse transcription and quantitative PCR (RT-qPCR) (Fig. 2A and fig. S2) (P = 0.0067; all P values were obtained using the Wilcoxon rank sum test). However, the majority of TERT transcripts are alternatively spliced variants that are not translated into a functional reverse transcriptase (*1*, *15*). We therefore measured the levels of TERT protein (Fig. 2, B and C) and telomerase enzymatic activity (Fig. 2, D and E) in each of the

[1]Howard Hughes Medical Institute, University of Colorado BioFrontiers Institute, Boulder, CO 80309, USA. [2]Department of Chemistry and Biochemistry, University of Colorado, Boulder, CO 80309, USA. [3]Department of Molecular, Cellular, and Developmental Biology, University of Colorado, Boulder, CO 80309, USA. [4]Department of Mathematics and Computer Science, Eastern Connecticut State University, Willimantic, CT 06226, USA. [5]Children's Medical Research Institute and University of Sydney, Westmead, NSW 2145, Australia. [6]University of Colorado Comprehensive Cancer Center, Aurora, CO 80045, USA. [7]Department of Pharmacology, University of Colorado Anschutz Medical Campus, Aurora, CO 80045, USA. [8]Department of Surgery, University of Colorado, Aurora, CO 80045, USA.
*These authors contributed equally to this work. **†Corresponding author. E-mail: thomas.cech@colorado.edu**

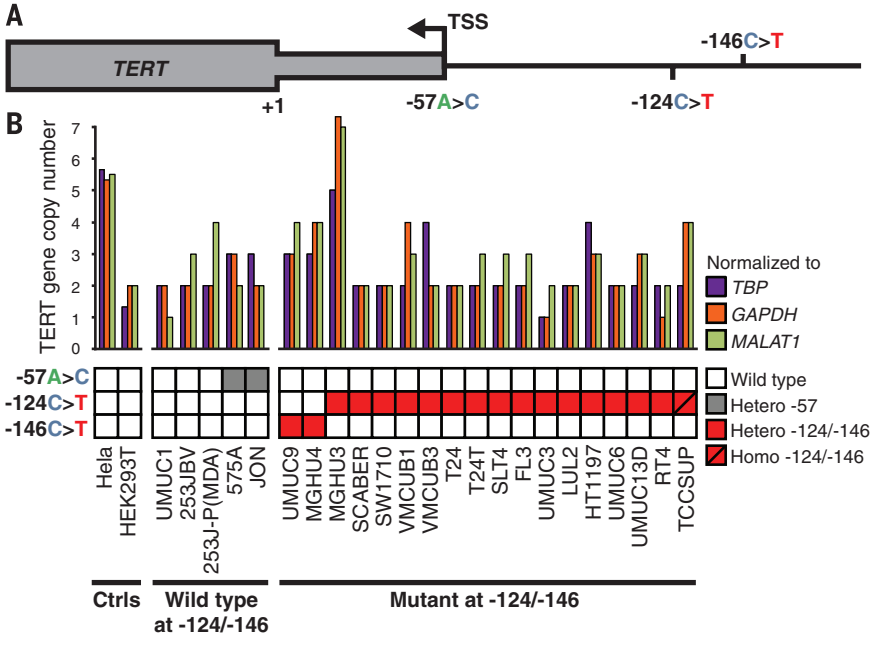

Fig. 1. *TERT* gene copy number and promoter mutations in UC cell lines. (**A**) Map of the proximal *TERT* promoter. Relevant mutations, the major annotated TSS, and the translational start codon (+1) are indicated. (**B**) *TERT* CNV (top) and *TERT* promoter genotype (bottom) in the UC23 and in reference cell lines (Ctrls). The genes TATA box binding protein (*TBP*), glyceraldehyde-3-phosphate dehydrogenase (*GAPDH*), or metastasis-associated lung adenocarcinoma transcript 1 (*MALAT1*) were used for normalization.

UC23, using immunopurification (IP) of TERT followed by immunoblot analysis and direct enzymatic activity assays, respectively (*25*, *26*). Both protein and telomerase activity levels were higher in cell lines harboring promoter mutations, although the twofold increases in median values were much more modest than the 18-fold increase in mRNA levels (Fig. 2, B and D). These more modest changes may reflect additional, posttranscriptional regulation of TERT expression. It is also possible that the mild lysis conditions used for IP, which are necessary to preserve integrity and activity of the telomerase RNP, were not sufficient to completely solubilize some of the UC23. This would result in reduced efficiency of TERT recovery in some cell lines and, subsequently, an underestimation of protein and activity levels. On the other hand, measurements of TERT mRNA levels and telomere lengths, for which harsher methods of cell disruption were used, were significantly different when comparing wild-type (WT) and mutant groups (Figs. 2A and 3B). Still, both TERT mRNA and protein levels correlated strongly with telomerase activity in the UC23 (Fig. 2, F and G, and fig. S3), whereas levels of the telomerase RNA (TR) subunit did not (Fig. 2H).

The eight cell lines with the greatest levels of TERT protein expression and the nine cell

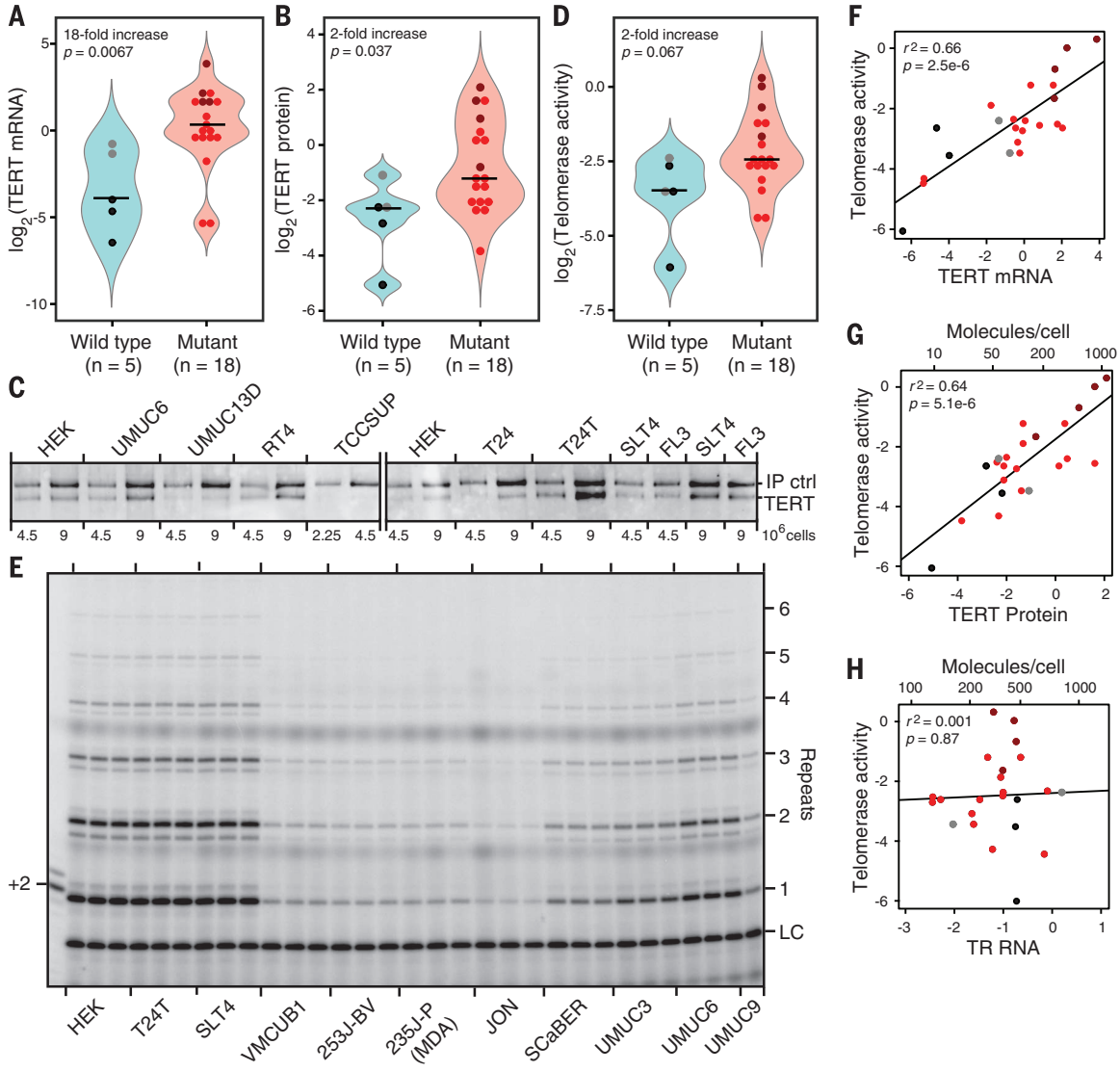

Fig. 2. *TERT* promoter mutations are associated with increased TERT mRNA and protein and telomerase activity. (**A**) Quantification of TERT mRNA in cell lines with WT (black and gray dots) versus mutant (red and magenta dots) *TERT* promoters by RT-qPCR amplification of exon 14 normalized to 18*S* ribosomal RNA or GAPDH mRNA. (Throughout this work, "mRNA" refers to transcripts containing TERT exon 14 or exon 3, which will include alternatively spliced variants that do not yield a functional reverse transcriptase.) Two cell lines that are WT at –124/–146 have the –57 A→C mutation (gray dots). T24T is a more tumorigenic variant of T24, and SLT4 and FL3 were derived from tumors that had metastasized in mice injected with T24T cells (these cell lines are indicated with magenta dots; also see tables S1 to S3). (**B**) Quantification of TERT protein by IP followed by immunoblot. (**C**) Representative immunoblots showing TERT protein levels in several of the UC23. IP ctrl, see supplementary materials and methods. The efficiency of IP was found to be similar from lysates prepared from each cell line (fig. S4). (**D**) Quantification of telomerase activities in UC23 cell extracts, measured by extension of a telomeric oligonucleotide in the presence of [α-^{32}P]dGTP (dGTP, 2′-deoxyguanosine 5′-triphosphate). (**E**) Representative autoradiogram of telomeric oligonucleotides extended by telomerase after TERT IP. LC, DNA loading control. (**F**) Log_2(telomerase activity) versus log_2(TERT mRNA) for each of the UC23. Cell lines are color coded as in (A). (**G**) Log_2(telomerase activity) versus log_2(TERT protein). (**H**) Log_2(telomerase activity) versus log_2(TR RNA). In (G) and (H), the number of molecules per cell was calculated as in (*25*).

lines with the greatest levels of telomerase activity all harbored the –124 or –146 mutation. These results support the assertion that, in UC, these mutations often result in higher levels of TERT reactivation than those achieved by other reactivating mechanisms and confirm that TERT, rather than TR or some other factor, is the limiting component for formation of the telomerase RNP in the UC23 (one notable exception is the SW1710 cell line, which was measured to have ~850 TERT protein molecules but only ~140 TR molecules per cell).

Whether a cell enters replicative senescence or becomes immortal is not thought to depend on telomerase activity per se, but rather on telomere maintenance. We therefore measured telomere lengths for each of the UC23 and found longer average lengths in promoter-mutant cell lines (Fig. 3 and fig. S5). Overall, telomerase activity correlated strongly with telomere length (fig. S6). No correlation was seen between increased *TERT* gene copy number and TERT mRNA or protein levels, telomerase activity, or telomere lengths (fig. S7). These data, alongside recent observations that there is no substantial *TERT* CNV in UC, suggest that gene amplification is not an important mechanism for telomerase reactivation in this type of cancer (*19*).

To determine the clinical relevance of these observations, we evaluated whether TERT mRNA expression was predictive of disease-specific survival (DSS) of UC patients. To make consistent comparisons, we focused our analysis on publically available gene expression profiles of patients for whom DSS endpoint data were available and who had undergone radical cystectomy as definitive treatment. This eliminated the confounding factor of patients who had undergone chemotherapy, because these treatment regimens varied among these individuals and can affect DSS (*27*). A subset of patients from two cohorts met these selection criteria, one from the Chungbuk National University Hospital (CNUH) (n = 35) (*28*) and the other from the Memorial Sloan Kettering Cancer Center (MSKCC) (n = 87) (*29*). We found that increased expression of TERT mRNA in the tumors of these patients correlated with reduced DSS in both of these cohorts (P = 0.0042 and 0.034, respectively) (Fig. 4). Considering our finding that increased TERT mRNA levels serve as a reliable indicator for increased telomerase activity in the UC23 (Fig. 2F), these results suggest that robust telomerase reactivation is important for UC tumor progression. In contrast, several previous studies found no correlation between the presence of promoter mutations and the severity of UC (*12*, *13*, *16*). This apparent discrepancy may be explained by the fact that, although these mutations do correlate with a more robust reactivation of the enzyme in general, other genetic or epigenetic differences also contribute. For example, the T24 and T24T cell lines have the same number of *TERT* copies and –124 promoter mutations, but the more tumorigenic T24T cells (*30*, *31*) have ~fivefold higher levels of TERT protein and ~fourfold higher levels of telomerase activity. Taken together, these data suggest that the better marker for patient prognosis is not promoter mutation per se, but TERT expression levels, which directly determine telomerase activity levels.

Reactivation of some mechanism for telomere maintenance is considered to be essential for oncogenesis. Because UC does not typically employ the alternative lengthening of telomeres mechanism (*32*), we originally hypothesized that all of the UC23 would have a similar level of telomerase up-regulation; that is, the promoter mutations would represent only one of several equally effective mechanisms for TERT reactivation (*5*, *12*, *13*, *16*, *33*). Instead, we observed that (i) the UC cell lines varied widely (~100-fold) in the level of TERT protein and telomerase activity (Fig. 2G), which correlated with their respective telomere lengths (Fig. 3), and (ii) although the mere presence of a promoter mutation did not necessarily lead to high telomerase activity, those cell lines with the highest levels of activity harbored such mutations (Fig. 2D). These results suggest that *TERT* promoter mutations provide a particularly effective mechanism for high-level telomerase reactivation in UC. Future studies will be needed to test whether UC tumors harboring high levels of telomerase activity are particularly susceptible to treatment with targeted telomerase inhibition.

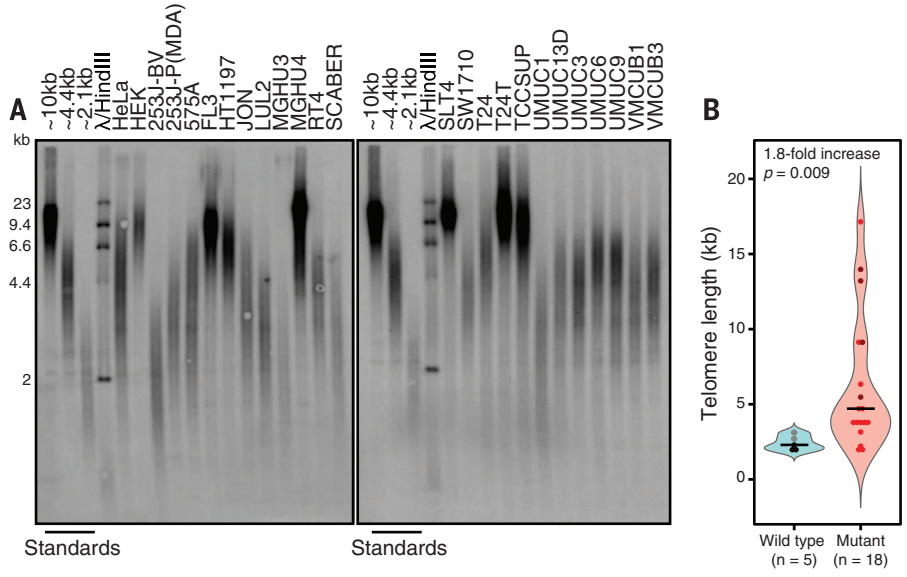

Fig. 3. *TERT* promoter mutations are associated with long telomeres in the UC23, as determined by telomeric restriction fragment (TRF) analysis. (**A**) Southern blot with a telomeric DNA probe was performed as in (*34*). Standards were TRFs from HeLa cell lines previously characterized as having long, intermediate, or short telomeres (*34*). (**B**) Quantification of TRFs in WT versus promoter-mutant cell lines. Dots colored as in Fig. 2.

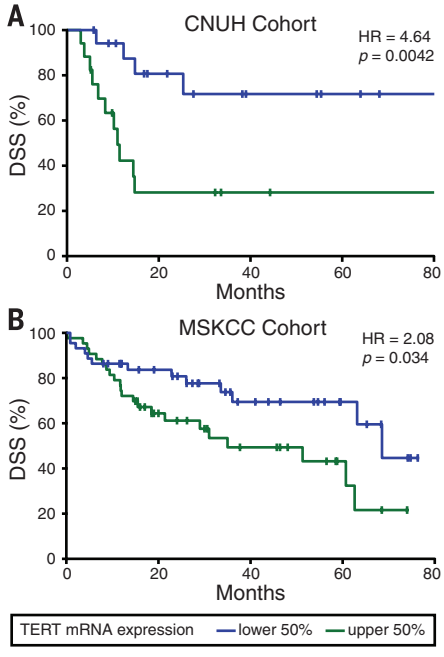

Fig. 4. Tumor expression level of TERT mRNA is inversely associated with disease-specific survival of patients with UC. The prognostic value of TERT mRNA expression for DSS in patients who underwent radical cystectomy and who did not receive chemotherapy or additional treatments before or after cystectomy in the (**A**) CNUH and (**B**) MSKCC cohorts. Kaplan-Meier curves for patients with low and high expression levels of TERT mRNA were generated (see supplementary materials), and the corresponding log-rank P values and hazard ratios (HR) are as indicated. CNUH data include only patients with muscle-invasive tumors, whereas MSKCC data include patients both with muscle-invasive and noninvasive tumors. A similar analysis could not be performed using The Cancer Genome Atlas because this data set is not limited to DSS.

REFERENCES AND NOTES

1. A. Kilian *et al.*, *Hum. Mol. Genet.* **6**, 2011–2019 (1997).
2. C. Günes, S. Lichtsteiner, A. P. Vasserot, C. Englert, *Cancer Res.* **60**, 2116–2121 (2000).
3. J. W. Shay, S. Bacchetti, *Eur. J. Cancer* **33**, 787–791 (1997).
4. S. Horn *et al.*, *Science* **339**, 959–961 (2013).
5. F. W. Huang *et al.*, *Science* **339**, 957–959 (2013).
6. P. J. Killela *et al.*, *Proc. Natl. Acad. Sci. U.S.A.* **110**, 6021–6026 (2013).
7. N. Weinhold, A. Jacobsen, N. Schultz, C. Sander, W. Lee, *Nat. Genet.* **46**, 1160–1165 (2014).
8. P. S. Rachakonda *et al.*, *Proc. Natl. Acad. Sci. U.S.A.* **110**, 17426–17431 (2013).
9. B. Heidenreich *et al.*, *Nat. Commun.* **5**, 3401 (2014).
10. J. C. Nault *et al.*, *Nat. Commun.* **4**, 2218 (2013).
11. A. Tallet *et al.*, *Oncogene* **33**, 3748–3752 (2014).
12. J. Vinagre *et al.*, *Nat. Commun.* **4**, 2185 (2013).
13. Y. Allory *et al.*, *Eur. Urol.* **65**, 360–366 (2014).
14. J.-I. Park *et al.*, *Nature* **460**, 66–72 (2009).
15. I. Listerman, F. S. Gazzaniga, E. H. Blackburn, *Mol. Cell. Biol.* **34**, 280–289 (2014).
16. C. D. Hurst, F. M. Platt, M. A. Knowles, *Eur. Urol.* **65**, 367–369 (2014).
17. Y. Lin *et al.*, *Clin. Cancer Res.* **2**, 929–932 (1996).
18. Y. Cao, T. M. Bryan, R. R. Reddel, *Cancer Sci.* **99**, 1092–1099 (2008).
19. K. A. Hoadley *et al.*, *Cell* **158**, 929–944 (2014).
20. A. Adey *et al.*, *Nature* **500**, 207–211 (2013).
21. E. Kjeldsen, D. Tordrup, G. M. Hübner, B. R. Knudsen, F. F. Andersen, *Anticancer Res.* **30**, 3257–3265 (2010).
22. M. Meyerson *et al.*, *Cell* **90**, 785–795 (1997).
23. L. H. Li, C. Nerlov, G. Prendergast, D. MacGregor, E. B. Ziff, *EMBO J.* **13**, 4070–4079 (1994).
24. Y. Gui *et al.*, *Nat. Genet.* **43**, 875–878 (2011).
25. L. Xi, T. R. Cech, *Nucleic Acids Res.* **42**, 8565–8577 (2014).
26. S. B. Cohen, R. R. Reddel, *Nat. Methods* **5**, 355–360 (2008).
27. H. B. Grossman *et al.*, *N. Engl. J. Med.* **349**, 859–866 (2003).
28. W. J. Kim *et al.*, *Mol. Cancer* **9**, 3 (2010).
29. M. Sanchez-Carbayo, N. D. Socci, J. Lozano, F. Saint, C. Cordon-Cardo, *J. Clin. Oncol.* **24**, 778–789 (2006).
30. J. J. Gildea, W. L. Golden, M. A. Harding, D. Theodorescu, *Genes Chromosomes Cancer* **27**, 252–263 (2000).
31. J. J. Gildea *et al.*, *Cancer Res.* **62**, 6418–6423 (2002).
32. C. M. Heaphy *et al.*, *Am. J. Pathol.* **179**, 1608–1615 (2011).
33. The use of microarray data sets to identify alternative mechanisms of TERT reactivation employed by those cell lines that were WT at positions −124 and −146 was unsuccessful. Average mRNA levels were roughly similar for (i) the ETS1 and ETS2 transcription factors (~1.1-fold higher in the WT group), (ii) the c-MYC transcription factor (~1.4-fold higher in the WT group), and (iii) the core components of the Polycomb repressive complex 2 (between ~0.91-fold and ~1.3-fold higher in the WT group).
34. J. Nandakumar *et al.*, *Nature* **492**, 285–289 (2012).

ACKNOWLEDGMENTS

We thank C. Owens for providing the UC23, as well as detailed information on their origins and growth conditions. This work was supported by NIH grants CA075115 and CA104106 to D.T., R01 GM099705 to T.R.C., and T32 GM08759 to L.X. S.B.C. is supported by Cancer Council NSW (Australia). T.R.C. is an investigator of the Howard Hughes Medical Institute and is on the board of directors of Merck.

SUPPLEMENTARY MATERIALS

www.sciencemag.org/content/347/6225/1006/suppl/DC1
Materials and Methods
Supplementary Text
Figs. S1 to S7
Tables S1 to S3
References (*35*, *36*)

20 August 2014; accepted 24 January 2015
Published online 5 February 2015;
10.1126/science.1260200

GENE REGULATION

Transcribed enhancers lead waves of coordinated transcription in transitioning mammalian cells

Erik Arner,*† Carsten O. Daub,*† Kristoffer Vitting-Seerup,*† Robin Andersson,*† Berit Lilje, Finn Drabløs, Andreas Lennartsson, Michelle Rönnerblad, Olga Hrydziuszko, Morana Vitezic, Tom C. Freeman, Ahmad M. N. Alhendi, Peter Arner, Richard Axton, J. Kenneth Baillie, Anthony Beckhouse, Beatrice Bodega, James Briggs, Frank Brombacher, Margaret Davis, Michael Detmar, Anna Ehrlund, Mitsuhiro Endoh, Afsaneh Eslami, Michela Fagiolini, Lynsey Fairbairn, Geoffrey J. Faulkner, Carmelo Ferrai, Malcolm E. Fisher, Lesley Forrester, Daniel Goldowitz, Reto Guler, Thomas Ha, Mitsuko Hara, Meenhard Herlyn, Tomokatsu Ikawa, Chieko Kai, Hiroshi Kawamoto, Levon M. Khachigian, S. Peter Klinken, Soichi Kojima, Haruhiko Koseki, Sarah Klein, Niklas Mejhert, Ken Miyaguchi, Yosuke Mizuno, Mitsuru Morimoto, Kelly J. Morris, Christine Mummery, Yutaka Nakachi, Soichi Ogishima, Mariko Okada-Hatakeyama, Yasushi Okazaki, Valerio Orlando, Dmitry Ovchinnikov, Robert Passier, Margaret Patrikakis, Ana Pombo, Xian-Yang Qin, Sugata Roy, Hiroki Sato, Suzana Savvi, Alka Saxena, Anita Schwegmann, Daisuke Sugiyama, Rolf Swoboda, Hiroshi Tanaka, Andru Tomoiu, Louise N. Winteringham, Ernst Wolvetang, Chiyo Yanagi-Mizuochi, Misako Yoneda, Susan Zabierowski, Peter Zhang, Imad Abugessaisa, Nicolas Bertin, Alexander D. Diehl, Shiro Fukuda, Masaaki Furuno, Jayson Harshbarger, Akira Hasegawa, Fumi Hori, Sachi Ishikawa-Kato, Yuri Ishizu, Masayoshi Itoh, Tsugumi Kawashima, Miki Kojima, Naoto Kondo, Marina Lizio, Terrence F. Meehan, Christopher J. Mungall, Mitsuyoshi Murata, Hiromi Nishiyori-Sueki, Serkan Sahin, Sayaka Nagao-Sato, Jessica Severin, Michiel J. L. de Hoon, Jun Kawai, Takeya Kasukawa, Timo Lassmann, Harukazu Suzuki, Hideya Kawaji,† Kim M. Summers,† Christine Wells,† FANTOM Consortium, David A. Hume,†‡ Alistair R. R. Forrest,†‡ Albin Sandelin,†‡ Piero Carninci,†‡ Yoshihide Hayashizaki†‡

Although it is generally accepted that cellular differentiation requires changes to transcriptional networks, dynamic regulation of promoters and enhancers at specific sets of genes has not been previously studied en masse. Exploiting the fact that active promoters and enhancers are transcribed, we simultaneously measured their activity in 19 human and 14 mouse time courses covering a wide range of cell types and biological stimuli. Enhancer RNAs, then messenger RNAs encoding transcription factors, dominated the earliest responses. Binding sites for key lineage transcription factors were simultaneously overrepresented in enhancers and promoters active in each cellular system. Our data support a highly generalizable model in which enhancer transcription is the earliest event in successive waves of transcriptional change during cellular differentiation or activation.

Regulated transcription initiation underlies state changes in cell phenotype and is coordinated by transcription factors binding to gene-proximal promoters or distal regulatory regions such as enhancers. The interaction between enhancers and transcription induction during cellular differentiation has been cited as one of the outstanding mysteries of modern biology (*1*). Enhancer chromatin landscapes change drastically between developing tissues and differentiated cells (*2*–*4*). Active enhancers initiate production of RNAs (eRNAs) (*5*) and enhancer action during differentiation can be assessed by sequencing of steady-state (*6*, *7*) or nascent RNA (*8*–*10*), demonstrating that eRNA and target gene expression are correlated. eRNA production is also correlated to physical proximity between enhancers and promoters (*8*, *9*). However, the general temporal relationship between enhancer and promoter activation across biological system is unknown.

Genome-scale 5′ rapid amplification of cDNA ends (cap analysis of gene expression, or CAGE) detects transcription start sites (TSSs), including the bidirectional TSS characteristic of active enhancers (*11*). Based on a large set of reporter assays, CAGE-defined enhancers are two to three times as likely to validate (*12*) as untranscribed chromatin-defined enhancer candidates from

The list of author affiliations is available in the Supplementary Text.
*These authors contributed equally to this work. †FANTOM5 Phase 2 Core authors. **‡Corresponding author. E-mail: david.hume@roslin.ed.ac.uk (D.A.H.); forrest@gsc.riken.jp (A.R.R.F.); albin@binf.ku.dk (A.S.); carninci@riken.jp (P.C.); yosihide@gsc.riken.jp (Y.H.)**

the ENCODE (Encyclopedia of DNA Elements) consortium (*13*). Here, we used CAGE to dissect the relationship between dynamic changes in mRNA and eRNA in 33 time courses of differentiation and activation. The time courses included stem cells (embryonic, induced pluripotent, trophoblastic, and mesenchymal stem cells) and committed progenitors undergoing terminal differentiation toward mesodermal, endodermal, and ectodermal fates, as well as fully differentiated primary cells and cell lines responding to stimuli (growth factors and pathogens) (Fig. 1, A and B; tables S1 to S3; and supplementary methods). In total, 1189 CAGE libraries from 408 distinct time points in the 33 time courses were analyzed (Fig. 1B and auxiliary data tables S1 and S2). Differentiation or response to stimulus was assessed by monitoring cell morphology changes, reproducible induction of known lineage markers, and similarity of the end-point transcriptome to differentiated cells from the steady-state samples of FANTOM5 (*14*) (auxiliary data table S1).

The current data expand the set of known human and mouse core promoters from the FANTOM5 body-wide steady-state atlas (*14*) to 201,802 and 158,966, and the set of transcribed enhancers to 65,423 and 44,459. Of all identified core promoters in human and mouse, 51% and 61% varied significantly in expression in at least one time course. Out of the 103,355 differentially expressed human promoters, 80,152 were within genes on the same strand. Of these, 55,626 are potential alternative promoters (see supplementary methods), overlapping a total of 13,138 genes. We found 65 human genes that had a dynamic switch between alternative promoters within a time course, leading to exclusion of exons encoding protein domains (table S4).

Of all enhancers identified in FANTOM5, 42,274 human (65%) and 34,338 mouse (77%) enhancers were expressed in at least one CAGE library in

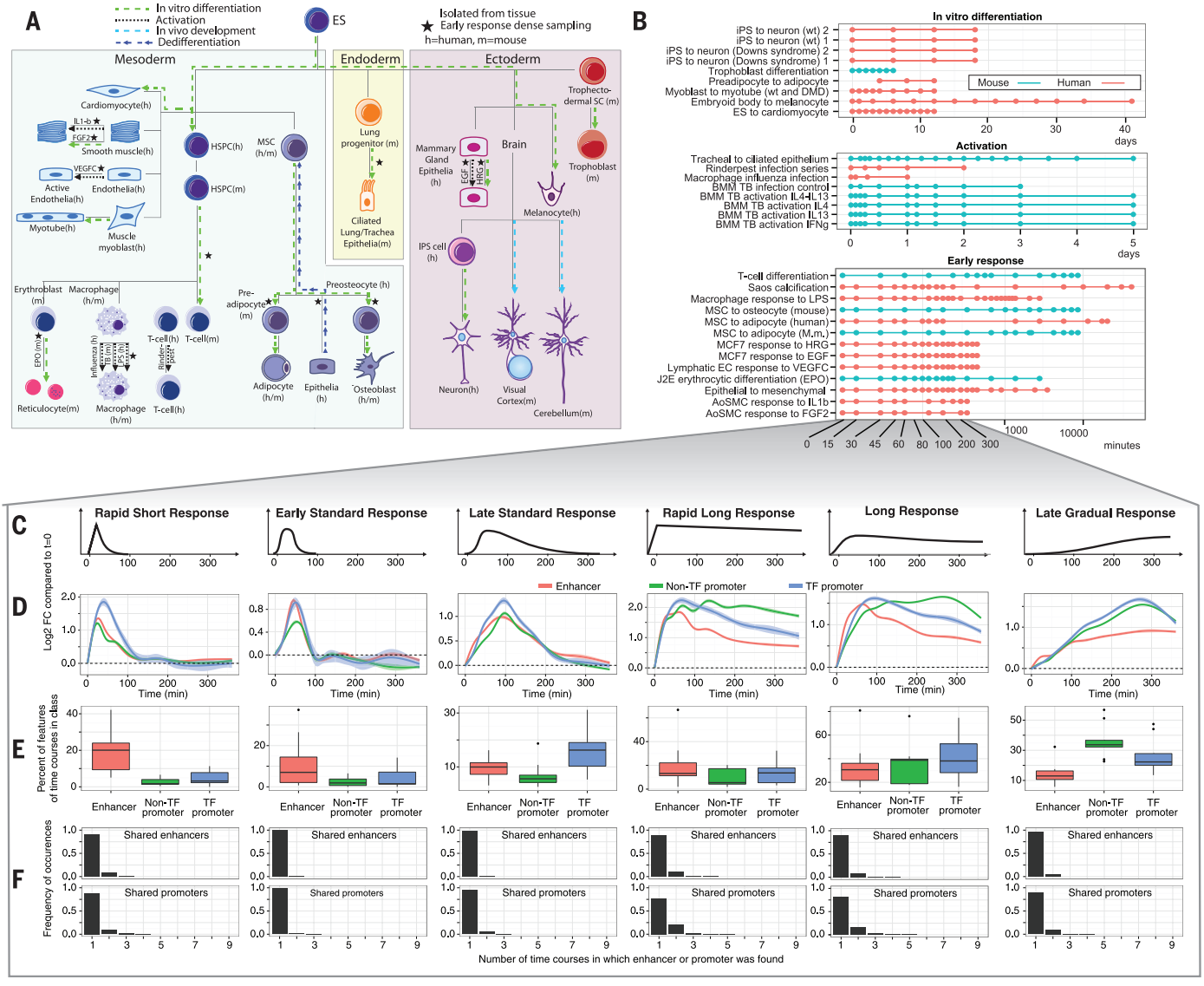

Fig. 1. Time course design and definition of response classes. (**A**) Schematic illustration of the time course experiments included in the study, arranged according to a development tree. Germ layers are shown as boxes. Black stars indicate time series sampled with high resolution. (**B**) Overview of time courses according to sampling strategy. The *x* axis indicates time after induction. Each dot indicates CAGE sampling, typically done in biological triplicates. (**C**) Stylistic representation of each of the major up-regulated response patterns (classes) identified as described in the main text. The *y* axis shows $\log_2$ fold change versus time 0; the *x* axis shows time in minutes. (**D**) Mean expression $\log_2$ fold change across time courses for enhancers and promoters classified into each response pattern [as in (C)]. The 95% confidence intervals of means are shown. (**E**) Boxplots of fractions showing the preference for enhancers, TF promoters, and other promoters for respective response class. (**F**) Overlap between time courses in terms of enhancers and promoters in respective class. Barplots show the frequency (*y* axis) of the number of time courses (out of 9) sharing a specific feature (*x* axis).

the current study. Of these, 5371 (13%) human and 6824 (20%) mouse enhancers changed expression significantly over time in at least one time course. Most of these enhancer changes were time-course specific (56% in human, 67% in mouse). In contrast, the fraction of promoters regulated in only a single time course was smaller (29% in human, 33% in mouse).

We profiled 13 cellular systems with high temporal resolution within the first hours of cellular induction (Fig. 1B). We focused on the first 6 hours in nine of these time courses (five human and four mouse having sufficient numbers of dynamic promoters and enhancers; table S1).

Based on unsupervised clustering, we identified a set of distinct response pattern classes, shared by multiple time courses, by analyzing expression fold changes versus time 0 in each time course. For each response class, we defined specific expression rules (fig. S1), enabling consistent response class labeling of any dynamically transcribed enhancer or TSS in a time-course–specific fashion (figs. S2 to S4). Transcription factor (TF) promoters were analyzed as a distinct group. Because most enhancers and promoters that were dynamically changing in this set were up-regulated over time (fig. S5), we focused on the six up-regulated response classes (Fig. 1C).

Multiple enhancers, TF promoters, and non–TF promoters were found in all response classes (Fig. 1D, fig. S6, and auxiliary data table S3), but with different preferences. Enhancers were more common in the early peaking classes ("rapid short," "early standard," and "rapid long" responses). TF promoters were generally induced after enhancers (preferring the "late standard" response and "long response" classes) and non–TF promoters were most common in the "late gradual response" class that increased gradually with time (Fig. 1E), suggesting that many of these genes were the direct or indirect targets of the induced transcription factors. Simulation studies, as well as gene-specific RNA half-life data (*15*), showed that differential degradation rates of RNA species (*11*) could not explain the observed class preferences (supplementary text and figs. S7 and S8). Although these patterns were evident across cell types and species, few promoters (mean 8.5% across classes) and even fewer enhancers (mean 5.1% across classes) were assigned to the same response class in two or more time courses (Fig. 1F).

We looked further at a literature-curated set of 232 immediate early response (IER) genes (table S5). Although 65% of the IER genes had at least one promoter that was up-regulated within the first 2 hours in at least two time courses, no consistent pattern of IER expression was obvious between time courses (fig. S9). For example, only 42 promoters were induced early in five or more human time courses (fig. S10A). Even fewer enhancers shared an early response: Only 11 were induced in three or more time courses (fig. S10B), and of these, half neighbored a known IER gene. Thus, the IER pattern is generalizable across different cell states, but the cohort of IER genes are not.

In general, up-regulated enhancers in the rapid short response class were transcribed earlier than their proximal (±200 kb) promoters (Fig. 2, A and B, and fig. S11). Proximal TF promoters were, in turn, more highly and more rapidly activated than proximal non–TF promoters. To compare the responses over time, we used the "center of mass" (CM) statistic identifying the time point by which 50% of the expression change in the enhancer or promoter had occurred. Enhancers changed most rapidly, followed by TF promoters, then non–TF promoters (Fig. 2C). The temporal differences were highlighted further when enhancers were compared to their proximal promoters (within ±200 kb) (Fig. 2C). For 85.8% of enhancer–non–TF promoter pairs and 74.6% of

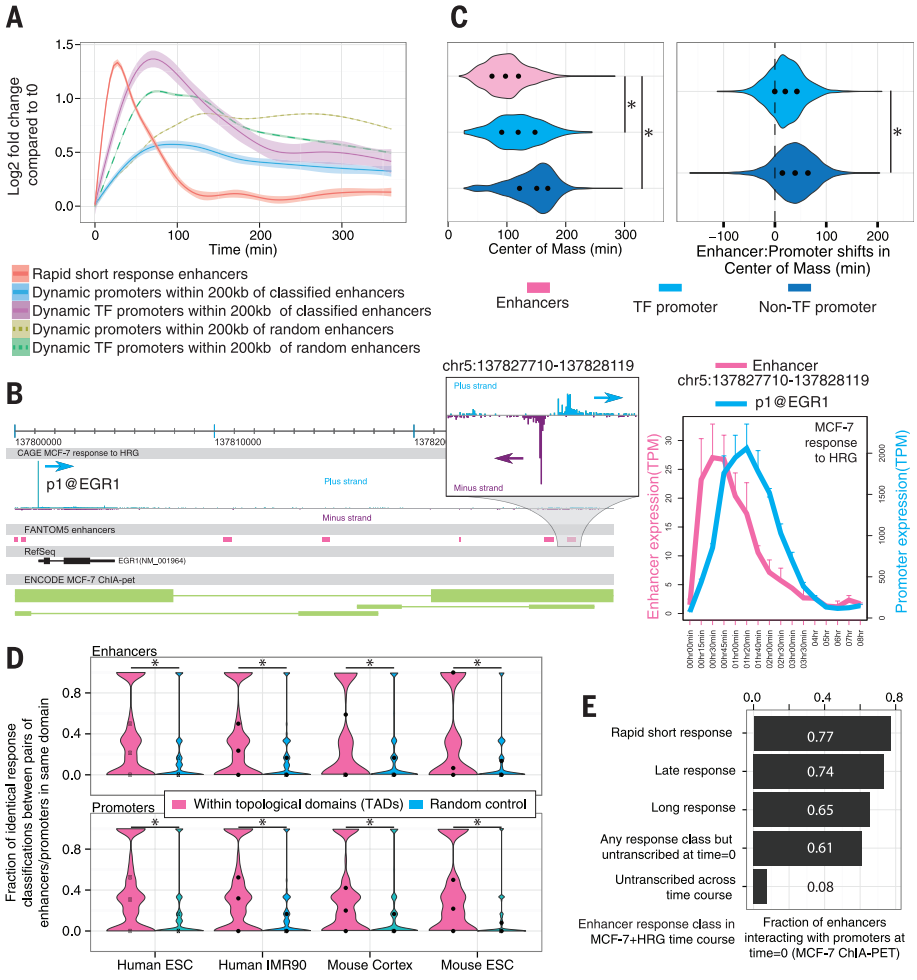

Fig. 2. Temporal shifts between enhancer and promoter activity. (**A**) Smoothed mean expression over time for all enhancers classified into the rapid short response group and all differentially expressed proximal (±200 kb) promoters, split by gene type. Controls for class specificity (dotted lines) constitute promoters proximal to randomly sampled enhancers from other classes. Shaded areas indicate 95% confidence intervals. (**B**) Example of expression timing in an enhancer-promoter pair (*EGR1*), showing activation of enhancers before promoter activation. MCF-7 ChIA-PET interaction data are visualized at the bottom as green lines; each line represents a cluster of ChIA-PET paired tags consisting of at least three pairs, where line end thickness is proportional to the number of paired tags in the cluster. Right panel shows the expression level of promoter and enhancer in MCF-7 cells after induction with HRG. Error bars indicate SD. (**C**) Left: Distribution of center of mass (CM) of expression changes (see main text) for enhancers, TF promoters, and promoters of other genes. Right: difference in CM ("shift") between enhancers-promoter pairs linked by proximity (±200 kb) split by gene type. Black dots indicate 25th, 50th, and 75th percentiles. Asterisks indicate significance ($P < 1.0 \times 10^{-106}$, Mann-Whitney U test). (**D**) The similarity of enhancer or promoter response classification (Fig. 1C) within each TAD was analyzed by calculating the frequency of identically classified enhancers or promoters in all pairwise comparisons. Frequency distributions are shown as violin plots. Controls are made by randomly sampling the same number of enhancers or promoters and calculating the classification similarity as above (repeated 100 times for each TAD). Asterisks indicate significance ($P < 0.01$, Mann-Whitney U test); dots represent percentiles, as in (C). (**E**) Fraction of enhancers that interact (by RNAPII-ChIA-PET) with promoters in unstimulated MCF-7 cells, split by enhancer response class in the MCF-7+HRG time course.

enhancer–TF promoter pairs, the CM occurred earlier for the enhancer ($P < 1.0 \times 10^{-106}$, Wilcoxon signed rank test). We hypothesized that these results might reflect larger chromatin structures; indeed, enhancer-promoter pairs defined by topological domains (TADs) (*16*) gave similar results (figs. S11 and S12), and moreover, enhancers (or promoters) within the same TAD were more likely to be in the same response class (Fig. 2D). Similarly, groups of enhancer-promoter pairs (defined either by genomic proximity or TAD boundaries) were more similar in terms of CM shifts than expected by chance (fig. S13, $P < 1.0 \times 10^{-14}$, Mann-Whitney U test).

We used ENCODE (*13*) data to demonstrate that enhancers dynamically expressed in the MCF-7+HRG time course were more likely to be marked with high deoxyribonuclease (DNAse) sensitivity and enriched in H3K27ac and RNA polymerase II (RNAPII) chromatin immunoprecipitation signal in steady-state MCF-7 cells than enhancers that were not active throughout the time course (fig. S14A). Indeed, chromatin interaction analysis with paired-end-tag sequencing (ChIA-PET) data from steady-state MCF-7 cells (*17*) showed that these dynamic enhancers interacted with promoters to a much larger extent than nonactive enhancers, but the fraction of promoter-interacting enhancers was high regardless of response class (Fig. 2E), suggesting that many dynamically changing enhancers are proximal to their promoter target(s) and primed beforehand in terms of chromatin state. However, chromatin patterns in the unstimulated state were not sufficient to distinguish between temporal enhancer classes (fig. S14B).

Transcription factor binding sites implicated in regulating enhancer and promoter expression were assessed by inferring motif activities (*18*)—a statistic that describes the ability of a DNA motif to explain observed expression changes across a given set of samples—based on motif occurrence in the regions –300 to +100 base pairs (bp) from the major TSSs of each promoter and ±200 bp from the center of each enhancer, resulting in a derived activity profile across time for each DNA binding motif and time course. Motif sets with high predictive power in enhancers and promoters overlapped significantly (false discovery rate < 0.05, Fisher's exact test) in 29 out of 33 time courses (Fig. 3A). Many of these highly contributing motifs described binding sites for known lineage-specific regulators in specific time courses, such as FOS in MCF-7 cells stimulated by HRG, GATA6 in cardiomyocyte differentiation, and nuclear factor κB (NF-κB) in macrophages. On average, motif activity scores correlated positively across time between enhancers and promoters, with significantly higher correlation for motifs identified as significantly active (supplementary text) in both enhancers and promoters ($P < 6.9 \times 10^{-8}$, Mann-Whitney test) (Fig. 3B); however, in general, motif activity reached a maximum in enhancers earlier than in promoters ($P < 1.8 \times 10^{-14}$, Wilcoxon signed rank test; Fig. 3, C and D). Thus, the general observation of enhancer transcription waves preceding those of promoters identified above was supported by motif activity.

In summary, by using a large-scale comparative analysis across many different tissues and time courses, and simultaneously sampling expression at gene promoters and enhancers, we reveal that enhancer transcription is the most common rapid transcription change occurring when cells initiate a state change. Enhancer RNA concentration peaked as early as 15 min after the transition trigger was applied in some time courses. Although earlier studies of single time courses have reported enhancer activity before gene activation in a small set of enhancer-gene pairs (*8*, *9*, *19*), we can now establish this phenomenon as a general feature of mammalian transcriptional regulation, across a multitude of biological systems. This challenges previous models that suggested that linked enhancers and promoters are coexpressed over

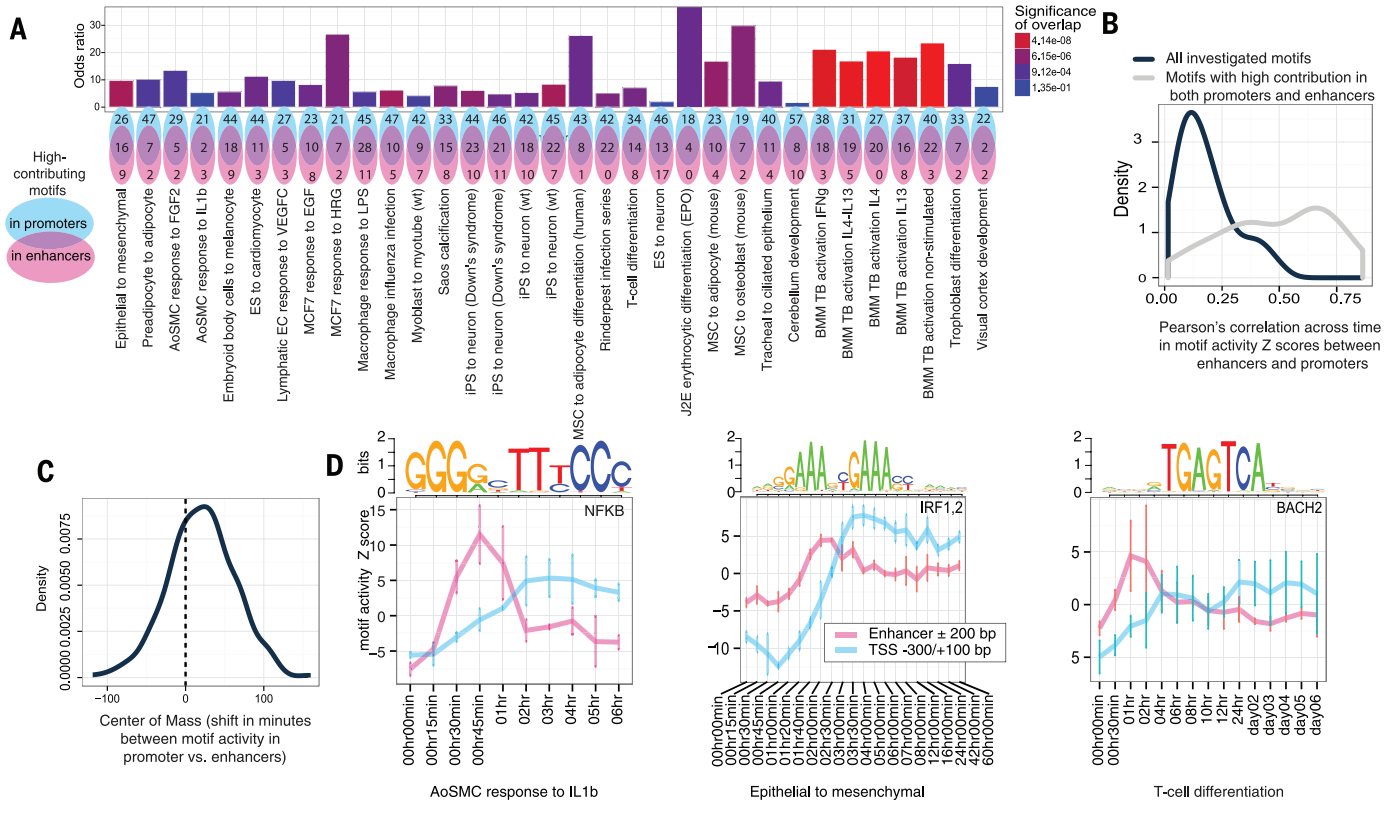

Fig. 3. Motif analysis of linked enhancers and promoters over time. (**A**) Overlap of motifs classified as significant for driving expression in enhancers and promoters. Top row: bar plot of motif overlap odds ratios, colored by significance. Bottom row: Venn diagrams of motif set overlap. (**B**) Distributions of average Pearson correlation coefficient between motif activities in enhancers and promoters in all motifs investigated (black) and motifs significantly active in both enhancers and promoters (gray). (**C**) Distribution of shift (minutes) in motif activity center of mass (see Fig. 2D) in promoters compared to enhancers. (**D**) Examples of motif activity in enhancers preceding that of promoters. Motif activity is plotted as the average of activity *Z* scores per time point. Error bars indicate the SD.

time [e.g., (*8*, *15*, *19*, *20*)]. Indeed, even in the case of late response classes, candidate enhancers appear to be activated in advance of promoters in their vicinity (fig. S11). The rapid burst of eRNA activity at 15 min was frequently followed by a rapid return to baseline (Fig. 1D). In these cases, it may be that once the target promoter has been activated, enhancer activity is no longer required. Other enhancers were rapidly activated and then continuously expressed. These eRNAs may have additional functional roles, such as the recently suggested role in promoting elongation (*15*).

REFERENCES AND NOTES

1. M. Levine, C. Cattoglio, R. Tjian, *Cell* **157**, 13–25 (2014).
2. S. Bonn *et al.*, *Nat. Genet.* **44**, 148–156 (2012).
3. A. S. Nord *et al.*, *Cell* **155**, 1521–1531 (2013).
4. A. B. Stergachis *et al.*, *Cell* **154**, 888–903 (2013).
5. T.-K. Kim *et al.*, *Nature* **465**, 182–187 (2010).
6. H. Wu *et al.*, *PLOS Genet.* **10**, e1004610 (2014).
7. M. Rönnerblad *et al.*, *Blood* **123**, e79–e89 (2014).
8. M. U. Kaikkonen *et al.*, *Mol. Cell* **51**, 310–325 (2013).
9. N. Hah, S. Murakami, A. Nagari, C. G. Danko, W. L. Kraus, *Genome Res.* **23**, 1210–1223 (2013).
10. W. Li *et al.*, *Nature* **498**, 516–520 (2013).
11. R. Andersson *et al.*, *Nat. Commun.* **5**, 5336 (2014).
12. R. Andersson *et al.*, *Nature* **507**, 455–461 (2014).
13. ENCODE Project Consortium, *Nature* **489**, 57–74 (2012).
14. FANTOM Consortium and the RIKEN PMI and CLST (DGT), *Nature* **507**, 462–470 (2014).
15. K. Schaukowitch *et al.*, *Mol. Cell* **56**, 29–42 (2014).
16. J. R. Dixon *et al.*, *Nature* **485**, 376–380 (2012).
17. G. Li *et al.*, *Cell* **148**, 84–98 (2012).
18. FANTOM Consortium *et al.*, *Nat. Genet.* **41**, 553–562 (2009).
19. C.-L. Hsieh *et al.*, *Proc. Natl. Acad. Sci. U.S.A.* **111**, 7319–7324 (2014).
20. N. E. Ilott *et al.*, *Nat. Commun.* **5**, 3979–3979 (2014).

ACKNOWLEDGMENTS

For a full list of acknowledgements and contributions, see supplementary text. FANTOM5 was made possible by a Research Grant for RIKEN Omics Science Center from the Ministry of Education, Culture, Sports, Science, and Technology of Japan (MEXT) to Y. Hayashizaki. It was also supported by Research Grants for RIKEN Preventive Medicine and Diagnosis Innovation Program to Y. Hayashizaki and RIKEN Centre for Life Science Technologies, Division of Genomic Technologies (from the MEXT, Japan). Additional funding is listed in the supplementary text. All CAGE data needed to reproduce the study have been deposited at the DNA Data Bank of Japan (DDBJ) under accession numbers DRA000991, DRA002711, DRA002747, and DRA002748. Additional visualizations of the data are available at http://fantom.gsc.riken.jp/5/. The human induced pluripotent stem cell lines that were subjected to cortical neuronal differentiation can be made available after completion of a materials transfer agreement with the Australian Institute for Bioengineering and Nanotechnology of The University of Queensland.

SUPPLEMENTARY MATERIALS

www.sciencemag.org/content/347/6225/1010/suppl/DC1
Materials and Methods
Supplementary Text
Figs. S1 to S14
Tables S1 to S5
Auxiliary data tables S1 to S3
References (*21*–*32*)

31 July 2014; accepted 26 January 2015
Published online 12 February 2015;
10.1126/science.1259418

EVOLUTION

Evolutionary resurrection of flagellar motility via rewiring of the nitrogen regulation system

Tiffany B. Taylor,[1]* Geraldine Mulley,[1]* Alexander H. Dills,[2] Abdullah S. Alsohim,[1,3] Liam J. McGuffin,[1] David J. Studholme,[4] Mark W. Silby,[2] Michael A. Brockhurst,[5] Louise J. Johnson,[1]† Robert W. Jackson[1,6]

A central process in evolution is the recruitment of genes to regulatory networks. We engineered immotile strains of the bacterium *Pseudomonas fluorescens* that lack flagella due to deletion of the regulatory gene *fleQ*. Under strong selection for motility, these bacteria consistently regained flagella within 96 hours via a two-step evolutionary pathway. Step 1 mutations increase intracellular levels of phosphorylated NtrC, a distant homolog of FleQ, which begins to commandeer control of the *fleQ* regulon at the cost of disrupting nitrogen uptake and assimilation. Step 2 is a switch-of-function mutation that redirects NtrC away from nitrogen uptake and toward its novel function as a flagellar regulator. Our results demonstrate that natural selection can rapidly rewire regulatory networks in very few, repeatable mutational steps.

A long-standing evolutionary question concerns how the duplication and recruitment of genes to regulatory networks facilitate their expansion (*1*) and how networks gain mutational robustness and evolvability (*2*). Bacteria respond to diverse environments using a vast range of specialized regulatory pathways, predominantly two-component systems (*3*), which are the result of adaptive radiations within gene families. Due to past cycles of gene duplication, divergence, and horizontal genetic transfer, there is often extensive homology between the components of different pathways (*4*), raising the possibility of cross-talk or redundancy between pathways (*5*). Here we monitor the recovery of microbial populations from a catastrophic gene deletion: Bacteria engineered to lack a particular function are exposed to environments that impose strong selection to re-evolve it, sometimes by recruitment of genes to regulatory networks (*6*–*9*).

In the plant-associated soil bacterium *Pseudomonas fluorescens*, the master regulator of flagellar synthesis is FleQ (also called AdnA), a σ^{54}-dependent enhancer binding protein (EBP) that activates transcription of genes required for flagellum biosynthesis (*10*, *11*). The starting *P. fluorescens* strain is AR2; this strain lacks flagella due to deletion of *fleQ* and is unable to move by spreading motility due to mutation of viscosin synthase (*viscB*), resulting in a distinctive, pointlike colony morphology on spreading motility medium (SMM) (*12*) (Fig. 1A). We grew replicate populations of AR2 on SMM (see supplementary materials and methods); when local nutrients became depleted, starvation imposed strong selection to re-evolve motility. To demonstrate that this finding was not strain-specific, we replicated these experiments in a different strain of *P. fluorescens*, Pf0-2x. This strain is a Δ*fleQ* variant of Pf0-1, already viscosin-deficient, and thus unable to move by spreading or swimming motility (*10*).

After 96 hours of incubation of AR2 and Pf0-2x at room temperature on SMM, two breakout mutations were visible, conferring first slow (AR2S and Pf0-2xS) and then fast (AR2F and Pf0-2xF) spreading over the agar surface (Fig. 1A). The AR2F strain produces flagella, but we could not detect flagella in electron microscopy samples for AR2S (Fig. 1B). Genome resequencing revealed a single-nucleotide point mutation in *ntrB* in strain AR2S, causing an amino acid substitution within the PAS domain of the histidine kinase sensor NtrB [Thr^{97}→Pro^{97} (T97P)] (*13*). The fast-spreading strain AR2F had acquired an additional point mutation in the σ^{54}-dependent EBP gene *ntrC*, which alters an amino acid (R442C) within the DNA binding domain (Table 1 and table S2).

NtrB and NtrC make up a two-component system: Under nitrogen limitation, NtrB phosphorylates NtrC, which activates transcription of genes required for nitrogen uptake and metabolism. To determine how mutations in this separate regulatory pathway restored motility in the absence of FleQ, we performed microarray and quantitative reverse transcription polymerase chain reaction analyses of the ancestral and evolved strains (fig. S1 and table S1). The expression of genes required for flagellum biosynthesis and chemotaxis was abolished in AR2 compared with wild-type (WT) SBW25 (Fig. 2A). The *ntrB* mutation in AR2S partially restores the expression of

[1]School of Biological Sciences, University of Reading, Whiteknights, Reading RG6 6AJ, UK. [2]Department of Biology, University of Massachusetts Dartmouth, 285 Old Westport Road, North Dartmouth, MA 02747, USA. [3]Department of Plant Production and Protection, Qassim University, Qassim, P.O. Box 6622, Saudi Arabia. [4]College of Life and Environmental Sciences, University of Exeter, Stocker Road, Exeter EX4 4QD, UK. [5]Department of Biology, University of York, Wentworth Way, York YO10 5DD, UK. [6]The University of Akureyri, Borgir vid Nordurslod, IS-600 Akureyri, Iceland. *These authors contributed equally to this work. **†Corresponding author. E-mail: l.j.johnson@reading.ac.uk**

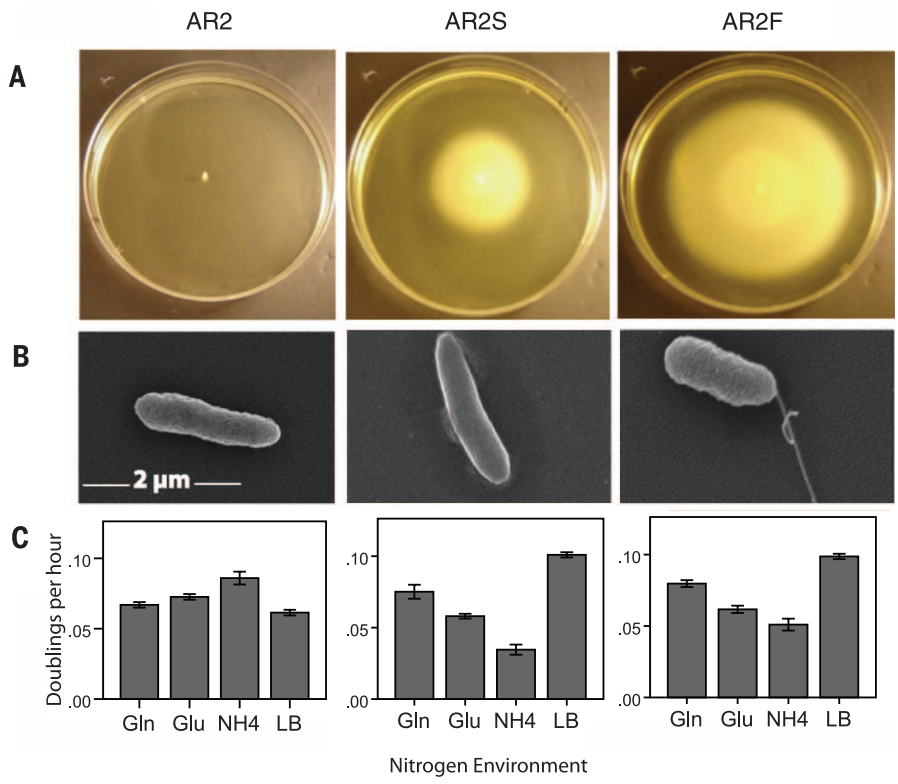

Fig. 1. Phenotypic assays of motility variants. (**A**) Surface-spreading motility assays of ancestral (AR2) and evolved slow-spreading (AR2S) and fast-spreading (AR2F) mutants, after 27 hours. (**B**) Electron microscopy confirms the presence of a flagellum in AR2F but fails to confirm presence in AR2S. (**C**) Mean (n = 4) cell doublings per hour (±1 SEM, error bars). Strains were grown in differing nitrogen environments: in 10 mM glutamine (Gln), glutamate (Glu), and ammonium (NH4) as the sole nitrogen source or in high-nutrient lysogeny broth (LB) (AR2: $F_{3,12}$ = 13.460, P < 0.001; AR2S: $F_{3,12}$ = 72.674, P < 0.001; AR2F: $F_{3,12}$ = 52.538, P < 0.001). There were also differences between the doubling rate of strains within each nitrogen medium [Glu: $F_{2,9}$ = 12.654, P = 0.002; NH4: $F_{2,9}$ = 40.529, P < 0.001], with the exception of Gln ($F_{2,9}$ = 3.703, P = 0.067).

Table 1. Mutational trajectory toward slow- and fast-spreading phenotypes. Mutations confirmed in slow-spreading motility variants are predicted to result in hyperphosphorylation of NtrC; mutations in fast-spreading variants lead to predicted switched specificity of NtrC-P toward FleQ targets. Slow- and fast-spreading variants share the same ancestry.

Strain	Slow spreaders (AR2/Pf0-2xS): hyperphosphorylation of NtrC	Fast spreaders (AR2/Pf0-2xF): switch of NtrC-P specificity
AR2	*ntrB* T97P*	*ntrC* R442C*
	ntrB V185K	*ntrC* K342E
	ntrB D179N	*ntrC* G452R
	ntrB L184Q / V185I	*ntrC* K342V / Frameshift: V342
Pf0-2x	*ntrB* D228A†	*ntrC* N454S
		ntrC R441S
		ntrC N454S
		ntrC P424L
		ntrC N454S
	ntrB D228A†	*ntrC* L418R
		ntrC G414D
		ntrC N454S
		ntrC F426V
	glnK Frameshift: I86*	*ntrC* R442H*
	glnA T237P*	*ntrC* A445V*
	glnA Frameshift: T205*	*ntrC* R442C*

*Identified by genome resequencing. †Independent *ntrB* mutant strains, parent to multiple *ntrC* mutant strains.

flagellar genes and overactivates the expression of genes involved in nitrogen regulation, uptake, and metabolism. The subsequent *ntrC* mutation in AR2F reduces the expression of nitrogen uptake and metabolism genes while further up-regulating flagellar and chemotaxis gene expression to WT levels (Fig. 2B). Although AR2S and AR2F showed higher growth rates than the ancestor in lysogeny broth (LB) medium (the medium on which the mutants arose; Tukey-Kramer post hoc test, growth in LB compared to AR2: AR2S, P < 0.001; AR2F, P < 0.001) (Fig. 1C), both mutants grew poorly in minimal medium with ammonium as the sole nitrogen source (Tukey-Kramer post hoc test, growth in M9 + ammonium compared to AR2: AR2S, P < 0.001; AR2F, P = 0.001). This is likely to be the result of ammonium toxicity due to the strong up-regulation of genes involved in ammonium uptake and assimilation, indicating a pleiotropic cost of this adaptation.

Sequencing of the *ntrBC* locus from independently evolved replicate strains showed that evolution often followed parallel trajectories in both AR2 and Pf0-2x: Mutation of *ntrB* gave a slow-spreading strain, and this was followed by mutation of *ntrC* yielding a fast-spreading strain (Table 1 and Fig. 3, A and C). Although all Pf0-2xF replicates carried mutations in *ntrC*, several Pf0-2xS strains were not mutated in *ntrB*, suggesting an alternative evolutionary pathway. Genome resequencing of these strains revealed mutations in *glnA* or *glnK* (Table 1 and Fig. 3B) that are likely to result in loss of function, leading to abnormally high levels of phosphorylated NtrC: Reduced ammonium assimilation by glutamine synthetase (*glnA*) would impose severe nitrogen limitation in the cell irrespective of nitrogen availability, whereas GlnK is a PII-protein that regulates both NtrB and glutamine synthetase activities.

These data suggest a predictable two-step evolutionary process: Step 1 increases levels of phosphorylated NtrC, via either (i) a direct regulatory route with mutations in NtrB or GlnK or (ii) a physiological route with loss-of-function mutations reducing glutamine synthetase activity and causing NtrB activation, partially or intermittently reactivating the flagellar cascade. In step 2, NtrC adapts to enhance activation of the flagellar genes and, in doing so, becomes a less potent activator of nitrogen uptake genes. This model explains the microarray data and is consistent with the predicted structural effects of the mutations (Figs. 2 and 3). Specifically, for NtrB the structural changes are likely to either increase kinase or reduce phosphatase activity. In support of this, the mutated NtrB(D228A) repeatedly emerging in Pf0-2xS resembles NtrB(D227A) in *P. aeruginosa*, which constitutively activates the Ntr system (*14*).

NtrC is a distant homolog of FleQ, sharing 30% amino acid identity and the same three structural domains (template modeling score > 0.7; P < 0.001) (Fig. 3D) (*15*): an N-terminal receiver domain, a conserved central σ^{54}-interacting domain, and a C-terminal DNA binding domain containing a helix-turn-helix (HTH) motif flanked by highly disordered regions. We posit that an overabundance

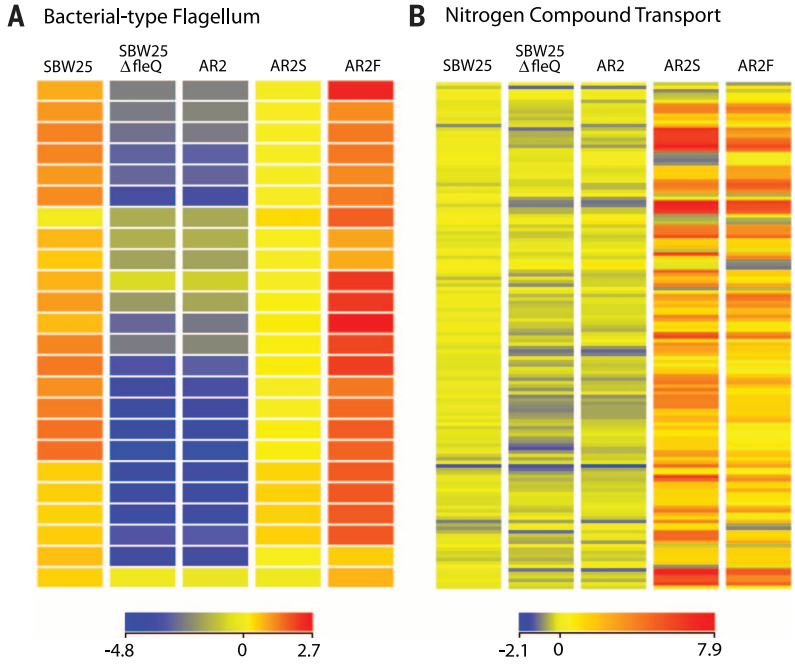

Fig. 2. Heat map of microarray expression profiles for all evolved and ancestral motility variants. Heat maps show where there is significant ($P \leq 0.05$) fold change of ≥2 in genes selected based on gene ontology terms for (**A**) bacterial-type flagellum (24 genes) and (**B**) nitrogen compound transport (146 genes) for all strains. The gradation of colors reflects normalized raw signal values across the entire array. Genes are ordered according to chromosomal position to enable clearer visualization of co-regulated gene clusters. Full transcriptome analysis is reported in the supplementary materials.

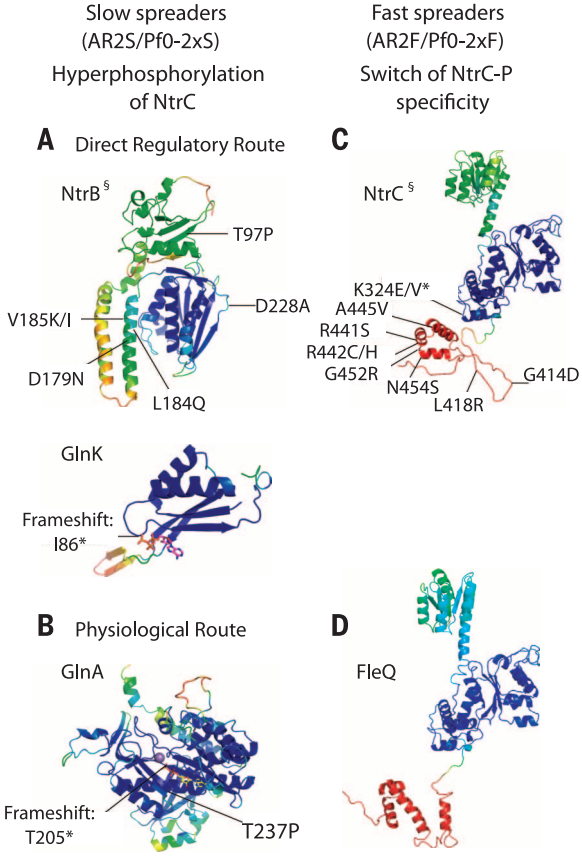

Fig. 3. Full-chain multi-template 3D models of protein structures of slow- and fast-spreading motility variants. Slow-spreading variants can follow either the direct regulatory route through mutation of NtrB or GlnK (**A**) or the physiological route through mutation of GlnA, causing overactivation of NtrB (**B**). Both routes are predicted to lead to hyperphosphorylation of NtrC. Fast-spreading variants all show mutational changes to NtrC (**C**), which has a similar global structure to FleQ (**D**). The color scheme represents the variation in models, which correlates with local (per-residue) quality and disorder. Regions colored in blue and green represent low local variability in structure, whereas those in red show high local variability (see Table 1 and table S2 for mutation details). § denotes all mutations mapped onto SBW25 WT protein structures for illustrative purposes; * indicates a truncated domain.

of phosphorylated NtrC activates transcription of flagellar genes through functional promiscuity (*16*). Consistent with this, the *ntrC* mutations in fast-spreading strains are predominantly located within or adjacent to the HTH domain and probably influence enhancer-binding specificity; one is a frameshift abolishing the HTH altogether (Fig. 3C). The evolved NtrC′ must be constitutively phosphorylated by overactive NtrB to enable its new multipurpose role, with the result that flagellum biosynthesis and nitrogen regulation are probably no longer responsive to environmental stimuli. Consequently, there is a trade-off between nitrogen use and motility (Fig. 1, A and C).

The flagellar regulatory network may have an unusually dynamic evolutionary history. Flagella are expensive to make and not always advantageous. Pathogens expressing flagella can trigger strong immune responses in the host, so rapid transitions are seen over short time scales between uniflagellate, multiflagellate, and aflagellate states (*17*). This volatility is reflected in the structure of regulatory networks: In close relatives of *Pseudomonas*, *fleQ* appears not to be involved in flagellar gene expression (*18*), and in *Helicobacter pylori*, a gene of unknown function can be used as a "spare part" to permit motility in *flhB* mutants (*19*). Our results illustrate that trans-acting mutations can contribute to gene network evolution (*20*), but that as predicted, such mutations bear severe pleiotropic costs (*21*, *22*). Genes can retain the potential to take on the functions of long-diverged homologs, suggesting that some degree of evolutionary resilience is a consequence of regulatory pathways that evolve via gene duplication. Although de novo origination of new functions in nature is likely to take longer and involve more mutational steps, this system enables us to understand the adaptive process in detail at the genetic and phenotypic level. We identified a tractable model for gene network evolution and observed, in real time, the rewiring of gene networks to enable the incorporation of a modified component (NtrC′) creating a novel regulatory function by a highly repeatable two-step evolutionary pathway with the same point mutations often recurring in independent lineages.

REFERENCES AND NOTES

1. J. R. True, S. B. Carroll, *Annu. Rev. Cell Dev. Biol.* **18**, 53–80 (2002).
2. M. Aldana, E. Balleza, S. Kauffman, O. Resendiz, *J. Theor. Biol.* **245**, 433–448 (2007).
3. J. A. Hoch, *Curr. Opin. Microbiol.* **3**, 165–170 (2000).
4. S. A. Teichmann, M. M. Babu, *Nat. Genet.* **36**, 492–496 (2004).
5. E. J. Capra, M. T. Laub, *Annu. Rev. Microbiol.* **66**, 325–347 (2012).
6. Z. D. Blount, C. Z. Borland, R. E. Lenski, *Proc. Natl. Acad. Sci. U.S.A.* **105**, 7899–7906 (2008).
7. J. R. Meyer *et al.*, *Science* **335**, 428–432 (2012).
8. B. G. Hall, *Genetica* **118**, 143–156 (2003).
9. D. Blank, L. Wolf, M. Ackermann, O. K. Silander, *Proc. Natl. Acad. Sci. U.S.A.* **111**, 3044–3049 (2014).
10. E. A. Robleto, I. López-Hernández, M. W. Silby, S. B. Levy, *J. Bacteriol.* **185**, 453–460 (2003).
11. N. Dasgupta *et al.*, *Mol. Microbiol.* **50**, 809–824 (2003).

12. A. S. Alsohim *et al*., *Environ. Microbiol.* **16**, 2267–2281 (2014).
13. Single-letter abbreviations for the amino acid residues are as follows: A, Ala; C, Cys; D, Asp; E, Glu; F, Phe; G, Gly; H, His; I, Ile; K, Lys; L, Leu; M, Met; N, Asn; P, Pro; Q, Gln; R, Arg; S, Ser; T, Thr; V, Val; W, Trp; and Y, Tyr.
14. W. Li, C.-D. Lu, *J. Bacteriol.* **189**, 5413–5420 (2007).
15. D. J. Studholme, R. Dixon, *J. Bacteriol.* **185**, 1757–1767 (2003).
16. R. Wassem, E. M. De Souza, M. G. Yates, F. D. Pedrosa, M. Buck, *Mol. Microbiol.* **35**, 756–764 (2000).
17. E. Amiel, R. R. Lovewell, G. A. O'Toole, D. A. Hogan, B. Berwin, *Infect. Immun.* **78**, 2937–2945 (2010).
18. R. León, G. Espín, *Microbiology* **154**, 1719–1728 (2008).
19. M. E. Wand *et al*., *J. Bacteriol.* **188**, 7531–7541 (2006).
20. H. E. Hoekstra, J. A. Coyne, *Evolution* **61**, 995–1016 (2007).
21. G. A. Wray, *Nat. Rev. Genet.* **8**, 206–216 (2007).
22. S. B. Carroll, *Cell* **134**, 25–36 (2008).

ACKNOWLEDGMENTS

T.B.T., L.J.J., R.W.J., and M.A.B. conceived and designed the study; T.B.T., G.M., and A.S.A. performed experiments; M.W.S. and A.H.D. performed independent lines of inquiry on Pf0-2x; D.J.S. conducted bioinformatics analysis of genome resequencing data, identified mutated genes, and handled sequencing data; L.J.M. conducted the protein structure prediction and analysis; and T.B.T., G.M., L.J.J., R.W.J., M.W.S., D.J.S., and M.A.B. wrote the paper. This work was supported by a Leverhulme grant to L.J.J., M.A.B., and R.W.J.; UK Biotechnology and Biological Sciences Research Council (BBSRC) grant BB/J015350/1 to R.W.J.; start-up funding from the University of York to M.A.B. and from Qassim University to A.S.A.; and Agriculture and Food Research Initiative Competitive grant 2010-65110-20392 from the U.S. Department of Agriculture's National Institute of Food and Agriculture Microbial Functional Genomics Program to M.W.S. We thank G. Bell, M. Pagel, A. Buckling, and J. Moir for useful discussions; P. Ashton for processing microarray data; and K. Paszkiewicz and the Exeter Sequencing Service facility for genome sequencing services. This work was also supported by the Wellcome Trust Institutional Strategic Support Fund (WT097835MF), Wellcome Trust Multi User Equipment award (WT101650MA), and BBSRC LOLA award (BB/K003240/1). Sequence data for genomic resequencing of AR2S and AR2F have been submitted to the Sequence Read Archive under accession numbers SRR1510202 and SRR1510203, respectively. The eArray design ID for the microarray is 045642. Microarray data have been submitted to the ArrayExpress database under accession number E-MTAB-2788 (www.ebi.ac.uk/arrayexpress).

SUPPLEMENTARY MATERIALS

www.sciencemag.org/content/347/6225/1014/suppl/DC1
Materials and Methods
Fig. S1
Tables S1 and S2
References (*23*–*30*)
Microarray Data

24 July 2014; accepted 28 January 2015
10.1126/science.1259145

TRANSCRIPTION

CTCF establishes discrete functional chromatin domains at the *Hox* clusters during differentiation

Varun Narendra,[1,2] Pedro P. Rocha,[3] Disi An,[4] Ramya Raviram,[3] Jane A. Skok,[3] Esteban O. Mazzoni,[4]* Danny Reinberg[1,2]*

Polycomb and Trithorax group proteins encode the epigenetic memory of cellular positional identity by establishing inheritable domains of repressive and active chromatin within the *Hox* clusters. Here we demonstrate that the CCCTC-binding factor (CTCF) functions to insulate these adjacent yet antagonistic chromatin domains during embryonic stem cell differentiation into cervical motor neurons. Deletion of CTCF binding sites within the *Hox* clusters results in the expansion of active chromatin into the repressive domain. CTCF functions as an insulator by organizing *Hox* clusters into spatially disjoint domains. Ablation of CTCF binding disrupts topological boundaries such that caudal *Hox* genes leave the repressed domain and become subject to transcriptional activation. Hence, CTCF is required to insulate facultative heterochromatin from impinging euchromatin to produce discrete positional identities.

Precise expression of *Hox* genes is required for cells to maintain their relative position within a developing embryo (*1*–*4*). For example, motor neurons (MNs) rely on *Hox* gene expression for the formation of position-dependent neural circuits that control voluntary movement (*5*–*7*). High concentration of retinoic acid (RA) signaling induces rostral *Hox* gene expression (*Hox1* to *Hox5*) and, thus, cervical identity to differentiating MNs (*8*). The in vivo development of MNs with a cervical positional identity can be faithfully recapitulated in vitro by exposing differentiating embryonic stem cells (ESCs) to RA and a sonic hedgehog signaling agonist [smoothened agonist (SAG)] (fig. S1A) (see supplementary materials and methods) (*9*). ESC-derived MNs exposed to RA activate the rostral portion of the *HoxA* cluster (*Hoxa1-6*), whereas *Hoxa7-13* remain repressed (Fig. 1A and table S1) (*10*, *11*). The transcriptional partitioning of the *HoxA* cluster is mirrored at the level of chromatin. As previously described, H3K27me3—the catalytic product of Polycomb repressive complex 2 activity—decorates the entire *HoxA* cluster in ESCs (*11*) (Fig. 1B, top). Upon differentiation into MNs, H3K4me3 and RNA polymerase II (RNAPII) access the rostral segment of the cluster, whereas H3K27me3 becomes restricted to the caudal segment (*11*) (Fig. 1B). Within the *HoxA* cluster, MNs display two clear discontinuities in H3K4me3 and H3K27me3 density: at the intergenic region between *Hoxa5* and *Hoxa6* (C5|6) and between *Hoxa6* and *Hoxa7* (C6|7) (Fig. 1C). The DNA sequence underlying each of these discontinuities contains a highly conserved binding site for the CCCTC-binding factor (CTCF) (*12*) (Fig. 1C and fig. S1, B and C) that is constitutively occupied in both ESCs and differentiated MNs (Fig. 1B). CTCF-demarcated chromatin boundaries were observed at the *HoxC* and *HoxD* clusters as well (Fig. 1C and fig. S2) and have recently been identified in the orthologous bithorax complex in *Drosophila melanogaster* (*13*).

It has been suggested that CTCF functions as a chromatin barrier insulator by restricting the spread of heterochromatin, though this remains in dispute (*14*–*16*). Therefore, we tested whether CTCF can perform *Hox* gene barrier insulation during differentiation to produce functional MN circuits. We employed the clustered regularly interspaced short palindromic repeat (CRISPR) genome-editing tool (*17*, *18*) in ESCs to disrupt CTCF binding sites that localize to chromatin boundaries within *Hox* clusters. We first generated a 9–base pair (bp) homozygous deletion within the core CTCF motif between *Hoxa5* and *Hoxa6* (Δ5|6) (Fig. 1D) and did not detect any mutations at potential off-target cleavage sites (table S2). The 9-bp deletion results in a total abrogation of CTCF occupancy (Fig. 1E). The neighboring CTCF binding site (C6|7) also shows a dramatic reduction in binding, suggesting an interdependence (Fig. 1E) (*19*, *20*). Δ5|6 ESCs exhibit no defect in their ability to differentiate into MNs (fig. S3). To examine the transcriptional consequence of deleting CTCF binding sites within the *HoxA* cluster in response to patterning signals during cell differentiation, we performed RNA sequencing (RNA-seq) on wild-type (WT) and Δ5|6 cells at two stages: ESCs and differentiated MNs. In ESCs, all *HoxA* genes are repressed in both lines (Fig. 2A, left, and table S1). Upon differentiation, *Hoxa1-6* are activated in the WT setting, whereas *Hoxa7-13* remain repressed, mirroring the distribution of active and repressive chromatin across the cluster. *Hoxa1-6* are equivalently activated in WT and Δ5|6 MNs. However, *Hoxa7*—the gene located immediately caudal to the affected C6|7 site—is up-regulated more than 25-fold relative to the WT control. *Hoxa9* shows very modest expression in Δ5|6 MNs, whereas *Hoxa10-13* remain fully repressed (Fig. 2A, right, and table S1). Furthermore, though

[1]Howard Hughes Medical Institute, Chevy Chase, MD 20815, USA. [2]Department of Biochemistry and Molecular Pharmacology, New York University School of Medicine, New York, NY 10016, USA. [3]Department of Pathology, New York University School of Medicine, New York, NY 10016, USA. [4]Department of Biology, New York University, New York, NY 10003, USA.
***Corresponding author. E-mail: danny.reinberg@nyumc.org (D.R.); eom204@nyu.edu (E.O.M.)**

Hoxa6—the gene located between the deleted C5|6 and C6|7 site—is equivalently expressed in terminally differentiated WT and Δ5|6 MNs, it is transcriptionally activated earlier in differentiating Δ5|6 cells than in WT cells, unlike the rostral *Hoxa5* control (fig. S4). Thus, CTCF occupancy regulates the spatial and temporal activation of the *HoxA* cluster. Demonstrating that CTCF boundary activity is not restricted to a single *Hox* cluster, deletion of a 13-bp sequence within a binding site at the *HoxC* chromatin boundary results in the equivalent transcriptional activation of genes located caudal to the site of mutation (fig. S5).

Hoxa7-specific transcriptional activation in Δ5|6 MNs suggests that the intact C7|9 peak serves as a new boundary. To study if there is a relocation of the chromatin boundary during MN differentiation in the mutant line, we investigated the chromatin state of ESCs and differentiated MNs. Site-specific ablation of CTCF does not affect the chromatin state of undifferentiated cells, as WT and Δ5|6 ESCs possess H3K27me3 distributed across the entire *HoxA* cluster (Fig. 2B, top). However, after differentiation, Δ5|6 MNs exhibit a 50% reduction in H3K27me3 levels, specifically within the region delimited by C5|6 and C7|9 (Fig. 2B and fig. S6, A and C). In agreement with C7|9 serving as the new boundary element in Δ5|6 MNs, H3K27me3 density recovers to WT levels immediately caudal to the C7|9 peak. Moreover, deletion of C5|6 results in a complementary expansion of H3K4me3 and RNAPII up to the C7|9 boundary (Fig. 2B and fig. S6, B and D). The Δ5|6 mutation does not produce pleiotropic effects, as chromatin boundaries are not disrupted in trans within the *HoxC and HoxD* clusters (fig. S6, C to E). Likewise, ablation of the C5|6 CTCF binding event within the *HoxC* cluster ($\Delta 5|6_{HoxC}$) results in an equivalent chromatin boundary relocation (fig. S5). Thus, CTCF does not function within the *Hox* clusters according to the traditional definition of a chromatin insulator—to restrict the spread of repressive chromatin into adjacent euchromatin—but rather serves to restrict in cis the exposure of Polycomb repressed genes to Trithorax activity.

CTCF-dependent insulation occurs via its ability to mediate looping interactions between nonadjacent segments of DNA (*21*). Accordingly, CTCF is enriched at boundaries between topologically associated domains (TADs) (*15*, *22*, *23*). To test how CTCF-mediated looping may regulate the dynamic spatial reorganization of the *HoxA* cluster during differentiation, we performed

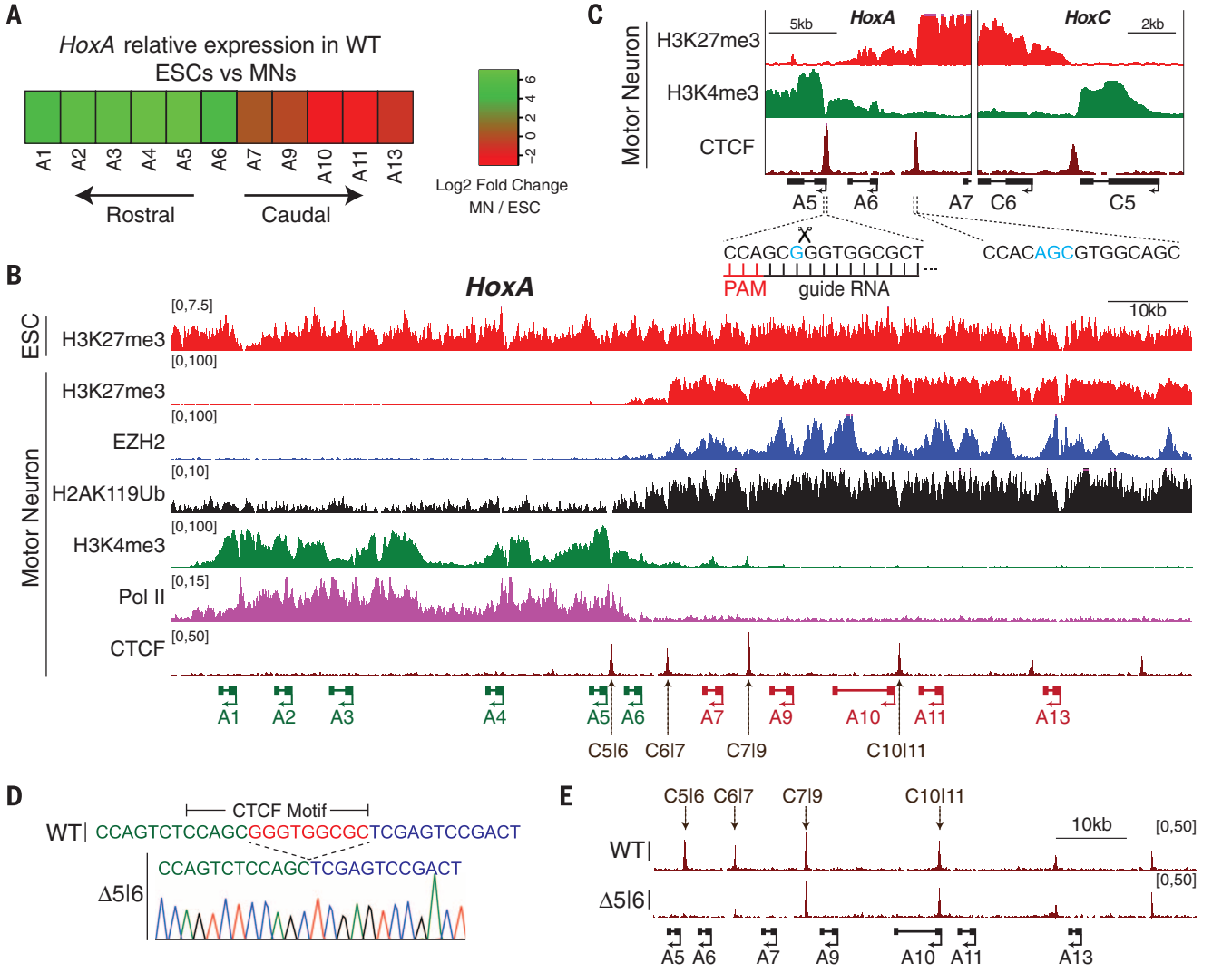

Fig. 1. CTCF localizes to a *HoxA* chromatin boundary in motor neurons. (**A**) Heat map of *HoxA* relative expression (log2) between WT ESCs and MNs. (**B**) Normalized chromatin immunoprecipitation followed by deep sequencing (ChIP-seq) read densities for the indicated proteins and histone modifications in ESCs and MNs from two merged biological replicates. Genes that are activated during differentiation are annotated in green; repressed genes are shown in red. (**C**) Zoomed-in view of H3K4me3 and H3K27me3 boundaries, along with CTCF peaks and their underlying binding motifs. Blue highlights nucleotides that diverge from the consensus motif. The guide RNA used to target C5|6 is shown. (**D**) Sequencing chromatogram of the Δ5|6 line depicts a 9-bp deletion overlapping the CTCF core motif. (**E**) Normalized ChIP-seq read densities for CTCF in WT and Δ5|6 MNs from two merged biological replicates. The deleted CTCF binding site (C5|6) is boxed, as well as the neighboring site (C6|7).

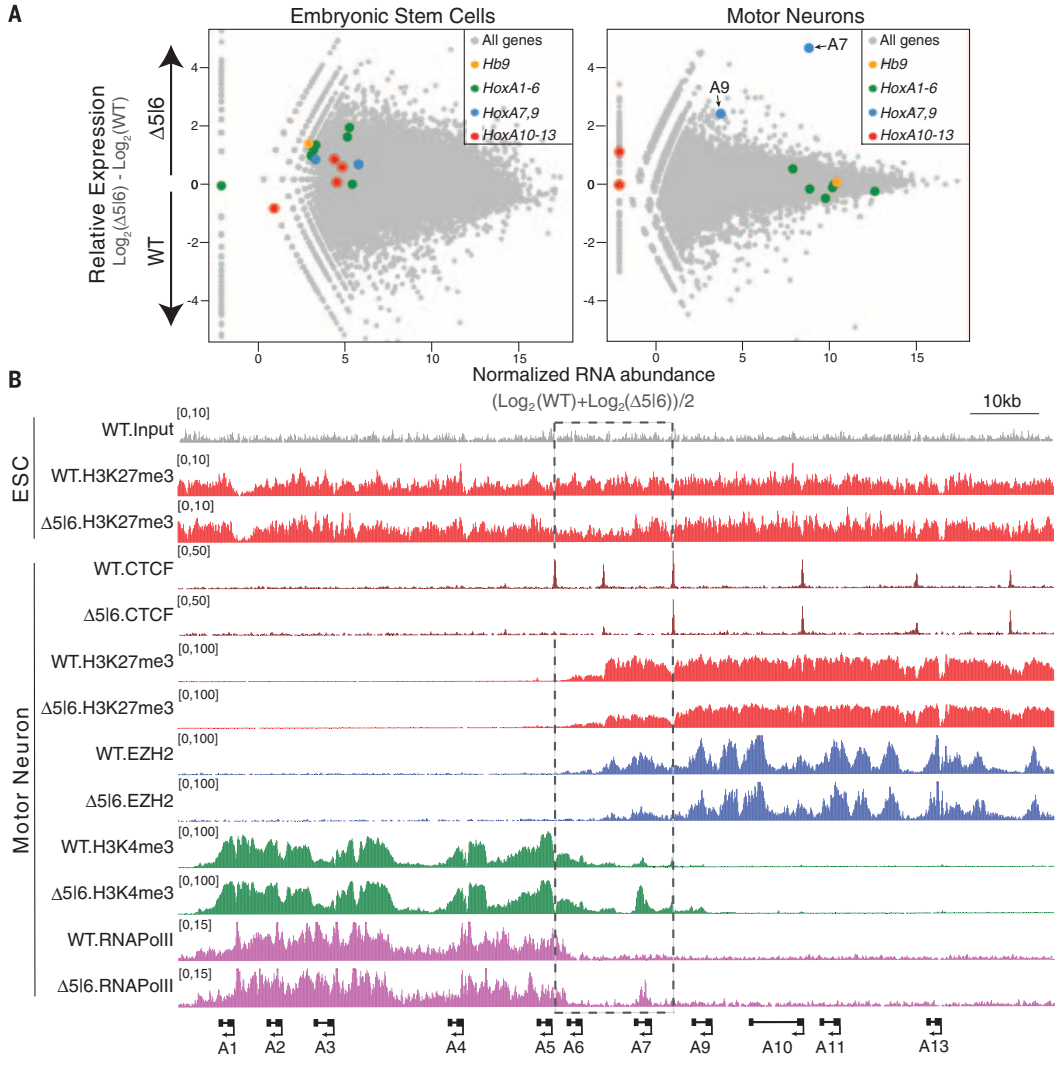

Fig. 2. The chromatin boundary is disrupted upon deletion of the C5|6 CTCF motif. (**A**) RNA-seq MA plot of WT versus Δ5|6 ESCs (left) and MNs (4 days after RA/SAG, right). MN data are representative of two biological replicate experiments; ESC data represent one experiment. Mean abundance is plotted on the *x* axis and enrichment is plotted on the *y* axis. Hb9 is a marker of motor neurons. (**B**) Normalized ChIP-seq read densities for the indicated protein and histone modifications along the *HoxA* cluster in ESCs and MNs (4 days after RA/SAG) from two biological replicates.

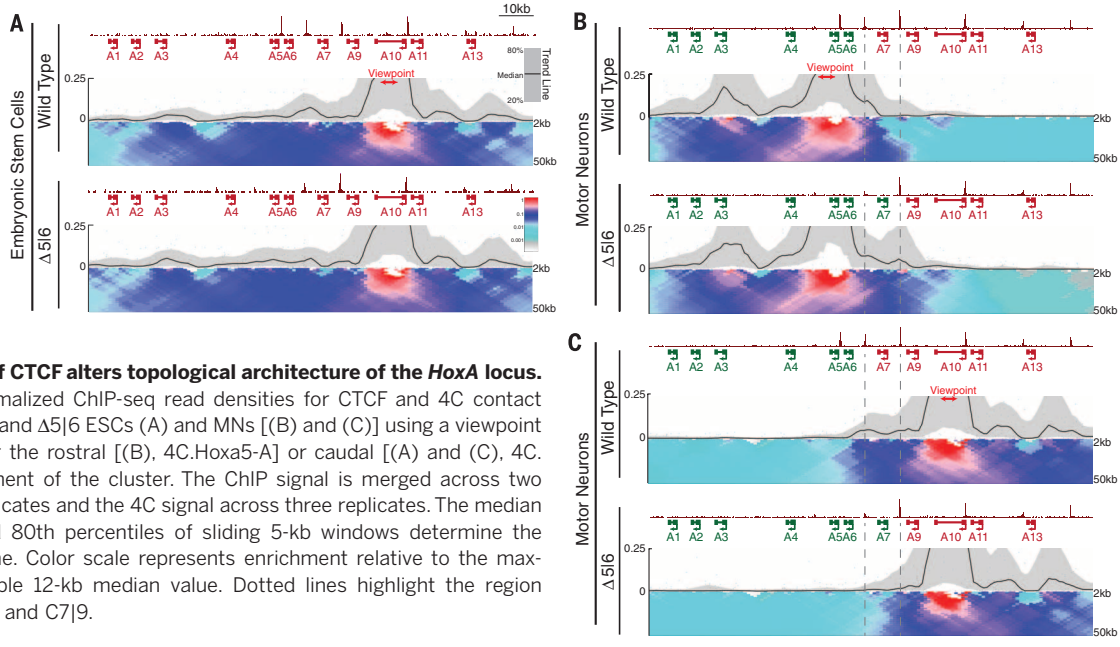

Fig. 3. Loss of CTCF alters topological architecture of the *HoxA* locus. (**A** to **C**) Normalized ChIP-seq read densities for CTCF and 4C contact profiles in WT and Δ5|6 ESCs (A) and MNs [(B) and (C)] using a viewpoint (red) in either the rostral [(B), 4C.Hoxa5-A] or caudal [(A) and (C), 4C.Hoxa10] segment of the cluster. The ChIP signal is merged across two biological replicates and the 4C signal across three replicates. The median and 20th and 80th percentiles of sliding 5-kb windows determine the main trend line. Color scale represents enrichment relative to the maximum attainable 12-kb median value. Dotted lines highlight the region between C6|7 and C7|9.

4C-seq in WT and Δ5|6 cells using viewpoints located within either the transcriptionally active (4C.Hoxa5-A) or repressive (4C.Hoxa10) domains of the *HoxA* cluster (Fig. 3). In WT and Δ5|6 ESCs, the strong interaction signal of both 4C-seq viewpoints extends to the perimeter of the *HoxA* cluster, suggesting an organization of the locus as a single architectural domain that the C5|6 binding site does not alter (Fig. 3A and fig. S7, A and B). As expected, in WT cells this domain partitions during differentiation into two at roughly the C6|7 position, mirroring the distribution of H3K4me3 in the rostral domain and H3K27me3 in the caudal domain (*24*, *25*). This is demonstrated by the strong interactions with the 4C.Hoxa5-A viewpoint that occur almost exclusively within the rostral domain (Fig. 3B) and interactions with the 4C.Hoxa10 viewpoint that are restricted to the caudal domain (Fig. 3C). Unlike the case in ESCs, deletion of the C5|6 CTCF binding site affects the spatial organization of the *HoxA* cluster in MNs. The Δ5|6 mutation repositions the topological boundary in MNs to the intact C7|9 site, matching the de novo chromatin boundary and thereby evicting *Hoxa7* from the caudal repressed domain and into the rostral active domain (Fig. 3, B and C, and fig. S8, A and B). Thus, the elimination of a CTCF binding site causes a structural reorganization of the *HoxA* cluster

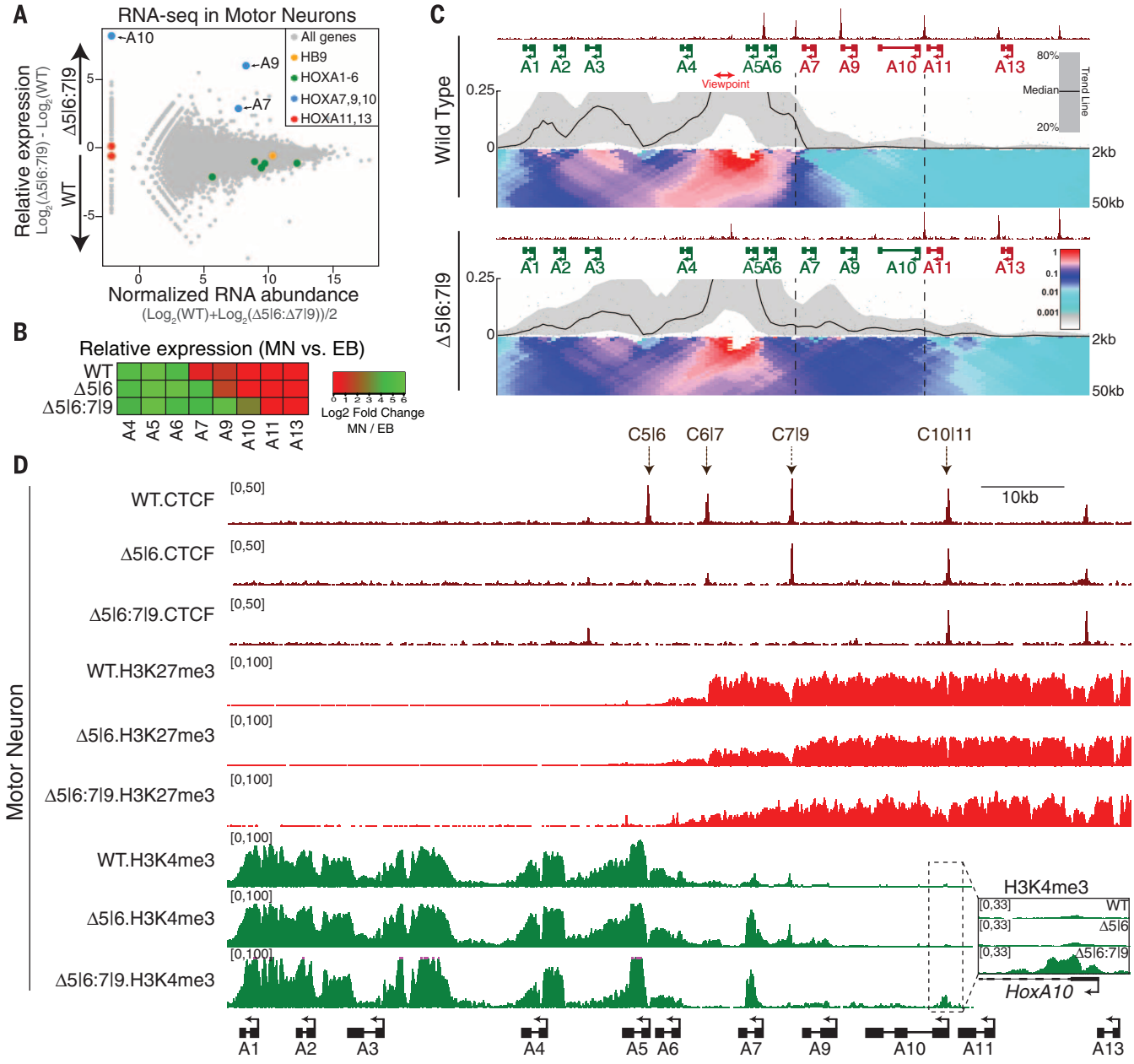

Fig. 4. Compound C5|6:7|9 deletion causes a further caudal spread of active transcription within the *HoxA* locus. (**A**) RNA-seq MA plot of WT versus Δ5|6:7|9 MNs. Mean abundance is plotted on the *x* axis, and enrichment is plotted on the *y* axis. (**B**) Heat map of *HoxA* relative expression in MNs (day 4) versus EBs (embryoid bodies) (day 0) across two biological replicates (single replicate in the Δ5|6:7|9 line). (**C**) Normalized ChIP-seq read densities for CTCF and 4C contact profiles in WT and Δ5|6:7|9 MNs using the 4C.Hoxa5-B viewpoint (red) from two biological replicates. The median and 20th and 80th percentiles of sliding 5-kb windows determine the main trend line. The color scale represents enrichment relative to the maximum attainable 12-kb median value. Dotted lines highlight the region between C6|7 and C10|11. (**D**) Normalized ChIP-seq read densities for the indicated proteins and histone modifications along the *HoxA* cluster in MNs (4 days after RA/SAG). A magnified view of the boxed region is presented on the right.

that results in an aberrant chromatin boundary and altered gene expression.

These data argue that in response to RA signaling, the most rostral CTCF binding event forges a topological boundary within the *HoxA* cluster that can insulate active from repressive chromatin and thus maintain proper gene expression. This model predicts that eliminating the C7|9 CTCF binding site in Δ5|6 MNs would cause aberrant activation of *Hoxa7-10* and caudal regression of the topological boundary to the C10|11 position. Using the CRISPR genome-editing tool in Δ5|6 ESCs, we mutated the C7|9 CTCF binding site. Δ5|6:7|9 ESCs harbor a 21-bp deletion spanning the C7|9 motif on one allele. The other allele contains a 20-bp insertion that disrupts the motif (fig. S9). *Hoxa7-10* are highly up-regulated in the double-mutant MNs relative to the WT control (Fig. 4, A and B, fig. S4, and table S1). *Hoxa9-10* are the most up-regulated genes in the polyA-selected transcriptome, whereas *Hoxa11-13* remain transcriptionally silent. This phenotype is specific to CTCF ablation, as deletion of a YY1 binding motif adjacent to the C7|9 site does not result in the transcriptional activation of caudal genes (fig. S10) (*26*). The transcriptional profile of Δ5|6:7|9 MNs suggests an underlying caudal boundary shift. Accordingly, 4C-seq using the active 4C.Hoxa5-B viewpoint shows a shift of the topological boundary from C6|7 to the intact C10|11 position in Δ5|6:7|9 MNs (Fig. 4C and fig. S8C), allowing for a parallel expansion of H3K4me3 onto the *Hoxa10* gene (Fig. 4D). Conversely, H3K27me3 density progressively decreases relative to the WT control in a rostral direction from the C10|11 CTCF site.

These results indicate that in response to patterning signals during differentiation, CTCF partitions the *Hox* clusters into insulated architectural domains, upon which Trithorax and Polycomb activities are superimposed in a mutually exclusive fashion to establish discrete *Hox* transcriptional programs. In agreement with our findings, deletion of a CTCF binding site at the boundary of a Polycomb domain containing the *Tcfap2e* locus resulted in its transcriptional activation (*27*). Whether the expansion of H3K4me3 activity that we observe in the *Hox* clusters is the result of aberrant enhancer contacts with caudal genes or an alternative local mechanism of Trithorax expansion remains to be tested. Our 4C-seq results agree with previous studies, which have shown that the caudal and rostral domains of the *HoxA* cluster in differentiated cells are incorporated into separate adjacent TADs, the borders of which align with the chromatin boundary. Our findings thus imply that CTCF is functionally required to delimit TAD boundaries, though a high-resolution all-versus-all (Hi-C) approach will be required to confirm this claim.

REFERENCES AND NOTES

1. R. Bonasio, S. Tu, D. Reinberg, *Science* **330**, 612–616 (2010).
2. P. W. Ingham, *Nature* **306**, 591–593 (1983).
3. E. B. Lewis, *Nature* **276**, 565–570 (1978).
4. R. Margueron, D. Reinberg, *Nature* **469**, 343–349 (2011).
5. J. S. Dasen, B. C. Tice, S. Brenner-Morton, T. M. Jessell, *Cell* **123**, 477–491 (2005).
6. H. Jung *et al*., *Neuron* **67**, 781–796 (2010).
7. Y. Wu, G. Wang, S. A. Scott, M. R. Capecchi, *Development* **135**, 171–182 (2008).
8. J. P. Liu, E. Laufer, T. M. Jessell, *Neuron* **32**, 997–1012 (2001).
9. H. Wichterle, I. Lieberam, J. A. Porter, T. M. Jessell, *Cell* **110**, 385–397 (2002).
10. E. O. Mazzoni *et al*., *Nat. Neurosci.* **16**, 1219–1227 (2013).
11. E. O. Mazzoni *et al*., *Nat. Neurosci.* **16**, 1191–1198 (2013).
12. H. S. Rhee, B. F. Pugh, *Cell* **147**, 1408–1419 (2011).
13. S. K. Bowman *et al*., *eLife* **3**, e02833 (2014).
14. S. Cuddapah *et al*., *Genome Res.* **19**, 24–32 (2009).
15. J. E. Phillips-Cremins, V. G. Corces, *Mol. Cell* **50**, 461–474 (2013).
16. F. Recillas-Targa *et al*., *Proc. Natl. Acad. Sci. U.S.A.* **99**, 6883–6888 (2002).
17. M. Jinek *et al*., *Science* **337**, 816–821 (2012).
18. F. A. Ran *et al*., *Nat. Protoc.* **8**, 2281–2308 (2013).
19. V. Pant *et al*., *Mol. Cell. Biol.* **24**, 3497–3504 (2004).
20. T. M. Yusufzai, H. Tagami, Y. Nakatani, G. Felsenfeld, *Mol. Cell* **13**, 291–298 (2004).
21. E. Splinter *et al*., *Genes Dev.* **20**, 2349–2354 (2006).
22. J. R. Dixon *et al*., *Nature* **485**, 376–380 (2012).
23. E. P. Nora *et al*., *Nature* **485**, 381–385 (2012).
24. D. Noordermeer *et al*., *eLife* **3**, e02557 (2014).
25. D. Noordermeer *et al*., *Science* **334**, 222–225 (2011).
26. P. Vella, I. Barozzi, A. Cuomo, T. Bonaldi, D. Pasini, *Nucleic Acids Res.* **40**, 3403–3418 (2012).
27. J. M. Dowen *et al*., *Cell* **159**, 374–387 (2014).

ACKNOWLEDGMENTS

All sequencing data have been deposited to the Gene Expression Omnibus as series GSE60240 and will be made immediately available upon publication. We thank L. A. Rojas, C. Leek, A. Singhal, S. Tu, R. Bonasio, and L. Vales for thoughtful discussions and revision of the manuscript. We also thank the New York University Genome Technology Center for help with sequencing. This work was supported by grants from the NIH (R37-37120 and GM-64844 to D.R., T32 GM007238 to V.N., R01HD079682 to E.O.M., and GM086852 and GM112192 to J.A.S.). D.A. was supported by the Project A.L.S. foundation. P.P.R. is a National Cancer Center postdoctoral fellow. J.A.S. is a Leukemia and Lymphoma Society scholar. V.N., E.O.M., and D.R. conceived the project, designed the experiments, and wrote the paper; V.N. performed most of the experiments and the bioinformatic analysis; D.A. performed the immunocytochemistry; and P.P.R., R.R., and J.A.S. advised on the 4C-seq procedure and analysis.

SUPPLEMENTARY MATERIALS

www.sciencemag.org/content/347/6225/1017/suppl/DC1
Materials and Methods
Figs. S1 to S10
Tables S1 to S3
References (*28*, *29*)

3 October 2014; accepted 9 January 2015
10.1126/science.1262088

NEW ENGLAND BioLabs® Inc.

The Next Generation of DNA Assembly and Cloning

NEBuilder® HiFi DNA Assembly

The next generation of DNA assembly and cloning has arrived. With NEBuilder HiFi DNA Assembly, you'll enjoy virtually error-free joining of DNA fragments. More efficient assembly is now possible, even with larger fragments, low inputs, or 5´- and 3´-end mismatches. Additionally, use NEBuilder HiFi to bridge two dsDNA fragments with a ssDNA oligo. Save time with less screening or re-sequencing, and benefit from no licensing fee requirements from NEB when choosing NEBuilder products.

Request a free sample* at www.NEBuilderHiFi.com

NEBuilder HiFi DNA Master Mix offers improved fidelity over Gibson Assembly Master Mix

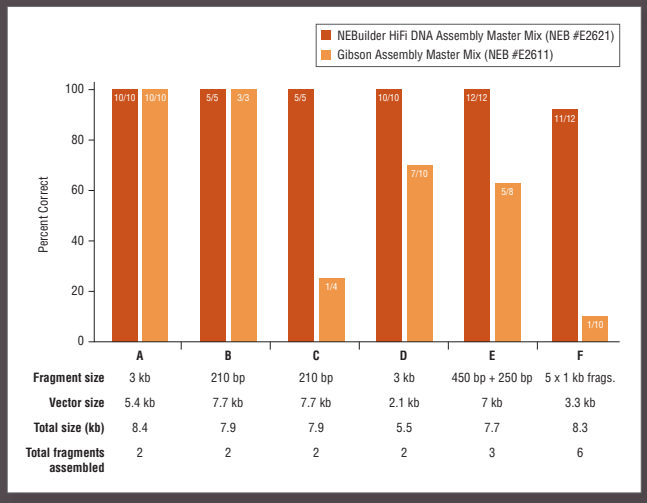

	A	B	C	D	E	F
Fragment size	3 kb	210 bp	210 bp	3 kb	450 bp + 250 bp	5 x 1 kb frags.
Vector size	5.4 kb	7.7 kb	7.7 kb	2.1 kb	7 kb	3.3 kb
Total size (kb)	8.4	7.9	7.9	5.5	7.7	8.3
Total fragments assembled	2	2	2	2	3	6

Fidelity of assembled products was compared between NEBuilder HiFI DNA Assembly Master Mix (NEB #E2621) and Gibson Assembly Master Mix (NEB #E2611). Experiments were performed using the various fragment and vector sizes, following suggested protocols. Experiments B and C vary because sequences of fragments are different. Experiments D and F were performed with fragments containing 3´-end mismatches.

* While supplies last. Offer valid in the US only. Limit one sample per customer.

ZymoPURE™

Pushing the limits

of midi, maxi, and giga plasmid purification

Transfection-ready plasmid DNA in 18 minutes

bind
rapid loading onto a spin-column
via vacuum or centrifuge

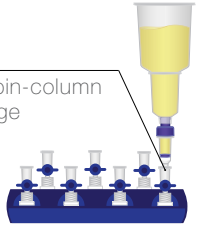

wash
for ultra-pure endotoxin free
plasmid DNA

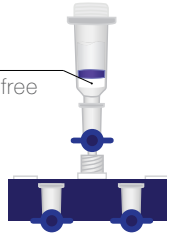

elute
transfection ready
plasmid DNA

	Learn more: www.zymoresearch.com/zymopure		
	Max. Recovery	Processing Time	Size (Cat. No.)
Midiprep	300 µg	18 min.	25 Preps (D4200) 50 Preps (D4201)
Maxiprep	1200 µg	18 min.	10 Preps (D4202) 20 Preps (D4203)
Gigaprep	10 mg	40-50 min.	5 Preps (D4204)

Plasmid DNA concentration and yield from the ZymoPURE™ Maxiprep kit compared to two separate kits from supplier Q. Plasmid DNA (pGL3®) was isolated from 150 ml of JM109 *E. coli* culture grown overnight following the manufacturer's suggested protocol (in duplicate). One (1) µl of eluted plasmid DNA was visualized post agarose gel electrophoresis. M, ZR 1 kb DNA Marker (Zymo Research).

Patent Pending

Tel: (949) 679-1190

ZYMO RESEARCH
The Beauty of Science is to Make Things Simple®

DNA Purification Made Simple™

www.zymoresearch.com

THE BRAIN FORUM

LAUSANNE, SWITZERLAND | March 30 – April 1 2015

SWISSTECH CONVENTION CENTER | thebrainforum.org

ORGANISED BY:
BRAIN MIND INSTITUTE
EPFL ÉCOLE POLYTECHNIQUE FÉDÉRALE DE LAUSANNE
W SCIENCE

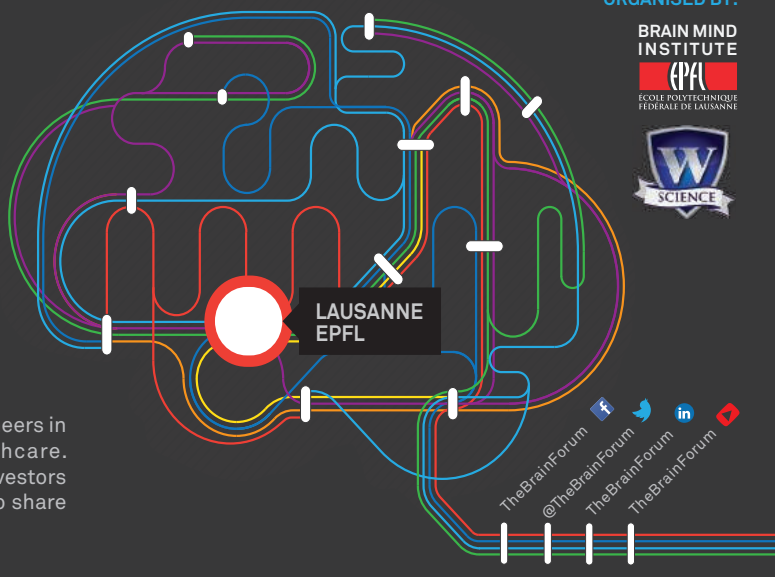

NEXT STOP: LAUSANNE

TURNING THE SPOTLIGHT ON BRAIN RESEARCH

The Brain Forum brings together novel thinkers and pioneers in the fields of brain research, technology and healthcare. Academics, entrepreneurs, healthcare professionals, investors and policy makers will meet at The Brain Forum 2015 to share their knowledge, experience and vision for the future.

PROGRAM OVERVIEW

- International Brain Initiatives: Progress, challenges & opportunities
- Philanthropists for brain science
- Emerging tools for neurotechnology
- Industry perspectives for neurotranslation
- Brain enhancement & repair technologies
- 21st century challenge: neurodegeneration
- Neuroscience funding and policy

REGISTRATION NOW OPEN
www.thebrainforum.org

AAAS *Travels*

TANZANIA
Wildlife & Eclipse Safari
August 19–September 3, 2016

See the Annular Solar Eclipse, September 1, 2016!

Join us on a Wildlife & Eclipse Safari in Tanzania to see the Annular Solar Eclipse. Enjoy splendid days looking for lions, leopards, elephants, rare rhinos, hippos, spectacular birds, and other wildlife in the finest wildlife parks in East Africa! $6,995 pp + air

For a detailed brochure, call (800) 252-4910
All prices are per person twin share + air

BETCHART EXPEDITIONS Inc.
17050 Montebello Rd, Cupertino, CA 95014
Email: AAASInfo@betchartexpeditions.com
www.betchartexpeditions.com

CALL FOR NOMINATIONS FOR A 1 MILLION DOLLARS PRIZE

THE 2015 ERIC AND SHEILA SAMSON PRIME MINISTER'S PRIZE FOR INNOVATION IN ALTERNATIVE FUELS FOR TRANSPORTATION

If you are actively engaged in innovative, paradigm-shifting research or technological development that is ground- breaking and worthy of significant and widespread attention you can qualify for this prestigious prize.

Deadline for nominations:
March 16, 2015
Nominations are open to citizens of any country

For further information and forms:
Go to: prize.fuelchoicesinitiative.com
Or contact: avi@most.gov.il

Fuel Choices Initiative
KEREN HAYESOD UNITED ISRAEL APPEAL
Israel
Ministry of Science, Technology and Space

Klaus J. Jacobs Awards

CALL FOR NOMINATIONS 2015

KLAUS J. JACOBS RESEARCH PRIZE

The Prize of 1 Million Swiss Francs awards outstanding scientific contributions of individuals from all disciplines aiming at the improvement of young people's development and perspectives worldwide.
It will be awarded in Zurich on December 4th, 2015.

Nominations can be submitted by e-mail by 15 March 2015 to *award@jacobsfoundation.org*. Self-nominations cannot be accepted.

For the nomination form and details of the nomination procedure, please visit:
www.jacobsfoundation.org/awards/research-prize-2015-2

NOMINATIONS WILL BE REVIEWED BY THE PRIZE JURY

Jürgen Baumert
Jere R. Behrman
Francesco C. Billari
Uta Frith
Kathleen Kiernan
Terrie E. Moffitt
Anne C. Petersen

PRIZE RECIPIENTS TO DATE

2009 **Laurence D. Steinberg**
2010 **Terrie E. Moffitt** and **Avshalom Caspi**
2011 **Michael Tomasello**
2012 **Dante Cicchetti**
2013 **Greg J. Duncan**
2014 **Michael J. Meaney**

Multiplexing System

The AlphaPlex reagent technology is a homogeneous, all-in-one-well multiplexing reagent system for performing ultrasensitive immunoassay analyses, while providing research professionals with more data in less time and with minimal human intervention. AlphaPlex reagents draw upon PerkinElmer's AlphaLISA technology and are designed to extract more information from each assay by simultaneously quantifying multiple analytes in a single well. Based on PerkinElmer's proven Alpha Technology, an alternative to enzyme-linked immunosorbent assays, AlphaPlex reagents are a homogeneous luminescent proximity technology. When the Donor and Acceptor beads are brought together, a cascade of chemical reactions is set in motion, causing a greatly amplified signal. By using multiple Acceptor beads which emit different wavelengths, multiple analytes can be detected.

PerkinElmer
For info: 800-762-4000
www.perkinelmer.com/alphaplex

Scanning Electron Microscope

The new Syncerity back-illuminated, deep-cooled CCD cameras with ultraviolet-visible (UV-Vis) and NIR-enhanced 2,048 x 70 sensors come equipped with a front illuminated 1,024 x 256 CCD sensor for UV-VIS-NIR applications. Its high-resolution 14 µm pixel size makes it ideal for Raman instrumentation. The camera offers ultralow etaloning and more than 40% Quantum Efficiency at 1,000 nm for the NIR version while the UV-Vis version exhibits a 60% QE at 250 nm. The Syncerity BI UV-Vis and BI NIR offer a broad spectral response for increased versatility. Its lifetime vacuum warranty, compact size, and sensor format make the Syncerity BI NIR and BI UV-Vis, the ideal candidate for microspectroscopy applications. The Syncerity is a research-grade spectroscopy camera that combines affordability, performance, and versatility for OEM as well as research applications. Ruggedized connectors ensure overall system integrity in industrial environments, and its all metal sealed technology provides a permanent vacuum which comes with a lifetime maintenance-free warranty.

HORIBA Instruments
For info: 732-623-8142
www.horiba.com/scientific

Full High-Definition Cameras

Life-like digital microscopy is now a reality with the DP27 and DP22 digital cameras. Both cameras deliver fluid imaging at full high-definition resolution via a USB 3.0 interface and enable easy optimization for each and every application with three distinct modes. Researchers can enjoy visualization on a monitor that is virtually identical to that of the oculars. The cameras offer a detailed full high-definition live image with 30 fps for the DP22 and 22 fps for the DP27. The progressive readout subsequently ensures a fluid and true-to-life experience, ideal for both analysis and viewing comfort. Moreover, when precise focusing of intricate samples is necessary, the DP27 can provide a fast 15 fps live image at 5 megapixels, allowing the user to effectively zoom in directly on the display. Addressing specific requirements, both cameras deliver their full image quality also in a stand-alone configuration, with the new DP2-SAL controller directly connecting the camera to a monitor.

Olympus
For info: +49-40-23773-5913
www.olympus-europa.com/microscopy

Exome Array

The CytoSure Medical Research Exome Array is highly targeted and exon-focused, enabling the accurate detection of medical research relevant microdeletions and microduplications. The high-density array (1x1M) contains over 4,600 hand-curated genes, which have been grouped into disease- and syndrome-specific panels. This research-validated gene content can also be customized for varying array formats (2x400K, 4x180K, or 8x60K) and diseases, enabling researchers to create bespoke solutions to suit both their content and throughput requirements. OGT's new array meets the needs of the medical research community by providing coverage of hand-curated, medically relevant genes on one array, enabling the detection of single or multiple exonic copy number variations (CNVs). As such, the array is an ideal complement to other genomic technologies, such as next generation sequencing, to provide accurate analysis of the full mutation spectrum.

Oxford Gene Technology
For info: +44-(0)-1865-856826
www.ogt.com

Image Databasing Software

The new server-based image databasing software ZEN browser aids users in storage, filing, and organization, and backup of large digital data sets, making the use of these data sets reliable and easy. This technology, invaluable to users in fields such as pathology research, provides storage and organization both in the lab and on the go for large virtual slide databases. The intuitive web interface allows users to organize virtual microscopy data online and across platforms. The software can be accessed through any Internet browser, and is password protected for security purposes. An additional user management function restricts access to authorized individuals only, while allowing others to view images without administrative rights. All images are filed together with relevant metadata and customizable supporting documents. Access and permissions can be individually assigned, allowing users to customize how data is shared and keep information organized.

ZEISS
For info: 800-233-2343
www.zeiss.com/micro

Electronically submit your new product description or product literature information! Go to www.sciencemag.org/products/newproducts.dtl for more information.

Newly offered instrumentation, apparatus, and laboratory materials of interest to researchers in all disciplines in academic, industrial, and governmental organizations are featured in this space. Emphasis is given to purpose, chief characteristics, and availability of products and materials. Endorsement by *Science* or AAAS of any products or materials mentioned is not implied. Additional information may be obtained from the manufacturer or supplier.

AAAS 2015 ANNUAL MEETING

12–16 FEBRUARY • SAN JOSE, CA

INNOVATIONS, INFORMATION, AND IMAGING

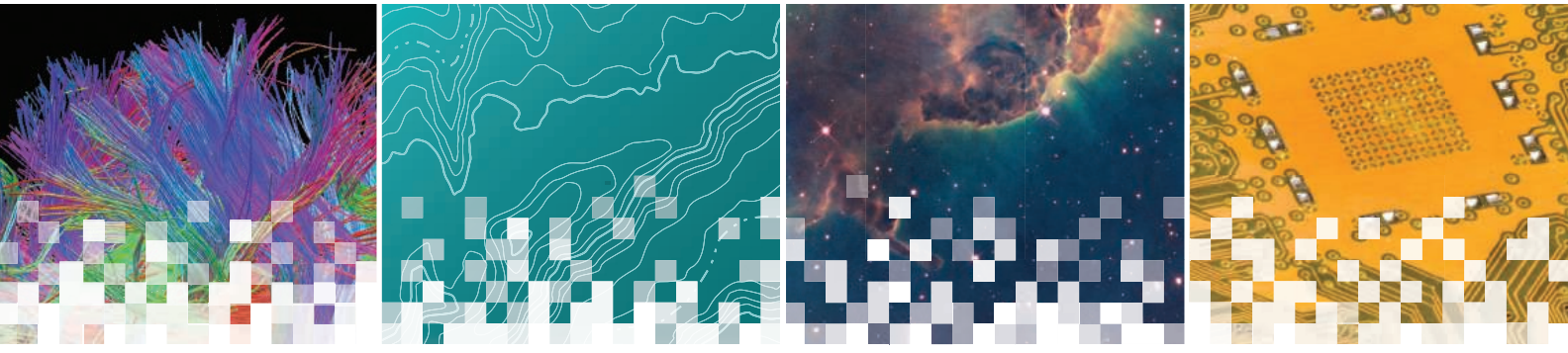

AAAS, publisher of *Science*, thanks the sponsors and supporters of the 2015 Annual Meeting

As of 16 February 2015

European Commission

Johnson & Johnson

SUBARU

RESEARCH COUNCILS UK

Genentech
A Member of the Roche Group

HELMHOLTZ ASSOCIATION

BBSRC
bioscience for the future

the Lemelson foundation
improving lives through invention

NANYANG TECHNOLOGICAL UNIVERSITY

DIGITAL science

UNIVERSITY OF WATERLOO

THE KAVLI FOUNDATION
for its generous support of
the Science Journalism Awards

THE GEORGE WASHINGTON UNIVERSITY
WASHINGTON, DC

Science Advances

www.aaas.org/meetings

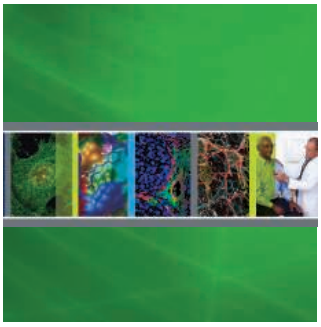

2015 SCIENTIFIC CONFERENCES

Presenting the most significant research on cancer etiology, prevention, diagnosis, and treatment

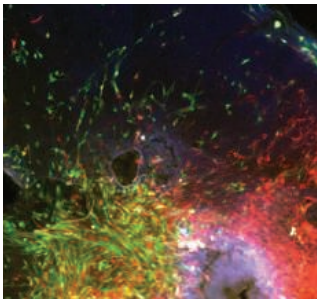

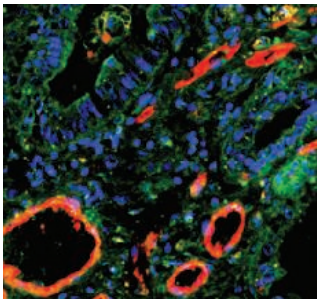

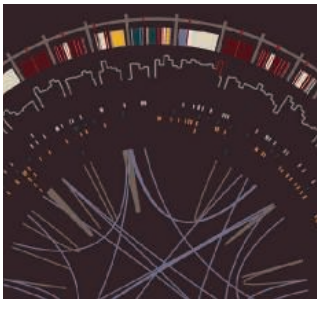

AACR Annual Meeting 2015
Program Committee Chairperson: Lewis C. Cantley
April 18-22, 2015 • Philadelphia, PA

Advances in Brain Cancer Research
Co-Chairpersons: Eric C. Holland, Franziska Michor, Martine F. Roussel, and Michael D. Taylor
May 27-30, 2015 • Washington, DC

Metabolism and Cancer
Co-Chairpersons: Ralph J. DeBerardinis, David M. Sabatini, and Almut Schulze
June 7-10, 2015 • Bellevue, WA

Methods in Cancer Biostatistics Workshop: Clinical Trial Designs for Targeted Agents
Chairperson: Steven Piantadosi
June 7-13, 2015 • Lake Tahoe, CA

AACR Precision Medicine Series: Integrating Clinical Genomics and Cancer Therapy
Co-Chairpersons: Charles L. Sawyers, Elaine R. Mardis, and Arul M. Chinnaiyan
June 13-16, 2015 • Salt Lake City, UT

EACR-AACR-SIC Special Conference on Anticancer Drug Action and Drug Resistance: From Cancer Biology to the Clinic
Co-Chairpersons: Richard M. Marais, Pasi Jänne, and Riccardo Dolcetti
June 20-23, 2015 • Florence, Italy

Chromatin and Epigenetics in Cancer
Co-Chairpersons: Peter A. Jones, Sharon Y. R. Dent, and Charles W. M. Roberts
September 24-27, 2015 • Atlanta, GA

CRI-CIMT-EATI-AACR The Inaugural International Cancer Immunotherapy Conference: Translating Science into Survival
September 27-30, 2015 • New York, NY

Advances in Breast Cancer Research
Co-Chairpersons: Matthew J. Ellis, Charles M. Perou, and Jane E. Visvader
October 17-20, 2015 • Bellevue, WA

Advances in Ovarian Cancer
Co-Chairpersons: Kathleen R. Cho, Douglas A. Levine, and Benjamin G. Neel
October 17-20, 2015 • Orlando, FL

Fourth AACR International Conference on Frontiers in Basic Cancer Research
Chairperson: M. Celeste Simon;
Co-Chairpersons: James P. Allison, John E. Dick, Nathanael S. Gray, and Victor E. Velculescu
October 23-26, 2015 • Philadelphia, PA

Basic Science of Sarcomas
Co-Chairpersons: Robert G. Maki, Angelo Paolo Dei Tos, Jonathan A. Fletcher, Lee J. Helman, and Brian Van Tine
November 3-4, 2015 • Salt Lake City, UT

New Horizons in Cancer Research
Co-Chairpersons: Lewis C. Cantley and Carlos L. Arteaga
November 2015 • Shanghai, China

AACR-NCI-EORTC International Conference on Molecular Targets and Cancer Therapeutics
Scientific Committee Co-Chairpersons: Levi A. Garraway, Lee J. Helman, and Jean-Charles Soria
November 5-9, 2015 • Boston, MA

Pediatric Oncology
Co-Chairpersons: Scott Armstrong, Charles G. Mullighan, Kevin M. Shannon, and Kimberly Stegmaier
November 9-12, 2015 • Fort Lauderdale, FL

Developmental Biology and Cancer
Co-Chairpersons: Hans Clevers, Stuart Orkin, and Suzanne Baker
November 30-December 3, 2015 • Boston, MA

Tumor Metastasis
Co-Chairpersons: Bruce R. Zetter, Melody A. Swartz, and Jeffrey W. Pollard
November 30-December 3, 2015 • Austin, TX

Noncoding RNAs and Cancer
Co-Chairpersons: Howard Y. Chang, Jeannie T. Lee, Joshua Mendell
December 4 - 7, 2015 • Boston, MA

www.AACR.org/Calendar

AACR American Association for Cancer Research

FINDING CURES TOGETHER℠

POSITIONS OPEN

GRADUATE PROGRAMS

Leadership Training for Early Career Researchers

A decade ago, the "sink or swim" culture was widespread in research. But academic institutions across the United States and Europe are now investing resources in helping young researchers gain the skills they need for climbing the career ladder. Top on the list are leadership skills, whether for conflict management, handling finances, or negotiating intellectual property rights in an international consortium, these are highly rated assets that can help researchers advance to senior roles. Here's a look at some of the most established leadership programs that hold alumni who are leaping ahead as a result of the training. **By Julie Clayton**

It was a daunting prospect for **Katie Garman** when she joined Duke University's Department of Medicine as a faculty member in 2011 and found herself in charge of a research group for the first time. She took on a technician, a graduate student, and "several clinical fellows and residents" for short-term gastroenterology projects.

With a clinical background focused on diagnosis and treating patients, Garman had little experience of managing budgets or people. Her position was similar to that of a postdoc facing their first tenure-track appointment.

"Although I had some exposure to research it was always with someone else as the principle investigator and without the responsibilities of being the person in charge," she recalls. "I really needed to learn more about how to manage a lab and manage a group and obtain a very different skillset than the one that I had acquired during medical school, residency, and fellowship."

Fortunately, the School of Medicine at Duke has a training program to help new faculty members develop leadership skills. Garman was nominated by her departmental chair to undertake the training in 2012, together with around 40 others from different departments.

Over three days, Garman joined seminars, discussion groups, and role-play exercises. These were aimed at understanding different personality types, creating strategies for dealing with challenging situations such as conflict, and forming a support network to help follow up with a personal action plan.

Personality differences

Garman found it especially useful to think about how personalities shape people's preferred way of communicating. "Even though I had developed a skillset in managing a difficult patient I really hadn't delved more deeply into that knowledge base of how people can have such different styles of communicating," she explains. "In order to really be a good listener and be innovative you have to be open to people who communicate in a very different way."

The role-play sessions are among the most popular at Duke, enabling faculty to practice their coaching skills on volunteer postdocs and students. "It lets them fumble around with their words in a safe environment so that when they're facing similar scenarios in their real lives they can draw from that memory," says **Jessica Womack**, who coordinates the Leader Program.

The lessons can help outside the lab too. "Happily, I have not encountered the role-play situations in real life but dealing with conflict and working through difficult situations is a life skill that comes in handy at work and in one's personal life," says Garman.

Duke University is one of many institutions in the United States and other countries that are investing in leadership training for early career researchers, often at the postdoc stage or earlier. The goal is to minimize the time and energy spent dealing with the difficulties of team leadership, and maximize the chance of a productive and successful career.

Many institutions use the classic Myers Briggs Type Indicator (MBTI) for understanding personality type. Individuals gain awareness of their own and others' personality preferences, for example, whether they tend towards being extrovert or introvert, and how this influences communication.

Duke's program was the initiative of **Ann Brown**, vice dean for faculty at Duke University School of Medicine. She adapted the idea from a program at the University of Pittsburgh, which in turn was based on the Making the Right Moves initiative of Howard Hughes Medical Institute. Brown knew that researchers needed to be better prepared for leadership, especially because the increasingly competitive nature of funding meant that there was more pressure to deliver results. "You wanted people to be able to hit the ground running and have a sense that managing people is now a part of their job. You want them to feel comfortable managing conflict, understanding [their] own communication style, understanding how other people receive information, and how to build [their] own team," says Brown. continued>

Upcoming Features

Regional Focus: Japan—March 27 ■ *Postdocs—August 28* ■ *Faculty—September 18*

Postdoc and young investigators opportunities in Brazil

Fifty percent of all science created in Brazil is produced in the State of São Paulo. The state hosts three of the most important Latin American universities: Universidade de São Paulo (USP), Universidade Estadual de Campinas (UNICAMP) and Universidade Estadual Paulista (UNESP). Other universities and 19 research institutes are also located in São Paulo, among them the Technological Institute of Aeronautics (ITA), the National Institute for Space Research (INPE) and the National Synchrotron Light Laboratory (LNLS), besides most of Brazilian Industrial P&D.

The São Paulo Research Foundation (FAPESP), one of the leading Brazilian agencies dedicated to the support of research, has ongoing programs and support mechanisms to bring researchers from abroad to excellence centers in São Paulo.

The **Young Investigators Awards** is part of FAPESP's strategy to strengthen the State research institutions, favoring the creation of new research groups. See more about it at www.fapesp.br/en/yia.

FAPESP **Post-Doctoral Fellowship** is aimed at distinguished researchers with a recent doctorate degree and a successful research track record.

The fellowship enables the development of research within higher education and research institutions in São Paulo. Postdoc fellowships are available when calls for applications are issued internationally, or as individual fellowships requested on demand.

In the first case, positions are advertised at www.fapesp.br/oportunidades and candidates are selected through international competition. In the second, the proposal must represent an addition to a pre-existent research group and should be developed in association with faculty in higher education and research institutions in São Paulo. More information at www.fapesp.br/en/postdoc.

Primary Contact Details:
Rua Pio XI, 1500 – Alto da Lapa
05468-901, São Paulo, SP – Brazil
Phone: +55-11-3838-4224

FAPESP
SÃO PAULO RESEARCH FOUNDATION
www.fapesp.br/en

Similarly, when **Lori Conlan** joined the National Institutes of Health's Office for Intramural Training and Education in 2009, she set up a Leadership and Management program that went beyond just lab management to consider leadership in other spheres. Statistically, many early career researchers are likely to move away from lab-based research, says Conlan.

So far, the NIH program has trained over 700 graduate students, postdocs, and early PIs. It involves 32 hours of training over one semester, addressing topics such as understanding personality types and conflict management focused specifically on the research environment. A more generic business-style model of training simply does not work for a scientific audience, even if the underlying ideas are common to both communities. "Every time we get a business school to come and do this, they do a great job and the material is didactically the same, but [it doesn't] resonate with scientists because they don't understand the culture," says Conlan.

Participants also learn about the influence of cultural background according to the Hofstede Model. "Science is the most international workforce, and we throw people in from different cultures and we ask them to work together," exclaims Conlan. The Hofstede model proposes that a person's perspective can vary depending on their background, such as how South versus North Americans view time. Likewise, attitudes toward hierarchy may vary—scientists from Asian cultures, where respect for authority is paramount, may wait for guidance rather than taking the initiative expected in the more individualist cultures of the United States or United Kingdom.

Leading peers

Besides leading their own team, academics increasingly need leadership skills for handling multidisciplinary collaborations. **Richard Trask**, a materials scientist at the University of Bristol in the United Kingdom, participated in the university's Preparing for Research Leadership training program while a postdoc in 2009. He knows the difficulties that arise during the coordination of grant proposals, writing papers and assigning intellectual property rights. These require cooperation among academics of equal status, and sometimes with collaborators of higher status than the initiator.

"It can lead to interesting technical and management challenges," says Trask, whose collaborations involve chemists, physicists, biologists, and medical colleagues. Typically, one discipline might prompt the collaboration, followed by the creation of shared documents, and a flurry of emails without the luxury of face-to-face meetings in order to reach agreement. "It's the academic space we'll find ourselves in more often in future." Adding to the challenge is the need for collaboration with industry, with its own sometimes conflicting timescales and priorities. Trask still harks back to leadership training regarding self-awareness and understanding of personality differences for managing increasingly dynamic and complex situations.

The training also helped Trask develop his individual leadership style, with a fairly flexible approach to supervision of 12 Ph.D. students and one postdoc. He avoids rigid micromanagement, for example, by allowing students to specify how often they want progress meetings to take place. By applying leading skills, Trask finds that the complex task of managing and supervising becomes less of a challenge, and more a collaborative culture.

> **"I really needed to learn more about how to manage a lab and manage a group and obtain a very different skillset than the one that I had acquired during medical school, residency, and fellowship."**
>
> **— Katie Garman**

PHOTO: DUKE, DEPARTMENT OF MEDICINE

The self-awareness training is invaluable, according to **Alison Leggett**, head of academic staff development at the University of Bristol. "That kind of people element is not something you really talk about in research—especially in the sciences. It's all about your technical skills and knowledge rather than these softer skills."

Bristol's program is aimed at those on the cusp of becoming leaders: postdocs and recently appointed lecturers. It involves attending eight training sessions over a period of three months, on topics such as personality awareness, people management, setting up a team, and structuring meetings. Activities include rehearsing scenarios and small-group peer coaching (also called action learning) over real-life problems. More recently, Leggett has organized similar training for more senior academics who "already had teams but were having to just muddle through."

Beyond the initiative of individual institutions, a U.K.-wide sharing of best practices is being encouraged by Vitae, a membership program which was initially funded by the U.K. Research Councils to promote professional development of doctoral researchers and research staff throughout the United Kingdom's higher education sector. To enhance provision of training across the country, Vitae created a suite of workshops and resources and established regional networks for university support staff to exchange ideas and materials. Over the past five years Vitae's Leadership in Action training program has helped researchers at all levels explore and develop their leadership potential while the more recent Preparing for Leadership program focuses on junior research staff and the transition to independence.

Alison Mitchell, director of development at Vitae, likens the effect to the rising tide that allows all the boats to float in a harbor. "We raise the tide by making resources available. The universities review the material and embed it within their provision so that it becomes continued>

Featured Participants

Duke University School of Medicine
www.medicine.duke.edu

GEOMAR Helmholtz Centre for Ocean Research Kiel
www.geomar.de/en

NIH Office of Intramural Training and Education
www.training.nih.gov/home

University of Bristol
www.bristol.ac.uk

Vitae
www.vitae.ac.uk

part of the system." Vitae also provides training programs on a national or regional basis directly for researchers.

Most importantly, the training helps researchers to develop leadership skills in advance of that coveted promotion. "The idea that you will suddenly develop these by experience isn't really the case and to be most effective in this fast changing world you have to be ready to lead," says Mitchell.

It's an increasingly shared view that academic institutions need to invest in staff development at the earliest possible opportunity rather than expecting staff to learn on the job. "Researchers who did it their own way maybe could have done better if they'd had more development," says Mitchell. "Putting in leadership training when [they are already] there is too late."

Leadership for women

In Germany, at least two leadership training programs focus specifically on women scientists as part of a broader political agenda of increasing the numbers of female university professors. One is Fast Track, offered by the Robert Bosch Foundation to outstanding female postdocs from within and outside Germany to speed their promotion to senior research roles. The second is ProFiL, a training program set up jointly in 2004 by the three closely linked universities of Berlin— Technical University (TU) Berlin, the Free University of Berlin, and Humbolt University—in a bid to improve gender equality.

One participant is **Katja Matthes**, now a full professor at the GEOMAR Helmholtz Centre for Ocean Research Kiel, who had come back to Germany after three years in the United States for the one-year return phase of her European Marie Curie fellowship at the Free University of Berlin. She was unsure about her future direction, but an advert for the ProFiL program piqued her interest. After a rigorous selection process, Matthes was picked to become one of 36 participants in the year-long program, including six sets of two- or three-day long seminars and discussion panels.

Matthes credits ProFiL with having motivated and supported her to stay in science. The program offered mentoring and guidance on career planning, and coaching on interviewing skills and leadership, including conflict resolution, negotiation, team building, project and time management, and governance in higher education. "Without ProFiL I would not hold the position I have now," she says.

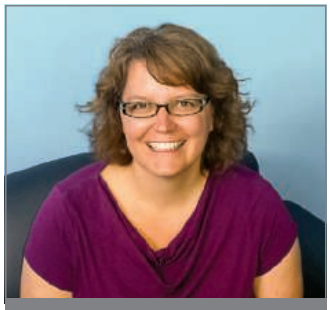

Lori Conlan

Matthes likes to tackle a conflict situation immediately by calling a meeting with those involved, listening to their viewpoint, and discussing possible solutions. "Sometimes [the conflict] is just a miscommunication or misunderstanding. I prefer to talk immediately and not let bad feelings develop."

She also uses meetings more effectively to promote team building, by acknowledging people's strengths and encouraging each person to state their intended contribution towards a team goal. "This works well—people like to know what their contribution is."

ProFiL goes further than many programs in establishing a formal peer-support network, with an annual conference and other events. "Internationally, I was well connected, but my network in Germany was very weak," says Matthes. With other ProFiL alumni Matthes has shared valuable experiences and gained advice, for example on developing a publication strategy and judging when to delegate administrative tasks.

While it would be difficult to obtain a truly objective measure of impact, up to mid-January 2015, out of 425 former and current ProFiL participants, 148 have achieved formal eligibility for professorial positions, and 176 have attained professorships, including two vice-chancellors, according to Dorothea Jansen, who established and leads the ProFil programme and has advised other institutions in Germany and Poland on similar programs.

Admitting when help is needed

It's a common mistake for researchers to assume that team leadership will come naturally. As the University of Bristol's Alison Leggett points out, "A lot of researchers have come up to these positions because they're really good at doing the research; they're academically very able. But this doesn't necessarily mean that they're good at setting up a team and leading people."

Garman agrees. "We're not always encouraged to be introspective enough to say these are the skills that are required, these are my strengths, my weaknesses, and these are the strategies that I need in order to account for those weaknesses." Training programs can provide a more objective way of identifying weaknesses. "You have to pause and give yourself the grace to say, 'no one is good at everything all the time.' If you had three things to work on, what would they be?" Garman asks.

Julie Clayton is a U.K.-based journalist and editor, and has worked briefly at the University of Bristol.

DOI: 10.1126/science.opms.r1500153

PHOTO: COURTESY OF LORI CONLAN

Stony Brook University

POSTDOCTORAL POSITIONS

Spring 2015

Stony Brook University is currently in the process of recruiting for multiple postdoctoral positions in various sub-specialties, for the upcoming spring and summer months.

Stony Brook has been characterized by innovation, energy and progress, and making ground-breaking discoveries since its beginning half a century ago.

Any interested candidature are invited to visit our new JOBS page.

www.stonybrook.edu/postdocjobs

Stony Brook University/SUNY is an equal opportunity, affirmative action employer.

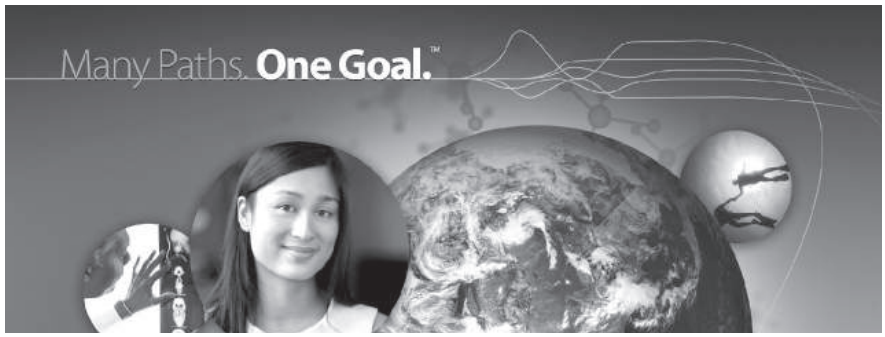

Pfizer Worldwide Research and Development Postdoctoral Program

At Pfizer, postdocs are trained in the art and science of drug discovery, and work side-by-side with scientists who are expert in cutting-edge biology, disease mechanisms, drug delivery and mechanisms of action, and the engineering of novel therapeutic proteins, vaccines, and nucleic acids. Areas of scientific focus include cardiovascular and metabolic diseases, clinical research, comparative medicine, drug safety, biotherapeutics/protein engineering, inflammation and immunology, human exploratory biology, medicinal chemistry, neuroscience and pain, oncology, pharmacology, and vaccines, among several others.

We recruit highly motivated Ph.D. recipients with an outstanding record of scientific productivity and a passion for ground-breaking, fast-paced research that facilitates the development of innovative therapies for human diseases. Our program promotes dissemination of research through publications and participation in scientific meetings, provides opportunities for collaboration with leading academic labs and industry consortia, and offers exceptional professional development training and networking opportunities.

To explore our program and research, visit us online at: www.pfizercareers.com/university-relations/postdoc.

Pfizer Working together for a healthier world®

www.pfizercareers.com

AAAS is here –
helping scientists achieve career sucess.

Every month, over 400,000 students and scientists visit ScienceCareers.org in search of the information, advice, and opportunities they need to take the next step in their careers.

A complete career resource, free to the public, *Science* Careers offers hundreds of career development articles, webinars and downloadable booklets filled with practical advice, a community forum providing answers to career questions, and thousands of job listings in academia, government, and industry. As a AAAS member, your dues help AAAS make this service available to the scientific community. If you're not a member, join us. Together we can make a difference.

To learn more, visit
aaas.org/plusyou/sciencecareers

AAAS + U = Δ

Post Doctoral Position: Immunology, Metabolism, and Chemical Communication Monell Chemical Senses Center

The Monell Chemical Senses Center is a nonprofit, basic research institute dedicated primarily to research in smell and taste. The Center is located on the campus of the University of Pennsylvania in Philadelphia and has close ties to Penn as well as other Universities in Philadelphia. Center research focuses on understanding how the chemical senses function and their importance in regulating behavior and physiology.

The current position involves working with a multidisciplinary group studying odor communication, the chemistry of biological odors and the role of inflammation in producing these odors in the laboratories of Gary Beauchamp and Bruce Kimball. We are seeking candidates who ideally have experience working on inflammatory pathways in mammals. Strong self motivation, an interest in obtaining new skills in metabolomics, and a desire to work in a multidisciplinary environment are highly valued. Preference will be given to candidates with expertise in inflammation and metabolic disorders. A background in chemosensory research is not required.

Requirements include a Ph.D. or equivalent degree in immunology or a related field. The stipend is in accordance with NIH standards. Send C.V., cover letter explaining your experience, research interests and career goals, and the names and means to contact three references to **hr0206gb@monell.org**.

Shriners Hospitals for Children™

Assistant Corporate Director of Research Shriners Hospitals for Children International

Shriners Hospitals for Children (SHC) invites applications for Assistant Corporate Director of Research Programs, at its headquarters in Tampa, Florida.

The applicant will assist in the management of an extensive program in basic, translational, and clinical research in pediatric congenital orthopedic diseases, spinal cord injury and burns at its 22 hospitals and eight Research Centers, with an annual departmental budget exceeding $32 million. Responsibilities include organizing peer review of grant applications, grants administration, site visit reviews of Research Centers, budget and program planning and evaluation, and research facilities development.

The applicant must have a Ph.D., M.D., or highest degree in a professionally related field, a track record of scholarly productivity, including publications and federal grants in biomedical/clinical research and knowledge of grant and research administration.

Applications should include a curriculum vitae, a letter summarizing professional accomplishments, and detailing administrative and management experience and philosophy, and the names and contact information of three potential references, and be submitted to: **shrinershqemployment@shrinenet.org**

Stony Brook University

Faculty Positions in the Institute for Advanced Computational Science

Applications are invited for four tenure-track faculty positions of any rank (including endowed chairs), in applied mathematics and computer science in the Institute for Advanced Computational Science (IACS) at Stony Brook University. Candidates wishing to apply should have a doctoral degree in Applied Mathematics or Computer Science, though a degree in related fields may be considered. Ten years of faculty or professional experience is required for a senior position along with a demonstrated record of publications and research funding. A demonstrated record of publications and a demonstrated potential for research funding is required for any junior faculty. The selected candidate is expected to participate in interdisciplinary program development within the Institute and to establish a research program with a solid funding base through both internal and external collaborations. Of specific interest is research in, for example, programming models, algorithms, or numerical representations that advance scientific productivity or broaden the benefit and impact of high-performance computing. The selected candidates will have access to world-class facilities including those at nearby Brookhaven National Laboratory.

The Institute for Advanced Computational Science (**http://iacs.stonybrook.edu/**) was established in 2012 with an endowment of $20M, including $10M from the Simons Foundation. The current ten faculty members will double in number over the next few years to span all aspects of computation with the intent of creating a vibrant multi-disciplinary program. IACS seeks to make sustained advances in the fundamental techniques of computation and in high-impact applications including engineering and the physical, life, and social sciences. Our integrated, multidisciplinary team of faculty, students, and staff overcome the limitations at the very core of how we compute, collectively take on challenges of otherwise overwhelming complexity and scale, and individually and jointly define new frontiers and opportunities for discovery through computation. In coordination with the Center for Scientific Computing at Brookhaven National Laboratory, our dynamic and diverse institute serves as an ideal training and proving ground for new generations of students and researchers, and provides computational leadership and resources across the SBU campus and State of New York.

The search will remain open until suitable candidates are found with the first round of applications due May 15, 2015. All candidates must submit the required documentation online through the link provided below. Please input a cover letter, your curriculum vitae, a research plan (max. 2 pages) which should also describe how graduate and undergraduate students participate, a one-page statement of your teaching philosophy, a publication list, your funding record, and three reference letters to: **https://iacs-hiring.cs.stonybrook.edu**.

Stony Brook University/SUNY is an equal opportunity, affirmative action employer.

EDCTP

The European & Developing Countries Clinical Trials Partnership (EDCTP), a non-profit organisation dedicated to advancing clinical research on poverty-related diseases in Sub-Saharan Africa, notably HIV/AIDS, tuberculosis, and malaria, seeks a new Executive Director. The Executive Director is responsible for overall management of the programme and for the leadership of its administrative organisation, which is based in The Hague, Netherlands, and in Cape Town, South Africa. For further information, see **www.edctp.org**.

Please contact EDCTP's search consultant for additional information or to apply: Craig Smith, PhD, Opus Partners (**craig.smith@opuspartners.net**). Expressions of interest and formal applications are due by **March 31, 2015.**

Female candidates are strongly encouraged to apply.

TEXAS TECH UNIVERSITY
HEALTH SCIENCES CENTER
School *of* Medicine™

TWO TENURE-TRACK FACULTY POSITIONS IN CANCER BIOLOGY AND WOMEN'S HEALTH

The Department of Cell Biology and Biochemistry at the Texas Tech University Health Sciences Center in Lubbock, TX invites applications for two tenure-track positions. One position will be at the **Associate or Professor level in the area of Cellular and Molecular Biology of Cancer** and the other position will be at the **Assistant or Associate level in Women's Health**. For the Cancer Biology position, an accomplished senior level scientist with a vigorous research program and a history of extramural funding is being sought to fill the Harry and Kayla Weitlauf Endowed Chair for Cancer Research. For the second position, an outstanding junior level candidate is being sought who works in any area of Women's Health, including but not limited to breast /ovarian cancer and or endocrinology/reproductive biology. Appointments will be in the School of Medicine and come with highly competitive start-up packages. Applicants should have a Ph.D. and/or M.D. degree, a funded independent research program, and be willing to contribute to the research and teaching missions of the department. TTUHSC has recently established imaging and molecular core facilities available to all faculty including a newly acquired Nikon Ti-E microscope with A1 confocal and STORM super resolution. The Department of Cell Biology and Biochemistry currently has thirteen full-time faculty members with research programs in biochemistry, cancer, cell and molecular biology and reproductive biology (http://www.ttuhsc.edu/SOM/cbb/). The TTUHSC Cancer Center has many resources available to researchers including the Texas Cancer Research Biobank, and the Texas Cancer Cell Repository (http://cancer.ttuhsc.edu). The Cancer Prevention Research Institute of Texas (CPRIT) (http://www.cprit.state.tx.us) provides outstanding opportunities for research funding (including recruitment grants) for cancer investigators in Texas. The Department of Cell Biology and Biochemistry is committed to diversity in education and employment and strongly encourages applications from women and minorities.

TTUHSC is in Lubbock, Texas, a city of over 230,000 residents on the South Plains of the Texas Panhandle. The region has a diverse economy that is strongly influenced by agriculture, health care, and higher education. Lubbock is home to Texas Tech University providing entertainment opportunities in collegiate athletics and the performing arts. Lubbock weather is mild and averages 262 days of sunshine/year.

Interested candidates must apply online at **http://www.ttuhsc.edu/som/cbb/positions.aspx**. Candidates should submit a single document in PDF format containing a cover letter describing their interest in the department including possible collaborations with current faculty, a curriculum vitae, and a brief summary of their research interests with the electronic application. Candidates should also arrange to have three letters of recommendation sent in electronic format to **cellbiology.biochemistry@ttuhsc.edu**. Review of applications will begin on **April 15, 2015** and will continue until the positions are filled.

The TTUHSC is an Equal Opportunity/Affirmative Action/Veterans/Disability Employer.

OUTSTANDING RESEARCH OPPORTUNITIES AT EMBL AUSTRALIA

Research Group leaders

- Join a world-class health & medical research facility
- Form and lead your own independent research group
- Modeled on the European Molecular Biology Laboratory (EMBL) to support independent, interdisciplinary, quality research
- Designed for high potential, early-career scientists who are dedicated to research excellence
- Excellent salary package, including (where required) arrangements for relocation, travel, work permits and visas for the successful candidate and their family
- Positions available in the beautiful cities of Adelaide in South Australia and Sydney in New South Wales

We encourage scientists interested in rapidly accelerating their research career in a highly supportive environment to apply. The position includes funding for a research team and a generous annual research budget. During the course of their tenure, applicants will be encouraged to apply for prestigious fellowships and grants to expand their research program.

EMBL Australia researchers benefit from close interactions with other EMBL Australia groups working on developmental biology and regenerative medicine, single molecule science, structural biology, and high resolution imaging, using a broad range of model organisms.

EMBL Australia researchers also gain access to the complementary facilities and expertise at EMBL in Europe and a growing network of groups at other national participating institutions in a dynamic, collaborative, internationally focused network.

GROUP LEADER in ORGANELLE BIOLOGY AND DISEASE AT SAHMRI IN ADELAIDE

SAHMRI (**www.sahmri.com**) is searching for a Group Leader to join the Lysosomal Diseases Research Unit and lead an independent research group investigating the general cell biological mechanisms underlying organelle biogenesis, regulation and turnover, and how aberrant organelle function contributes to the onset and progression of conditions such as dementia, stroke and cancer. We seek a dynamic, independent scientist with an excellent track record and demonstrated experience or interest in cell biology, and a desire to work in a multidisciplinary environment.

We encourage applicants addressing fundamental questions in cell biology with an emphasis on models of human disease, using modern genetics, genomics, biochemical and advanced imaging analysis, and an interest in recent CRISPR- and iPSC-technologies to prepare appropriate specific cell types for these studies.

GROUP LEADER IN SINGLE MOLECULE SCIENCE AT THE UNIVERSITY OF NEW SOUTH WALES, IN SYDNEY

The UNSW Centre in Single Molecular Science (**www.sms.unsw.edu.au**) seeks future research leaders to develop novel conceptual and experimental approaches to elucidate the molecular mechanisms of fundamental cell biological and medical problems. The successful applicant will define and drive a new research field that emerges at the interface between 'bottom-up' single molecule biophysics/biochemistry and cell biology/physiology. For example, it is now possible to combine system-wide proteomics and genomics information with single molecule imaging in cells and tissue, and propose models of biological processes and systems that integrate single molecule behaviour with functional outcomes.

Applicants with trans-disciplinary research experience are strongly encouraged. Research questions in cancer, immunology, neuroscience, cardiovascular biology and other fields are welcome. The successful applicant will lead a research team in a dynamic, highly collaborative, and internationally focused environment and the opportunity to further expand their research program through external grants and fellowships.

UNSW has unique microscopy capabilities in super-resolution and single molecule imaging developed by the ARC Centre of Excellence in Advanced Molecular Imaging (**www.imagingcoe.org**) and supported by the Biomedical Imaging Facility. Group Leaders also have access to UNSW facilities in nanofabrication, drug development, genomics, proteomics, animal models and the Mark Wainwright Analytical Centre.

Director, SBI Australia

We are seeking a self-motivated, internationally recognised academic in systems biology as Director for SBI Australia; an EMBL Australia initiative and the first international node of The Systems Biology Institute (SBI) of Japan.

SBI Australia, located at Monash University, promotes Australia's capacity and reputation for systems biology through an extensive program of research, training and outreach, and through engagement with Australian and international government, industry and research organisations.

The Director will be responsible for providing dynamic leadership and vision in setting the academic direction for SBI Australia and facilitation of its research programs. The Director will be the lead advocate for research and best practice in systems biology at Monash and throughout Australia especially through the EMBL Australia (**www.emblaustralia.org**) and Systems Biology Institute (**www.sbi.jp**) initiatives.

The Director will establish collaborative links with national and international research organisations in related fields and establish new opportunities for funding of systems biology research and teaching through competitive grants, government funding and philanthropy.

This is an ideal opportunity for someone looking to lead SBI Australia into its next phase of development, capitalising on the existing strong international linkages that have already been created.

A competitive package commensurate with the skills and experience of the successful applicant will be offered.

Further Information

Information regarding each of these positions and the relevant organisations in South Australia, Victoria and New South Wales along with application details please go to **http://www.emblaustralia.org/About_us/jobs.aspx**

NANYANG TECHNOLOGICAL UNIVERSITY | NUS National University of Singapore | SUTD SINGAPORE UNIVERSITY OF TECHNOLOGY AND DESIGN

TEMASEK RESEARCH FELLOWSHIP (TRF)

A globally connected cosmopolitan city, Singapore provides a supportive environment for a vibrant research culture. Its universities Nanyang Technological University (NTU), National University of Singapore (NUS) and Singapore University of Technology and Design (SUTD) invite outstanding young researchers to apply for the prestigious TRF awards.

Under the TRF scheme, selected young researchers with a PhD degree have an opportunity to conduct and lead defence-related research. It offers:

- A 3-year research grant of up to S$1 million commensurate with the scope of work, with an option to extend for another 3 years
- Postdoctoral or tenure-track appointment (eligibility for tenure-track will be determined by the university)
- Attractive and competitive remuneration

Fellows may lead, conduct research and publish in these areas:

- Advanced Protective Materials
- Cyber Security
- Machine Intelligence
- Photonics Engineering
- Visual and IR Technologies

For more information and application procedure, please visit:

NTU – **http://www3.ntu.edu.sg/trf/index_trf.html**
NUS – **http://www.nus.edu.sg/dpr/funding/trf.html**
SUTD – **http://www.sutd.edu.sg/trf**

Closing date: 27 April 2015 (Monday)

Shortlisted candidates will be invited to Singapore to present their research plans, meet local researchers and identify potential collaborators in **September 2015.**

Wadsworth Center
New York State Department of Health
Science in the Pursuit of Health®

Tenure Track Research Positions in Vector Borne Zoonotic Diseases

The Wadsworth Center (Albany, NY) is seeking outstanding scientists at the Assistant or Associate Professor level to establish competitive, grant-funded research programs in the area of Vector-Borne Zoonotic Diseases. Research on tick and mosquito-borne pathogens is of particular interest. Two positions are available:

- Research focused on vector-pathogen interactions, including areas such as vector biology, pathogen transmission dynamics, and the ecology/ epidemiology of disease emergence.
- Research focused on host-pathogen interactions, including areas such as pathogen virulence and immune response, and mechanisms of disease pathogenesis.

The incumbent will enjoy a vibrant community of research scientists and epidemiologists in the Wadsworth Center. The Zoonotic and Vector-borne Diseases research focus area includes established research programs studying arboviruses, coronaviruses, rabies viruses, and plague, including their hosts and vectors. The successful applicant will receive a competitive start-up package and have access to a BSL2/3 insectary and AAALAC accredited BSL2/3 animal space. The Wadsworth Center also has outstanding scientific cores, which provide advanced light and electron microscopy, immunology, bioinformatics, and next generation sequencing. Teaching opportunities are available through faculty appointments in the Wadsworth Center Masters of Laboratory Science program and the State University at Albany Department of Biomedical Sciences, School of Public Health. The Wadsworth Center (www.wadsworth.org) is the country's most comprehensive state public health laboratory, with a staff of 700 including 100 doctoral-level scientists. The Center provides a dynamic research environment focused on infectious, genetic and environmental diseases and their impact on human health. These activities complement strong programs in public health sciences that perform applied research and advanced diagnostic testing.

A Ph.D. degree or equivalent and relevant postdoctoral research experience is required. Applicants should submit their curriculum vitae, research plan and contact information for at least three references to **wcphgc@health.ny.gov**, referencing 'Zoonosis' in the subject line. Applications will be accepted and reviewed until the positions are filled. *AA/EOE.*

TOURO COLLEGE

Faculty Positions
Touro College of Pharmacy

The Department of Pharmaceutical and Biomedical Sciences at the Touro College of Pharmacy, located in historic Harlem, New York, invite applications for 3 full time faculty positions at the Assistant/Associate Professor level in the fields of Pharmacology/Medicinal Chemistry; and Physiology/ Pathophysiology and Pharmaceutical Sciences. Candidates will be engaged in didactic teaching, participate in academic, scholarly, and service functions within the College of Pharmacy, and are expected to engage in research and seek and obtain extramural funding.

The successful candidate must have a Ph.D. degree in the abovementioned fields, a record demonstrating academic and scientific accomplishments and excellent written and oral communication skills. Experience teaching at a College of Pharmacy or a similar program in some capacity (Teaching assistants, Graduate assistant, Lecturer, Instructor, Assistant Professor, etc.) is preferred.

Interested applicants should submit a cover letter summarizing professional experience, curriculum vitae, a brief statement of teaching philosophy, research plans and contact information for three references to: **Dr. Zvi Loewy (zvi.loewy@touro.edu**) Chair, Department of Pharmaceutical and Biomedical Sciences.

Touro College of Pharmacy is proud to be an Affirmative Action, Equal Opportunity Employer M/F/D/V. We are committed to seeking qualified candidates who can contribute to the diversity and excellence of our academic community. We encourage applications from women, minorities, veterans, and persons with disabilities. Hiring is contingent on eligibility to work in the United States.

Biofilm Director

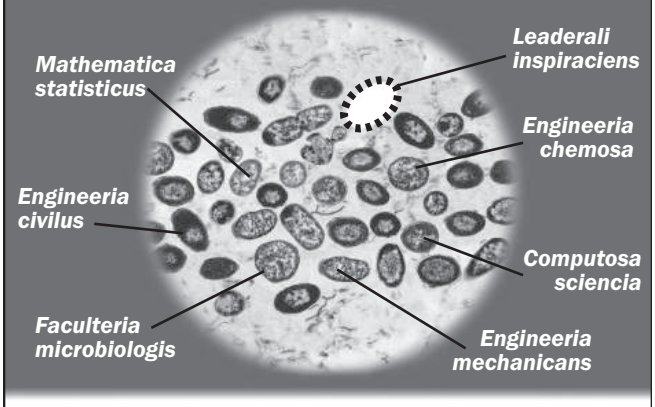

Center for Biofilm Engineering at Montana State University in Bozeman, MT seeks Director for:

World-class research in microbial biofilms
Interdisciplinary education
Industrial interaction

Take a closer look:

www.biofilm.montana.edu

Montana State University is an ADA/EEO/AA employer.

UCONN HEALTH

Tenure-Track Immunology (Tumor) Faculty Position

The Department of Immunology at the University of Connecticut Health Center seeks an outstanding investigator for a tenure-track position at the Assistant or Associate Professor rank to establish an extramurally funded laboratory. All areas of tumor immunology will be considered with emphasis on cancer immunotherapy, cancer vaccines, immune regulation of cancer, tumor tolerance mechanisms, and innate immunity during tumorigenesis. The ideal candidate's research program should include in vivo models, and be open to translational studies. The ideal candidate will participate in a vibrant graduate student training program, and have access to a growing translational research community and an expanding scientific community in the capital region. Salary and start-up funds are highly competitive and outstanding core facilities are available. Applicants must have a Ph.D. and/or M.D. with several years of postdoctoral training and a high impact publication record. For Associate Professor level a history of sustained extramural funding is expected. In addition to the beauty of the picturesque New England countryside, the Hartford area offers a vibrant arts and cultural scene and an exceptional outdoor sports environment. Interested applicants should apply at **https://jobs.uchc.edu/** search number 2015-691, and submit a curriculum vitae, a two-page summary of research accomplishments and interests, and the names and contact information of three references. Questions regarding this search should be directed to Anthony Vella, Ph.D., Chairman, Department of Immunology, School of Medicine, UConn Health Center, Farmington, CT. Email: **immunology@uchc.edu**. For further information on UCHC, please visit **http://immune.uchc.edu**. The deadline to submit applications is May 1, 2015.

UCHC is an Affirmative Action/Equal Opportunity Employer M/F/V/PwD

UCONN HEALTH

Tenure-Track Immunology (Diabetes) Faculty Position

The Department of Immunology at the University of Connecticut Health Center seeks an outstanding investigator for a tenure-track position at the Assistant or Associate Professor rank to establish an extramurally funded laboratory. We are specifically interested in an individual with research interests in autoimmunity of diabetes. The ideal candidate's research program should utilize immunobiological approaches and models to study autoimmune diabetes. Areas of priority include, but are not limited to, T cell tolerance and innate immunity of disease, including signal transduction, transcriptional control, and metabolism. The new hire will participate in a vibrant graduate student training program, and have access to a growing translational research community and an expanding scientific community in the capital region. Salary and start-up funds are highly competitive and numerous outstanding core facilities are available. Applicants must have a Ph.D. and/or M.D. with several years of postdoctoral training and a high impact publication record. For Associate Professor level a history of sustained extramural funding is expected. In addition to the beauty of the picturesque New England countryside, the Hartford area offers a vibrant arts and cultural scene and an exceptional outdoor sports environment. Interested applicants should apply at **https://jobs.uchc.edu/** search number 2015-692, and submit a curriculum vitae, a two-page summary of research accomplishments and interests, and the names and contact information of three references. Questions regarding this search should be directed to Anthony Vella, Ph.D., Chairman, Department of Immunology, School of Medicine, UConn Health Center, Farmington, CT. Email: **immunology@uchc.edu**. For further information on UCHC, please visit **http://immune.uchc.edu**. The deadline to submit applications is May 1, 2015.

UCHC is an Affirmative Action/Equal Opportunity Employer M/F/V/PwD

NIMS ICYS

Research Position at ICYS, NIMS, Japan

The International Center for Young Scientists (ICYS) of the National Institute for Materials Science (NIMS) is now seeking a few researchers. Successful applicants are expected to pursue innovative research on broad aspects of materials science using most advanced facilities in NIMS (**http://www.nims.go.jp/eng/index.html**).

In the ICYS, we offer a special environment that enables young scientists to work independently based on their own idea and initiatives. All management and scientific discussions will be conducted in English. An annual salary between 5.03 and 5.35 million yen (level of 2013) will be offered depending on qualification and experience. Additional research grant of 2 million yen per year will be supplied to each ICYS researcher. The initial contract term is two years and may be extended by one more year depending on the person's performance.

All applicants must have obtained a PhD degree within the last ten years. Applicants should submit an application form, which can be downloaded from our web site, together with a resume (CV), a publication list, and a research proposal to be conducted during the ICYS tenure. All documents should reach the following address via e-mail by **MARCH 30, 2015 JST**. Please visit our website for more details (**http://www.nims.go.jp/icys/**).

ICYS Administrative Office,
National Institute for Materials Science
Sengen 1-2-1, Tsukuba, Ibaraki 305-0047, Japan
e-mail: icys-recruit@nims.go.jp

THE UNIVERSITY OF ARIZONA CANCER CENTER

The University of Arizona Cancer Center is a Comprehensive Cancer Center designated by the National Cancer Institute

Director
Therapeutic Development Research Program
Faculty Leadership Position

The NCI-designated University of Arizona Comprehensive Cancer Center (UACC) seeks an outstanding leader for its Therapeutic Development Program, which currently has 28 full members and $6.5M in cancer funding. The ideal candidate will be eligible for appointment at the rank of associate or full professor, hold a PhD or an MD degree in chemical or cancer biology, medicinal chemistry, or a closely related discipline, and have an established NCI funded research program. The Program Director will lead collaborative research efforts of multidisciplinary teams of physicians and biomedical scientists to accelerate all facets of therapeutic development, encompassing target identification and validation, iterative preclinical improvements, and clinical translation. This position will bridge advances in preclinical basic drug discovery with novel therapeutic interventions that provide significant improvements in patient outcome.

The UACC in Tucson is located on the University of Arizona campus in a freestanding research facility (107,000 sq. ft.) with separate clinical outpatient buildings (110,000 sq. ft.) and >$40M in cancer research grants. Four outstanding basic, translational/clinical, and cancer prevention and control research programs (Cancer Prevention and Control, Cancer Biology, Cancer Imaging, and Therapeutic Development) are supported by 10 UACC Shared Resources.

To apply, please complete the on-line application at **http://www.uacareers.com/57578**, and email a curriculum vitae to the address below:

Andrew S. Kraft, M.D.
Director, University of Arizona Cancer Center
Email: LFrazier@uacc.arizona.edu

The University of Arizona is an EEO/AA - M/W/D/V Employer.

Southwest Jiaotong University, P.R.China Anticipates Your Working Application

Southwest Jiaotong University (SWJTU), founded in 1896, situates itself in Chengdu, the provincial capital of Sichuan. It is a national key multidisciplinary "211" and "985 Feature" Projects university directly under the jurisdiction of the Ministry of Education, featuring engineering and a comprehensive range of study programs and research disciplines spreading across more than 20 faculties and institutes/centers. Boasting a complete Bachelor-Master-Doctor education system with more than 2,500 members of academic staff, our school also owns 2 first-level national key disciplines, 2 supplementary first-level national key disciplines (in their establishment), 15 first-level doctoral programs, 43 first-level master programs, 75 key undergraduate programs, 10 post-doctoral stations and more than 40 key laboratories at national and provincial levels.

Our university is currently implementing the strategy of "developing and strengthening the university by introducing and cultivating talents". Therefore, we sincerely look forward to your working application.

More information available at http://www.swjtu.edu.cn/

I. Positions and Requirements

A.High-level Leading Talents

It is required that candidates be listed in national top talents programs such as ***Program of Global Experts, Top Talents of National Special Support Program, "Chang Jiang Scholars", China National Funds for Distinguished Young Scientists and National Award for Distinguished Teacher.***

Candidates are supposed to be no more than 50 years old. The limitation could be extended in the most-needed areas of disciplinary development.

Candidates who work in high-level universities/institutes and reach the above requirements are supposed to be no more than 45 years old.

B. Young Leading Scholars

Candidates are supposed to be listed in or qualified to apply for the following programs:

•National Thousand Young Talents Program

•The Top Young Talents of National Special Support Program(Program for Supporting Top Young Talents)

•Science Foundation for the Excellent Youth Scholars

Candidates should have good team spirit and leadership, outstanding academic achievements, broad academic vision and international cooperation experience and have the potential of being a leading academic researcher.

C. Excellent Young Academic Backbones

Candidates under 40 years old are expected to graduate from high-level universities/institutes either in China or other countries. Those who are professors, associate professors and other equal talents from high-level universities/institutes overseas could be employed as professors and associate professors as well.

D. Excellent Doctors and Post Doctoral Fellows

Candidates under 35 years old are supposed to be excellent academic researchers from high-level universities either in China or other countries.

II. Treatments

The candidates will be provided with competitive salaries and welfares that include settling-in allowance, subsidy of rental residence, start-up funds of scientific research, assistance in establishing scientific platform and research group as well as international-level training and promotion . As for outstanding returnees, we can offer further or specific treatments that can be discussed personally.

III . Contact us:

Contacts: Ye ZENG & Yinchuan LI Telephone number: 86-28-66366202 Email: *talent@swjtu.edu.cn*

Address: Human Resources Department of SWJTU, the western park of high-tech zone, Chengdu, Sichuan, P.R.China, 611756

http://www.swjtu.edu.cn/

Anhui University of Technology (AHUT) Recruits

1. University Introduction

Anhui University of Technology (AHUT) is located in a national civilized city named as Ma'anshan in Anhui Province which is adjacent to Nanjing. It is a multidisciplinary university with distinctive industry characteristics, taking engineering as its focus while maintaining balanced development in engineering, economics, management, humanities, science, laws and arts. It is the key construction university of Anhui province. We recruit students from 25 provinces (city, and municipality) in China, possessing three levels of degree-conferring rights namely bachelor's degree, master's degree and doctor's degree. We expect to openly recruit 22 leading personnel in various fields and 71 talents with doctor's degree at home and abroad. Excellent specialists and scholars at home and abroad are sincerely welcomed.

2. Recruitment (discipline, major)

Metallurgical Engineering, Materials Engineering, Power Engineering and Engineering Thermophysics, Environmental Science and Engineering, Materials Science and Engineering, Chemical Engineering and Technology, Pharmacy, Civil Engineering, Engineering Management, Safety Science and Engineering, Architecture, Urban and Rural Planning, Mechanical Engineering, Electric Engineering, Control Science and Engineering, Information and Communication Engineering, Computer Class, Electronic Class, Control Class, Industrial Engineering, Information Management and System, Logistics Management and Engineering, Project Cost, Business Administration, Practical Economics, Theoretical Economics, Statistics, Public Management, English, Mathematics, Lamps and Lighting, Optical Engineering, Arts, Design, Fine Arts.

3. Recruitment Treatment

Treatment for leading personnel and doctors is diversified for each one with liberal wages and benefits.

4. Recruitment Method

Please delivery your Resume to the specialized mailbox of Anhui University of Technology ahgydxzp@163.com (the first letter of Pinyin of "Anhui University of Technology Recruitment") by email, indicate application discipline, and provide detailed information like achievements in scientific research, scientific research plan, etc.

5. Contact information

Tel: 86-555-2311647/2311644

E-mail: ahgydxzp@163.com

Contact person: Ms. Jiang, Mr. Shi

Address: HR Dept. of Anhui University of Technology (AHUT), Maanshan City, Anhui Province, 243002

For more information, please visit www.ahut.edu.cn

Job Vacancies in China's Universities

赛尔互联 CERNET ScienceCareers AAAS

赛尔互联：《科学》在中国大陆高校人才引进服务独家合作伙伴

CER is Science's exclusive agent for recruitment advertisement service in mainland China universities and colleges

China's Rapid Development —— More Opportunities

Xi'an Jiaotong University (Xi'an,China)

Faculty positions in Department of Sustainable Energy:
Mission: To pioneer forward-looking education and undertake cutting-edge research in energy science and technologies to support sustainable development.

Faculty Positions in Department of Sustainable Materials:
Mission: To provide a broad-based education in materials science and engineering for sustainability and undertake cutting-edge research in the field to support sustainable development.

Faculty Positions in Department of Sustainable Systems:
Mission: To provide an education and research platform to study interrelationships among eco- nomic and urban development, governance, public policy and regional, national and global ecosystem, focusing on the social and physical systems needed for sustainability.

For further information about JSSD, please visit the following websites: http://jssd.xjtu.edu.cn or http://jssd.ust.hk

Beijing Institute of Technology (Beijing, China)

Open Senior Faculty Positions offered: Equipment Science & Technology Engineering/ Mechanical Engineering/ Information and Communication Engineering/ Mathematics...

Peking University (Beijing, China)

The School of Life Sciences (SLS)at Peking University invites applications for multiple faculty positions at tenure-track assistant professor, associate professor and full professor levels.

For more details, visit http://www.eol.cn/

广告联系：赵佳 zhaojia@cernet.com +86 10 62603373

eol 中国教育在线 是赛尔互联旗下品牌

天津大学 Tianjin University

FACULTY POSITIONS AT TIANJIN UNIVERSITY

Positions

Tianjin University, one of the top universities in China, invites outstanding applicants for a full-time professorship, and seeks candidates in the following areas.

In Science or Engineering:
Engineering, natural science, life science, marine science and technology, information technology, relevant emerging inter-disciplines.
In Other Academic Fields:
Architecture, economics, business, management, social sciences, relevant emerging inter-disciplines.
Applicants with a multi-disciplinary scientific background and nontraditional research approaches are highly preferred.

Qualifications

Competitive applicants with outstanding academic performance are expected to be academic staff from leading universities or researchers from renowned institutions and companies. Research excellence and potential for future productivity are essential. Additional criteria include leadership and communication skills.
In Science or Engineering:
Applicants shall apply for National Recruitment Program of Global Youth Experts (the National Youth 1000-Talent Program) through Tianjin University. Successful candidates will be employed as the appointee.
In Other Academic Fields:
Applicants will be selected according to their qualifications, academic performance, innovation capability, and leadership.

Responsibilities

Responsibilities include establishing a vigorous research program, teaching undergraduate and graduate students, and providing professional/institutional services.

Salary and Support

The university offers an attractive remuneration package. Salary will be commensurate with candidates' qualifications, academic performance and experience. In addition, the start-up package from the university provides a research grant, lab/office space and support for the research team.
In Science or Engineering:
● An annual pre-tax salary ranging from 400K to 600K RMB will be offered to appointee.
● An annual pre-tax salary ranging from 350K to 400K RMB will be offered to the candidates who are shortlisted for interview but not selected in the National Youth 1000-Talent Program.
In Other Academic Fields:
● Salary offered is the same as that for Science or Engineering.

Application Procedure

Please submit a complete application package electronically consisting of the following documents to oplan@tju.edu.cn. The application deadline is 6th April 2015.
(1)Application form
(2) Detailed curriculum vitae
(3) Publications list and five full-text representative publications
A detailed application information and the application form can be downloaded from http://hr.tju.edu.cn/zpxx/js/.

Contacts

Contact Persons: Ms. ZHANG Yinlu, Ms. CHANG Xin
Human Resource Department,Tianjin University, China
E-mail: oplan@tju.edu.cn
Telephone: (+) 86-022-27403932, (+) 86-022-27402079
Fax: (+) 86-022-27404177
Address: 223/Building 9, 92 Weijin Road, Nankai District, Tianjin, 300072

POSITIONS OPEN

NIST National Institute of Standards and Technology U.S. Department of Commerce

NATIONAL INSTITUTE OF STANDARDS AND TECHNOLOGY
U.S. Department of Commerce

The National Institute of Standards and Technology (NIST), Information Technology Laboratory (ITL) is seeking a highly qualified individual for the position of **DIVISION CHIEF** for the Information Access Division. The Division carries out interdisciplinary collaborations with industry, academia, and other government agencies to accelerate the research development, and adoption of standards and testing tools that improve access to multimedia and other complex information in topic areas such as Human Language Technology, Biometrics Technology, Identification and Verification Technology, Multimedia Technology, Usability Engineering, Data Science, and Human-System Interaction.

Title of Position: Supervisory Computer Scientist, ZP-1550-V; Supervisory IT Specialist, ZP-2210-V; Supervisory Mathematician, ZP-1520-V. Salary Range: $126,245 - $158,700; Geographic Location of Position: Gaithersburg, Maryland; Tenure: Permanent; Work Schedule: Full Time; Relocation expenses: Relocation Expenses are authorized.

Qualifications required: For each series, there are different requirements. Please visit the **website: http://go.usa.gov/SMXz** to view the requirements.

In addition to the basic requirements, to qualify for this position you must also have: One year, 52 weeks, of specialized experience equivalent to at least the GS-14, or ZP-IV at NIST.

For further information and to apply for this position, visit the **website: http://www.usajobs.gov**. The Job announcement number associated with this position is **NISTITL-2015-0019**. The vacancy opens February 13, 2015 and closes March 13, 2015.

U.S. Citizenship is required. The Department of Commerce is an Equal Opportunity Employer.

☑ More scientists agree—we are the most useful website.
ScienceCareers.org

WORKSHOPS

POSITIONS OPEN

Massachusetts Institute of Technology

Come work with us!

Assistant Professor
Environment and Climate Change

The MIT Media Lab (www.media.mit.edu) is seeking a candidate to fill a tenure-track position.

The Media Lab is a cross-disciplinary research organization focusing on the invention of new media technologies that radically improve the ways people live, learn, work, and play.

We are looking for faculty candidates who aspire to mitigate climate change and environmental degradation in ways that are highly innovative, technically deep and credible, yet wouldn't fit into traditional academic departments. We seek applicants who can think boldly across disciplinary boundaries in areas such as environmental sensing, connecting people to changes in their environment, new frontiers in citizen science, efficient techniques to sense and reduce greenhouse gas emission, development and rapid exploitation of new "green" power sources, energy distribution and storage, new approaches to energy conservation, behavior change at local and policy levels to encourage conservation and transition away from carbon-emitting fuel, geo-engineering, and new technologies for mitigating the effects of climate shift.

Successful candidates will be expected to: establish and lead their own research group within the Media Lab; pursue creative work of the highest international standard; engage in collaborative projects with industrial sponsors and other Media Lab research groups, supervise master's and doctoral students and participate in the Media Arts and Sciences academic program.

To apply, please fill out the application at apply.interfolio.com/28496

APPLICATION DEADLINE: March 15, 2015

Appointments will be within the Media Arts and Sciences academic program, principally at the Assistant Professor level.

MIT is committed to building a culturally diverse educational environment; women and minorities are strongly encouraged to apply. EOE.

program in media arts & sciences

http://web.mit.edu

POSITIONS OPEN

ETH zürich

Assistant Professor (Tenure Track) of Biochemical or Nanomaterials Engineering

→ The Institute for Chemical and Bio-engineering of the Department of Chemistry and Applied Biosciences (www.chab.ethz.ch) at ETH Zurich invites applications for the above-mentioned position.

→ The successful candidate should demonstrate a strong background in biochemical engineering and chemistry and the potential to develop an ambitious, world-class program in emerging areas of biochemical and nanomaterial engineering.

→ Candidates should have a PhD degree in chemical engineering, bioengineering, or a related field and have an excellent international record of accomplishments. The successful candidate will be expected to teach undergraduate level courses (German or English) and/or graduate level courses (English) in chemical and biochemical engineering.

→ This assistant professorship has been established to promote the careers of younger scientists. The initial appointment is for four years with the possibility of renewal for an additional two-year period and promotion to a permanent position.

→ **Please apply online at www.facultyaffairs.ethz.ch**

→ Applications should include a curriculum vitae, a list of major achievements, a list of refereed publications, a teaching statement and a five year research plan. The letter of application should be addressed **to the President of ETH Zurich, Prof. Dr. Lino Guzzella. The closing date for applications is 31 May 2015.**
ETH Zurich is an equal opportunity and family friendly employer and is further responsive to the needs of dual career couples.
We specifically encourage women to apply.

By **Elisabeth Pain**

Follow your star

Theoretical physicist Ulf Leonhardt is not afraid to pursue audacious scientific ideas. Leonhardt is best known for his work on how metamaterials—materials engineered to have properties not found in nature—can be used to fashion invisibility devices and how fiber optics can be used to produce analogs of the event horizon, the point of no return in black holes. Last December at the TEDxBrussels conference, *Science* Careers asked Leonhardt, a professor of physics at the Weizmann Institute of Science in Rehovot, Israel, to share his thoughts about his research and career. The interview has been edited for brevity and clarity.

Q: What qualities are necessary to succeed as a scientist?
A: Be stubborn. Believe in yourself. Don't do what others are saying. Also very important is to stand up again and again. You will fall all the time. There will be disasters, small and great.

Each step in my career began with disasters. I studied for 1 year at Moscow State University to become a specialist in high-energy physics. I didn't really like that, so I started over. I then did my master's degree in half a year, so I almost caught up. For my Ph.D., which I did in the former East Germany, I started a project in the atomic physics of hot, dense plasmas. I worked for 2 years in this subject, but then I decided to start again. So, instead, I did a Ph.D. in quantum optics in one of the newly founded Max Planck Research Groups. I did the Ph.D. in 1 year and 3 months, so at the end I was really on time for a Ph.D., even though I had failed the initial phase.

And so it went, on and on. Usually the first attempt fails, but you learn from it. Maybe you don't even learn all the time, but from the beginning, you should not be afraid of failure.

"There will be disasters, small and great."

Q: How did you find a permanent position?
A: I had fellowships until the point when I got a full professorship, so I never went through the hurdles of a tenure-track or lecturer position. This keeps you independent and active, and you're not forced to adjust to the academic system at an earlier stage. For theorists, I think this is an approach that people should think about.

Q: What idea did you think would be hardest to pull off?
A: This is not really what happens. I've always felt that if I have an idea, it's going to work. Only when it fails do I realize that it doesn't. Then comes, usually, a long period of desperation, but the idea is lingering. Then suddenly a possible solution comes to mind.

It's not that you think it's crazy at first. You may think that there is a chance that it works, and it may not completely work, but you should always believe in it. It's surprising if something works the first time—usually it doesn't—so then you need to be persistent and try to correct it to make it work.

Q: Have people tried to dissuade you from following your ideas?
A: Of course, all the time. Whether it affects me or not depends on the people and the style of the discussion. If people criticize me in a nonscientific way, I completely ignore them because it's not an argument. If it's a scientific attack I take it seriously, and then I respond and I learn from it.

Q: Any advice for young scientists?
A: What I have observed in some very good young scientists is that they think too much about their careers. This is all wrong: Build yourself, not your CV. Otherwise, you succeed in the short term, but then you may burn out and lose the fun in science. Young scientists should first think about what they want to do. Know how science and the scientific establishment works, but don't take it too seriously. Listen to what other people are saying, but don't apply it automatically. Other people may see some aspects of your situation, but they don't have the knowledge of it all. Only you have that. ■

Elisabeth Pain is Science *Careers' contributing editor for Europe. For more on life and careers, visit sciencecareers.org. Send your story to SciCareerEditor@aaas.org.*

ILLUSTRATION: ROBERT NEUBECKER

Published by AAAS